DFT Perspectives on the Activity and Stability of Electrocatalysts

Calle Vallejo, Federico

Publication date:
2011

Document Version
Early version, also known as pre-print

DFT Perspectives on the Activity and Stability of Electrocatalysts

Federico Calle Vallejo

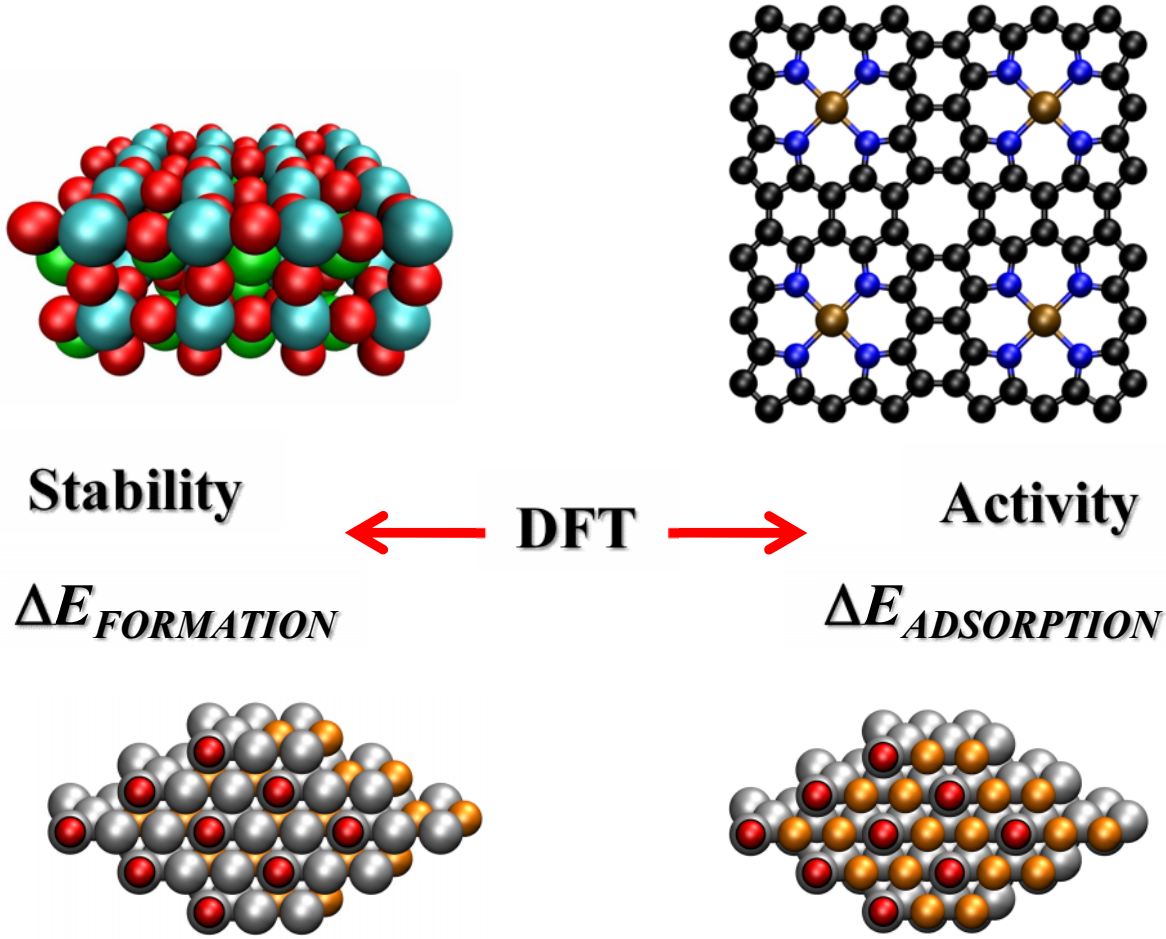

DFT Perspectives on the Activity and Stability of Electrocatalysts

Federico Calle Vallejo

PhD Thesis

December 2010

Center for Atomic-scale Materials Design

Department of Physics

Technical University of Denmark

DK-2800 Kgs. Lyngby, Denmark

CONTENTS

PART I: Perovskite Oxides

PREFACE

This thesis is submitted in candidacy for the PhD degree in Physics from the Technical University of Denmark (DTU). All the scientific material included here comes as the result of 3 years of research from November 1st 2007 to October 31st 2010 at the Center for Atomic-scale Materials Design (CAMD), Department of Physics, DTU, under the supervision of Associate Professor Jan Rossmeisl and the co-supervision of Professor Jens K. Nørskov.

ACKNOWLEDGEMENTS

After 3 years in Denmark there are many people to thank and memories to keep gratefully for the rest of my life. Let me commence from the very beginning by thanking Mogens Mogensen and Karin Vels Hansen, the people who, by considering and accepting my PhD application in July 2007, triggered the amazing chain of events that changed my life. I gratefully acknowledge financial support provided by the Danish Council for Strategic Research via the SERC project through the grant No. 2104-06-0011.

Moreover, I thank all the staff at CAMD for basing their research on a quiet and collaborative day-to-day work. The atmosphere in the group was essential for the advance of my projects and for my scientific growth. I specially acknowledge help and patience from José Ignacio Martínez, Juan María García and Tao Jiang. They introduced me into the world of DFT and atomic-scale physics and chemistry. Besides, I thank David Landis, André Kelkkanen, Jess Wellendorf Pedersen, Vladimir Tripkovic and the rest of the people who inhabited at some point during the past 3 years the fantastic office 254. I also wish to thank to Duncan Mowbray, Aleksandra Vojvodic, Klas Andersson, Frank Abild-Pedersen, Isabela Man, Nilay Inoglu, Hai-Yan Su, Ifan Stephens, and Alexander Bondarenko for all the hard work together. Thanks to Lone Bech, Ask Hjorth Larsen and Birgitte So-Young Ahn for writing the Resumé in Danish. Thanks as well to Francisco Pérez and Juan María García for proofreading this thesis.

Furthermore, this would not have been such an adventure if I had been alone. I had the joy of meeting five wonderful people who I consider now as friends: Nacho, Juanma, Paco, So-Young, and Billie. I thank them for all the shared moments, good and bad, and hope that the future will continue gathering us in nice and “cozy” places.

Finally, let me thank my family and friends in Colombia in a way that all of them can understand: in Spanish.Agradezco profundamente a mi familia y amigos por estos 3 años de constancia. A pesar de haber abandonado sus calles, de no rondar ya sus esquinas, de no aparecer en las fotos de los viernes en la noche ni en las de las reuniones familiares, los llevo a todos en mi corazón y sé que estoy en el de cada uno. Dedico a mis padres esta tesis y les pido que la consideren uno más de sus logros. Natalia, gracias por tu paciencia y tu cariño y por haber venido hasta aquí a reunir tus sueños con los míos.

ABSTRACT

In this thesis we use Density Functional Theory (DFT) simulations to demonstrate that trends in stability and activity of some selected electrocatalysts can be explained with simple physical and chemical considerations. Moreover, the trends can be used as a basis to pinpoint at appealing catalysts that may in the future be used in technological applications.

The main body of this dissertation consists of 3 parts:

The first part is mainly devoted to the thermodynamic stabilities of several families of perovskite oxides (AMO_3) and their activities towards the Oxygen Reduction and Evolution Reactions (ORR and OER, respectively). Moreover, we report our main conclusions about the energetics of their transition and dissociated states and their implications for Brønsted-Evans-Polanyi (BEP) relations.

The second part shows the results of our studies on graphene layers functionalized with 4 nitrogen atoms and transition metals for ORR and OER. Besides, we present a simple method to estimate the oxidation states of the transition metal atoms anchored to the active sites.

The third part focuses on alloys of Pt with transition metals. In this part we focused initially on Pt-Cu Surface Alloys (SAs) and Near-Surface Alloys (NSAs). Furthermore, we extended our observations to SAs and NSAs of Pt and late transition metals. Finally, we studied the trends in adsorption energies of NSAs of Pt with 3d, 4d, and 5d metals and several kinds of adsorbates. Since the trends cannot be rationalized within the d-band model, in each case we propose alternative models that have predictive power.

Our analyses are in most cases straightforward and easy to follow, and generally do not require the calculation of Densities of States (DOS) or d-band centers, since simpler and more intuitive variables such as d electrons or alloy compositions can be used instead, thereby saving computational time.

RESUMÉ

I denne afhandling bruger vi simuleringer inden for tæthedsfunktionalteori (Density Functional Theory/DFT) til at demonstrere, at tendenser i stabiliteten og aktiviteten af nogle udvalgte elektrokatalysatorer kan forklares med simple fysiske og kemiske betragtninger. Desuden kan disse tendenser bruges som basis for at fastslå passende katalysatorer, som muligvis i fremtiden kan finde teknologisk anvendelse.

Afhandlingen består overvejende af tre dele:

Første del omhandler hovedsageligt termodynamisk stabilitet i adskillige familier af perovskit-oxider (AMO_3) og deres aktiviteter i oxygenreduktions- og oxygenevolutionsreaktioner (henholdsvis Oxygen Reduction Reactions/ORR og Oxygen Evolution Reactions/OER). Endvidere rapporteres hovedkonklusionerne på energirelationerne for deres dissociation og overgangstilstande, samt betydningen for Brønsted-Evans-Polanyi-relationerne (BEP).

Anden del viser resultaterne af vores studier på graphenlag funktionaliseret med 4 nitrogenatomer og overgangsmetaller for ORR og OER. Desuden præsenteres en simpel metode til at estimere oxidationstilstandene af metalatomerne forankret til de aktive sider.

Tredje del fokuserer på legeringer af Pt med overgangsmetaller. I denne del fokuserer vi først på Pt-Cu-overfladelegeringer (Surface Alloys/SA'er) og næroverfladelegeringer (Near-Surface Alloys/NSA'er). Derudover udbygges vores observationer til SA'er og NSA'er af Pt og sene overgangsmetaller. Endelig studerer vi tendenser i adsorptionsenergierne fra NSA'er af Pt med 3d-, 4d-, og 5d-metaller og flere slags adsorbater. Eftersom tendenserne ikke kan rationaliseres inden for d-båndsmodellen, foreslår vi for hvert af tilfældene alternative modeller med gode forudsigelsesevner.

Vores analyser er i de fleste tilfælde ligetil og lette at følge. Generelt kræver de ikke beregning af tilstandstætheder (Densities of States/DOS) eller d-båndscentre, da mere simple og intuitive variable såsom d-elektroner eller legeringssammensætninger kan bruges i stedet, hvorved der spares beregningstid.

INTRODUCTION

"Mathematics would certainly have not come into existence if one had known from the beginning that there was in nature no exactly straight line, no actual circle, and no absolute magnitude."

Friedrich Nietzsche

I wanted to start my PhD dissertation in the same way as I did in my bachelor thesis in Colombia: with a quote by Nietzsche that describes my overall opinion about Science as a method for obtaining the closest factual approximation to an object of study. Throughout the work presented here, I have assumed the validity of several manmade abstractions of the universe tended to be called "natural laws" and represented formally by mathematical equations. They constitute the very basis of Science and suppose the existence in Nature of topological objects like straight lines, points, or perfect circles. From these laws one can create theories and models to explain certain phenomena which, in general, idealize the real situations in order to facilitate both the comprehension of their object of study and their mathematical solution [1-2]. Furthermore, these idealizations come from neglecting or assuming constant in the equations some terms believed to be less important than others. In the end, we evaluate the validity of the whole framework by its degree of approach to real phenomena, its consistency with other theories or models, and its predictive power.

On the other hand, I will not replicate here the well-known data about our current dependence in fossil fuels, their foreseen shortage in some years and the need of relying on sustainable and clean sources of energy that do not use expensive and/or scarce materials. One of the main advantages of the present global situation is that, at least, some future problems are known nowadays and the solutions are being sought. Since the times of the Industrial Revolution human kind has aimed to develop at all costs and it has only been recently that we are willing to do it sustainably.

One of the conditions for a "clean" progress is the replacement of internal combustion engines for transportation applications. Fuel cells appear to be a good alternative to those due to their characteristics. Nevertheless, these environmentally-friendly electrochemical devices may only be extensively used after solving two of their most remarkable problems at the cathode, where the ORR takes place: the high overpotential and the use of Pt, a scarce and expensive metal. In

order to tackle these problems several approaches can be taken. Along my PhD, I used DFT calculations to get insight into the following two: first, we tried to reduce the load of Pt used in the cathode by alloying with other elements. Second, we looked for other inexpensive cathode materials that could display similar or improved performance compared to Pt.

Our methodology for identifying promising candidate materials with DFT calculations consists basically of the following steps:

1) Calculation of the bulk structure of the selected material and determination of its stability.
2) Calculation of the surface structure of the selected material using as input the lattice parameters obtained in 1).
3) Calculation of the adsorption energies of the reaction intermediates on the optimized surface structures.
4) Determination of possible scaling relations between the adsorption energies of the reaction intermediates.
5) Construction of a volcano plot based on the scaling relationships and identification of active materials.
6) Analysis of trends in reactivity based on the d-band model if possible, or on the number of d electrons of the active site and the composition of the compounds.

1. THEORETICAL BACKGROUND

1.1. Electronic Structure Calculations [3-5]

The description of the structures and properties of neutral atoms, ions, molecules, and extended systems can be done with the Schrödinger equation. The stationary version of this equation is given in (1.1).

$$\left(\hat{T}_e + \hat{T}_n + \hat{V}_{en} + \hat{V}_{ee} + \hat{V}_{nn} + \hat{V}_{ext}\right)\Psi = E\Psi \tag{1.1}$$

In this equation, $\hat{T}$ and $\hat{V}$ are the kinetic and potential operators, respectively. The subscripts *e* and *n* refer to electrons and nuclei, while *ext* refers to an external influence. Equation (1.1) is an eigenvalue equation that provides the wave function (Ψ), which contains all the possible information about the system. Assuming the Born-Oppenheimer approximation to be valid, i.e. that the electronic and nuclei movements can be decoupled due to the large weight difference, the Hamiltonian operator that describes the electronic part of the wave function for a system with *M* electrons is given below, in atomic units.

$$\hat{H} = \hat{T} + \hat{V}_{ee} + \hat{V} \tag{1.2}$$

The kinetic operator is defined in Equation (1.3).

$$\hat{T} = \frac{-1}{2}\sum_{j=1}^{M}\nabla_j^2 \tag{1.3}$$

The electron-electron repulsion operator is given in Equation (1.4).

$$\hat{V}_{ee} = \frac{1}{2}\sum_{i\neq j}\frac{1}{\left|r_i - r_j\right|} \tag{1.4}$$

The one-body potential operator is given in Equation (1.5). This operator accounts for the Coulomb potential exerted by the nuclei over the electrons. It can also include other external potentials.

$$\hat{V} = \hat{V}_{en} + \hat{V}_{ext} = \sum_{j=1}^{M} \upsilon(r_j) \tag{1.5}$$

The solution of Equation (1.1) for many-body systems is not possible analytically. Therefore, there is a need to approximate the solutions to ground-state electronic structure problems with reasonable accuracy, but also with no prohibitive computer time consumption. There exist many approaches to solving this difficulty such as Hartree-Fock (HF), configuration interaction, coupled cluster, Møller-Plesset perturbation theory, and DFT. Instead of writing the ground-state energy in terms of Ψ, a function of 3*M* variables, DFT uses the electronic density, $n(r)$, which depends only on the 3 spatial coordinates. This enormous simplification on the number of parameters explains why DFT is the most widespread method of electronic structure calculation in condensed-matter physics and one of the most widely used in quantum chemistry.
The electronic density is subject to the two following physical constraints:

$$n(r) \geq 0 \tag{1.6}$$

$$\int n(r) d^3 r = M \tag{1.7}$$

1.1.1. Basics of DFT [3-5]

The ground-state energy (E_0) satisfies the variational principle:

$$E_0 = \min_{\Psi} \langle \Psi | \hat{H} | \Psi \rangle \tag{1.8}$$

This means that the energy of the ground state corresponds to the minimum expectation value of the Hamiltonian of the system. Since the one-body potential depends only on the density, we can define separately a universal operator *F*[*n*], independent of $\upsilon(r)$, as follows.

$$F[n] = \min_{\Psi \to n} \langle \Psi | \hat{T} + \hat{V}_{ee} | \Psi \rangle \tag{1.9}$$

In Equation (1.9), the minimization is over all antisymmetric wave functions yielding a given density n(r). *F*[*n*] is a functional of the density since it assigns a number to each density. The energy of the ground state can be obtained by reformulating (1.8) in the following way:

$$E_0 = \min_n \left\{ F[n] + \int \upsilon(r) n(r) d^3 r \right\} \tag{1.10}$$

Now the minimization takes place over all reasonable densities satisfying the constraints of Equations (1.6) and (1.7). Moreover, the exact electronic density of the system satisfies the following relation between the functional derivative of $F[n]$ and the one-body potential:

$$\frac{\delta F}{\delta n(r)} = -\upsilon(r) \tag{1.11}$$

These Equations prove that the energy is a functional of the electronic density. However, they do not state how to obtain that functional. In order to so, Kohn and Sham (KS) replaced the real system by a fictitious set of non-interacting electrons having the same electronic density as the real system. These electrons are still spin-½ fermions obeying the Pauli principle so their wave function can be represented by a Slater determinant, i.e. an antisymmetrized product of states of each spin, $\phi_{j,\sigma}(r)$, with $j = 1, \ldots, M$, and $\sigma = \uparrow, \downarrow$. The KS electrons satisfy a non-interacting Schrödinger equation:

$$\left\{ \frac{-1}{2} \nabla^2 + \upsilon_{s,\sigma}(r) \right\} \phi_{j,\sigma}(r) = \varepsilon_{j,\sigma} \phi_{j,\sigma}(r) \tag{1.12}$$

The coefficients $\varepsilon_{j,\sigma}$ and the functions $\phi_{j,\sigma}(r)$ are known as KS eigenvalues and eigenstates, respectively. Since the ground-state energy corresponds to the expectation value of the KS Hamiltonian, the energy in terms of KS quantities is summarized below.

$$E_0 = T_s + U + V + E_{xc} \tag{1.13}$$

The terms in the right hand side of this equation correspond, in that order, to the kinetic energy, the Hartree electrostatic self-repulsion of the electron density, the one-body potential, and the exchange-correlation energy. The latter is explained in detail in the next subsection and the Hartree energy is defined below.

$$U = \frac{1}{2} \int d^3 r \int \frac{n(r) n(r')}{|r - r'|} d^3 r' \tag{1.14}$$

1.1.2. Exchange-correlation Energy [3-5]

The exchange-correlation energy is normally the smallest contribution to the total energy in Equation (1.14). However, the contribution from E_{XC} is typically about 100% or more of the chemical bonding or atomization energy. Consequently, E_{XC} is generally identified as the "glue" without which atoms would bind weakly if at all, and accurate approximations are essential for DFT to be of practical usefulness.

Traditionally, E_{XC} is decomposed into exchange and correlation. E_X is due to the Pauli exclusion principle and is usually the largest contribution to E_{XC}. It can be exactly determined with HF. Moreover, E_C is due to correlations, which are said to be any effects not considered by the other terms in Equation (1.13). Therefore, the exact value of this term is uncertain. The standard approximations (but not the only existing ones) to calculate E_{XC} include the Local Density Approximation (LDA), the Generalized Gradient Approximation (GGA), and the hybrids.

- The LDA exchange-correlation energy is shown in Equation (1.15).

$$E_{XC}^{LDA} = \int e_{XC}^{unif}\left(n_\uparrow(r), n_\downarrow(r)\right) d^3r \tag{1.15}$$

In this expression, $e_{XC}^{unif}\left(n_\uparrow(r), n_\downarrow(r)\right)$ is the exchange-correlation energy per particle for an electron gas of uniform spin densities $n_\uparrow(r), n_\downarrow(r)$, and is a known expression.

- The GGA exchange-correlation energy is shown in Equation (1.16).

$$E_{XC}^{GGA} = \int f\left(n_\uparrow(r), n_\downarrow(r), \nabla n_\uparrow(r), \nabla n_\downarrow(r)\right) d^3r \tag{1.16}$$

In this expression, *f* is an exchange-correlation energy per particle that depends on the spin densities and their gradients. That function is not unique and thus several GGAs exist. The most widespread GGAs are PBE, PW91, and RPBE. The latter is said to have improved performance for the estimation of adsorption energetics [6].

- The hybrid exchange-correlation energy is shown in Equation (1.17).

$$E_{XC}^{HYB} = a\left(E_X - E_X^{GGA}\right) + E_{XC}^{GGA} \quad (1.17)$$

Hybrid functionals mix in a fixed fraction the exact exchange from HF with the GGA exchange. The most widespread hybrids are PBE0 and B3LYP.

Table 1.1 summarizes the performance of various approximations for the calculation of atomization energies of some molecules.

Table 1.1. Mean Absolute Error (MAE) of the atomization energies for 20 molecules, evaluated by various approximations. Adapted from Refs. [3-4].

Approximation	MAE (eV)
Unrestricted HF	3.1 (underbinding)
LDA	1.3 (overbinding)
GGA	0.3 (mostly overbinding)
Hybrid	0.15
Desired "chemical accuracy"	0.05

1.2. Basic Thermodynamics

1.2.1. Gibbs Energies of Reaction and Formation

The Gibbs energy of a chemical reaction is defined as the difference between the Gibbs energies of the products and the reactants. This convention applies as well to adsorption reactions. According to this, when the reactants X_i (with i = 1 to L, being L the total number of reactants) combine with each other with stoichiometric coefficients α_i to give Z_j products ((with j = 1 to N, being N the total number of products) with stoichiometric coefficients γ_i, the chemical reaction and the Gibbs energy of reaction are given by Equations (1.18) and (1.19). Moreover, if reactants and products are in their standard state at 298.15 K and 1 atm of pressure, we obtain the standard Gibbs energy of reaction (ΔG_{rxn}^0).

$$\alpha_1 X_1 + \alpha_2 X_2 + ... \rightarrow \gamma_1 Z_1 + \gamma_2 Z_2 + ... \quad (1.18)$$

$$\Delta G_{rxn} = \sum_{i=1}^{L} \gamma_i G_{Z_i} - \sum_{j=1}^{N} \alpha_i G_{X_i} \quad (1.19)$$

Moreover, if the reactants X_i are the monatomic or diatomic elements that compose a single product Z, we have a reaction whose energetics is said to be the formation energy of Z. Besides, if reactants and products are in their standard state at 298.15 K and 1 atm of pressure, we obtain the standard Gibbs energy of formation. As an example, the following reaction gives the formation energy of the perovskite oxide $LaNiO_3$.

$$La + Ni + \frac{3}{2} O_2 \rightarrow LaNiO_3 \quad (1.20)$$

$$\Delta G_f = G_{LaNiO_3} - G_{La} - G_{Ni} - \frac{3}{2} G_{O_2} \quad (1.21)$$

1.2.2. Relation between Gibbs Energy and Cell Potential

The standard Gibbs energy of reaction (ΔG^0_{rxn}) in an electrochemical cell is related to the reversible cell voltage ($\Delta E^0_{cell} = E^0_{cathode} - E^0_{anode}$) in the following way:

$$\Delta G^0_{rxn} = -n \Delta E^0_{cell} \quad (1.22)$$

In Equation (1.22), n is the number of electrons transferred along the reaction. In fuel cells, important electrochemical devices, $\Delta E^0_{cell} > 0$ and thus $\Delta G^0_{rxn} < 0$, which implies that the reaction is spontaneous.

In practice, when electronic current is drawn from the fuel cell, the voltage decreases with increasing current density. The reversible cell voltage is not realized even under open-circuit (zero current) conditions due to the irreversibilities associated with the operation of the cell. The difference between the actual cell voltage at a given current density and the reversible cell

voltage is known as overvoltage (overpotential when referring to a single electrode), and various factors for its appearance in fuel cells will be explained in Subsection 1.3.2.

1.2.3. Gibbs energies of formation within DFT. Conventions and simplifications

The way we calculate free energies of substances is the following:

$$G = E^{DFT} + ZPE - TS \tag{1.23}$$

Where E^{DFT} is the total energy given by DFT simulations, *ZPE* is the zero-point energy calculated from vibrational analyses, and *TS* is the product of Temperature and Entropy [7]. In the calculation of the Gibbs energies of formation we neglect the entropy (S) and zero point energy effects (ZPE) in the bulk crystals, i.e. $G_{crystal} \approx E^{DFT}{}_{crystal}$, and consider only those of gas-phase molecules. These quantities have been previously estimated from vibrational analyses for some representative metals and metal oxides, and were found to modify free energies of formation in less than 0.1 eV [8]. Moreover, the omission of the entropy of crystals is a common approximation in thermodynamics when calculating reaction energies [9].

There exist well-known limitations in O_2 description by DFT, and some alternatives have been proposed to circumvent the problem, obtaining remarkable agreements with experimental data [8, 10]. We find a trustworthy value for the total energy of oxygen indirectly from the tabulated standard Gibbs energy of formation of water and from the DFT energies of H_2 and H_2O, which are accurately described by the GGA-RPBE functional [6]. The reaction of formation of water and its Gibbs energy of formation are given below.

$$H_2 + \frac{1}{2}O_2 \rightarrow H_2O \tag{1.24}$$

$$\Delta G^{f}_{H_2O} = G_{H_2O} - G_{H_2} - \frac{1}{2}G_{O_2} \tag{1.25}$$

The total DFT energy of O_2 can be obtained by combining Equations (1.23) and (1.25), at given temperature and pressure conditions. The analytical expression is the following:

$$E^{DFT}_{O_2} = 2\left[\left(E^{DFT}_{H_2O} - E^{DFT}_{H_2}\right) + \Delta ZPE^{f}_{H_2O} - T\Delta S^{f}_{H_2O} - \Delta G^{f}_{H_2O}\right] \tag{1.26}$$

1.3. Fuel Cells

1.3.1. Description and Classification of Fuel Cells [11-13]

Fuel cells are electrochemical devices that directly convert chemical energy into electrical energy. They have zero or ultra-low emissions of pollutants and particulates and reduced noise emissions. The reactants (fuel and oxidant) are continuously fed to the system, where the free energy coming from their spontaneous oxidation and reduction processes is utilized to produce electricity. Fuel cells consist basically of two electrodes, anode and cathode, and an electrolyte medium between them. A schematic plot of these devices is shown in Figure 1.1.

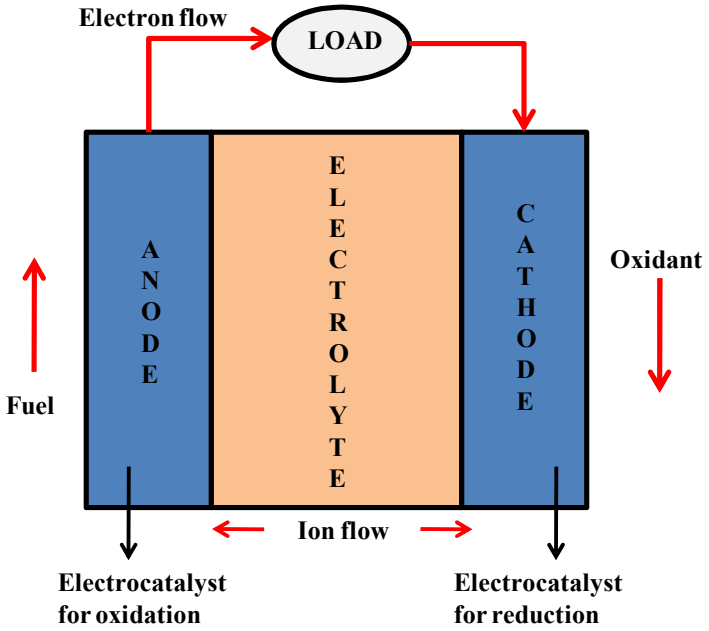

Figure 1.1. Schematic plot of fuel cells. Adapted from Ref. [11].

The electrochemical oxidation of the fuel takes place at the anode, while the cathode promotes the electrochemical reduction of the oxidant. In both electrodes catalyst loadings promote the half-cell reactions. The ions generated during the oxidation or reduction reactions are transported from one electrode to the other through the ionically conductive but electronically insulating electrolyte. In this way, the electrons generated at the anode during oxidation pass through the external circuit, hence generating electricity, and reach the cathode, where they complete the reduction reaction.

Fuel and oxidant do not mix at any point, and no actual combustion occurs. Therefore, fuel cells are not thermal machines and their performance is not limited by the Carnot Efficiency. Theoretically, although not practically, fuel cells can yield 100% efficiency.

There exist several kinds of fuel cells that can be classified according to their cell reactions, electrolytes, among others. Table 1.2 summarizes the different classes of fuel cells, their cathodic and anodic reactions and operating temperature, based generally on the temperature required to reach acceptable conductivity of the electrolyte.

Table 1.2. Classification of fuel cells. Adapted from Refs. [11, 13]. PEM, Proton Exchange Membrane; YSZ, Yttria-Stabilized Zirconia.

Fuel Cell	Electrolyte	Temperature	Electrode Reactions
PEM	PEM	60-90 ºC	Anode: $H_2 \leftrightarrow 2H^+ + 2e^-$
			Cathode: $O_2 + 4(H^+ + e^-) \leftrightarrow 2H_2O$
Direct Methanol	PEM	20-90 ºC	Anode: $CH_3OH + H_2O \leftrightarrow CO_2 + 6(H^+ + e^-)$
			Cathode: $\frac{3}{2}O_2 + 6(H^+ + e^-) \leftrightarrow 6H_2O$
Alkaline	KOH	80 ºC	Anode: $H_2 + 2OH^- \leftrightarrow H_2O + 2e^-$
			Cathode: $\frac{1}{2}O_2 + H_2O + 2e^- \leftrightarrow 2OH^-$
Phosphoric acid	H_3PO_4	180-220 ºC	Anode: $H_2 \leftrightarrow 2H^+ + 2e^-$
			Cathode: $O_2 + 4(H^+ + e^-) \leftrightarrow 2H_2O$
Molten Carbonate	Li_2CO_3/K_2CO_3	650 ºC	Anode: $H_2 + CO_3^{2-} \leftrightarrow H_2O + CO_2 + 2e^-$
			Cathode: $\frac{1}{2}O_2 + CO_2 + 2e^- \leftrightarrow CO_3^{2-}$
Solid Oxide	YSZ	800-1000 ºC	Anode: $H_2 + O^{2-} \leftrightarrow H_2O + 2e^-$
			Cathode: $\frac{1}{2}O_2 + 2e^- \leftrightarrow O^{2-}$

The different types of electrolytes are aqueous and non-aqueous solutions, ionically conducting polymers, molten salts and solid-state ionic materials. The required functionalities that electrolytes for fuel cells must have are the following:

● High specific electrolyte conductivity

● High chemical stability in oxidizing and reducing environments

● High electronic resistance to avoid ohmic shorting of the fuel cell

● Good structural stability

● Low permeability for fuel and oxygen

● Low cost

1.3.2. Overpotential in Fuel Cells

As mentioned in Subsection 1.2.2, the combined sources of overvoltage cause the cell potential to decrease with increasing current density, thus reducing the efficiency of these devices. The most prominent sources of overvoltage in a PEM fuel cell are listed below.

● Mixed potential at the electrodes: it arises due to unavoidable parasitic reactions that tend to lower the equilibrium electrode potential. Most of the times, they are caused by the crossover of fuel through the electrolyte and oxidation of the catalyst and/or support at the cathode. The mixed potential is the dominant source of losses at open circuit conditions.

● Activation overpotential (η_{ORR}): the so-called cathode overpotential, originated by the sluggish kinetics of the oxygen reduction reaction (ORR) at the cathode [14]. It is most pronounced at low current density values (~0-100 $mAcm^{-2}$) [12].

● Ohmic losses (ΔE_{ohmic}): they are resistive losses due to both electronic contact resistances between the flow fields and the diffusion media as well as the ohmic

resistance due to proton conduction through the membrane [14]. Their effect is most significant at intermediate current densities (~100-500 $mAcm^{-2}$) [12].

● Concentration overpotential (η_{tx}): incurred by poor O_2-transport through the diffusion medium and the electrode layer. Gasteiger et al showed that both kinetic and mass-transport losses of the hydrogen electrode (anode) can be neglected [14]. The concentration overpotential is considerably large at high current densities (>500 $mAcm^{-2}$) [12].

Figure 1.2 shows a typical polarization curve, extracted from Ref. [12].

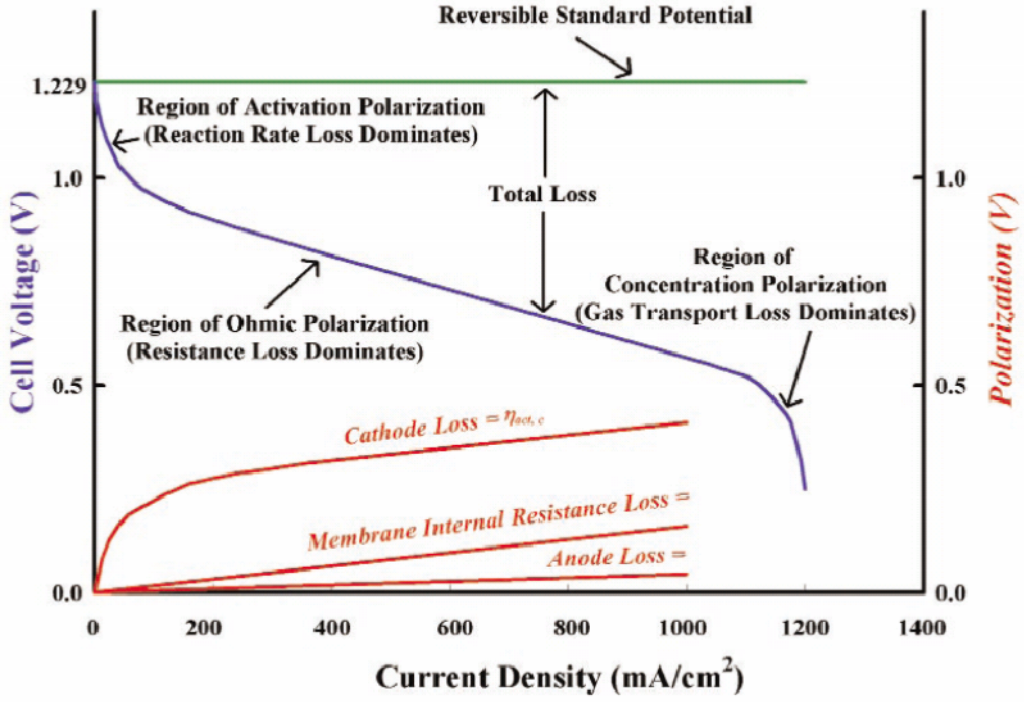

Figure 1.2. Typical polarization curve of a fuel cell including the reversible standard potential (green), the actual potential of the cell (blue) and the losses (red). Taken from Ref. [12].

1.3.3. Challenges for Future Spread of Fuel Cells [11, 13]

Generalized application of fuel cells for portable applications, stationary applications and ultimately for automotive applications, has not been achieved yet due to the expensive materials required for their production and their relatively low lifetime compared to competitive technologies. Each type of fuel cell has its own advantages and limitations:

Alkaline fuel cells allow the use of non-precious catalysts because of the facile oxygen reduction kinetics at high pH, but if CO_2-containing reactants are used, carbonates precipitate in the electrolyte, leading to increased electrolyte resistance and structural destruction of the electrodes. On the other hand, molten carbonate fuel cells have sealing problems, operate at high temperatures (precluding rapid start-up), and suffer from electrode corrosion. In spite of their high performance, solid oxide fuel cells also have low start-up, limited electrolyte conductivity, and cathode losses. Currently, reduction of the operating temperature without compromising the efficiency is a challenge in these fuel cells.

There is current interest in running PEM fuel cells at temperatures over 100 °C to minimize the poisoning of CO_2 impurities in the fuel stream, enable fast heat removal with a radiator of reasonable size (for transportation applications), and to enhance reaction kinetics and ease water management. In order to do this, the properties of the membranes currently used, e.g. Nafion, need to be improved so that they have high conductivities at elevated temperatures and low relative humidity [12]. Moreover, another important challenge of PEM fuel cells is a significant improvement of the ORR kinetics at the cathode [12, 14]. This can be done in 2 ways: alloying Pt with other elements to increase its catalytic activity towards ORR [15-17]; and searching for alternative inexpensive materials such as oxides [18-19], and/or carbon-based materials [20-21]. In the following chapters we will study in detail both options taking into account the activity and stability of electrocatalysts, from the perspective offered by DFT calculations.

2. THERMODYNAMIC STABILITY OF PEROVSKITE OXIDES [22]

2.1. Introduction

Perovskite oxides have the chemical formula AMO_3. The ideal crystal structure of perovskites, corresponding to the Pm3m space group, is shown in Figure 1. The M site is coordinated to 6 oxygen atoms, 4 in the xy plane and 2 in the z axis, one below and another over M. These MO_6 complexes form an octahedral framework in which the interstices are occupied by A atoms, which are 12-fold coordinated to the surrounding oxygen atoms. Therefore, for a given pair of atoms X and Y the A position should be occupied by that with the largest ionic radius, the smallest should occupy the M site, and the sum of the oxidation states of both should be +6. This is the reason why, in general, A is an alkaline metal like Li, Na, or K, i.e. a metal with an oxidation state +1; an alkaline-earth metal like Mg, Ca, Sr or Ba, i.e. a metal with an oxidation state +2 ; or a rare-earth element like Sc, Y, La, or Ce, i.e. a metal with an oxidation state +3. On the other hand, M is usually a transition metal with an oxidation +5, +4, or +3, respectively. Metal trioxides MO_3 are a special member of this group of oxides, since they are considered to be perovskites with complete A-site vacancies and M having +6 as oxidation state.

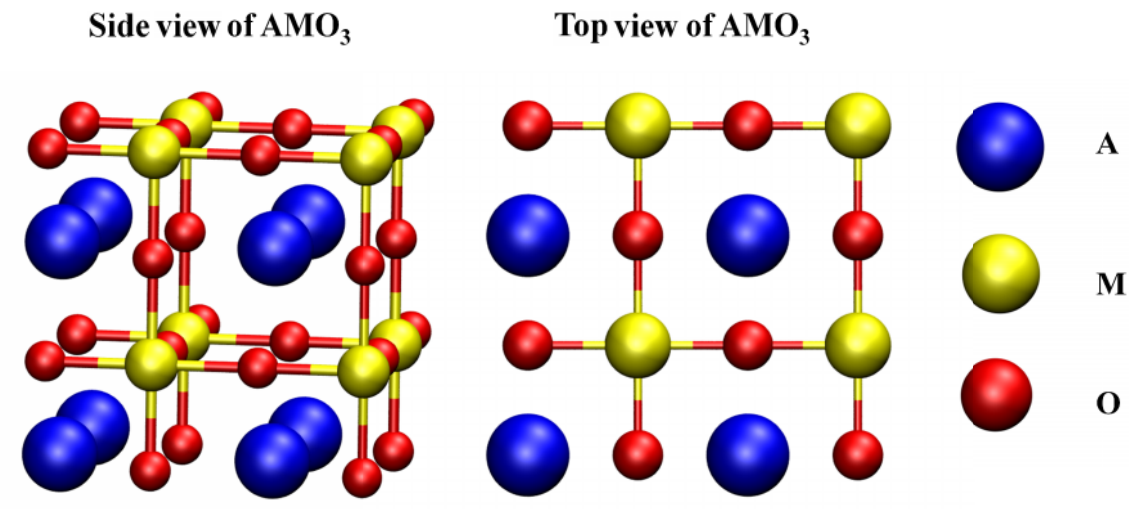

Figure 2.1. Side and top views of the ideal cubic structure of a perovskite oxide, repeated twice in each direction. Blue spheres represent A atoms, yellow spheres correspond to M atoms, and oxygen atoms appear as red spheres.

Perovskite oxides possess a large variety of applications as dielectrics and piezoelectrics [23], ferroelectrics [24] and/or ferromagnetic materials [25-26], among others. In particular, rare-earth and alkaline-earth perovskites are useful as catalysts for hydrogen generation [27], as oxidation catalysts for hydrocarbons [28], and as effective and inexpensive electrocatalysts for state-of-the-art fuel cells [29-30], mainly due to the possibility of tuning their mixed ionic-electronic conductivity, done via A and M substitution and subsequent oxygen vacancy formation. Despite the general interest in perovskites, before our studies there had been no ab initio studies devoted to their formation energies, and the overall trends in stability were unknown.

2.2. Deviations from the Ideal Perovskite Structure

Perovskite oxides not only exist in the ideal cubic structure shown in Figure 2.1. There exists a variety of distorted, non-cubic structures with lower symmetries [31]. The distortions tend to occur as a tilting in MO_6 complexes and/or by an enlargement/stretch of the M-O distances. The origin of these distortions is attributed in chemistry to the size of the ions [31] and in physics to the Jahn-Teller and pseudo Jahn-Teller effects [32].

2.2.1. Chemical Approach to Distortions in Perovskites [31-32]

The chemical approach to why structural distortions occur in perovskite oxides is that the atoms occupying the A and/or the M sites do not have the right size to fit in the ideal cubic structure. Furthermore, there exists a "tolerance" factor (t) or Goldschmidt factor, created to estimate how well the sizes of a particular combination of atoms meet the requirements for an ideal perovskite. The definition of the tolerance factor is given by Equation (2.1).

$$t = \frac{\sqrt{2} r_{A-O}}{2 r_{M-O}} \tag{2.1}$$

An ideal perovskite should have a t value of 1, but in practice cubic perovskites can form in the range $0.9 < t < 1.0$. For $t > 1$ the M site larger than necessary. For instance, $BaTiO_3$ has $t = 1.06$ and even though the structure is tetragonal at room temperature, it is basically a perovskite in which Ti displace towards one of the surrounding oxygen atoms. This kind of distortion is known as ferroelectric instabilities. For larger deviations from $t = 1.0$, the ion in the M position

demands a smaller site of lower coordination, as in $BaSiO_3$ which has tetrahedral Si complexes, and the perovskite structure vanishes.

For tolerance factors in the range, $0.85 < t < 0.90$, the atom in the A site is too small for its site and the MO_6 octahedra are tilted in an alternating, zigzag fashion as in $GdFeO_3$. The tilting has the effect of reducing the size of the A site and therefore the coordination number is reduced from 12 to 8.

Finally, for AMO_3 with $t < 0.85$ the perovskite structure is no longer stable and the atom in the A site requires a smaller site, as in the case of $LiNbO_3$ and $FeTiO_3$ where both sites are octahedral.

2.2.2. Physical Approach to Distortions in Perovskites [32-33]

The physical approach to why structural distortions occur in perovskites deals with orbital filling and symmetry considerations. In MO_6 octahedra the five levels coming from the d orbitals of M are split into a low-energy triplet and a high-energy doublet belonging to t_{2g} and e_g irreducible representations, respectively. The orbital splitting in octahedral complexes is shown in Figure 2.2.

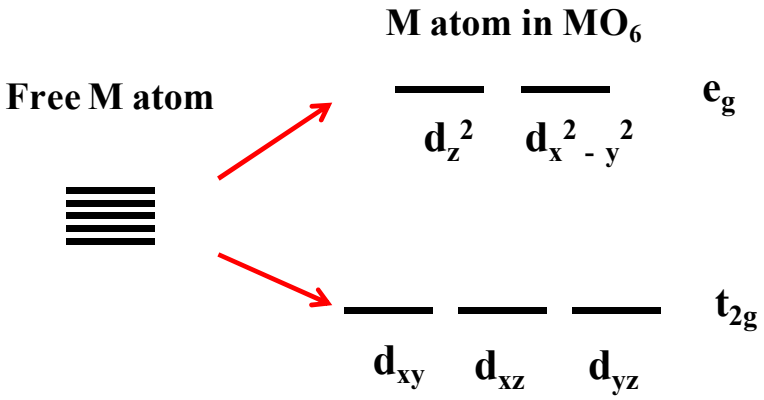

Figure 2.2. Orbital splitting in MO_6 complexes. The splitting causes the formation of a high-energy doublet and a low-energy triplet.

If the filling of t_{2g} is uneven, meaning that the occupation in all orbitals is not identical, there will be a weak distortion in the octahedron, due to the degeneracy of the electronic ground state. Moreover, if the filling of e_g is not uniform, there will be a strong distortion in the octahedron. These deformations in the MO_6 octahedra are explained by the Jahn-Teller (JT) theorem: "any nonlinear system with a degenerate electronic ground state will undergo geometrical distortions

that will remove the degeneracy and lower the overall energy". These distortions consist of enlargements of the M-O distance within a given axis, e.g. z, and a stretch in the other two, e.g. x and y. Table 2.1 shows the presence of JT distortions and their strength.

Table 2.1. Presence of Jahn-Teller (JT) distortions and their strength in MO_6 complexes in high-spin and low-spin configurations. N_d corresponds to the number of d electrons of M, W stands for weak JT distortions, S for strong JT distortions, and N for no distortions.

N_d	1	2	3	4	5	6	7	8	9	10
High spin	W	W	N	S	N	W	W	N	S	N
Low spin	W	W	N	W	W	N	S	N	S	N

On the other hand, when there is not a strict degeneracy between electronic states but they are close in energy, the so-called pseudo Jahn-Teller (PJT) effect may produce severe deformations such as zigzag tilting of the octahedra and off-centre displacements. When these distortions are cooperative phenomena in these crystals, i.e. they alter the whole framework and have long-range coherence; they can be responsible for the ferroelectricity of some perovskites.

Due to the interactions between adjacent octahedra in the lattice, the JT and PJT distortions become cooperative phenomena, thus altering the whole framework and having long-range coherence. This cooperative PJT effect is responsible for the ferroelectricity of some perovskites like $BaTiO_3$.

2.3. Experimental vs. Calculated Formation Energies

Among the available theoretical techniques to investigate perovskites, DFT is an appealing candidate since it has proved useful for understanding metals and alloys at the atomic scale [16, 34-35]. Nevertheless, the well-known shortcoming of DFT to describe strongly correlated systems has prevented its use for the estimation of properties such as band gaps or electron localization-delocalization of oxides, and there are numerous corrections like LDA+U, GGA+U and GW [36-38]. Despite these limitations, Figure 2.3.a) shows the experimental Gibbs energies of formation from elements and O_2 of 20 perovskites at 298 K and the calculated Gibbs energies

of formation with standard DFT, using the RPBE-GGA [6] exchange-correlation functional. The simulations are able to reproduce trends in the formation energies, except that the calculated energies are shifted by ~0.75 eV compared to experiments.

Moreover, it is possible to combine the formation energies of these compounds with those of their sesquioxides (A_2O_3 and M_2O_3), rutile dioxides (MO_2), monoxides (AO and MO), and O_2 to reproduce the energetics of several reactions (Figures 2.3.b), 2.3.c), 2.3.d)). The reactions in Figure 2.3 are described below.

Reactions taking place in Figure 2.3.a) in the main text can be summarized by Equation (2.2). In all of the following reactions O_2 is in gas phase and the other compounds are crystalline.

$$(1-x)\,A' + xA'' + M + \frac{3}{2}O_2 \rightarrow A'_{1-x}\,A''_{x}\,MO_3 \tag{2.2}$$

In Equation (2.2) A' is either La or Y and A'' is either Ca, Sr, Ba; x denotes the Sr content in the perovskite (ranging from 0 to 1). In the case of doped perovskites A' is only La and A'' is only Sr. Reactions used in Figure 2.3.b) can be summarized by Equations (2.3) and (2.4).

$$\frac{1}{2}A'_2O_3 + MO + \frac{1}{4}O_2 \rightarrow A'MO_3 \tag{2.3}$$

$$A''O + MO + \frac{1}{2}O_2 \rightarrow A''MO_3 \tag{2.4}$$

Reactions used in Figure 2.3.c) can be summarized by Equation (2.5).

$$\frac{(1-x)}{2}A'_2O_3 + xA''O + \frac{1}{2}M_2O_3 + \frac{x}{4}O_2 \rightarrow A'_{1-x}\,A''_{x}\,MO_3 \tag{2.5}$$

In Equation (2.5) A' is La and A'' is either Sr; x denotes the Sr content in the perovskite (ranging from 0 to 1). Reactions used in Figure 2.3.d can be summarized by:

$$\frac{1}{2}A'_2O_3 + MO_2 \rightarrow A'MO_3 + \frac{1}{4}O_2 \quad (2.6)$$

$$A''O + MO_2 \rightarrow A''MO_3 \quad (2.7)$$

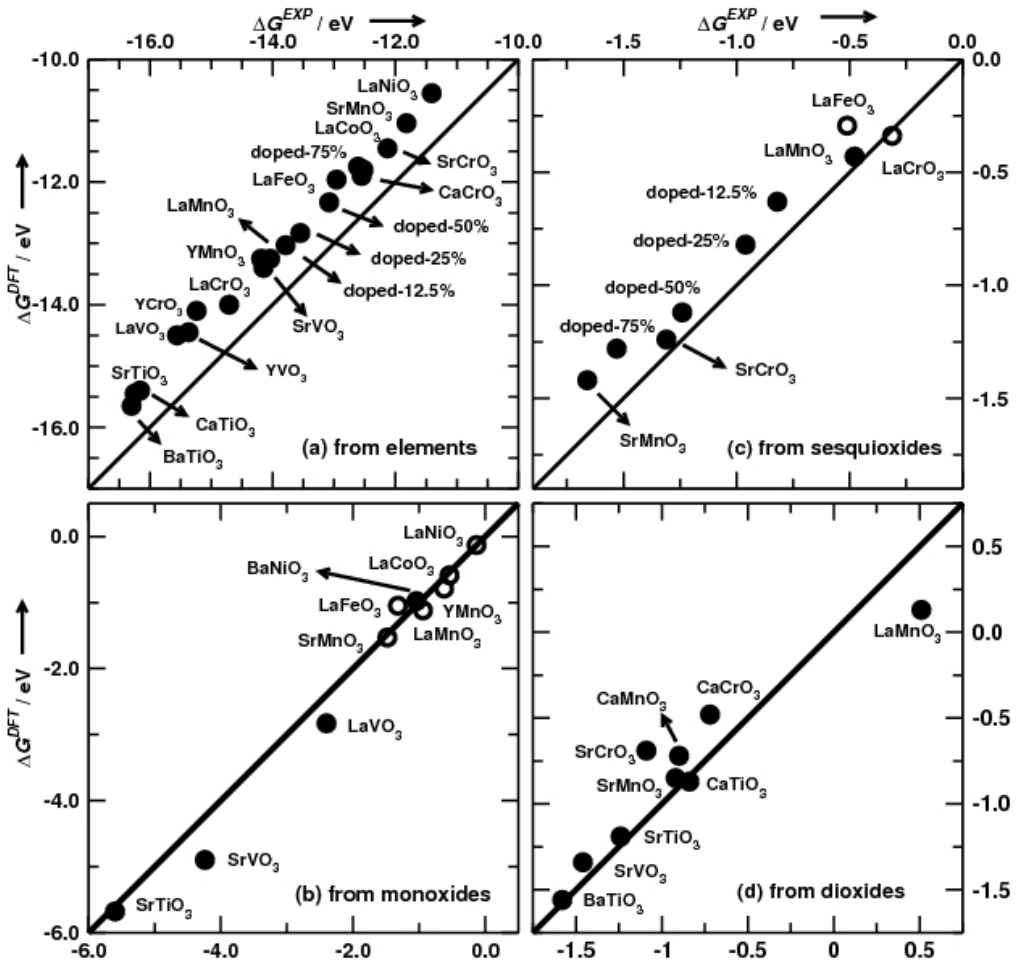

Figure 2.3. DFT calculated free energies of several reactions versus experimental values available in the literature, from (a) A = Y, La, Ca, Sr, Ba, and elements; (b) A_2O_3/AO and monoxides; (c) A_2O_3/AO and sesquioxides; and (d) A_2O_3/AO and dioxides. As a guide to the eye, the perfect agreement is marked with a y=x line. The percentage in the doped perovskites represents the amount (x) of Sr in $La_{1-x}Sr_xMnO_3$. Reactions at 298 K are represented by (●), whereas (○) denote reactions at 1273 K. References for the experiments and the actual numbers in the plot are provided in the Appendix A.

In equation (2.6) A' is La and in (2.7) A'' is either Ca, Sr, or Ba. The formation energies of the rutile oxides appearing in the formation energies of Figure 2.3.d) are taken from Ref [8]. The formation energies at 298 K of the monoxides and sesquioxides appearing in the aforementioned reactions are shown in the Appendix A. In all cases the reaction energies are calculated as the difference between the Gibbs energies of products and reactants, as shown in Chapter 1.

The excellent correspondence between experiments and theory in Figures 2.3.b), c), d), shows that DFT very accurately captures the mixing energies between oxides, i.e. when oxides are present both in the reactants and the products of the reactions. This is of paramount importance to support the idea that our calculations can accurately predict trends in adsorption energies, as will be shown in a later chapter.

The origin of the ~0.75 eV shift in Figure 2.3.a) may be attributed to several factors. The limitations in O_2 description by DFT are well known and some alternatives have been proposed, obtaining remarkable agreements with experiments [8, 38]. We obtain the total DFT energy of O_2 indirectly from the tabulated Gibbs energy of formation of water and from the DFT energies of H_2 and H_2O, which are accurately described using the exchange achieved by the RPBE-GGA functional, as shown in Chapter 1 [38-39]. This reference had previously been used to obtain accurate formation energies of rutile oxides and had also been applied to calculate the adsorption energies of various oxides, including some lanthanum perovskites [8, 40]. The reason for the shift is therefore not due to the reference state. We speculate that the localized nature of d-electrons of the 3d metals in these perovskites is not well captured at this level of theory due to their self-interaction, giving rise to a large part of the constant shift in Figure 2.3.a).

2.4. Trends in Formation Energies

In spite of the aforementioned shift, the differences in formation energies between perovskites are very accurately accounted for by standard DFT, as shown in Figure 2.4. We remark that the use of another exchange-correlation functional or a different value for O_2 would only shift the calculated stabilities by a constant number, while the qualitative trends and the relative differences would remain unchanged.

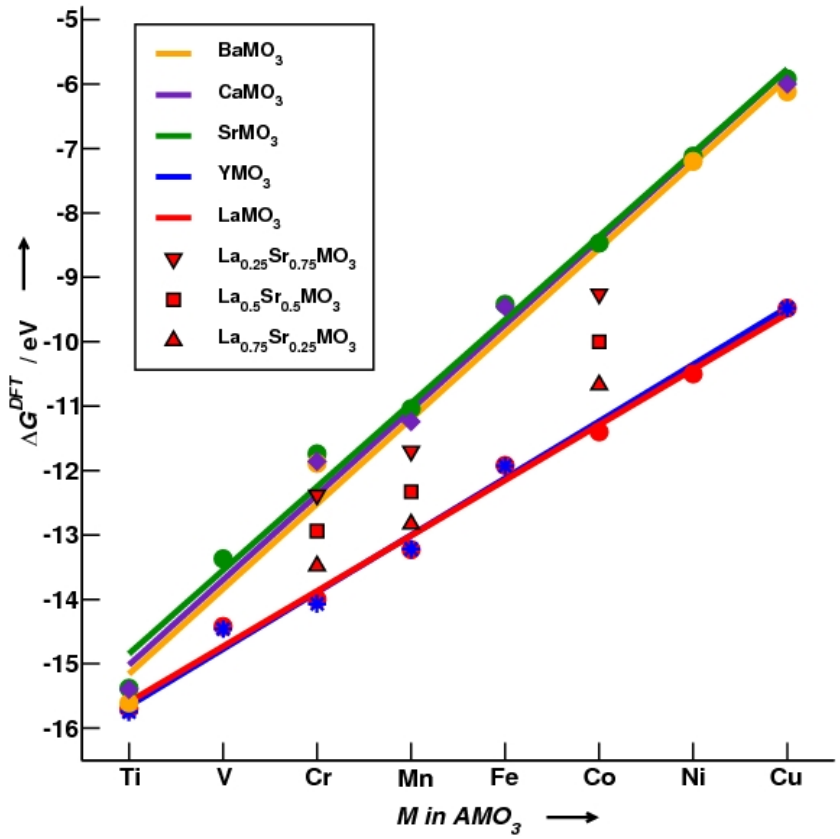

Figure 2.4. Trends in formation energies from elements for various families of AMO_3, according to the number of d electrons of M. Symbols indicate calculated values for individual perovskites, and lines show the best fit for each family. Perovskites having equal oxidation states for A and M (+3, A=Y, La) are more stable than the ones having them different (+2 and +4, A=Ca, Sr, Ba) and their decay in stability is less pronounced. The positions of $La_{1-x}Sr_xMO_3$ perovskites, shown as (▼), (■), (▲), support the idea that the effect is due to the oxidation states of the constituents. Note that the stability against elements does not guarantee the overall stability of the compounds.

All families of perovskites exhibit a systematic linear scaling between their energetics and the number of d electrons of M. The scaling in Figure 2.4 had been previously revealed by experiments only for some La-perovskites at 1273 K [41]. We extended this behavior to other families of perovskites and the insight allows the following generalization: the slope of the lines is determined by the oxidation states of A and M. Therefore, these compounds could be divided into 2 groups: perovskites with the same oxidation state for A and M (+3 for A'MO_3, A'=Y, La), and perovskites with different oxidation states for them (+2 and +4 for A''MO_3, A''= Ca, Sr, and Ba). The former are more stable than the latter and their stabilities along the 3d series decrease more slowly, i.e. their lines have less steep slopes. This could be attributed to the higher

oxidation state forced into M in A''MO_3. A further discussion on this respect is provided in the following sections. It is worth noting that the formation energies of perovskites in each group are approximately constant for materials with the same M constituent, independently of A. For example, the energetics of $SrCrO_3$ gives a good estimative of those of $CaCrO_3$ and $BaCrO_3$. Besides, doped perovskites (A'A"MO_3) have intermediate formation energies between the pure counterparts, according to the degree of doping. This behavior supports the idea that the difference between the groups is a matter of oxidation states and that the formation energies change continuously between the two lines when doping.

The use of simple parameters like the number of d electrons to estimate the formation energies of perovskites is easier and more intuitive than the common use of structural parameters such as the Goldschmidt factor or the Shannon radii (ionic radii of the ions in the complexes) [42-43].

2.4.1. Origin of the Differences in Stability among Families of Perovskites

The trends in energies of formation from elements for various families of perovskites (AMO_3) shown in Figure 2.4 can be classified in two groups: Ca/Sr/Ba perovskites in one group with the A ion having +2 as oxidation state and that of the M ion being +4, and Y/La perovskites in another group with both A and M ions having +3 as oxidation state. The differences in the behavior of these families of perovskites, i.e. the origin of the different slopes in Figure 2.4, can be understood through a simple Hückel approximation, taking into account the 2p orbitals of the O^{2-} ions and the 3d orbitals of the M atoms into the perovskite lattice, as shown in Figure 2.5. We assume that the contribution of the A atoms is constant along each of the aforementioned families of perovskites. This assumption is supported by the behavior exhibited by perovskite oxides in Figure 2.4, in which a single line can describe the energetics of Ca/Sr/Ba perovskites and another one does the same with those of Y/La perovskites.

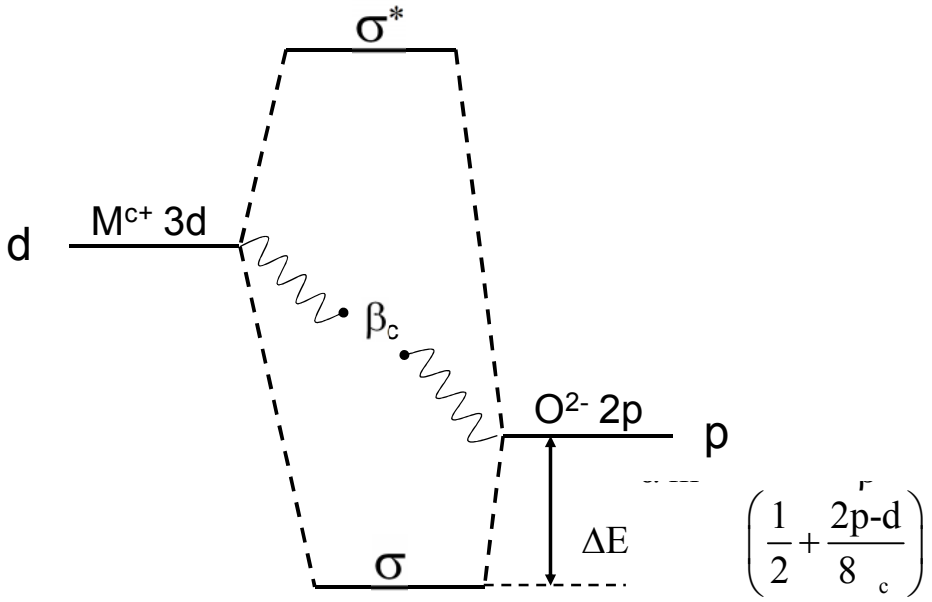

Figure 2.5. Molecular orbital scheme for the hybridization of the 3d levels of the metal c+ ions (c=3, 4) and the 2p orbitals of the O^{2-} with a β_c overlap interaction. ΔE is the stabilization energy of the 2p orbitals of O^{2-} after hybridization with M^{c+} 3d orbitals. The meaning of m is explained in the text.

In this model the orbital energies, *E*, can be obtained by solving the secular determinant:

$$\begin{vmatrix} p-E & \beta_c \\ \beta_c & d-E \end{vmatrix} = 0 \qquad (2.8)$$

Where *p* is the energy of the 2p orbitals of the O^{2-} ions, d the energy of the 3d orbitals of the M^{c+} (c=3, 4) ions and β_c is the overlap between them (it is normally negative at the equilibrium bond lengths). The solution to Equation (2.8) is:

$$E = \frac{p+d \pm \sqrt{(p-d)^2 + 4\beta_c^2}}{2} \qquad (2.9)$$

Taking the solutions for the bonding orbitals and Taylor-expanding $\sqrt{(p-d)^2 + 4\beta_c^2}$, *E* can be written as:

$$E = \frac{p+d}{2} - \beta_c \left(1 + \frac{(p-d)^2}{8\beta_c^2} \right) = W_c + d\left(\frac{1}{2} - \frac{d}{8\beta_c} + \frac{p}{4\beta_c} \right) \quad (2.10)$$

With W_c defined as follows:

$$W_c = \frac{p}{2} - \frac{p^2}{8\beta_c} - \beta_c \quad (2.11)$$

The formation energy can be estimated from the difference in the energy of the 2p level of the free O^{2-} ion and the energy of the bonding orbital, E, from Equation (2.10). In this way, assuming that β_c is constant along each M^{c+} (c=3, 4) series, it is expected that the slope, m, of a line relating the formation energy of the perovskite vs. the d energy is:

$$m = -\left(\frac{1}{2} + \frac{2p-d}{8\beta_c} \right) \quad (2.12)$$

Thus, the value of this slope should be close to -0.50. The predictions of this simple model are confirmed in Figure 2.6, where it is shown that the aforementioned slope is ~ -0.50 for the M^{4+} ions and ~-0.44 for the M^{3+} ones.

On the other hand, the origin of each line is different, since β_3 is different from β_4 and therefore W_3 is not equal to W_4. Indeed we expect β_4 to be bigger in magnitude than β_3 due to the shorter distances between the transition metal and the oxygen atoms in the M^{4+} complexes compared to those of M^{3+} complexes. This is again in good agreement with the results showed in Figure 2.6. The most important feature inferred from Figure 2.6 is that, as a consequence of the fixed value for the slope m, larger energy differences from one member of the 3d series to the next exist for 4+ ions compared to 3+ ions, due to the higher valence forced into the atom occupying the M position. These larger differences between the energies of consecutive ions in the former group are compensated by larger differences in formation energies, thereby keeping constant the slope of the line. Now, when the descriptor is the number of d electrons of the M component, as in Figure 2.4, the slopes of the lines are not anymore fixed and the observed faster decays in the formation energies of (Ca/Sr/Ba) perovskites compared to (Y/La) perovskites appear.

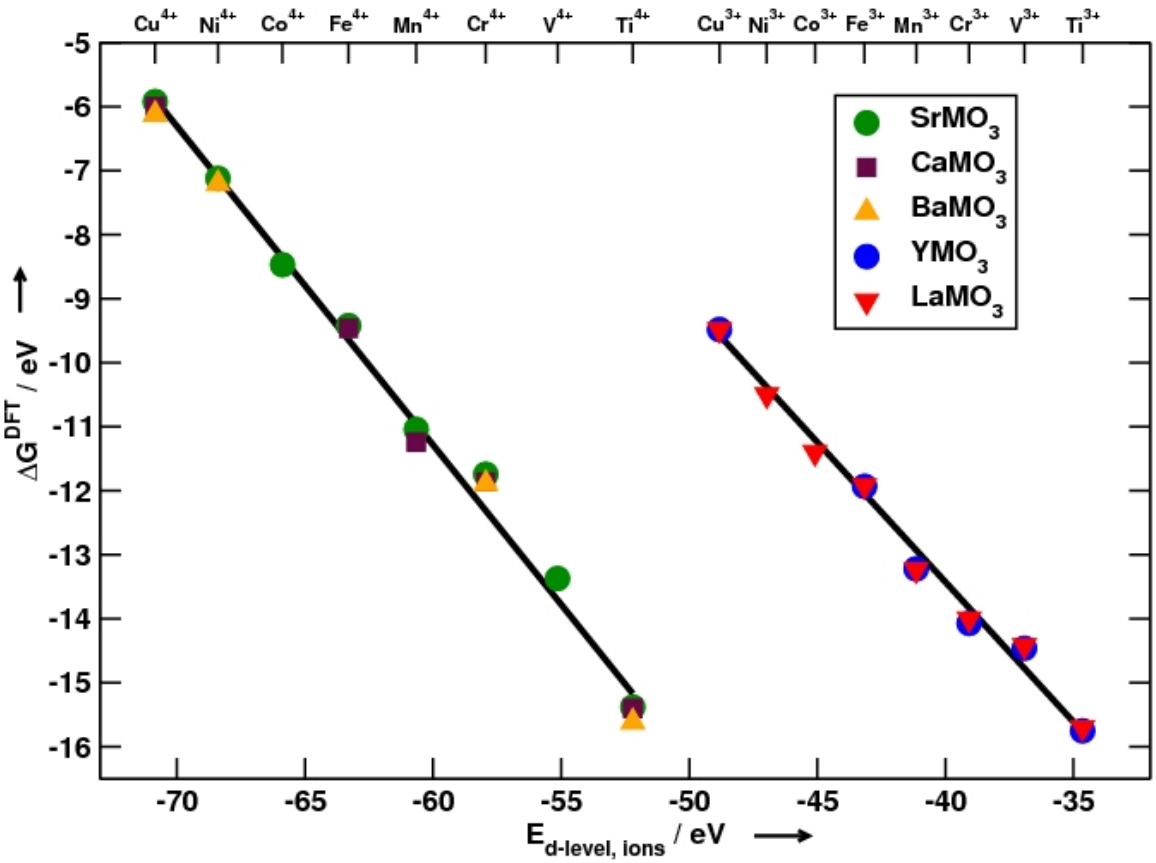

Figure 2.6. Trends in energies of formation from elements for various families of perovskites (AMO_3), according to the energy of the d-level of M ions. Perovskites having +3 as oxidation state for M (A=Y, La) belong to the line to the right. Perovskites having +4 as oxidation state for M (A=Ca, Sr, Ba) belong to the line to the left. Note that both lines have similar slopes (~-0.44 and ~-0.50, respectively) in agreement with the Hückel model, but different lengths.

2.4.2. Origin of the Differences in Stability within a Given Family

Finally, let us explain by means of Figure 2.7 the origin of, on one hand, the intrinsic stability of A'MO_3 (A' = Y, La), and, on the other hand, of the differences in formation energies among different AMO_3. Equation (2.13) represents the formation energy from elements of A'MO_3, according the chemical reaction shown in Equation (2.2).

$$\Delta G^{form} = G_{A'MO_3} - G_{A'} - G_M - \frac{3}{2}G_{O_2} \qquad (2.13)$$

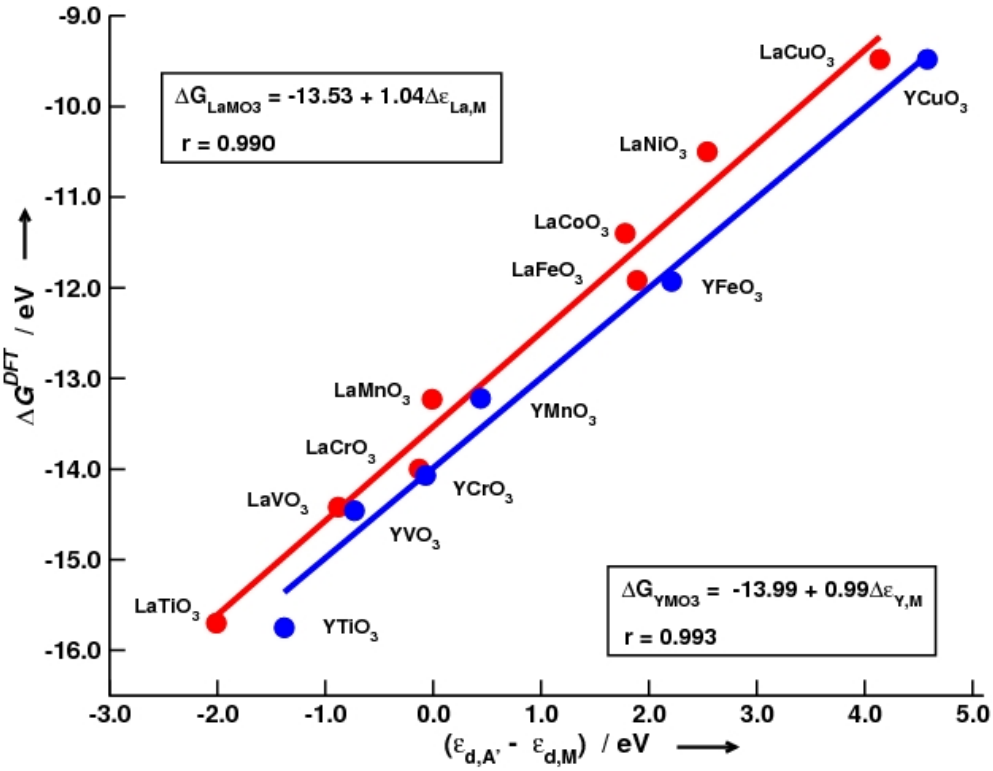

Figure 2.7. DFT calculated free energies of formation of $LaMO_3$ (red) and YMO_3 (blue) oxides versus the differences in d-band centers of La/Y and M. The intercept with the y-axis is equivalent to the formation energy of the sesquioxides A'_2O_3 (A'=Y, La) plus the deformation energy of these oxides from their most stable symmetries to the Pm3m. Therefore, the formation of these perovskites can be seen as destabilizations of the A'_2O_3 oxides via M-A' swapping.

Besides, Equation (2.14) represents the formation energy of A'_2O_3 (La_2O_3 and Y_2O_3) from elements.

$$\Delta G^{form} = G_{A'_2O_3} - 2G_{A'} - \frac{3}{2}G_{O_2} \tag{2.14}$$

By adding and subtracting $G_{A'}$ to and from Equation (2.13), and combining that with the formation energy of the sesquioxides, Equation (2.14), one gets the following:

$$\Delta G^{form} = \Delta G_{A'_2O_3} + \left(G_{A'MO_3} + G_{A'} - G_M - G_{A'_2O_3} \right) \tag{2.15}$$

The term in parentheses in Equation (2.15) corresponds to a hypothetical reaction in which A' in an A'_2O_3 lattice is replaced by M in order to form the perovskite structure, as in Equation (2.16).

$$A'_2O_3 + M \rightarrow A'MO_3 + A' \tag{2.16}$$

Thus, the reaction of formation of $A'MO_3$ could be seen as the formation of A'_2O_3, followed by a lattice deformation, and a swapping between atoms giving $A'MO_3$ as a result. The formation energy may then be presented as:

$$\Delta G^{form} = \Delta G_{A'_2O_3} + \Delta G_{deformation} + \Delta G_{swap} \tag{2.17}$$

The DFT formation energies of La_2O_3 and Y_2O_3 are −16.98 eV and −17.85 eV, respectively, and −17.70 eV [44] and −18.79 eV [45], experimentally. The deformation energy is approximately 3.3 eV for La_2O_3, calculated as the energy difference of this oxide in the space groups P3m1 and Pm3m with a perovskite lattice constant of 3.97Å. This difference is approximately 4.1 eV for Y_2O_3, calculated as the change from the space group Ia3 to the Pm3m with a lattice constant of 3.88Å. Additionally, the interchange between A' and d-metal atoms in Equation (2.16) implies the breaking and creation of bonds, so the swapping energy may be estimated as the difference in the d-band centers (ε_d) of these atoms. This turns Equation (2.17) into the following:

$$\Delta G^{form} = \gamma_{A'_2O_3} + \left(\varepsilon_{d,A'} - \varepsilon_{d,M} \right) \tag{2.18}$$

Where $\gamma_{A'2O3}$ is a constant that collects the formation energy of the sesquioxide and its deformation and is ~ −13.6 eV for La_2O_3 and ~ −13.7 eV for Y_2O_3. This constant may be regarded as an intrinsic stability conferred to $A'MO_3$ by its A' component. As a result, the differences in energies among these perovskites can be attributed to the relative ease for swapping atoms, being Ti the easiest and Cu the hardest along the 3d metal series.

Furthermore, our model is also in agreement with the works by Gelatt et al [46] devoted to the theory of bonding between transition metals and non-transition elements. Based on those works, one could find a similar expression to Equation(2.18) for the family of Ca/Sr/Ba perovskites. Moreover, the model presented here uses the d-band centers of transition metals as key

descriptors for understanding the properties of their compounds as in the model by Hammer and Norskov [47], developed for adsorption energies.

In conclusion, DFT has provided an atomic-scale insight of perovskite oxides sufficient to study their formation energies, both qualitatively and quantitatively except for a constant shift, and important linear trends are found. Moreover, based on simple physical-chemical considerations we rationalized those trends in formation energies and explained the origin of both the slopes and the intercepts in the lines. The analysis shown here could be extended to perovskites with 4d and 5d constituents, to perovskites containing alkaline elements, and to $ScMO_3$. The combination of the energetics of several reactions and their variations with pH and applied potential can give raise to Pourbaix diagrams for perovskites, not yet available in the literature. This and other stability considerations are of paramount importance in any application, especially if perovskites are to be used in alkaline or proton exchange membrane fuel cells.

2.5. Beyond the Trends in Stability

Throughout this chapter we have presented and discussed some trends in formation energies of perovskite oxides. We varied the atoms both in the A and M positions in AMO_3 and observed the effect on stabilities. In particular, the variation of M was done over 3d metals ranging from Ti to Cu, and the variation of A was done between alkaline-earth elements (Ca, Sr, Ba) and rare earth elements (Y, La). After looking at the trends in Figure 2.4 many questions arise. Two of them will be whether the trends hold for 4d and 5d metals and whether the trends can be extended to include perovskites with alkaline elements (Li, Na and K) occupying the A position. The answer to those questions is in both cases affirmative, but we will not show nor discuss those results here. Nevertheless, we pose the following important question: what happens when the M position is occupied by an element before Ti and after Cu? The answer to this question appears in Figure 2.8.

In this figure, the M position is now occupied by elements from Ca to Ge, i.e. we extended the trends two elements to the left of Ti and 3 to the right of Cu, so that the whole 3d block is included into the trends and some 4s and 4p elements are include as well. This gives an overall perspective of the trends in formation energies and allows for further analyses.

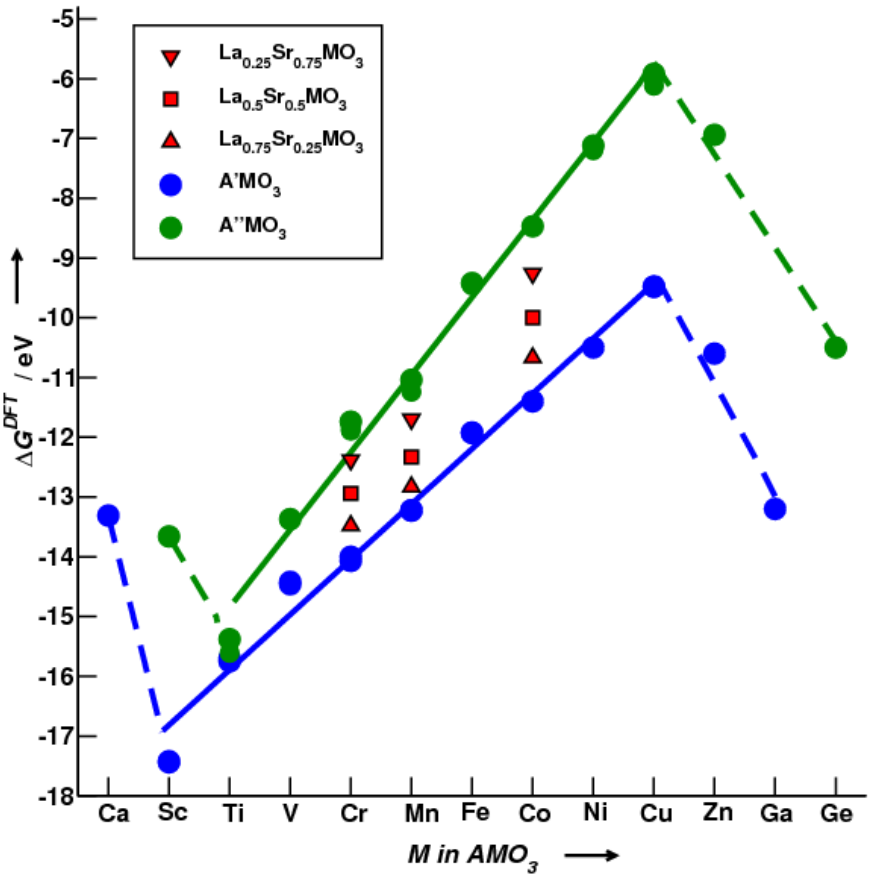

Figure 2.8. Extended trends in formation energies of perovskite oxides. The A position is either occupied by La or Y (blue) or by Ca, Sr or Ba (green). Doped perovskites are shown in red. The M position is occupied by elements ranging from Ca to Ge. The previous trends in Figure 2.4 are shown as solid lines and the extended as dashed lines.

We observe in Figure 2.8 that the trends for A'MO_3 continue linearly up to Sc, whereas they break for A''MO_3. The minimum in stability is, therefore, found at (Y/La)ScO_3 for the (+3,+3) group, whereas for the (+2,+4) one it is found at (Ca/Sr/Ba)TiO_3. To the left of these perovskites, the stability starts to decrease.

The reason for this is simple and is based on the electronic structure of the atom in the M position, since the atoms in the A position have always closed shells, i.e. Ca^{2+} has the electronic distribution of Ar; Sr^{2+} and Y^{3+} have that of Kr, and Ba^{2+} and La^{3+} have that of Xe. On the other hand, in the M position one has, in general, elements with open shells. As one moves to the left of the d series, there are less d electrons in the shell and the ionicity of the bonds increases, thereby increasing the stability of the compound. The maximal stability will thus be found when the atoms in the M position have closed shells, i.e. Sc^{3+} in (Y/La)ScO_3, and Ti^{4+} in

(Ca/Sr/Ba)TiO_3, since they will have the electronic distribution of Ar. When A'MO_3 has an element like Ca in the M position, as in $LaCaO_3$, the p shell will be affected and the stability will decrease. Similarly, when A''MO_3 has an element like Sc in the M position, as in $SrScO_3$, the stability will also decrease.

On the other hand, perovskites with M atoms to the right of Cu tend to gain some stability. Figures 2.4 and 2.8 show that along the 3d series from Ti to Cu the stability decreases as the number of d electrons of M increases. The electronegativity of transition metals tends to decrease as well, as one moves to the right of the periodic table. Therefore, when the shells are not closed, the more ionic the bonds are in perovskites, the more stable these compounds are. Table 2.2 presents the electronegativities of the elements considered in Figure 2.8.

Table 2.2. Electronegativities of selected elements in the fourth period of the periodic table.

Element	Ca	Sc	Ti	V	Cr	Mn	Fe	Co	Ni	Cu	Zn	Ga	Ge
Electronegativity	1.00	1.36	1.54	1.63	1.66	1.55	1.83	1.88	1.91	1.90	1.65	1.81	2.01

The numbers in Table 2.2 help explaining why the trends change for Zn, which gains stability compared to Cu in AMO_3. There is a dramatic drop in electronegativity from Cu (1.90) to Zn (1.65), and therefore, the ionicity increases and so does the stability. The argument for $SrGeO_3$ and $LaGaO_3$ is identical to that of $SrTiO_3$ and $LaScO_3$. Since Ge ends its electronic distribution in $4s^2$ $4p^2$, Ge^{4+} has a closed shell and hence $SrGeO_3$ corresponds to the minimum along the 4p series for A''MO_3. On the other hand, Ga has a neutral electronic distribution that ends in $4s^2$ $4p^1$, so Ga^{3+} has also a closed shell and $LaGaO_3$ is the minimum along the 4p series for A'MO_3.

The overall behaviour of the perovskite stabilities is somehow more complicated than we initially thought. Nevertheless, that behaviour can be understood in terms of simple physical-chemical concepts and, as will be shown in the next chapters, it is not exclusive of the formation energies of perovskites and appears as well in adsorption energies of perovskites and alloys.

2.6. Methods

The DFT calculations were performed with the plane wave code DACAPO [6], using the RPBE exchange-correlation functional, a converged plane wave cutoff of 400 eV and a density cutoff of 500 eV. DACAPO uses ultrasoft pseudopotentials to represent the ion-electron interaction. Atomic relaxations were done with the quasi-Newton minimization scheme, until a maximum force below 0.05 $eV\AA^{-1}$ between atoms was reached. Besides, we have optimized the lattice vectors by minimizing the strain on 2x2x2 supercells in all periodically repeated directions. The Brillouin zone of all systems was sampled with Monkhorst-Pack grids, guaranteeing in all cases that the product of the supercell dimensions and the k-points was at least 25Å in all directions. The self-consistent RPBE density was determined by iterative diagonalization of the Kohn-Sham Hamiltonian at k_BT = 0.1 eV, using Pulay mixing of densities, and all total energies were extrapolated to k_BT = 0 eV. Spin polarized calculations were carried out when needed.

3. CATALYTIC ACTIVITY OF PEROVSKITE OXIDES

3.1. Introduction

The high catalytic activity of perovskite oxides towards several chemical reactions has been studied for decades. Table 3.1 condensates some of the wide variety of reactions in which these oxides have been used.

Table 3.1. Chemical reactions in which perovskite oxides can be used as catalysts. Adapted from References [48-49].

Reaction	Reference
Oxygen equilibration and oxygen exchange	[50-52]
Total oxidation of CO, hydrocarbons and oxygenates	[53-54]
Partial oxidation of hydrocarbons and oxygenates	[55-57]
H_2 oxidation	[58]
NH_3 oxidation	[59]
NO reduction	[53]
CO and CO_2 hydrogenation	[60-61]
Hydrogenation and hydrogenolysis of hydrocarbons	[27, 62-64]
H_20_2 decomposition	[65-66]
$N0_x$ decomposition	[67-68]
Electrocatalysis and fuel cells	[18-19, 69-72]
Photocatalysis	[58, 73-74]

Perovskite oxides constitute a wide source of inexpensive, versatile and stable materials that have been traditionally used at high temperatures and start nowadays being attractive for low-

temperature applications [18, 30, 75]. Substantial effort has been devoted to firstly rationalize the trends in the of these oxides and based on that, pinpoint active and stable oxide catalysts that may help reducing or completely replacing the use of noble metals in technological applications [19, 22, 76]. Since the adsorption energies of reaction intermediates determine to a large extent the catalytic performance of materials in general, it is of paramount importance to find the electronic structure factors that influence them, and, if possible, correlate those in such a way that one is able to predict the adsorption properties based on simple electronic considerations. This kind of analysis, is well-known for pure transition metals and some alloys and overlayers and is based on the relative position of the average energy of the d-states with respect to the Fermi level [47]. Electronic and geometric effects are fully captured by the so-called d-band model with the advantage of having predicting power. However, little is known about the applicability of the "d-band" model on transition metal oxides in which the actual adsorption energies will result from the combination of several factors as e.g. the number and the spatial configuration of the metal atoms and the ligands, the oxidation state of the transition metals in the metal-ligand complexes and, last but not least, their interactions with the adsorbates.

Here we present a first attempt to understand the role of some factors that alter the reactivity of transition metal perovskite oxides. On one hand, we analyze the effect over adsorption properties of changing the number of d-electrons while keeping fixed the configuration of the metal and the ligands and their oxidation states. To do so, we consider the adsorption of the intermediate species of the ORR and OER, namely *O, *OH, and *OOH [47]. On the other hand, we analyze the effect of changing the oxidation states of a given transition metal on its reactivity while keeping fixed its coordination.

3.2. Thermochemical Derivation of the Scaling Relations

We define the adsorption energies of *O, *OH, and *OOH, according to the following equations.

$$* + H_2O \rightarrow *O + H_2 \tag{3.1}$$

$$\Delta E_O = (E_{*O} - E_*) - (E_{H_2O} - E_{H_2}) \tag{3.2}$$

$$* + H_2O \rightarrow *OH + \frac{1}{2}H_2 \tag{3.3}$$

$$\Delta E_{OH} = (E_{*OH} - E_*) - (E_{H_2O} - \frac{1}{2}E_{H_2}) \tag{3.4}$$

$$* + 2H_2O \rightarrow *OOH + \frac{3}{2}H_2 \tag{3.5}$$

$$\Delta E_{OOH} = (E_{*OOH} - E_*) - (2E_{H_2O} - \frac{3}{2}E_{H_2}) \tag{3.6}$$

The scaling relations reported for pure metals and some alloys [77] are also fulfilled by (001) surfaces of perovskite oxides, as shown in Figure 3.1.

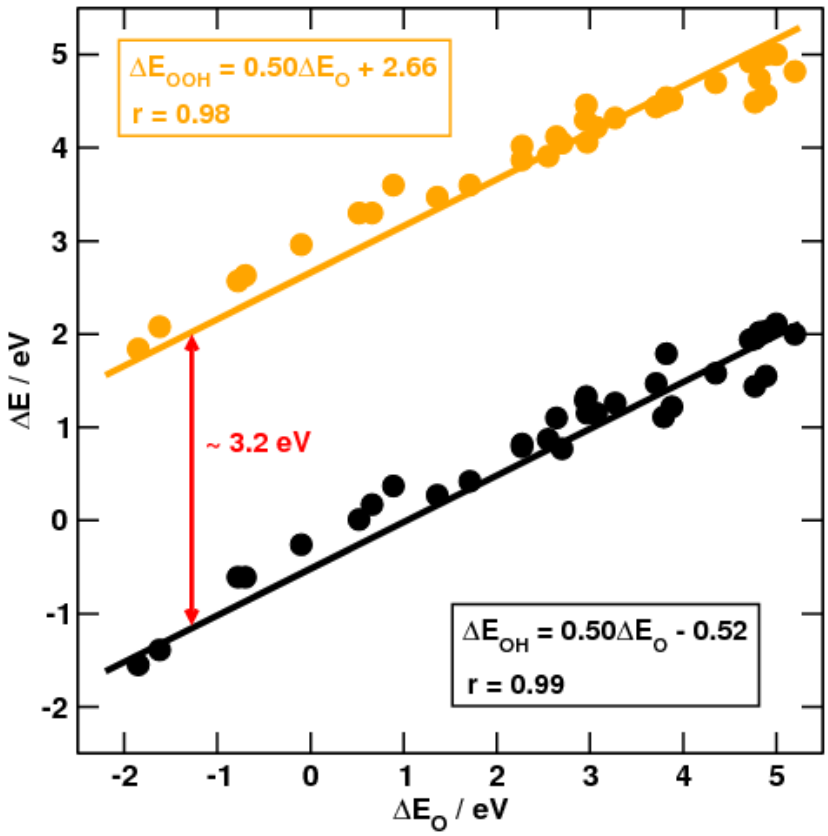

Figure 3.1. Scaling relations between the ORR intermediates adsorbed on (001) surfaces of perovskite oxides.

The adsorption energies are provided in Appendix 2, and we remark that the correlations shown in Figure 3.1 do not correspond to the best fitting of the points, but come from a larger set of data (See No 3 in List of Included Articles).

The binding energies of *O, *OH, and *OOH scale linearly with each other and the slopes are supposed to be ~ 0.5, due to the number of bonds between the surface and the adsorbates, which are 2 for *O and 1 for *OH and *OOH. In Figure 3.1 we also observe that the separation between the energy levels of *OH and *OOH is constant along the whole range of binding energies, and that separation is approximately 3.2 eV.

This constant energy difference seems to be important, but its origin remains elusive. Besides, the origin of the intercept of the scaling relations was not explained in Ref. [77] and counting bonds appears to be only a rule of thumb for calculating the slopes. In my personal opinion, the scaling relations are simply the results of the definitions given in Equations (3.1) to (3.6), where one only has to balance the chemical equations and accept that the adsorption sites (*) are the same for *O, *OH and *OOH. In the following subsections, I will prove this hypothesis.

3.2.1. Scaling between Adsorption Energies of *O and *OH

By subtracting Equation (3.3) from Equation (3.1), one gets Equation (3.7).

$$*OH \rightarrow *O + \frac{1}{2} H_2 \tag{3.7}$$

In terms of energetics, this process is also equivalent to subtracting Equation (3.4) from Equation (3.2). Therefore, the reaction energy of Equation (3.7) is the following:

$$\Delta E_{OH/O} = \Delta E_O - \Delta E_{OH} \tag{3.8}$$

According to this, the adsorption energy of *OH is related to that of *O in the following way:

$$\Delta E_{OH} = \Delta E_O - \Delta E_{OH/O} = \Delta E_O - (E_{*O} - E_{*OH} + \frac{1}{2} E_{H_2}) \tag{3.9}$$

We can add $1/2E_*$ and $1/2E_{H_2O}$ to Equation (3.9) and subtract them from it in order to get Equation (3.10).

$$\Delta E_{OH} = \Delta E_O - \left(\frac{1}{2} E_{*O} + \frac{1}{2} E_{H_2} - \frac{1}{2} E_* - \frac{1}{2} E_{H_2O} \right) - \left(\frac{1}{2} E_{*O} + \frac{1}{2} E_* + \frac{1}{2} E_{H_2O} - E_{*OH} \right) \quad (3.10)$$

The term in the first parenthesis is equivalent to $1/2\Delta E_O$. Moreover, for convenience, we will represent the term in the second parenthesis by $1/2\Delta E_{O/OH/H_2O}$. Thus, Equation (3.10) turns into the following:

$$\Delta E_{OH} = \frac{1}{2}\Delta E_O - \frac{1}{2}\Delta E_{O/OH/H_2O} = \frac{1}{2}\Delta E_O - \frac{1}{2}(E_{*O} + E_* + E_{H_2O} - 2E_{*OH}) \quad (3.11)$$

In that equation it is already possible to see that the coefficient of ΔE_O is 0.5. Moreover, the term in parenthesis corresponds to the following reaction:

$$2*OH \rightarrow *O + * + H_2O \quad (3.12)$$

We note that the ratio of *O to *OH is ½ in this reaction. Moreover, as can be seen in Appendix 2, the energetics of this reaction is essentially constant on all perovskite surfaces and equal to 0.41 eV. Thus, we conclude that this reaction is surface independent among the compounds considered; nonetheless, we do not discard the idea of this constant being characteristic of a given type of active site.

3.2.2. Scaling between Adsorption Energies of *O and *OOH

The subtraction of Equation (3.5) from Equation (3.1), leads to Equation (3.13).

$$*OOH + \frac{1}{2} H_2 \rightarrow *O + H_2O \quad (3.13)$$

In terms of energetics, this process is also equivalent to the subtraction of Equation (3.6) from Equation (3.2). As a result, the reaction energy of Equation (3.13) is the following:

$$\Delta E_{OOH/O} = \Delta E_O - \Delta E_{OOH} \quad (3.14)$$

According to this, the adsorption energies of *OOH and *O are related in the way shown below.

$$\Delta E_{OOH} = \Delta E_O - \Delta E_{OOH/O} = \Delta E_O - (E_{*O} - E_{*OOH} + E_{H_2O} - \frac{1}{2}E_{H_2}) \quad (3.15)$$

The addition to and the subtraction from Equation (3.15) of the terms $1/2E_*$, $1/2E_{H_2}$ and $3/2E_{H_2O}$, leads to Equation (3.16).

$$\Delta E_{OOH} = \Delta E_O - \left(\frac{1}{2}E_{*O} + \frac{1}{2}E_{H_2} - \frac{1}{2}E_* - \frac{1}{2}E_{H_2O}\right) - \left(\frac{1}{2}E_{*O} + \frac{1}{2}E_* + \frac{3}{2}E_{H_2O} - E_{*OOH} - E_{H_2}\right) \quad (3.16)$$

The term in the first parenthesis is equivalent to $1/2\Delta E_O$. Moreover, for convenience, the term in the second parenthesis will be represented by $1/2\Delta E_{O/OOH/H_2/H_2O}$. Thus, Equation (3.16) turns into the following:

$$\Delta E_{OOH} = \frac{1}{2}\Delta E_O - \frac{1}{2}\Delta E_{O/OOH/H_2/H_2O} = \frac{1}{2}\Delta E_O - \frac{1}{2}(E_{*O} + E_* + 3E_{H_2O} - 2E_{*OOH} - 2E_{H_2}) \quad (3.17)$$

Again, we see that the coefficient of ΔE_O is 0.5. Moreover, the term in parenthesis corresponds to the following reaction:

$$2*OOH + 2H_2 \rightarrow *O + * + 3H_2O \quad (3.18)$$

We note that the ratio of *O to *OOH is also ½ in this reaction. As can be seen in Appendix 2, the energetics of this reaction is essentially constant on all perovskite surfaces and equal to 2.69 eV. Thus, we conclude that the reaction in Equation (3.18) is also surface independent among the compounds considered; nonetheless, we do not discard the idea of this constant being characteristic of a given type of active site.

3.2.3. Scaling between Adsorption Energies of *OH and *OOH

Now that we have derived expressions for the adsorption energies of *OH and *OOH in terms of that of *O, it is possible to use both expressions to obtain a scaling relation between *OH and *OOH. This is done by combining Equations (3.11) and (3.17). The result is shown below.

$$\Delta E_{OOH} = \Delta E_{OH} - \frac{1}{2}\Delta E_{O/OOH/H_2/H_2O} + \frac{1}{2}\Delta E_{O/OH/H_2/H_2O} = \Delta E_{OH} + (E_{*OOH} + E_{H_2} - E_{*OH} - E_{H_2O}) \quad (3.19)$$

The term in parenthesis in Equation (3.19) corresponds to the chemical reaction shown below.

$$*OH + H_2O \rightarrow *OOH + H_2 \quad (3.20)$$

This reaction shows that *OH and *OOH behave similarly, being *OOH an oxygenated product of *OH or, alternatively, being *OH a deoxygenated product of *OOH. Besides, their ratio is 1:1. The energetics of this reaction is essentially constant and equivalent to 3.10 eV for the set of data considered. This justifies the constant difference between the energy levels of *OH and *OOH in Figure 3.1. Moreover, the intercepts and slopes shown in that figure are in excellent agreement with the values obtained from the proposed thermochemical analysis.

3.3. Trends in Adsorption Energies in Perovskite Oxides

So far we have shown that perovskite oxides fulfill the scaling relations. That is an overall analysis that helps explaining the origin of the trends in Figure 3.1. The next point in the discussion is to find out whether the points that compose the trends have special arrangements and explain them.

The adsorption behavior of the two families of perovskite oxides (A'MO_3 and A''MO_3, with oxidation states +3, +3 and +2, +4, respectively for A and M) studied in the precedent chapter appear in Figure 3.2a) and b) for A'MO_3 and A''MO_3, respectively, with M = Sc, Ti…, Cu.

In the case of A'MO_3, the trends start to the left with A'TiO_3, which tend to bind the ORR adsorbates strongly, and end in A'CuO_3, which in turn bind them weakly. Again, as for the case of the energies of formation, the adsorption energies decrease with increasing number of d electrons of the atom in the M position. There is, however, an exception to this statement along the 3d series: A'ScO_3.

Moreover, for A''MO_3 the trends start in A''VO_3 and end in A''CuO_3. Similar to the other case, as the number of d electrons of M increases, the adsorption energies weaken. In this family there are two exceptions to the trends: A''TiO_3 and A''ScO_3.

a)

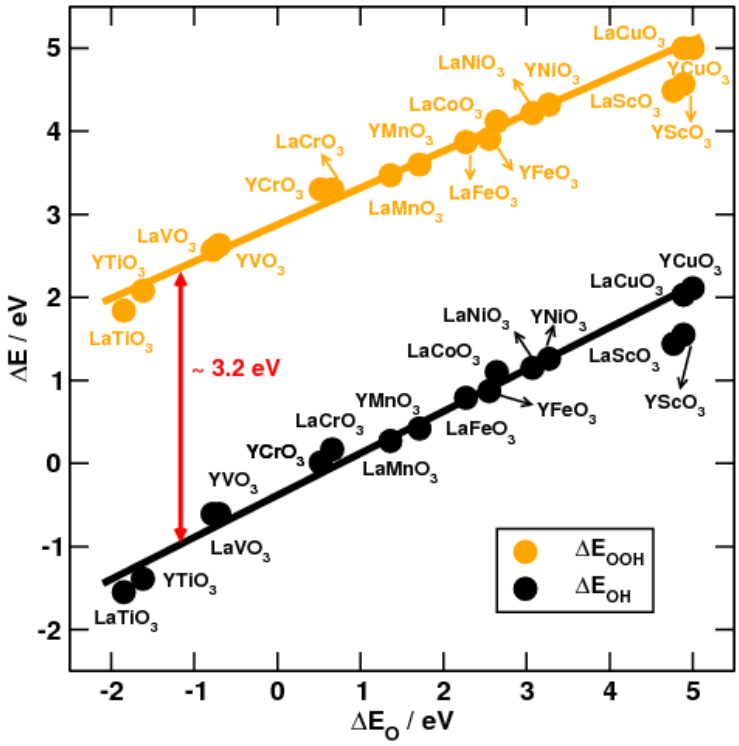

b)

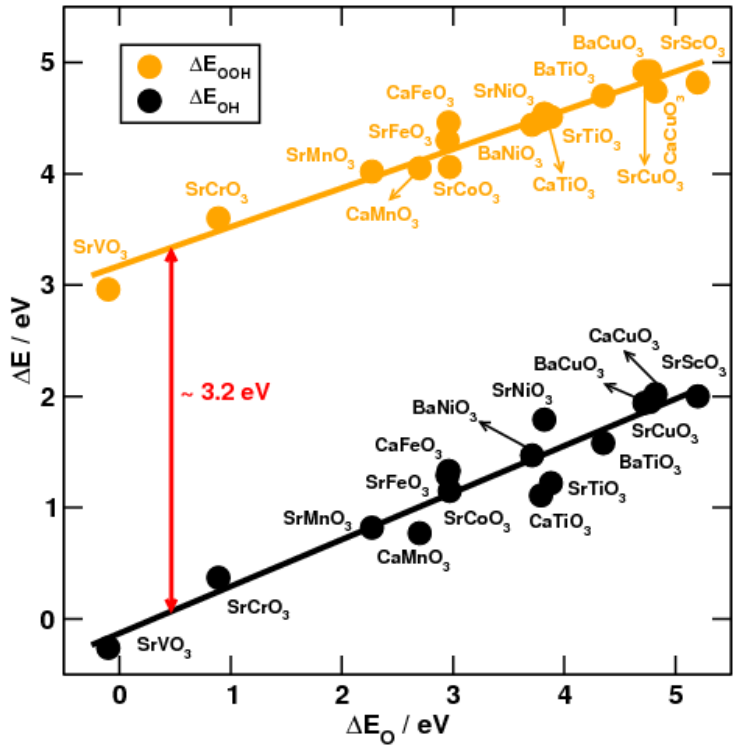

Figure 3.2. Scaling relations between ORR intermediates on a) A'MO3 and b) A''MO3 (001) surfaces.

The individual variations of the adsorption energies of the ORR intermediates on A'MO_3 and A''MO_3 can be viewed in Figure 3.3. In it we observe that the binding strength changes methodically as the atom in the M position is changed along the 3d series. In all cases, A'MO_3 perovskites bind stronger than A''MO_3 perovskites for a given M. This is due to the high oxidation state forced into M and the subsequent reduction of charge availability in the surface. The aforementioned exceptions in the linear trends clearly appear; nonetheless, the energy levels of *OH and *OOH preserve in all cases their constant separation of ~ 3.1 eV.

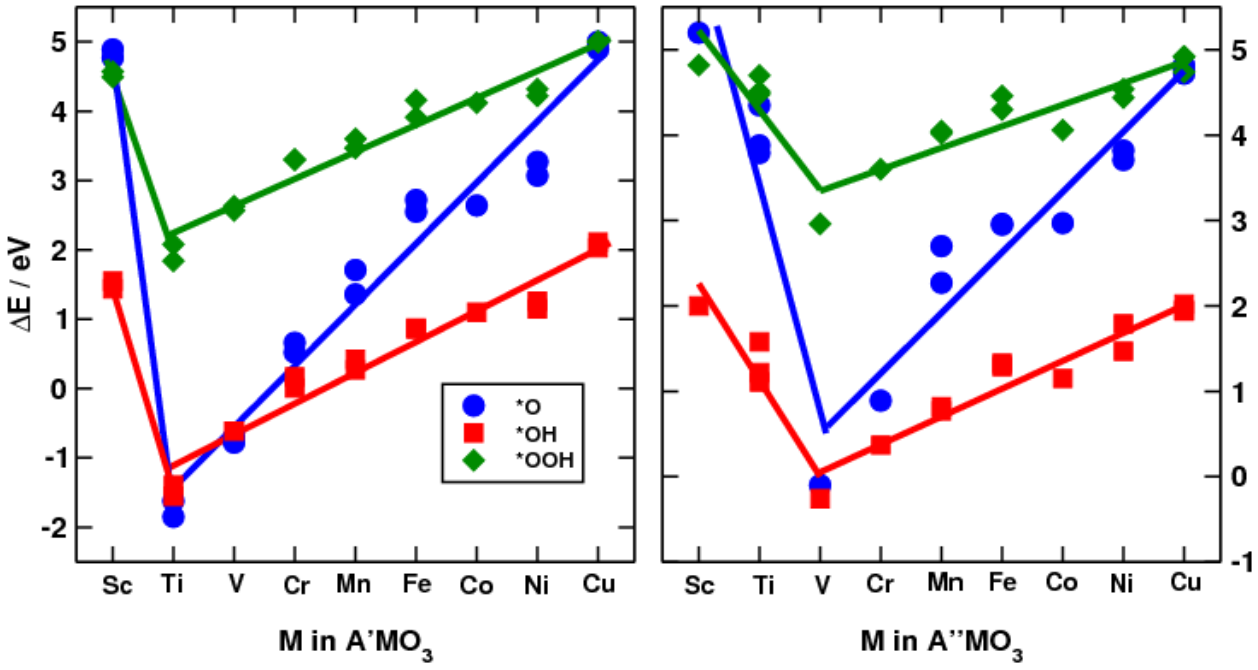

Figure 3.3. Trends in adsorption energies of *O (blue circles), *OH (red squares) and *OOH (green diamonds) on A'MO_3 (A' = Y, La) and A''MO_3 (A'' = Ca, Sr, Ba).

The origin of these deviations can again be explained with simple chemical considerations. The (001) surfaces of perovskite oxides have two possible terminations: AO and MO_2. We remark here that we have only considered MO_2-terminated surfaces, which are known to be the active terminations for catalysis [48]. Figure 3.4 shows the top views of both surfaces. We note that clean MO_2-terminated surfaces lack one vertical bond with an oxygen atom; for this reason, the generally preferred adsorption site of gas-phase atoms and molecules on these surfaces is the

atop site over M. Moreover, when an atom is adsorbed on top of M, the complex is again MO_6, so the octahedral symmetry of the bulk is restored.

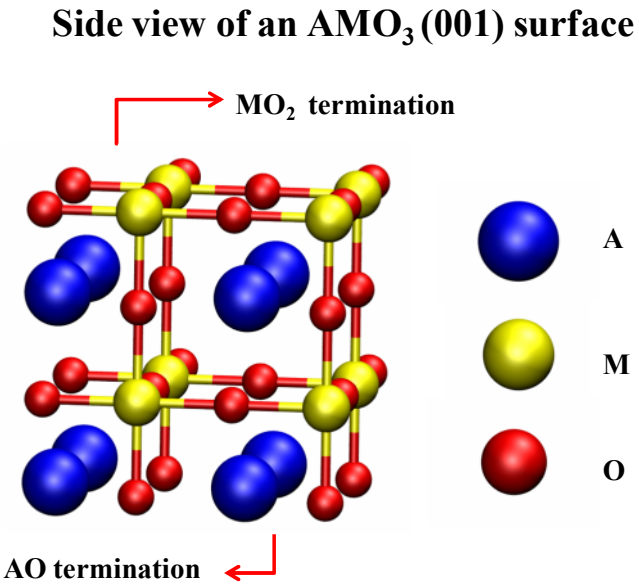

Figure 3.4. Side view of an AMO3 (001) surface with the two possible terminations, MO2 (up) and AO (below).

According to the oxidation states of A and M, the surfaces can either be charged or neutral. This means that for A'MO_3, we will have charge separation between the surfaces and their configuration will be A'O^+ and MO_2^-, e.g. LaO^+ and TiO_2^-. By contrast, for A''MO_3, we have the following two neutral configurations: A''O and MO_2, e.g. SrO and TiO_2. According to this, the (001) surface of $SrTiO_3$ (TiO_2-terninated) is rather stable due to the closed shells of both the Ti and O atoms and, therefore, the surface will tend to bind the ORR adsorbates weakly. Conversely, $LaTiO_3$ binds the ORR adsorbates strongly due to the excess of charge in the TiO_2^- surface. This excess makes the surface attractive for highly electrophilic adsorbates.

Furthermore, $SrScO_3$ binds the ORR adsorbates weakly due to the electronic distribution of the Sc ions in the surface. We saw in the last chapter that +4 is not a stable oxidation state for Sc due to the involvement of p electrons in the bonding with the surrounding oxygen atoms. Sc atoms in the topmost layer will lack a bond with oxygen and consequently their "effective" oxidation state will decrease, trying to reach +3, which gives a closed shell configuration. This is why Sc ions in the surface of $SrScO_3$ will tend to bind electrophilic adsorbates weakly, but, on the other hand, this increases the reactivity of the surface oxygen atoms, which are normally inert. In the ScO_2-terminated surface of $LaScO_3$ there is also an excess charge, like in the TiO_2-terminated surface

of $LaScO_3$. The charge should be distributed on the surrounding oxygen atoms, since Sc^{3+} has a closed shell configuration and is a very electropositive ion. Again, as in $SrScO_3$, the oxygen atoms become reactive, tending to combine with adsorbates.

Finally, as can be seen in Figure 3.3, it is noteworthy that the adsorption energies of AMO_3 do not depend strongly on A for a given M, within a group of perovskites. A similar effect was observed in the formation energies studied in Chapter 2. For instance, the energetics of $LaTiO_3$ and $YTiO_3$ are almost identical. Moreover, we observe the same behavior for A''MO_3. Examples of this are the energetics of $CaTiO_3$, $SrTiO_3$ and $BaTiO_3$. Nevertheless, the energetics of A'MO_3 and A''MO_3 are quite different for a given M and the former tend to bind the adsorbates stronger than the latter.

3.4. Volcano Plot and Active Perovskites towards ORR and OER

Now that we know the trends in adsorption energies, we can construct the so-called volcano plot. We assume the 4-electron reaction path for the ORR shown below. The ORR reactants are O_2 and $4(H^+ + e^-)$, and the products will be $2H_2O$. Alternatively, when the reactants are $2\ H_2O$ and the products are O_2 and $4\ (H^+ + e^-)$, the reaction is OER and will not be spontaneous but is of interest as well to construct electrolyzers that produce H_2.

$$O_{2(g)} + (H^+ + e^-) + * \leftrightarrow *OOH \quad (3.21)$$

$$\Delta G_4 = \Delta E_{OOH} - 4.92 + 0.4 \quad (3.22)$$

$$*OOH + (H^+ + e^-) \leftrightarrow *O + H_2O \quad (3.23)$$

$$\Delta G_3 = \Delta E_O - \Delta E_{OOH} - 0.35 \quad (3.24)$$

$$*O + (H^+ + e^-) \leftrightarrow *OH \quad (3.25)$$

$$\Delta G_2 = \Delta E_{OH} - \Delta E_O + 0.30 \quad (3.26)$$

$$*OH + (H^+ + e^-) \leftrightarrow * + H_2O \quad (3.27)$$

$$\Delta G_1 = -\Delta E_{OH} - 0.35 \quad (3.28)$$

We convert into Gibbs free energies our calculated DFT energies by adding to them the values of the entropic and zero-point energy corrections reported by Nørskov et al [78], and provided in Appendix 2. Moreover, the fact that the binding energies of *OH and *OOH can be expressed in terms of that of *O drastically simplifies the problem, since the only independent parameter in the model is then ΔE_O. By plotting the 4 free energy changes shown above versus the adsorption energy of oxygen, the combined volcano plot shown in Figure 3.5 for ORR and OER appears.

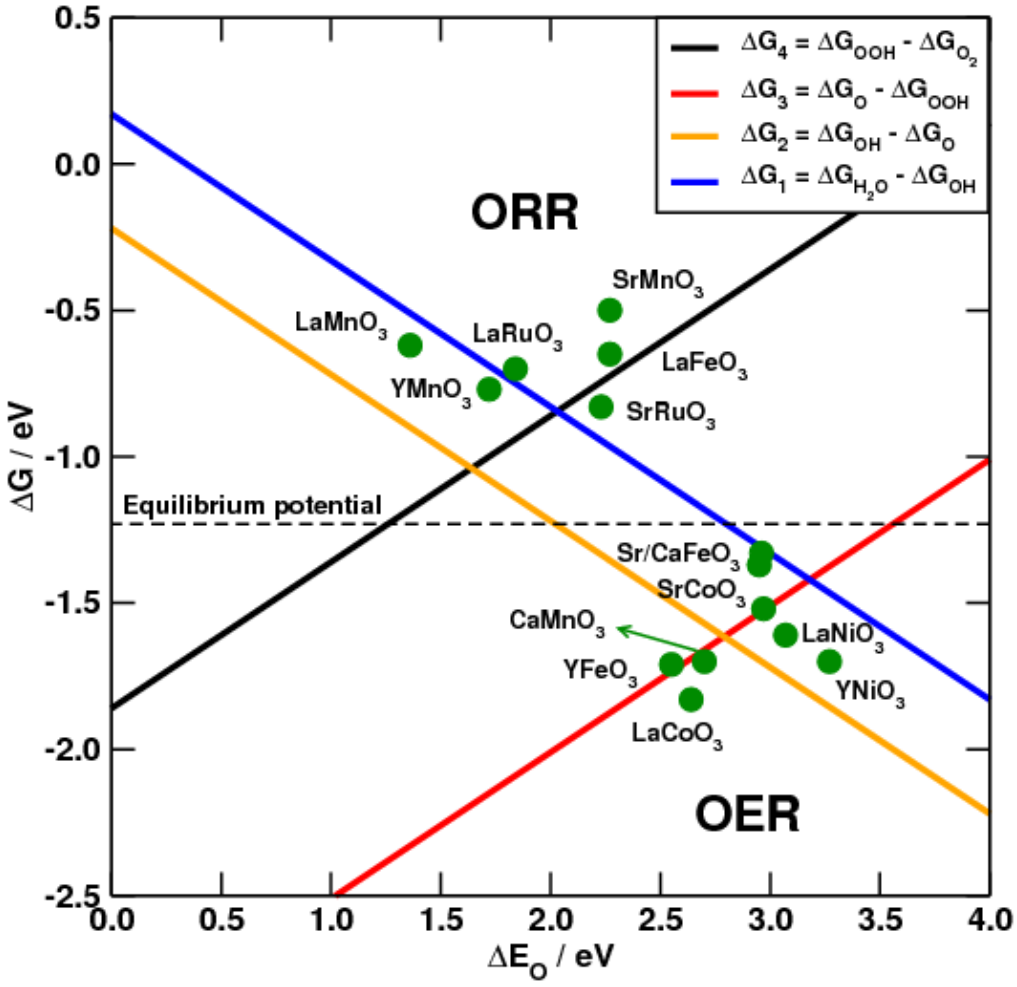

Figure 3.5. Combined volcano plot for ORR (top) and OER (bottom). Only the most active perovskite oxides are shown in green. The Gibbs energy changes of the reaction steps ΔG_1 to ΔG_4 correspond, in that order, to the blue, orange, red, and black lines.

The tops of the volcanoes for ORR and OER are located, respectively, at oxygen adsorption energies of ~2.0 eV and ~2.8 eV. The highest ORR activities on the strong-binding side of the volcano are displayed by $LaMnO_3$, $YMnO_3$ and $LaRuO_3$, while on the weak-binding side we found $SrRuO_3$, $LaFeO_3$, and $SrMnO_3$. Therefore, we conclude that perovskites containing Mn and Ru are rather active towards ORR and, what seems promising is the fact that the proximity to the top of the volcano can be engineered by doping the A site. Let us consider the case of Ru perovskites: $LaRuO_3$ has oxygen adsorption energy of ~1.8 eV, i.e. 0.2 eV to the left of the top of the volcano. On the other hand, $SrRuO_3$ has oxygen adsorption energy of ~2.2 eV, i.e. 0.2 eV to the right of the top. As we pointed out before, by oxidizing the atoms in the M site, the binding strength is decreased. Thus, it seems reasonable to think that A-site doping of $LaRuO_3$ surfaces with Sr will decrease their adsorption energies, approaching the top of the volcano. We see that in Figure 3.6, where the optimum doping is ~50% Sr in the second layer (see Figure 3.4) in MO_2-terminated (001) surfaces. These perovskites are worth trying experimentally.

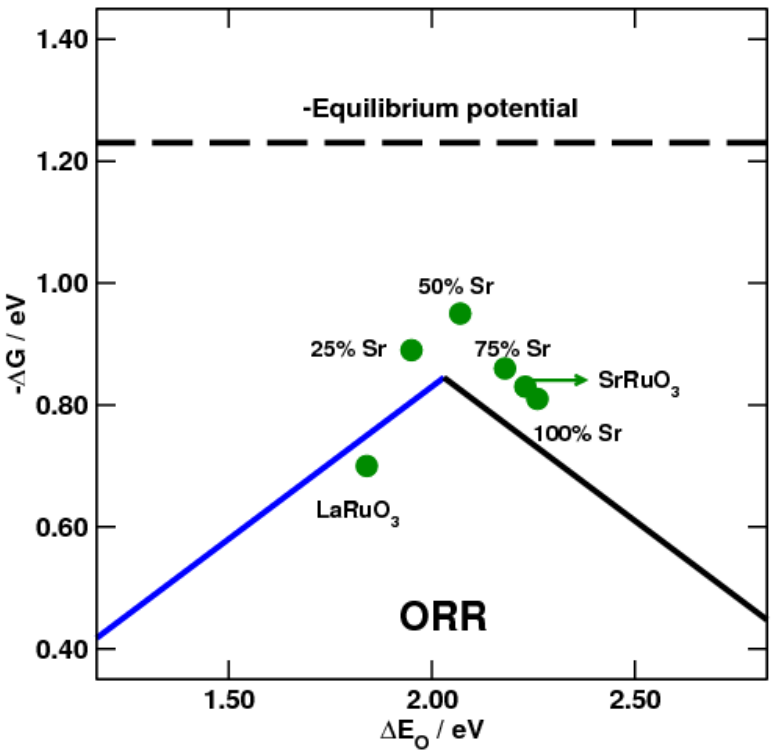

Figure 3.6. Effect of doping $LaRuO_3$ with Sr in the second layer of its (001) surface. The optimum doping is found to be ~50% Sr. Blue line: $-\Delta G_1$; black line: $-\Delta G_4$; the dashed line represents the location of the equilibrium potential (-1.23 eV in terms of free energy).

These conclusions may also be extended for $LaMnO_3$ and $YMnO_3$ doped with Sr. On the other hand, the highest OER activities on the strong-binding side of the volcano are displayed by $YFeO_3$, $LaCoO_3$ and $CaMnO_3$, while on the weak-binding side we found $SrFeO_3$, $CaFeO_3$, $SrCoO_3$, $LaNiO_3$, and $YNiO_3$. Hence, we conclude that the OER is efficiently catalyzed by late transition metals, namely Fe, Co, and Ni. Again, as for ORR, careful doping in the A site can lead to improved catalytic activity.

We note that not many data are available in the literature to compare with those in Figure 3.5. Nonetheless, Bockris and Otagawa [19, 79] reported OER measurements recorded at 10 $mAcm^{-2}$, room temperature, and pH = 14. Comparisons between theoretical and experimental overpotentials are provided in Figure 3.7. We define the theoretical overpotential as the difference between the activity (y-axis) in Figure 3.5 and the constant line corresponding to the equilibrium potential of 1.23 V (located at -1.23 eV, according to the theory in Chapter 1).

Figure 3.7 reveals good agreement between our theoretical calculations and experiments. This is important to verify the applicability of the model in oxides, and most importantly, to corroborate the organized dependence of the catalytic activity of perovskite oxides on the number of d electrons of the M-site atoms. Additionally, the data for $LaFeO_3$ and $SrFeO_3$ confirm that increasing the oxidation state of M-site atoms tends to reduce the binding strength of the intermediates and can help moving towards the top of the volcano.

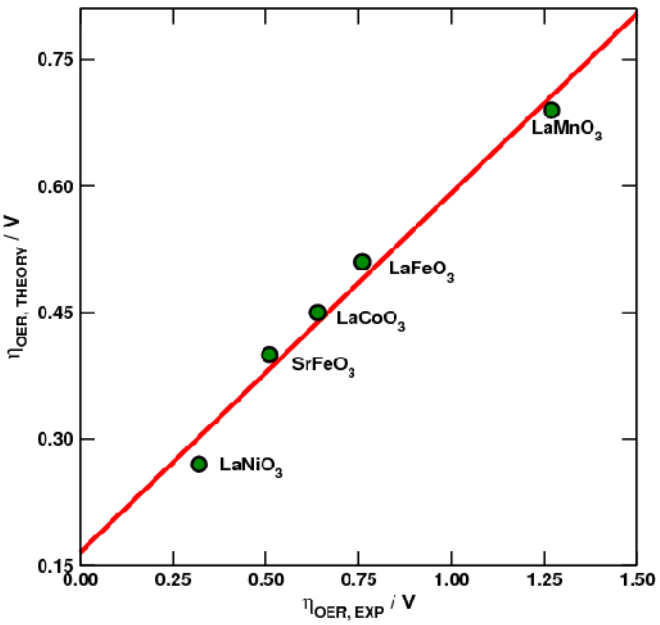

Figure 3.7. Comparison between DFT-calculated and experimental (from Refs [19, 79]) OER overpotentials.

It is worth mentioning at this point that perovskite oxides are appealing as ORR and OER cathode materials when the electrolyte used is alkaline [18]. They may not be suitable in acidic media due to stability problems. Even though these materials are very stable against thermal decomposition, as shown in Chapter 2, they can be corroded by acids. The harsh environment of PEM fuel cells may thus be destructive for them.

To verify this statement we consider now the specific example of $LaNiO_3$, a very active perovskite for OER. Its decomposition reaction into elements in aqueous solution is the following:

$$LaNiO_3 + 6\left(H^+ + e^-\right) \leftrightarrow La + Ni + 3H_2O \tag{3.29}$$

The Gibbs energy of that reaction is ~3.40 eV at pH = 0. Besides, there are 6 electrons transferred, so the decomposition potential is around -0.57 V. Thus, $LaNiO_3$ is stable against element decomposition in acidic media over that potential. However, the ionic decompositions of La and Ni, given by Reactions (3.30) and (3.31), start at potentials of -2.07 V and -0.25 V [80] (-6.21 eV and -0.50 eV in terms of free energy), respectively, at all pHs.

$$La \leftrightarrow La^{3+} + 3e^- \tag{3.30}$$

$$Ni \leftrightarrow Ni^{2+} + 2e^- \tag{3.31}$$

Assuming the initial stability of Ni and La atoms in $LaNiO_3$ to be -3.40 eV, then the dissolution energy is 2.9 eV for Ni, equivalent to 1.45 V, and 0.88 eV for La, equivalent to 0.29 V. Consequently, for $LaNiO_3$ to be electrochemically stable, one will need to operate the cell at a potential below 0.29 V, to guarantee that atoms in both A and M sites do not dissolve. This very low potential is neither of interest for ORR nor for OER. Nevertheless, this analysis constitutes only a first approximation and each perovskite might display different properties. A full analysis needs to include kinetic data to account for effects such as passivation or decomposition into individual oxides (La_2O_3 and NiO in the case of $LaNiO_3$).

3.5. Transition State Theory Studies of Perovskite Oxides

In order to study more complicated reactions than ORR/OER microkinetic modeling is required, which requires knowledge of transition-state energy barriers. These can be estimated from relations of the Brønsted-Evans-Polanyi (BEP) type [81-82], which are linear relations between the adsorption energies of the transition and final states of elementary reactions. A typical dissociation reaction is given below.

$$AB + 2* \leftrightarrow A* + B* \tag{3.32}$$

The dissociation energy is defined as follows:

$$\Delta E_{DISS} = E_{A*+B*} - 2E_{*} - E_{AB} \tag{3.33}$$

The energy of the transition state is defined similarly. BEP lines relate these two energies in the way shown in Equation (3.34).

$$\Delta E_{TS} = \alpha \Delta E_{DISS} + \beta \tag{3.34}$$

In general, the intercept should be positive and the slope equal to one or less, since the transition state is by definition as stable as the dissociated state or less. In the limit where the transition state resembles completely the dissociated one, the slope is unity, the intercept null and the line is called “recombination line”. Therefore, the slope of the BEP lines quantifies the degree of similarity between transition and dissociated states.

In recent years, BEP relations have been established from density DFT calculations for a number of molecules on different transition-metal surfaces [83-87] and for a few transition-metal compound systems [88-89]. Several reactions on transition metals are found to follow a universality rule, that is, they obey a reactant-independent linear BEP relation, however, it depends on the structure of the active site [84]. Together with scaling relations [40, 77], linear relations between molecular adsorption energies and atomic adsorption energies, BEP lines lay the basis for microkinetic modeling of different reactions where the considered molecules are a part of. It has been shown that the existence of linear BEP relations directly leads to volcano curves where the key parameter is the dissociative energy of the key reactant [90].

As shown in Figure 3.8, $LaMO_3$ perovskites display BEP relations between their energetics, but they tend to deviate from the recombination line when the surfaces are very reactive, i.e. to the left of Figure 3.8. Data for CO are shown in Appendix 2.

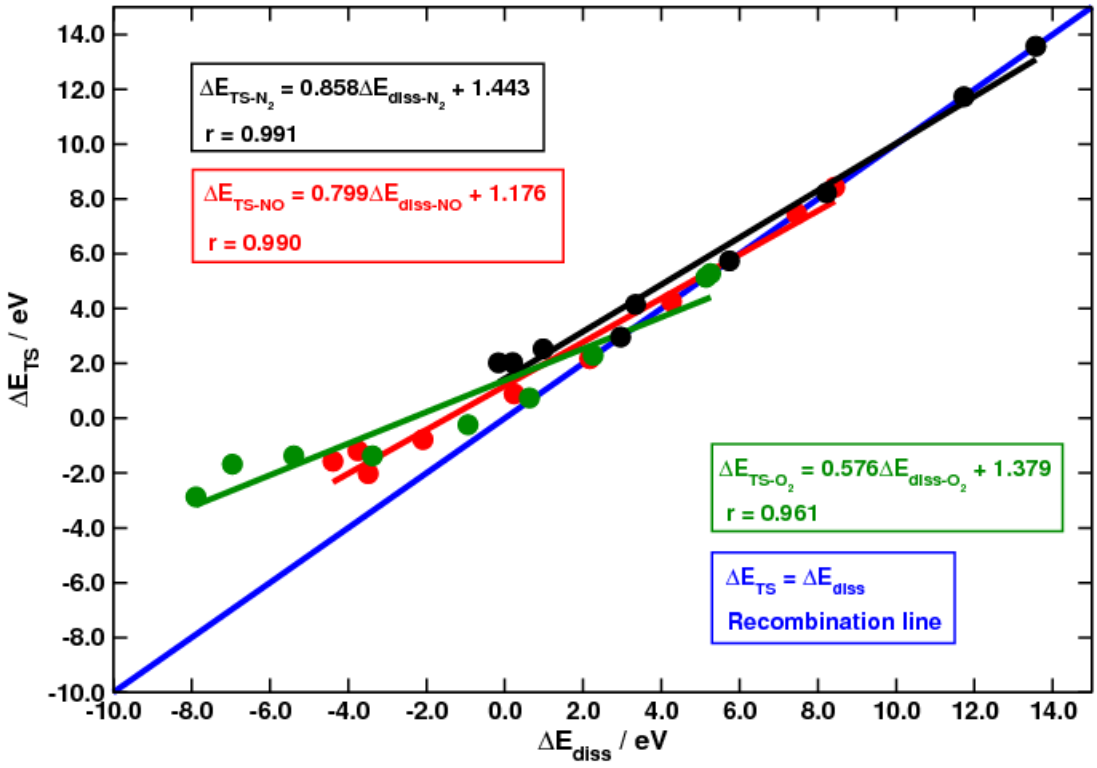

Figure 3.8. BEP relations for dissociation of diatomic molecules on (001) surfaces of $LaMO_3$, with M = Sc to Cu. Blue line: recombination; black line: N_2; red line: NO dissociation; green line: O_2.

We observe that the slopes decrease with increasing combined electronegativity of the adsorbed atoms. The electronegativities of C, N and O are 2.55, 3.04, and 3.44, respectively. In this way, the combined electronegativities of C+O, N+N, N+O, and O+O, are, in that order, 5.99, 6.08, 6.48, and 6.88. This ordering is exactly the same as for the slopes: 0.90 (CO), 0.86 (N_2), 0.80 (NO), and 0.58 (O_2).

This is not a coincidence, since the electronegative order is also displayed by the bond enthalpies, as shown in Table 3.2. Moreover, there seems to be a close relation between the point where the BEP lines cross the recombination line and the bond enthalpy of the molecules.

Table 3.2. Bond enthalpies of gaseous molecules. Values taken from Ref. [91]. RL: Recombination line.

Molecule	Bond enthalpy (eV)	Crossing point with RL (eV)
CO	11.15	9.06
N_2	9.80	10.15
NO	6.55	5.85
O_2	5.17	3.25

Since the dissociation of this kind of compounds is a one-dimensional process, one can assume that the molecule with the smallest bond energy (O_2) in Table 3.2 will dissociate at the shortest distance. In such case, the transition state resembles the initial state. On the other hand, the molecule with the largest bond energy (CO) will dissociate at the longest distance. In such case, the transition resembles the final state. This is indeed what we see in Figure 3.8 and in Appendix 2: the BEP line for CO is close to the recombination line (with a slope of 0.9), while that for O_2 deviates remarkably at highly negative dissociation energies (with a slope of 0.58).

Now the question is again whether the points forming the BEP lines follow certain order and why. Figure 3.9 helps answering that question. The reactivity of $LaMO_3$ perovskites for N_2 dissociation is: $LaScO_3 < LaCuO_3 < LaNiO_3 < LaCoO_3 < LaFeO_3 < LaTiO_3 < LaMnO_3 < LaVO_3 < LaCrO_3$. The reactivity decreases with decreasing number of d electrons of the atoms in the M position, with the exception of $LaScO_3$, $LaTiO_3$, and $LaVO_3$. This is also the ordering for CO dissociation.

Besides, the reactivity for NO dissociation is the following: $LaScO_3 < LaCuO_3 < LaNiO_3 < LaCoO_3 < LaFeO_3 < LaMnO_3 < LaCrO_3 \approx LaTiO_3 < LaVO_3$. The exceptions are now $LaScO_3$ and $LaTiO_3$.

Moreover, the reactivity for NO dissociation is: $LaScO_3 \approx LaCuO_3 < LaNiO_3 < LaCoO_3 < LaFeO_3 < LaMnO_3 < LaCrO_3 < LaVO_3 < LaTiO_3$. The exception is only $LaScO_3$ in this case. Based on these data, the minima of the BEP lines in the ranges studied correspond to $LaCrO_3$ (N_2 and CO), $LaVO_3$ (NO), and $LaTiO_3$ (O_2), while the maximum is in all cases at $LaScO_3$. Based on this we conclude that the reactivity depends both on the surface and on the adsorbed molecule. In the following we will rationalize this dependence.

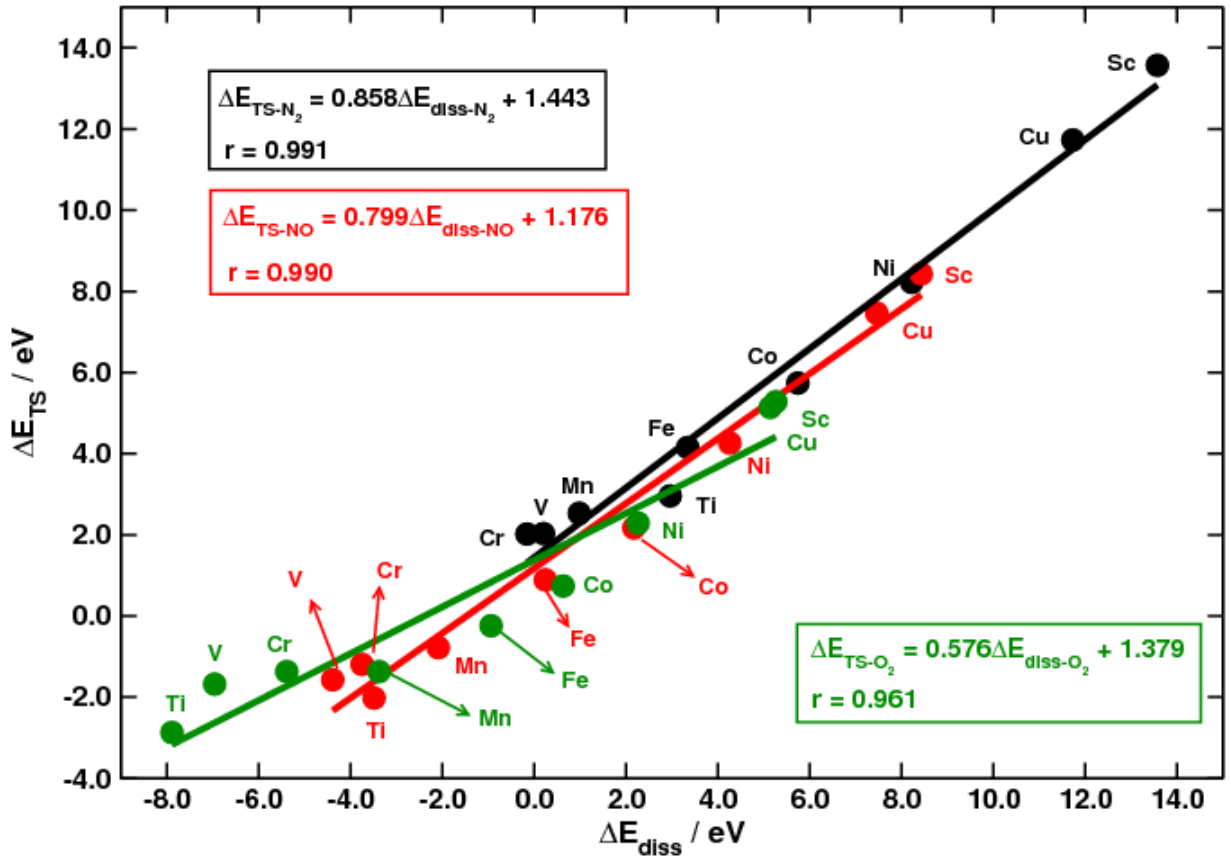

Figure 3.9. BEP lines for dissociation of small diatomic molecules on (001) surfaces of $LaMO_3$. Metals occupying the M site in $LaMO_3$ are shown. Black: N2 dissociation; red: NO dissociation; green: O2 dissociation.

One can think of the BEP lines as a scaling relation between two energies (ΔE_{DISS} and ΔE_{TS}) that behave similarly with some electronic structure parameter, namely the number of d electrons of the M component, in the case of perovskite oxides. In that way, the simultaneous observation of the variations of these energies with the scaling parameter may explain the particularities of each BEP line. This is in fact what we observe in Figure 3.10, where both dissociation and transition-state energies are plotted versus the number of d electrons of the metal in the M site.

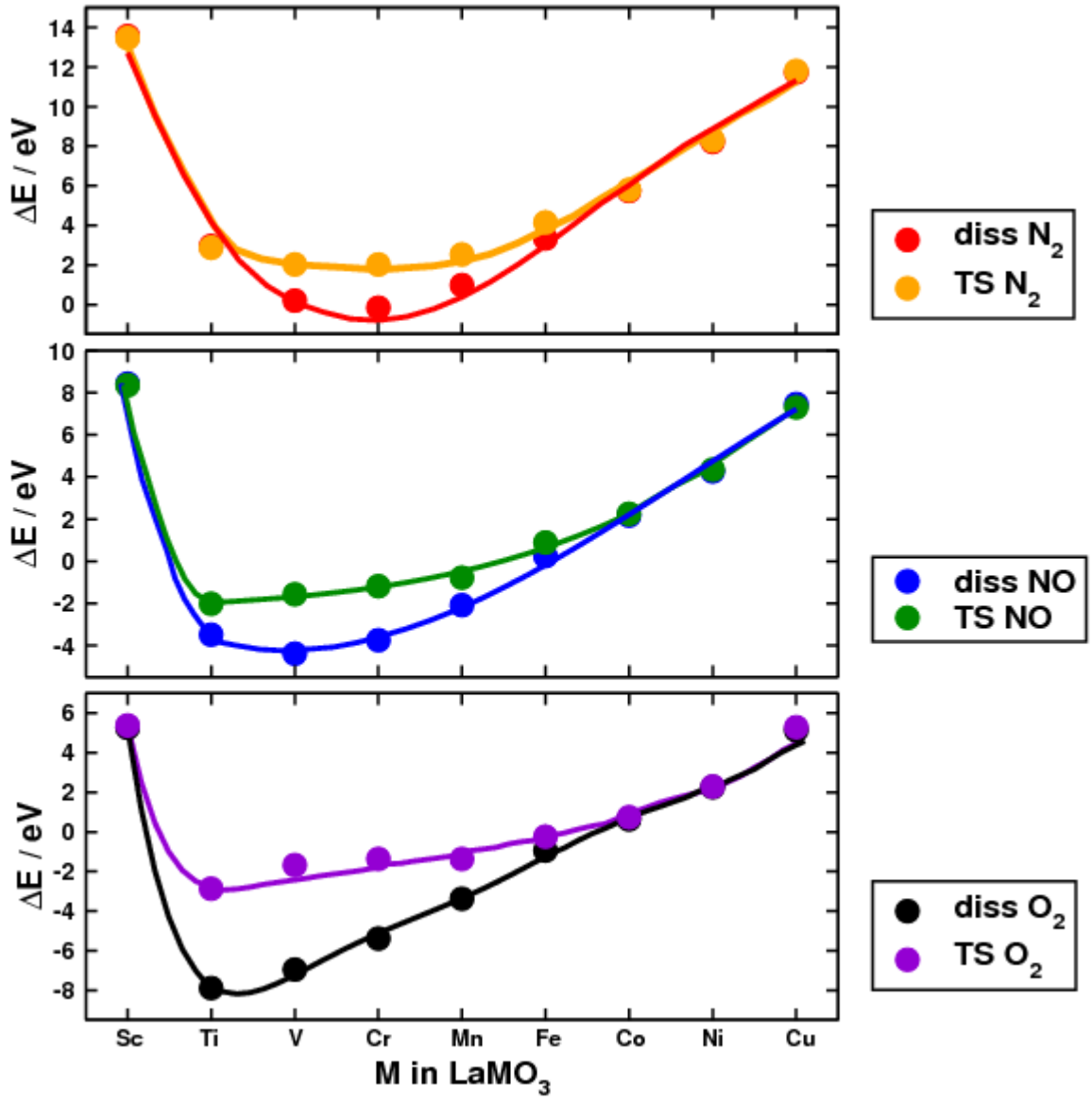

Figure 3.10. Energetic variations of the dissociation and transition states according to the M-site atom in $LaMO_3$. Top: N_2; middle: NO; bottom: O_2. Fits (solid lines) as guide to the eye are provided in each case to evidence the trends.

In each panel of this figure we notice 3 main features that account for all of the particularities of the BEP lines in Figures 3.8 and 3.9:

- Regions where the two curves overlap, i.e. to the right and to the left of each panel, have points that belong to the recombination line. This is because those compounds have

transition states that resemble completely their corresponding final states. Points in the middle deviate from the recombination line.

● The vertical distance between points for a given perovskite determines the degree of deviation of each perovskite from the ideal behavior given by the recombination line in Figure 3.8. Therefore, the largest deviations correspond to the minima in Figures 3.9 and 3.10: $LaCrO_3$ (N_2), $LaVO_3$ (NO), and $LaTiO_3$ (O_2).

● The minima correspond to $LaCrO_3$, $LaVO_3$ and $LaTiO_3$ because of the availability of electrons in the surface and the lack of electrons of the atoms in gas phase. As a first approximation, let us say that Ti^{3+}, V^{3+}, and Cr^{3+} offer, respectively, 1, 2 and 3 ionic bonds to the adsorbates. Cr^{3+} is a d^3 ion and nitrogen has 5 valence electrons. Therefore, N atoms can establish triple bonds to the surface atoms and this is why their transition state looks as the final state does. V^{3+} is a d^2 ion and nitrogen and oxygen have 5 and 6 valence electrons, respectively. Given this, O atoms can make their needed double bonds with the surface atoms, but N atoms need another one. Thus, the transition state requires that the adsorbates have some interaction with each other and with the surface, hence deviating from the final state configuration. Finally, Ti^{3+} is a d^1 ion and oxygen has 6 valence electrons, respectively. Therefore, O atoms cannot make their needed double bonds with the surface atoms and the transition state looks as an initial state does, due to the considerable interaction between O atoms. We summarize these observations in Figure 3.11.

To the right of the BEP lines we reach the ideal behavior given by the recombination line. In this limit, the adsorbates have no direct interaction and they are only bonded to the surface. To the left, deviations appear and are largest at the extremes of each line. Hence, the minima of the curves seem, as well, to determine the slope of the BEP lines, since the right ends behave identically due to their connection to the recombination line. This means that O atoms in O_2 will have one half of the surface bonds they need when dissociating on two active sites of Ti^{3+}. This is equivalent to $(1/2+1/2)/2=0.5$, which is similar to 0.576. Similarly, N and O in NO on V^{3+} will have $(2/3+2/2)/2=0.83$, which is again similar to 0.799. C and O in CO on Cr^{3+} will have $(3/4+2/2)/2=0.875$, which is again similar to 0.900.

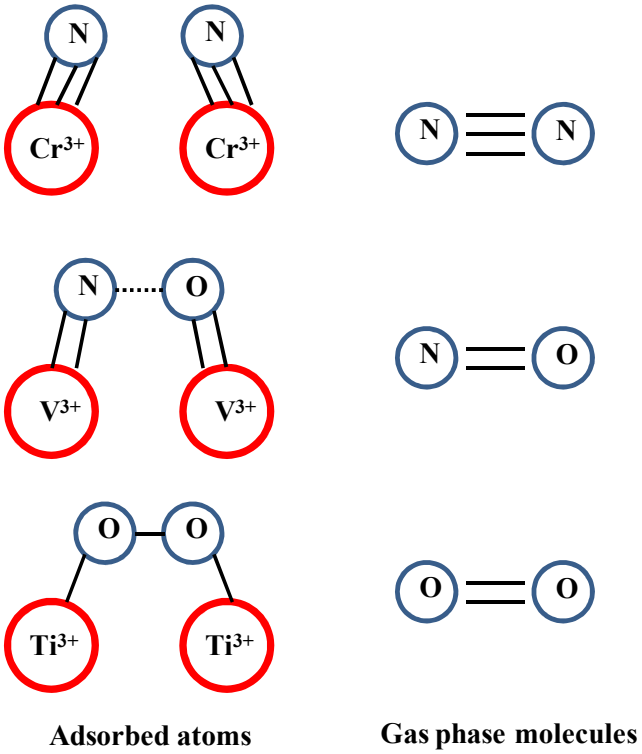

Figure 3.10. Schematics of the transition-state configurations of N_2, NO, and O_2 on the surface of perovskite oxides. The normal gas phase configurations of the molecules are shown to the right.

Finally, N atoms in N_2 on Cr^{3+} will have $(3/3+3/3)/2=1.00$, which is similar to 0.858, but differs more than the rest of the slopes. Better estimations of the degree of existence of the theoretical bonds and their strength may improve these values, but as a first approximation based on simple chemical considerations, those values are acceptable.

4. CATALYTIC ACTIVITY OF GRAPHITIC MATERIALS TOWARDS ORR/OER

4.1. Introduction

In order for low-temperature fuel cells to be a commercially-viable alternative to the conventional internal combustion engines for transportation applications, effective, stable and low-cost catalysts are needed for the ORR, which takes place at the cathode and is known to be the main source of losses in these devices [14, 92-94]. Due to the limited world supply and the elevated cost of Pt, the material commonly used as ORR catalyst, the efforts in this field of science are currently devoted to alloys of non-precious metals with Pt, and to inexpensive materials such as perovskite oxides and carbon nanostructures [15-18, 21, 30, 93]. The latter materials, in particular graphene, exhibit extraordinary thermal, mechanical and electro-optical properties [95-99].

The unusual semimetallic behavior of graphene, a single layer of graphite, was first studied theoretically by Wallace in 1947 [100] and lately synthesized experimentally for the first time by Novoselov et al. [101]. It is remarkable that graphene is a gapless semiconductor, with no gap at the Dirac point [97], i.e. the K and K' points in Figure 4.1.

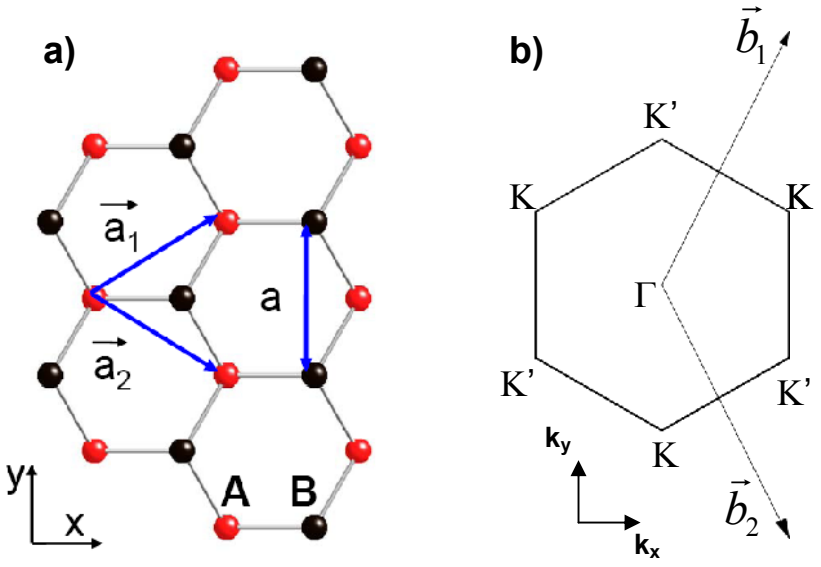

Figure 4.1. a) Basis vectors of the hexagonal lattice of graphene. **b)** First Brillouin zone of graphene. Adapted from Ref. [102].

The basis vectors of the honeycomb lattice of graphene are shown below.

$$\vec{a}_1 = \frac{a}{2}\left(\sqrt{3},1\right) \quad , \quad \vec{a}_2 = \frac{a}{2}\left(\sqrt{3},-1\right) \tag{4.1}$$

Besides, the lattice vectors of the reciprocal unit cell shown in Figure 4.1.b) are given in (4.2).

$$\vec{b}_1 = \frac{2\pi}{a}\left(\frac{1}{\sqrt{3}},1\right) \quad , \quad \vec{b}_2 = \frac{2\pi}{a}\left(\frac{1}{\sqrt{3}},-1\right) \tag{4.2}$$

The term a in Equation (4.1) is related to the carbon-carbon distance, d_{C-C}, in the following way.

$$a = \sqrt{3} \cdot d_{C-C} \tag{4.3}$$

Atoms in A (B) sites are in red (black). The coordinates of the A and B sites in the unit cell at the origin are (0,0) and $1/3\left(\vec{a}_1 + \vec{a}_2\right)$, respectively.

The first Brillouin zone of the lattice is shown in Figure 4.1.b). The energy gap between the valence band and the conduction band vanishes at the K and K' points, the so-called Dirac points, located at $K',K = \left(0, \pm 4\pi/3a\right)$. This discrete overlap between those bands is responsible for the semimetallic behaviour of graphene.

In order to change/tune the properties of graphitic materials and, in particular of graphene, the doping with boron, nitrogen and other atoms depending on the targeted functionality has been explored [103-105]. Experimentally, techniques for N-doping of carbon nanostructures have been discussed extensively by Ewels and Glerup [106]. This N-functionalization is remarkably interesting by itself and also due to the possibility of the formation of stable sites that bind other types of ligands and can have multiple electronic, chemical, catalytic and mechanical applications [105, 107-108]. A step forward in this area was made when transition metals were anchored in graphitic materials functionalized with pyridinic nitrogen atoms. Dodelet and coworkers have deeply investigated catalysts based on Fe and Co anchored on different nitrogen-modified carbon supports [20-21, 109-110]. They found that the active sites created in the interstices between graphitic crystallites in highly porous materials are particularly active towards the ORR. Nitrogen atoms bond to the edges of the crystallites forming pyridinic sites,

where a Fe^{2+} cation is subsequently inserted. The main advantage of these novel catalysts is given by the porosity of the material, since it increases the formation of pyridinic sites available for the metal atoms per unit volume. Besides, some other works have shown the catalytic activity of phtalocyanines [111-112], porphyrins [113], and enzymes [114], which have similar active sites.

4.2. Graphitic Materials Functionalized with Nitrogen and Transition Metal Atoms

Based on the work of Lefevre et al [21], we constructed two different graphene sheets functionalized with 4 nitrogen atoms and transition metals. Figure 4.2 shows those two different arrangements. Both of them contain active sites composed of 4 nitrogen atoms and an anchored transition metal in the center. However, in Cell A there are 3 carbon atoms between the nitrogen atoms in the active site, while in Cell B the number alternates between 2 and 3 carbon atoms. As will be shown later, this cell difference will be reflected as a strain effect on the adsorption properties, which tends to be larger for active sites with small transition atoms to the left of the periodic table.

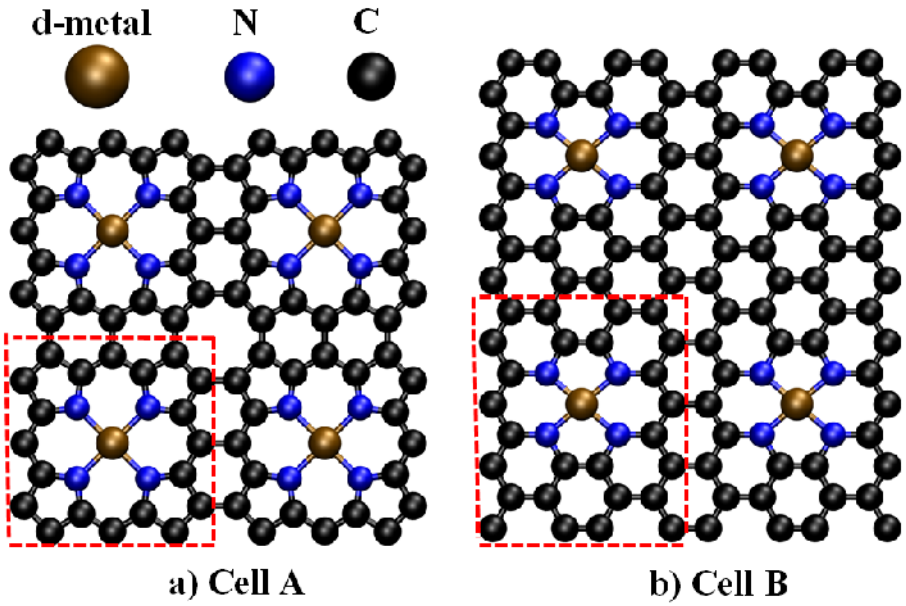

Figure 4.2. 2x2 repetitions of the unit cells used in this study, a) Cell A, with 3 carbon atoms between the nitrogen atoms in the active site, and b) Cell B, with alternating 2 and 3 carbon atoms between the nitrogen atoms in the active site. The unit cells are marked in red.

Moreover, since the transition metals and the nitrogen atoms form square planar complexes, the d states of the former will present a special splitting. Upon adsorption on atop position, the complexes will turn into square pyramidal. We checked the Density of States (DOS) of a Co atom in these complexes in order to determine the energetic ordering of the d-band. Figure 4.3 shows the DOS projected onto the d-states of a Co atom in cell B with and without adsorbates.

a)

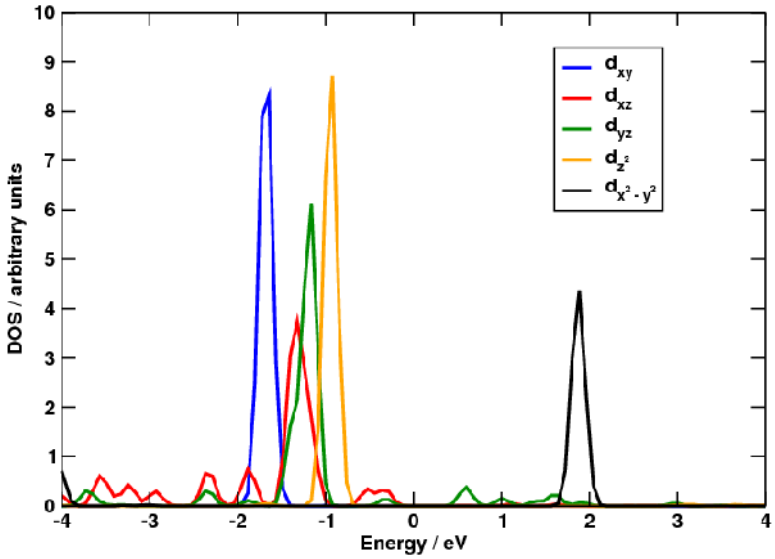

b)

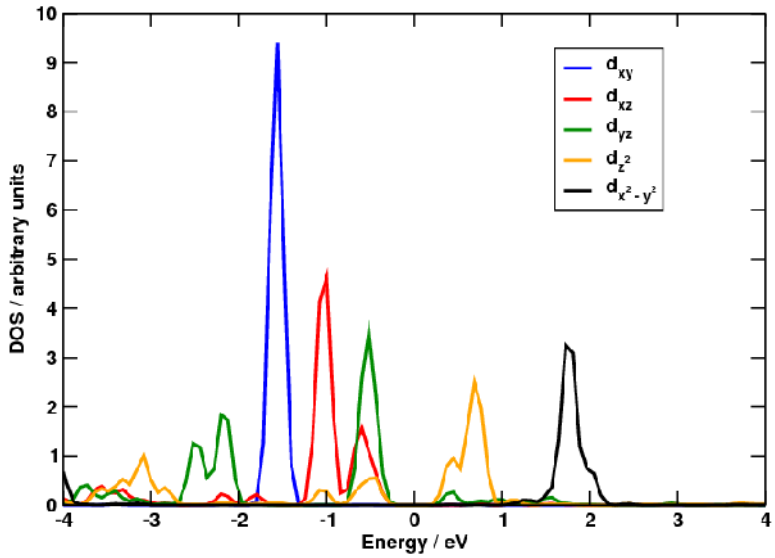

Figure 4.3. DOS projected onto the d-states of the Co atom in cell B. a) without adsorbates, b) with *OH adsorbed on atop position on Co.

From Figure 4.3.a) it is possible to determine that the increasing energetic ordering of the d-states is the following: $d_{xy} < d_{xz} \approx d_{yz} < d_{z^2} < d_{x^2-y^2}$. This ordering is typical of square planar complexes, where d_{xy} may also be located over d_{z^2}. Furthermore, the ordering remains approximately constant as expected upon adsorption on atop position. Interestingly, the $d_{x^2-y^2}$ is in all cases unoccupied and above the Fermi level, whereas the d_{z^2} is occupied when the active site is clean, but unoccupied when *OH is adsorbed, evidencing an ionic bond between Co and OH.

Now that the orbital splitting has been determined, the question to solve is whether Co will have an oxidation state of +2 or +3. The electronic distribution of a neutral Co atom is as follows: $1s^2$ $2s^2$ $2p^6$ $3s^2$ $3p^6$ $4s^2$ $3d^7$. Therefore, the distribution ends in s^2d^7. If we had Co^{2+}, the orbital splitting would be that of a d^7 atom. On the other hand, if we had Co^{3+}, the orbital splitting would be that of a d^6 atom. Our spin polarized calculations show that the resulting magnetic moment on Co is S = 1. Moreover, in the presence of *O, S = 1; whereas in the presence of *OH and *OOH, S = 0.

Figure 4.4 shows the low-spin state electronic distribution in the d-bands of Co^{2+} and Co^{3+}, taking into account the orbital ordering inferred from Figure 4.3.

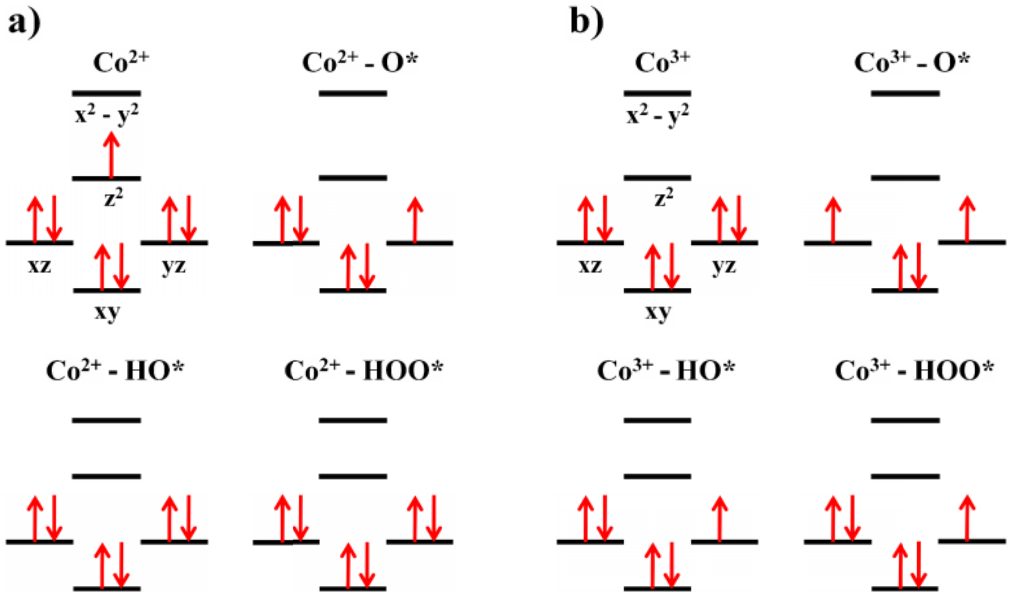

Figure 4.4. Low-spin state distribution of electrons in the d-band of Co ions a) Co^{2+}, and b) Co^{3+}, in square planar and square pyramidal complexes with 4 nitrogen ligands. The distribution resulting upon adsorption of the ORR intermediates is also shown.

According to Figure 4.4, the expected magnetic moments of a Co^{2+} would be: S = 1 or S = 3 with no adsorbates; S = 1, 3, or 5 with *O; and S = 0, 2, or 4 with *OH and *OOH. Besides, the expected magnetic moments of a Co^{3+} ion would be: S = 0, 2, or 4 with no adsorbates; S = 2 or 4 with *O; and S = 1, 3, or 5 with *OH and *OOH. The different possibilities in each case correspond to low-spin, intermediate-spin (if any), and high-spin states. The ground-state spin will correspond to the arrangement with the lowest energy. Based on this, we find that the ion present in the complex is Co^{2+} and has a low-spin ordering of its d-states. Similar analyses can be made to the rest of elements considered in this study, in order to find the oxidation states reported in Table 4.1.

Table 4.1. Possible oxidation states of the transition metals in the active sites, based on the spin analysis shown in Figure 4.4). When certain oxidation states render identical spin numbers, we use the preposition "or". On the other hand, when the oxidation state increases upon adsorption of *O, we use the preposition "and".

Element in the active site	Oxidation States
Cr	+2 and +3
Mn	+2 or +4
Fe	+2
Co	+2
Ni	+2
Cu	+2
Ru	+3 and +4
Rh	+2
Pd	+2
Ag	+1 and +2
Ir	+2
Pt	+2
Au	+1 or +3

4.3. Trends in Adsorption Energies of ORR/OER Intermediates

Following the ideas exposed in the Introduction of this chapter, it seems particularly attractive the possibility of screening theoretically and developing experimentally carbon nanostructures functionalized with N and transition metals, for catalytic applications. The latest advances in Density Functional Theory (DFT) make it possible to accurately determine adsorption energies that can hence be used as ORR activity descriptors, long time ago predicted to determine the ORR and OER activity of materials and confirmed lately [16, 19, 115]. We have exhaustively investigated the trends in the catalytic performance of graphitic layers with late transition metals anchored to pyridinic active sites towards the ORR, on the base of computational routines including calculation of the adsorption energies of the ORR intermediates (*O, *OH, *OOH), and the scaling relations between them [40, 77]. The insight allows for the identification of promising candidates through a Sabatier analysis [116].

The adsorption energies of the ORR intermediates, *O, *OH, and *OOH, were calculated relative to H_2O (g) and H_2 (g), according to Eqns (4.4) to (4.9), where *GrM* represents the active site in the functionalized graphene sheet.

$$GrM + H_2O_{(g)} \leftrightarrow GrM - O + H_{2(g)} \tag{4.4}$$

$$\Delta E_O = E_{GrM-O} - E_{GrM} - (E_{H_2O} - E_{H_2}) \tag{4.5}$$

$$GrM + H_2O_{(g)} \leftrightarrow GrM - OH + \frac{1}{2}H_{2(g)} \tag{4.6}$$

$$\Delta E_{OH} = E_{GrM-OH} - E_{GrM} - (E_{H_2O} - \frac{1}{2}E_{H_2}) \tag{4.7}$$

$$GrM + 2H_2O_{(g)} \leftrightarrow GrM - OOH + \frac{3}{2}H_{2(g)} \tag{4.8}$$

$$\Delta E_{OOH} = E_{GrM-OOH} - E_{GrM} - (2E_{H_2O} - \frac{3}{2}E_{H_2}) \tag{4.9}$$

The trends in adsorption energies of the ORR intermediates in graphitic materials with active sites composed of 4N and transition metals are shown in Figure 4.5. Interestingly, we note that an increase in the number of d-electrons of the transition metals in the active sites tends to

decrease the strength of the interaction between the active site and the adsorbates. This systematic behavior is explained by taking into consideration the splitting of the d-band of the transition metal in this kind of complexes, shown in Figure 4.4 for the specific case of Co. On the other hand, we observe in Figure 4.5 a constant separation of ~3.18 eV between the energy levels of *OH and *OOH, while that of *O moves in between those two. This in agreement with our previous analyses carried out on oxide surfaces which concluded that the energy levels of *OH and *OOH have a constant separation of ~3.2 eV (No 3 in List of Included Articles).

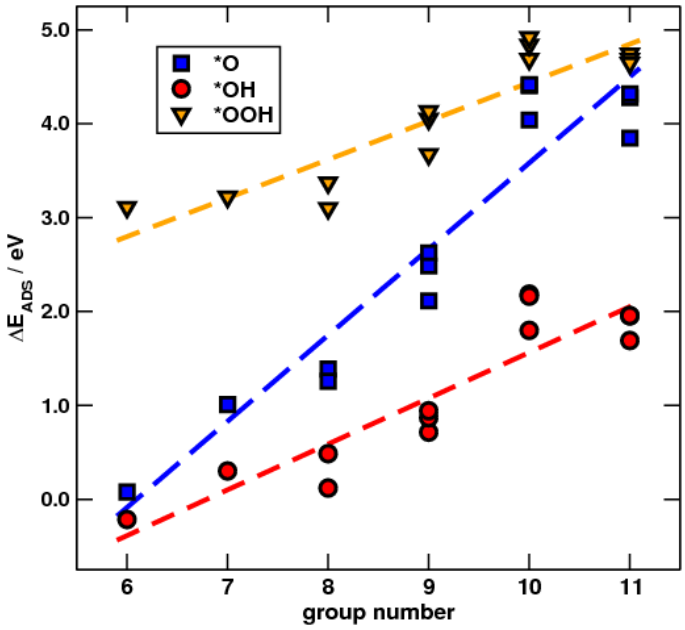

Figure 4.5. Trends in adsorption energies of the ORR/OER intermediates for Cell B. Dashed lines as guides to the eye show the trends and the constant separation of ~3.2 eV between the energy levels of *OH (red) and *OOH (yellow), while that of *O (blue) is in between. Generally, an increase in the number of d-electrons of the transition metals decreases the strength of the interaction between the active site and the adsorbates.

From a chemical point of view, we find two limiting cases in Figure 4.5: (1) When the *O level equals that of *OH, i.e. for active sites to the left of the figure, the stability of the *OOH intermediate is limited by the O-O bond strength, which will tend to decompose into tightly bound *O and free OH. This is the case for elements in group 6 and before. This extreme is not convenient due to the instability of the *OOH intermediate and the exaggerated *O adsorption

energy which will poison the active site. (2) When the *O level equals that of *OOH, i.e. to the right of the figure, the stability of the *OOH intermediate will be limited by the M-O bond strength and *OOH will then be loosely bound to the surface or will not stick to it at all. This is the case for elements in groups 10 and 11. This extreme is inconvenient due to the weak binding of *OOH, which is the first intermediate of the ORR.

The reaches of Figure 4.5 can also be seen explicitly in Figure 4.6. In it we present the scaling relations between the adsorption energies of the ORR adsorbates. We note that the positions of the different transition metals along the lines are given by their number of d electrons. Furthermore, the gaps of ~1 eV in the *O adsorption energies and ~0.5 eV observed in the *OH and *OOH adsorption energies in both panels in Figure 4.6, strictly separate active sites with metals belonging to groups 9 and before, from those in groups 10 and 11. This evidences the antibonding nature of the d orbitals in these complexes and the discrete energetic leaps implied in their filling. The linear behavior with an ideal slope of 0.5 in Figure 4.6 has already been reported for metals and oxides [40, 77] and is of special use to construct the volcano plot in Figure 4.7, by using Equations (3.21) to (3.28).

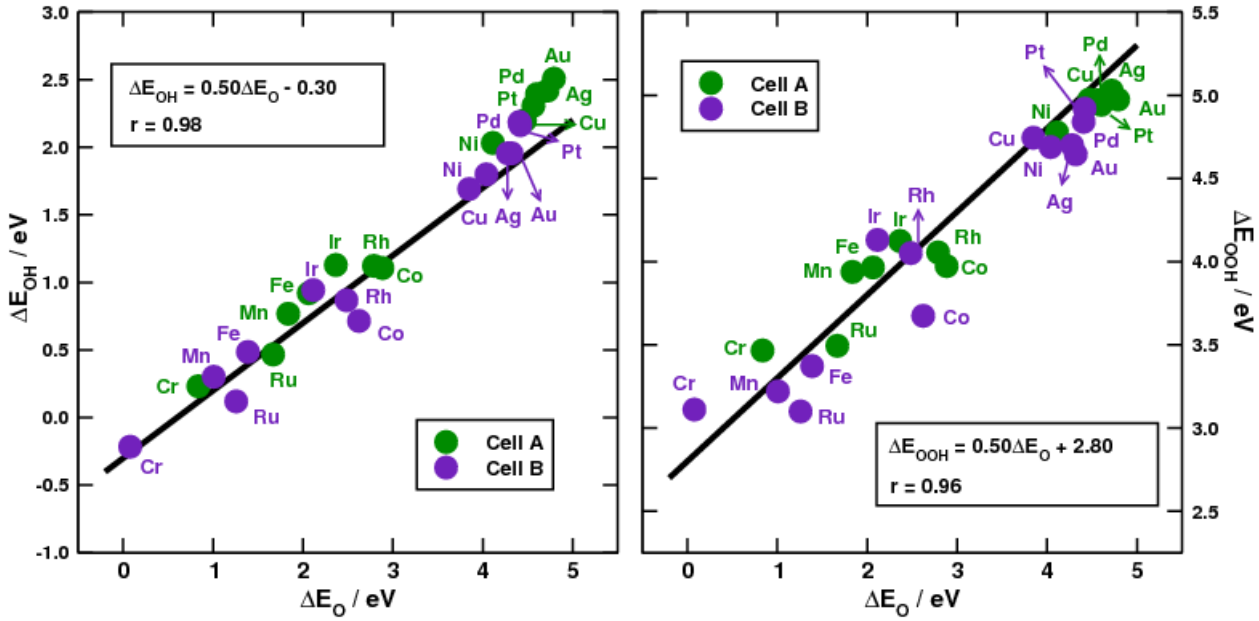

Figure 4.6. Scaling relations between the adsorption energies of the ORR/OER adsorbates. Right panel: *O vs. *OH; left panel: *O vs. *OOH. Data for cells A and B are given in green and purple, respectively; the transition metal anchored to the 4N active site is also given. The position of the different transition metals along the lines is given by their number of d-electrons.

4.4. Combined Volcano Plot for ORR/OER

We assume the 4-electron reaction path for the ORR shown in Chapter 3. We convert into Gibbs free energies our calculated DFT energies by adding to them the values of the entropic and zero-point energy corrections given in Appendix 2, and by adding a solvation correction to the ORR adsorbates which we have estimated as ~0.30 eV.

$$O_{2(g)} + (H^+ + e^-) + GrM \leftrightarrow GrM - OOH \tag{4.10}$$

$$\Delta G_4 = \Delta E_{OOH} - 4.92 + 0.4 + 0.30 \tag{4.11}$$

$$GrM - OOH + (H^+ + e^-) \leftrightarrow GrM - O + H_2O \tag{4.12}$$

$$\Delta G_3 = \Delta E_O - \Delta E_{OOH} - 0.35 - 0.30 \tag{4.13}$$

$$GrM - O + (H^+ + e^-) \leftrightarrow GrM - OH \tag{4.14}$$

$$\Delta G_2 = \Delta E_{OH} - \Delta E_O + 0.30 + 0.30 \tag{4.15}$$

$$GrM - OH + (H^+ + e^-) \leftrightarrow GrM + H_2O \tag{4.16}$$

$$\Delta G_1 = -\Delta E_{OH} - 0.35 - 0.30 \tag{4.17}$$

The volcano plot in Figure 4.7 contains the lines representing the Gibbs free energies of each step in the following mechanism for the metals considered, and the tops for ORR (at ~2.3 eV) and OER (at ~2.6 eV) result from the intersection of those lines. We have marked in Figure 4.7 only the closest sites in activity to the tops of ORR and OER: the former will be efficiently catalyzed by sites with Fe, Ir, Mn, Ru, and Rh; while the latter will be catalyzed by active sites of Co, Rh, and Ir. Our findings on graphitic materials with sites composed of Fe are in excellent agreement with previous experimental results [20-21, 109-110]. However, the insight given by DFT goes beyond to pinpoint sites with elements belonging to groups 7 to 9 in the periodic table as active materials towards ORR and OER.

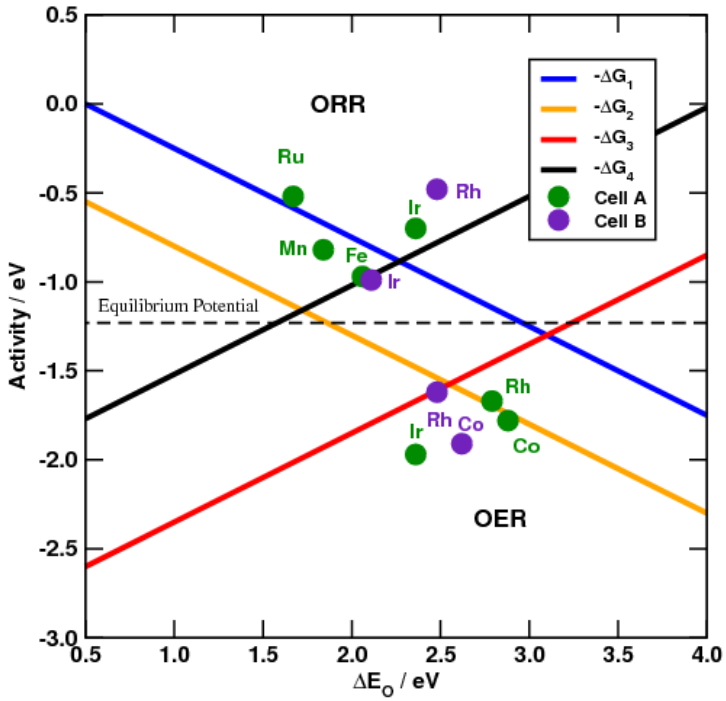

Figure 4.7. Combined volcano plot for the ORR (up) and OER (below), resulting from the thermodynamic analysis shown in the main text. Only the most active metals in cells A and B are shown in green and purple, respectively. For the ORR the lowest overpotentials are achieved by active sites containing Fe, Ir, Mn and Ru, whereas for OER are achieved by active sites of Co, Rh and Ir.

The optimal ORR and OER catalysts belong to these groups of elements since they have a good compromise between the M-O and O-O bond strengths, so that the *O level is adequately placed in between those of *OH and *OOH. In this respect, active sites composed of Ir seem particularly interesting, since they seem to be active both for ORR and OER. This alternative is worth trying experimentally, especially since Ir porphyrins and phtalocyanines have been used before for ORR [117-118].

Furthermore, we observe that the most active sites have commonly the oxidation state +2. From a chemical point of view this is important, since it shows the important role that coordination and oxidation state play in the activity of determined species towards certain reaction. For instance, noble metals like Pt or Pd which have null oxidation states in metal phase, are the most active towards the ORR, whereas in the graphitic environment considered here, having a different coordination and oxidation state, tend to bind too weakly. On the other hand Fe, normally seen as a reactive metal, displays high activity in this graphitic environment. We remark here that, as in

the case of pure metals, the range of active elements is not large, but in the case of graphitic materials the promising candidates contain more non-noble options. This is why these materials are appealing for conducting the ORR in fuel cells and/or the OER in electrolyzers. Nonetheless, issues like the low density of active sites and mass transport limitations at high current densities are practical issues that need to be solved before these inexpensive catalysts can spread in technological applications [21].

5. TRENDS IN ADSORPTION ON NEAR-SURFACE AND SURFACE ALLOYS OF PLATINUM AND LATE TRANSITION METALS

5.1. Introduction

Following extensive studies of the surfaces of pure elements over the past few decades, more complex material structures such as alloys and oxides have in recent years received considerable attention as candidate materials for the computational design of catalytic surfaces [34, 77-78]. In particular, alloys of Pt have proved high structural and compositional versatility, and the synergy between components introduces the so-called "bifunctionalities" and other new and unexpected features to the materials in addition to ligand and/or strain effects which can improve the catalytic performance of pure Pt for a number of diverse reactions [16-17, 119-120].

In real alloys ligand and strain effects are normally entangled, nonetheless electronic structure simulations have successfully been used to de-convolute and study them separately [7-8]. Strain is the major effect in the case of Pt overlayers or "dealloyed" core-shell nanoparticles [17, 121-122], where a thin layer of Pt is stretched or compressed according to the lattice constant of the host, thereby attaining a higher or lower reactivity, respectively.

Near-Surface Alloys (NSAs) and Surface Alloys (SAs) have the great advantage of preserving the lattice constant of Pt, and therefore no compressing/stretching effects influence the reactivity. This absence of lateral strain allows for systematic studies of the ligand effect, introduced by the alloying metals and their concentration in the surface and subsurface layers, on the catalytic activity. Previously, the effect of ligands on the reactivity has been studied on NSAs of Pt where the subsurface layer was exchanged with a different metal [123]. In the present study we focus on trends in the ligand effect as the concentration of the alloying metal in the two top layers is varied. We illustrate the differences in adsorption behavior of CO between NSAs and SAs of Pt with Cu as a particular case study. There has been recent interest in Pt-Cu alloys due to their surprising properties and possible technological applications in important reactions such as Water- Gas Shift and Oxygen Reduction [17, 119-120]. Moreover, we extend our findings to other late transition metals, in a first attempt to systematize the behavior of these compounds in

terms of a simple parameter which is possible to observe and control experimentally: the proportion of the components of the alloying element in the 2 top layers of the surface.

5.2. Adsorption Energies within the d-band Model

NSAs and SAs ($M_{3-x}Pt_x$ / $M_{3-y}Pt_y$, where M is a late transition metal and $x,y \in [0, 1, 2, 3]$) were formed by replacing atoms from the 2 top layers of a slab of 12 atoms with Pt and M in the ratio indicated by the stoichiometry, as shown in Figure 5.1.

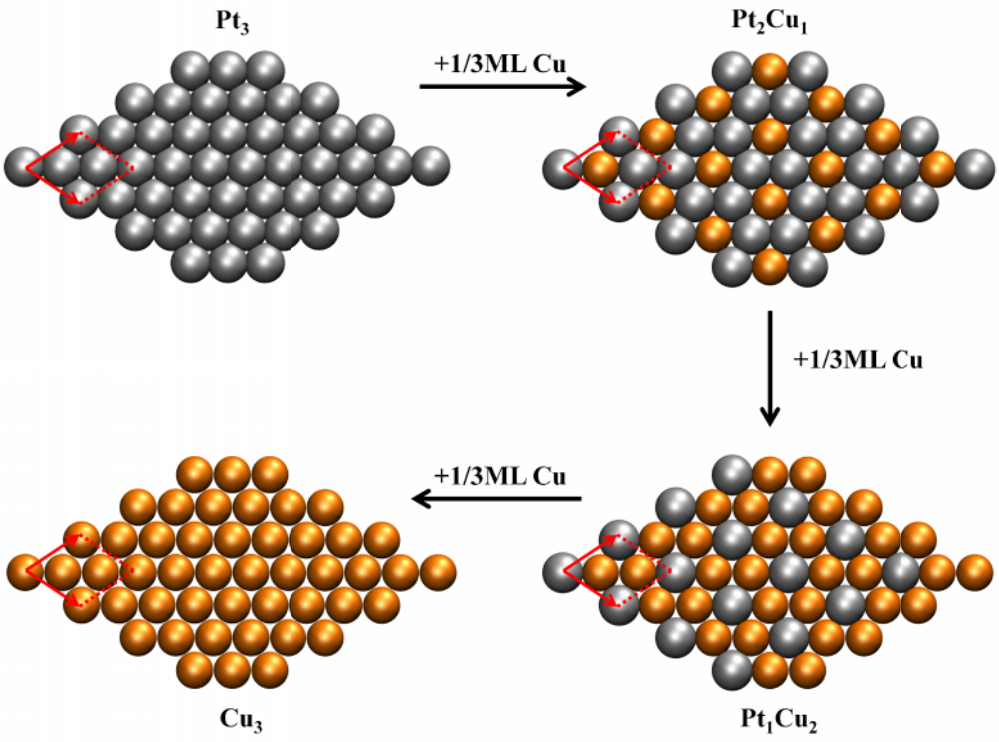

Figure 5.1. Structural schematics for the top layers of the studied NSAs and SAs of Pt (gray) and Cu (orange). The labels of the structures, i.e. Pt_3, Pt_2Cu_1, Pt_1Cu_2 and Cu_3, indicate the stoichiometry of the layer. Red arrows are used to show the ($\sqrt{3}$x$\sqrt{3}$) *R*30° (111) unit cell.

The adsorption energies were calculated relative to CO (g) and clean slabs, denoted here as *PtM*, according to Equations (4.4) and (4.5).

$$PtM + CO_{(g)} \leftrightarrow PtM - CO_{(ads)} \tag{5.1}$$

$$\Delta E_{CO} = E_{PtM-CO} - E_{PtM} - E_{CO} \tag{5.2}$$

The left panel in Figure 5.2 shows the variation of ΔE_{CO} from Eqn (4.5) versus the d-band center (ε_d) of the Pt atom on top of which CO is bound. The compositions of the 2 top layers of each alloy are also given.

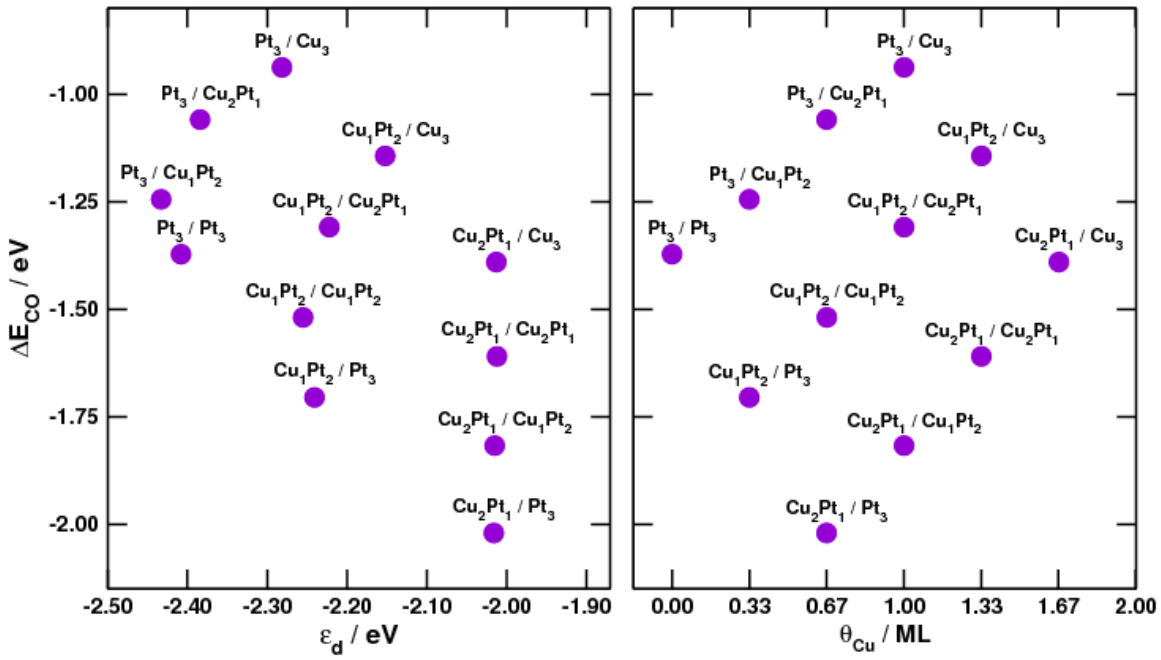

Figure 5.2. Adsorption energies of CO for various NSAs and SAs of Pt and Cu versus the d-band center of the Pt atom to which CO is bound (left panel), and versus the total amount of Cu in the 2 top layers, θ_{Cu} (right panel). Labels over the points indicate the layer compositions. The use of θ_{Cu} instead of ε_d generates a well-defined grid that allows further interpolations.

That panel in Figure 5.2 clearly shows that ε_d is essentially constant, within a range of approximately 0.1 eV, for alloys with the same composition in the first layer, independently of the proportions in the second. Interestingly, these alloys have quite different adsorption energies, the biggest difference being around 0.6 eV (between Cu_1Pt_2/Pt_3 and Cu_1Pt_2/Cu_3). This is an exception to the d-band model by Hammer and Nørskov [47], since ε_d is constant but the adsorption energy changes and, therefore, the variations in the d-band do not describe those of binding energies. Therefore, ε_d and ΔE_{CO} are unlikely influenced by the composition of the alloy,

since ε_d is highly independent of the influence of the second layer, whereas ΔE_{CO} is strongly dependent on it. These variations give raise to a plane instead of a line (not necessarily straight) relating ΔE_{CO} and ε_d, as shown in Figure 5.2. However, we also note in the left panel of Figure 5.2 the existence of 4 different lines in which the composition of the second layer is fixed, while the variations along the lines are given by the composition of the first layer. For example, the bottom line goes from Pt_3/Pt_3 to Cu_2Pt_1/Pt_3, passing by the intermediate composition Cu_1Pt_2/Pt_3, and having all of them in common a full monolayer of Pt in the subsurface layer. Moreover, the 4 lines have, for all intents and purposes, identical slopes.

On the other hand, the dissimilar variations of ΔE_{CO} with ε_d are not exclusive of the Pt-Cu alloys. Figure 5.3 shows the behavior of various NSAs and SAs of Pt and selected late transition metals. We observe that the dissimilarities do not permit a univocal characterization of the considered alloys.

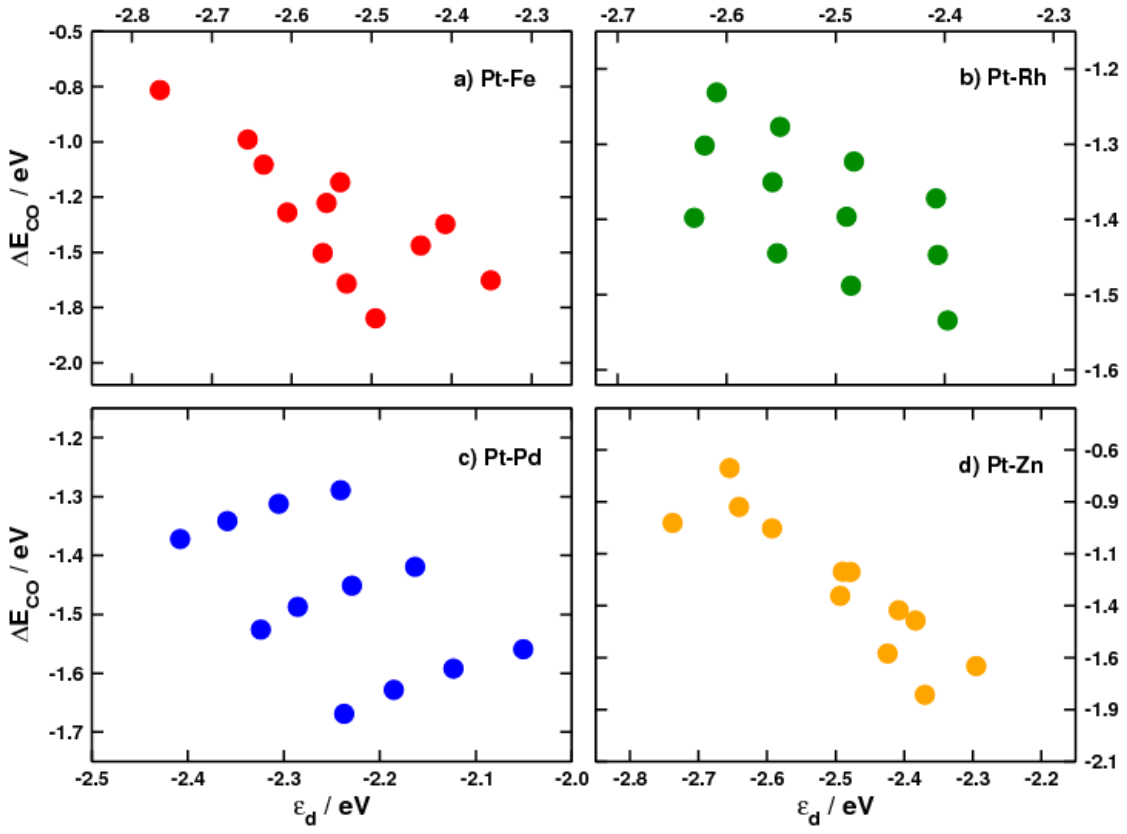

Figure 5.3. Variations of ΔE_{CO} with ε_d for selected alloys of Platinum and late transition metals: a) Pt-Fe, b) Pt-Rh, c) Pt-Pd, and d) Pt-Zn.

The behavior of Pt-Pd and Pt-Rh is similar to that of Pt-Cu, and the trends suggest again the formation of several lines with constant composition in the second layer. On the other hand, Pt-Zn and Pt-Fe tend to be linear, but the deviations from a least-squares fit would be rather large. It is also a noteworthy fact that the range of values of ε_d is smaller or at least equal to that of ΔE_{CO}. Therefore, the adsorption energies change rapidly and small differences in ε_d are usually accompanied by large differences in ΔE_{CO}.

5.3. Trends in Adsorption Energies with Alternative Descriptors

Since it is the addition of the alloying metal what causes the changes in the adsorption properties, we speculated that the composition (θ_M) of the NSAs and SAs might be used as a descriptor for their adsorption energies. This is in fact what the right panel in Figure 5.2 confirms. The use of the total amount of Cu in the alloy generates a well-defined grid where one is able to determine the adsorption energy of any alloy given the composition of the 2 top layers. Interestingly, the vertical lines in this Figure corresponding to alloys with constant amounts of Cu reveal an important feature of the alloying process: the effect of Cu on the adsorption energies is layer-dependent. Cu in the first layer will strengthen the Pt-C bond compared to pure Pt, whereas Cu in the second layer will weaken it. Nevertheless, an important question at this point would be whether these findings are applicable to other alloys of Pt. Figure 5.4 shows this is indeed the case for the other selected surface alloys of Pt with late transition metals. We note that the effect of dosing the alloying metal on Pt (111) surfaces is qualitatively the same over the binding energies, but quantitatively different, according to the energy scales in the 4 panels of Figure 5.4, and we will come back to this later.

As shown in Figure 5.3, these alloys have dissimilar ΔE_{CO} vs. ε_d correlations, while those of ΔE_{CO} vs. θ_M are identical, according to Figure 5.4, and these similarities allow for further systematization. The dissimilarities in the ΔE_{CO} vs. ε_d correlations reflect that the effect of the SA compared to NSA on the electronic structure of Pt changes as the ligand metal is changed. For Pt-Rh SAs and NSAs ε_d is mainly influenced by the composition of the second layer, Pt-Pd has a characteristic somewhere in between Pt-Cu and Pt-Rh SAs and NSAs. This means that we cannot predict trends in reactivity directly from trends in electronic structure, and some calculations of adsorption energy are necessary.

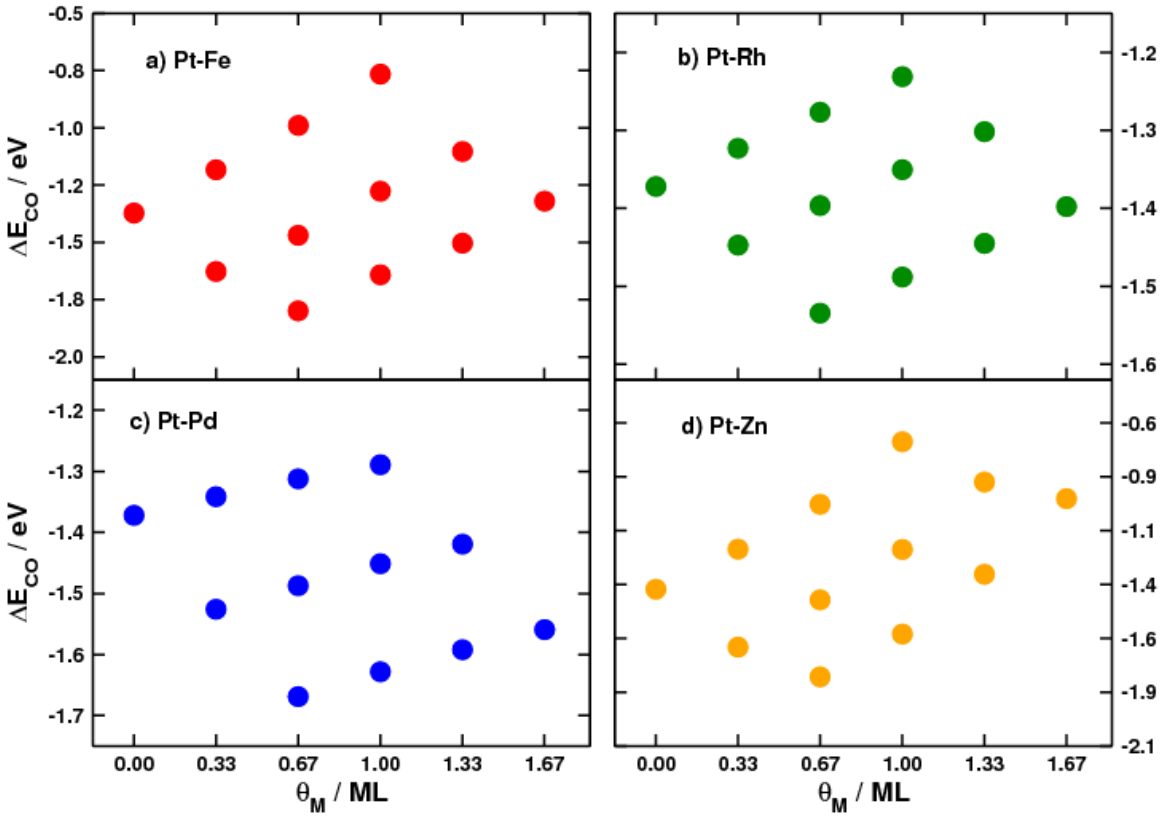

Figure 5.4. DFT calculated adsorption energies of CO versus the composition (θ) of the top 2 layers for selected alloys of Pt and late transition metals (M): a) Pt-Fe (group 8); b) Pt-Rh (group 9); c) Pt-Pd (group 10); d) Pt-Zn (group 12). In all cases a well-defined grid is formed.

5.4. Adsorption Energy vs Composition Maps

The procedure for the creation of adsorption energy vs. composition maps for a given alloy consists of the 3 following steps. Figure 5.5 schematizes the methodology.

1) Set of the origin and calculation of the 2 first maxima: pure Pt (o), universal for all alloys and therefore used as origin; the alloy with the maximum amount of M only in the second layer, i.e. Pt_3/M_3 in the unit cell we used (m_2); and the alloy with the maximum amount of M only in the first layer, i.e. M_2Pt_1/Pt_3 (m_1). The 3 points are plotted in a ΔE_{CO} vs. θ_M plane.

2) Calculation of the 2 composition vectors: μ_1 goes from o to m_1 and corresponds to the first layer composition; and μ_2 goes from o to m_2 and corresponds to the second layer composition.

3) Location of the third maximum: by adding μ_1 and μ_2 with the parallelogram rule we get μ_3, which has m_3 as tip and the maximum amount of M in both layers (M_2Pt_1/M_3) since it is the sum of the vectors with the maximum amount of M in the 2 top layers, separately.

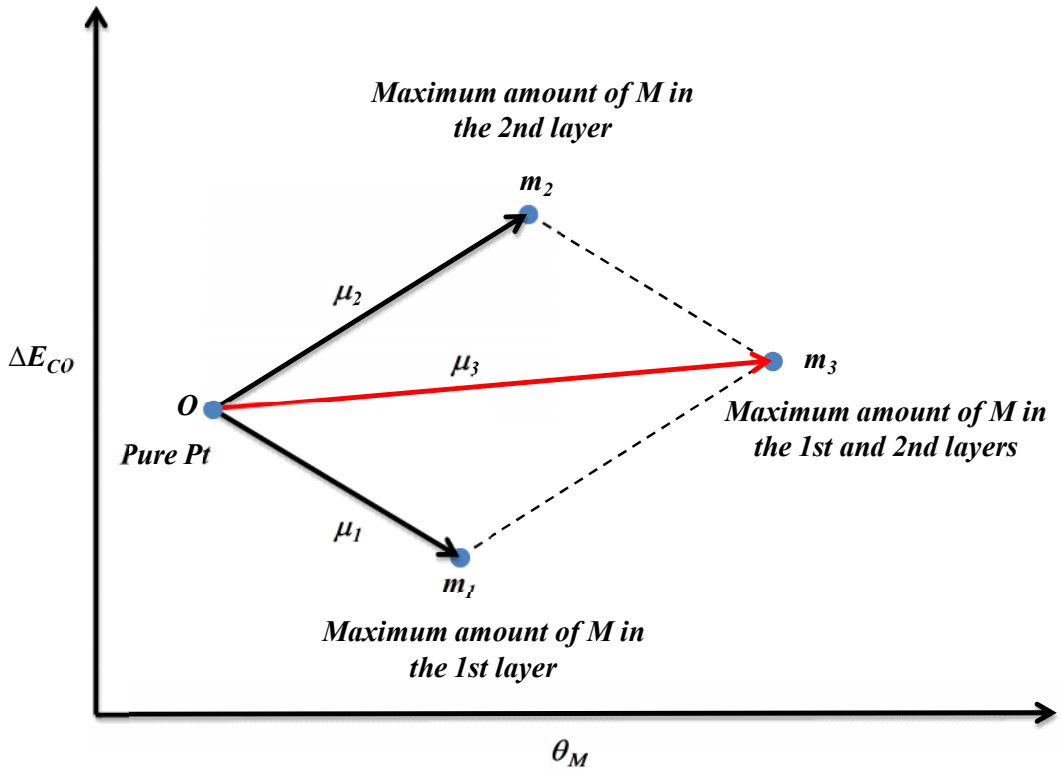

Figure 5.5. Schematics of the proposed vector analysis for CO adsorption energies versus the composition of Pt alloys with late transition metals. The binding energy of a NSA or SA can be found with a linear combination of μ_1 and μ_2, the vectors of the first and second layer compositions, respectively.

It is worth noticing that the effect of the subsurface layer composition is basically independent on the effect of the surface composition, which means that only 2 binding energies are required (m_1 and m_2, since o is universal and m_3 is derived from m_1 and m_2). Moreover, a direct consequence of this vector analysis is that any intermediate composition can be approximately calculated by a linear combination of the independent vectors μ_1 and μ_2, and it can be said that these vectors span the whole range of compositions and binding energies delimited by o, m_1, m_2 and m_3. This saves considerable computational time and allows for fast screening studies and avoids Densities of States (DOS) calculations. This analysis also applies if CO induces a complete segregation of M from the subsurface to the surface or vice versa [119, 124], since one

of the vectors will be null while the other will still represent the compositional variations of the alloy.

Figure 5.6 collects the different planes formed when the composition of the alloys is used as descriptor for the variation of the binding energies. It can be seen in this figure that the magnitudes and the directions of the layer vectors depend upon the alloying metal, being the sizes of the planes smaller for alloying atoms with d-state radii ($r_d^{(M)}$) close to that of Pt (1.116 Å), as for Pd (1.012 Å) and Rh (1.066 Å), but dissimilar for Fe (0.864 Å), Cu (0.721 Å), and Zn (not available, but presumably close to that of Cu) [125]. We remark here that the shapes of the planes are approximately parallelogram-like, but they are not perfect.

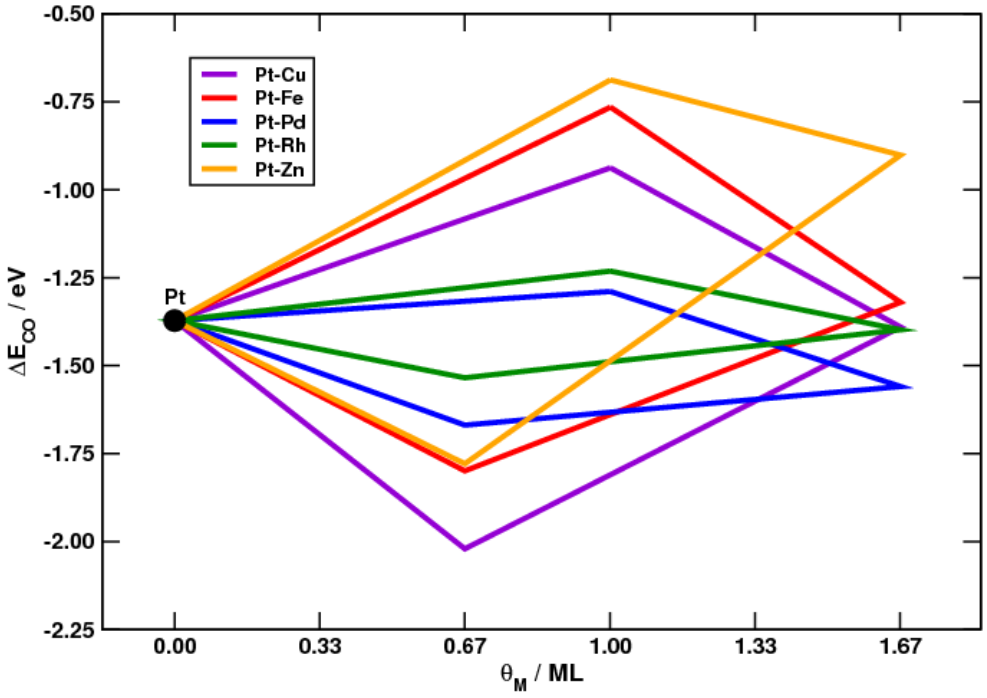

Figure 5.6. Parallelograms formed by the variations of ΔE_{CO} with θ_M for selected alloys of Platinum and late transition metals: Pt-Cu (violet), Pt-Fe (red), Pt-Pd (blue), Pt-Rh (green), and Pt-Zn (orange). The black point represents pure Pt (111).

5.5. Geometrical Observations

Continuing with the Pt-Cu system as case study we present some geometrical observations on the behavior of these alloys. The left panel of Figure 5.7 shows that in all NSAs and SAs of Pt and

Cu there is a contraction of the interlayer distance compared to that of pure Pt due to the lack of coordination of the top layer. The differences between alloys will again be given by the amount of Cu in the 2 top layers. On the other hand, the right panel of Figure 5.7 shows that the effect of adding Cu to Pt will, in general, cause an increase of the CO bond length to the surface.

From the trends in that figure it follows that the formation of NSAs, SAs or a combination of both over the 2 top layers will result in a reduction of the interlayer distance. By contrast, the effect over Pt-C distances will be repulsive, the strength of the effect being dependent on the location of Cu. For a given composition, the alloy having most Cu in the second layer will have the longest bond length to CO and the weakest adsorption energy.

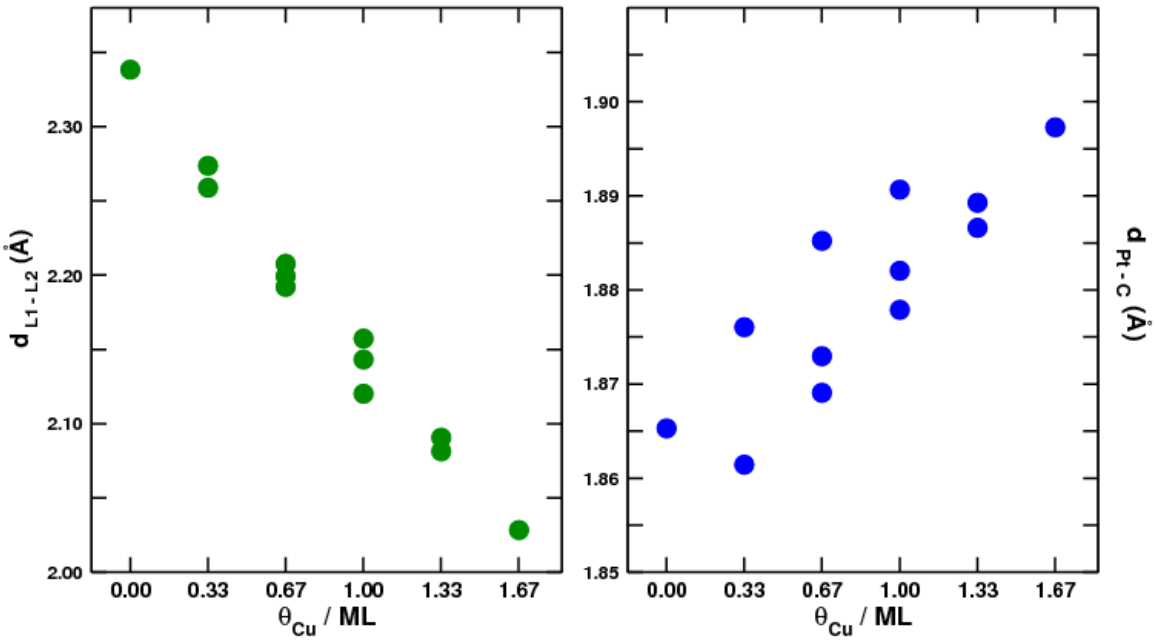

Figure 5.7. Distance between the first and the second layers, and between Pt and C in CO adsorption versus the amount of Cu present in the alloys (right and left panels, respectively). The addition of Cu has an attractive effect on the 2 top layers, whereas the effect on CO is repulsive.

Table 5.1 shows the internuclear Pt-Pt and/or Pt-Cu distances between the Pt atom binding CO and its 3 nearest neighbors in the second layer for all alloys considered. Pt-C distances and matrix elements (defined and used in the next section) are also given, indicating in all cases the amount of Cu and the stoichiometry of the layers.

We note that the difference between layer distances with and without CO is in average 0.02Å. This means there will be no important relaxation between layers due to CO adsorption. Given this, gas phase CO will (in an Effective Medium Theory (EMT) picture [77, 126]) have to find its equilibrium position as an adsorbate by getting closer to/further apart from the surface, in order to optimize the embedding electron density from the surface, which varies according to the amount of Cu and its specific location.

Table 5.1. Geometrical and bonding interaction data for Pt-Cu alloys.

Alloy	θ_{Cu} (ML)	d_{1L-2L} / Å	d_{Pt-Pt} / Å	d_{Pt-Cu} / Å	d_{Pt-C} / Å	V^{Pt}_{ddm} / eV	V^{Pt}_{pdm} / eV
Cu_1Pt_2 / Cu_1Pt_2	0.667	2.208	2.756	2.749	1.873	0.428	1.874
Cu_1Pt_2 / Cu_2Pt_1	1.000	2.157	2.704	2.711	1.882	0.408	1.838
Cu_1Pt_2 / Cu_3	1.333	2.081	-	2.645	1.889	0.387	1.810
Cu_1Pt_2 / Pt_3	0.333	2.274	2.807	-	1.861	0.442	1.921
Cu_2Pt_1 / Cu_1Pt_2	1.000	2.143	2.729	2.730	1.878	0.354	1.854
Cu_2Pt_1 / Cu_2Pt_1	1.333	2.091	2.668	2.681	1.887	0.336	1.820
Cu_2Pt_1 / Cu_3	1.667	2.028	-	2.603	1.897	0.316	1.780
Cu_2Pt_1 / Pt_3	0.667	2.192	2.768	-	1.869	0.373	1.890
Pt_3 / Cu_1Pt_2	0.333	2.259	2.797	2.783	1.876	0.499	1.862
Pt_3 / Cu_2Pt_1	0.667	2.199	2.747	2.743	1.885	0.481	1.826
Pt_3 / Cu_3	1.000	2.120	-	2.681	1.891	0.461	1.805
Pt_3 / Pt_3	0.000	2.338	2.857	-	1.865	0.509	1.905

5.6. Electronic Structure Considerations

Finally, we will make use of the geometric considerations exposed in Section 5.5 and some simple electronic structure considerations to give a plausible physical explanation to the observations presented along this chapter.

According to Section 5.5, we have 2 separate effects: the interaction between layers, and the interaction of the surface with the adsorbate. The former will take place before the adsorption process, while the latter is adsorption itself, and the two processes can be considered independent from each other since the difference between layer distances with and without CO is in average 0.02Å.

It has been shown in other works [122-123, 125] that within a tight-binding framework, the matrix element describing the bonding interaction between Pt (in this specific case) and its 9 nearest neighbors in a (111) surface, which could be either Pt or Cu, can be estimated with Equation (5.3).

$$V_{ddm}^{Pt} = \frac{\eta_{ddm}\hbar^2}{m}\sum_{j=1}^{9}\frac{\left[r_d^{(Pt)}r_d^{(j)}\right]^{3/2}}{d_{Pt-j}^5} \tag{5.3}$$

Here we take η_{ddm} to be unity, as it was done before for uniformity purposes [122-123]. The term d_{Pt-j} is the internuclear distance between Pt and its 9 nearest neighbors (2.84 Å for the 6 nearest neighbors in the first layer, and the average values for the 3 neighbors in the subsurface are shown in Table 5.1. On the other hand, the matrix element accounting for the interaction of Pt and C when CO is adsorbed on top of is given by Equation (5.4).

$$V_{pdm}^{Pt} = \frac{\eta_{pdm}\hbar^2}{m}\frac{\sqrt{(r_d^{(Pt)})^3 r_p^{(C)}}}{d_{Pt-C}^4} \tag{5.4}$$

The p-state radius (6.59 Å) is taken again Ref. [125], and d_{Pt-C} is the distance between Pt and C calculated with DFT (the Pt-C distances are listed in Table 5.1), and we take η_{pdm} to be unity. The correlation between V_{ddm}^{Pt} and V_{pdm}^{Pt} is shown in Figure 5.8. This figure shows that the overall

effect of Cu in the alloys is the reduction of both kinds of matrix elements. Furthermore, 3 lines of constant first layer composition appear in the plot and resemble the approximately vertical lines of constant d-band center in the right panel of Figure 5.2. The appearance of those lines shows again that for a constant first layer composition, the addition of Cu into the second layer will only modify slightly the interaction of Pt with its nearest metal neighbors, while the interaction with the C atom in CO will decrease significantly. This means that ΔE_{CO} and ε_d are differently affected when forming NAs and SAs of Pt, and that the effect should be stronger in ΔE_{CO}, as we pointed out before.

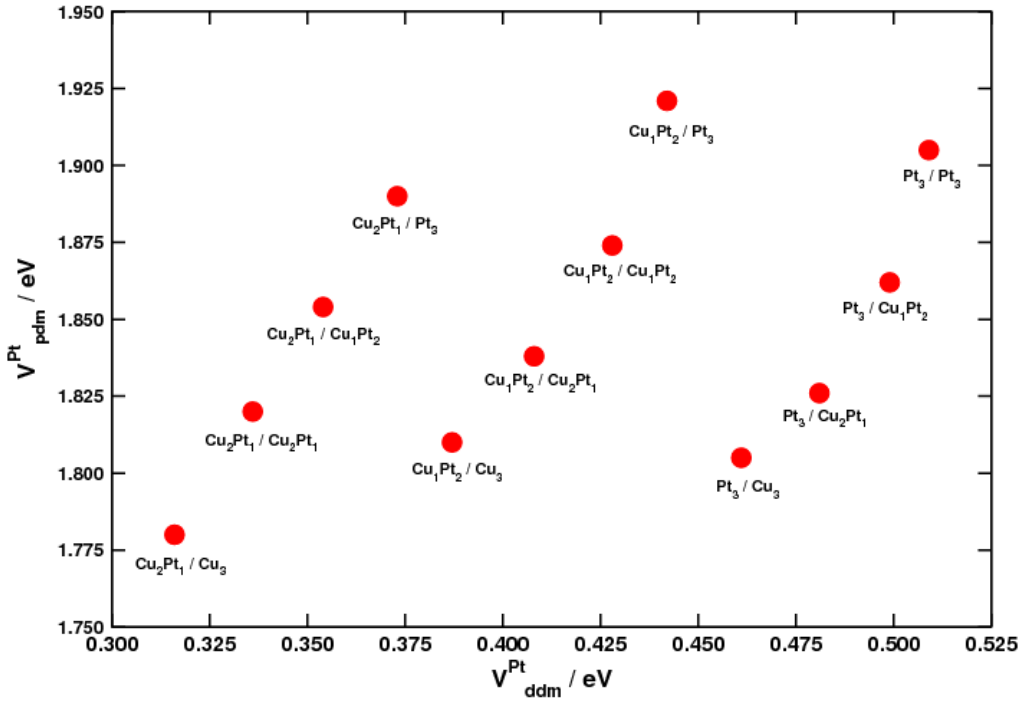

Figure 5.8. Variations of the matrix elements accounting for the bonding interactions of a surface Pt atom with its 9 nearest neighbors (x axis) and with C in adsorbed CO (y axis). In general, the addition of Cu to Pt diminishes both matrix elements, and 3 lines of constant first layer composition with similar slopes seem to form.

At this point, it is convenient to mention that the composition-based analysis shown throughout this chapter could be taken as a chemical approach to the problem. The method is easy to apply and has predictive power. Alternatively, a physical approach can be obtained by combining the matrix elements accounting for the interaction of Pt and C when CO is adsorbed on top of Pt and the energies of the states involved in the bonding process, via a Tight Binding analysis.

Assuming that the difference in binding energies will come from the interaction of the d-states of Pt with the p-states of C and that the interaction will include 1 electron from the former and 2 from the latter, the hybridization process can be summarized by Figure 5.9.

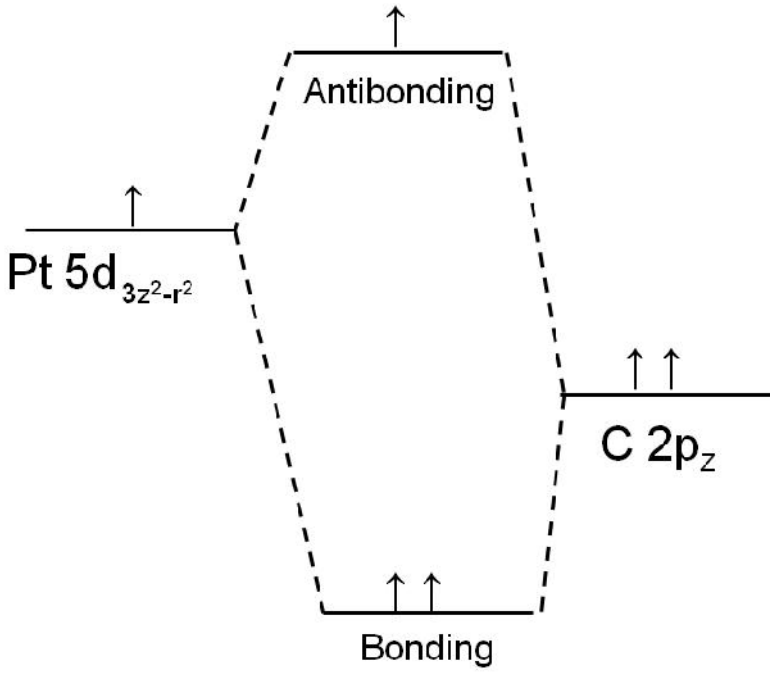

Figure 5.9. Tight Binding scheme of the hybridization of a 5d level of Pt with a 2p orbital of a C atom.

Within this formalism the orbital energies, E, can be obtained by solving the following secular determinant:

$$\begin{vmatrix} \varepsilon_d - E & V_{pdm}^{Pt} \\ V_{pdm}^{Pt} & \varepsilon_p - E \end{vmatrix} = 0 \tag{5.5}$$

Where ε_d and ε_p (fixed at -3.50 eV) represent the energies of the d and p states involved in the hybridization, respectively, and V_{pdm}^{Pt} is the matrix element representing the bonding interaction between Pt and C. Equation (5.5) turns into the following:

$$E^2 - (\varepsilon_d + \varepsilon_p)E + (\varepsilon_d \varepsilon_p - V_{pdm}^{Pt\ 2}) = 0 \tag{5.6}$$

Equation (5.6) has the solution shown below.

$$E = \frac{(\varepsilon_d + \varepsilon_p) \pm 2V_{pdm}^{Pt}\sqrt{1 + \frac{(\varepsilon_d - \varepsilon_p)^2}{4V_{pdm}^{Pt\ 2}}}}{2} \tag{5.7}$$

By making a first-order Taylor expansion on the square root in Equation (5.7), the energies of the bonding (E_B) and antibonding (E_{AB}) states can be approximated by:

$$E_B = -\frac{(\varepsilon_d - \varepsilon_p)^2}{8V_{pdm}^{Pt}} + \frac{\varepsilon_d + \varepsilon_p}{2} - V_{pdm}^{Pt} \tag{5.8}$$

$$E_{AB} = \frac{(\varepsilon_d - \varepsilon_p)^2}{8V_{pdm}^{Pt}} + \frac{\varepsilon_d + \varepsilon_p}{2} + V_{pdm}^{Pt} \tag{5.9}$$

The gain in energy upon adsorption compared to the isolated states, i.e. the adsorption energy, which according to Figure 5.9 is equivalent to twice the energy of a bonding state plus the energy of an antibonding minus the energy of the isolated d and p states, is given by Equation (5.10).

$$\Delta E_{ADS} = 2E_B + E_{AB} - 2\varepsilon_p - \varepsilon_d = -\frac{(\varepsilon_d - \varepsilon_p)^2}{8V_{pdm}^{Pt}} + \frac{\varepsilon_d - \varepsilon_p}{2} - V_{pdm}^{Pt} \tag{5.10}$$

Figure 5.10 shows the correlation between the DFT adsorption energies of CO and the expression on the right side of Equation (5.10), which is a second order expansion in ε_d. The combination of d-band centers with the coupling interactions between Pt and C (using now $\eta_{pdm} = -3\sqrt{15}/2\pi$ as in Ref. [125]) within a single model is able to capture the continuous variations of the binding energies with the change in the composition of the alloys. However, this approach is only explanatory but not predictive since it uses distances and matrix elements obtained as outputs of the DFT calculations. Therefore, at the moment we use the chemical approach since it avoids the calculation of densities of states and matrix elements and distances and, most importantly, has predictive power.

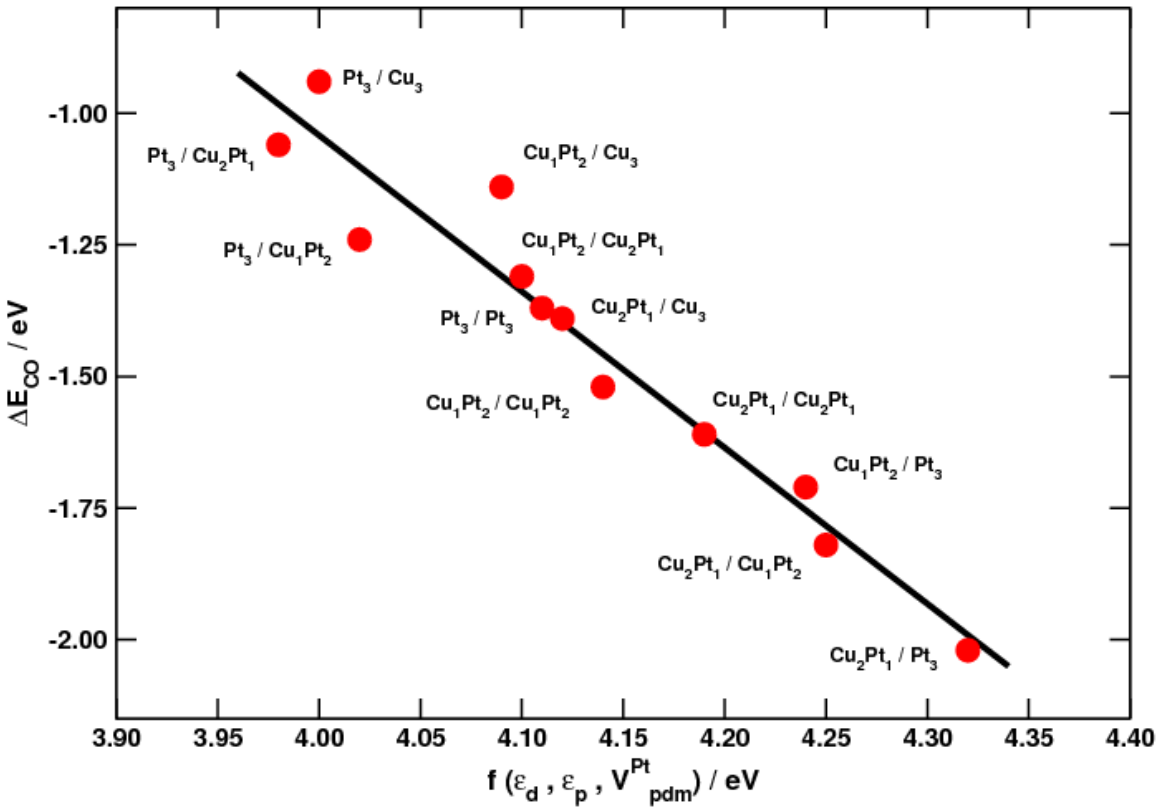

Figure 5.10. Correlation between DFT adsorption energies and electronic structure parameters. The inclusion of more parameters into the model shows a single linear variation between electronic structure variables and adsorption energies in which the addition of Cu has the effect of decreasing the adsorption energy of CO.

5.7. METHOD

The DFT calculations of CO adsorbed on NSAs and SAs were performed in the plane wave code Dacapo [127] with the RPBE exchange-correlation functional [6]. A periodic (√3x√3) *R*30° (111) unit cell with 1/3 ML coverage of CO on top of Pt with 4 layers of metal atoms for each slab and approximately eight equivalent layers of vacuum between successive slabs were used in the present studies. The 2 top layers and the adsorbates were free to move vertically, while the 2 bottom layers were kept fixed at the optimized bulk positions of Pt with a lattice constant of 4.02 Å. The relaxations of the atoms were carried out with a Quasi-Newton minimization scheme, until the maximum force on any atom was below 0.05 eV $Å^{-1}$. Ionic cores were described by ultrasoft pseudopotentials [128]. The Kohn-Sham one-electron states were expanded in a sum of plane waves with an energy cutoff of 450 eV and a density cutoff of 500 eV. The Brillouin zones of all systems were sampled with 6x6x1 Monkhorst-Pack grids [129]. The self-consistent RPBE density was determined by iterative diagonalization of the Kohn-Sham Hamiltonian at an electronic temperature of k_BT = 0.1 eV, using Pulay mixing of densities, and all total energies were extrapolated to k_BT = 0 eV. Spin polarization effects were taken into account only for PtFe alloys.

6. APPLICATIONS OF THE NEAR-SURFACE ALLOYS AND SURFACE ALLOYS OF PLATINUM AND COPPER

We present in Subsection 6.1 the results of the work done in collaboration with the experimentalists Dr Klas Andersson and Professor Ib Chorkendorff, from CINF, DTU [119]. Moreover, in Subsection 6.2 we show the results of the work done in collaboration with Bondarenko et al, from CINF, DTU (See No 6 in List of Included Articles).

6.1. Thermochemical Stability of the NSAs and SAs of Pt and Cu

6.1.1. Introduction

Bimetallic alloys offer a way of tuning electronic structure and catalytic properties of metal surfaces [130-135]. It is of paramount importance to the catalytic performance of an alloy surface its composition and structure under reaction conditions, since the bonding of adsorbates may induce changes in local atomic composition and surface structure, thereby changing the activity and selectivity of the catalyst. Capitalizing on such effects for catalyst preparation means greater flexibility in alloy surface design for low-temperature applications. Generally, the exposure to adsorbates induces segregation of the more reactive alloy component to the surface [136-143], i.e. the one forming the strongest chemical bond with the adsorbates. Counterintuitive to this picture, we show that CO adsorption induces surface segregation of the *less* reactive alloy component, Cu, switching a Pt-Cu NSA [120] to a novel well-ordered Pt-Cu SA. The Pt-Cu NSA was recently suggested as a promising catalyst for the water-gas shift ($CO + H_2O \rightarrow H_2 + CO_2$) because of reduced Pt-CO bonding strength on a Pt catalyst surface with Cu present in the second layer [120], alleviating possible CO-poisoning problems [144].

We show here that the NSA is unstable at elevated CO pressures and sample temperatures, forming instead a self-organized CO/Pt-Cu SA. Previous DFT studies [120] indicated increased Pt-CO bonding when Cu is present in the first layer, similar to what is observed for other coinage/Pt-group metal systems [145-148], and supported by the vector analysis presented in Chapter 5. Here we prove Cu surface segregation induced by drastically stronger Pt-CO adsorption energetics in the self-organized CO/Pt-Cu SA.

6.1.2. Experimental Findings [119]

Initially, a Pt-Cu NSA was prepared by depositing one atomic layer of Cu (θ_{Cu} = 1 ML) on Pt (111) and annealing to 800 K. X-ray Photoelectron Spectroscopy (XPS), Ion Scattering Spectroscopy (ISS), and Low-Energy Electron Diffraction (LEED) analyses [119] supported prior findings [120] that, after deposition and subsequent annealing, Cu is preferentially located in the second layer. The sample was exposed to CO at a pressure of 2 mbar for 10 min at various sample temperatures and then cooled to room temperature over 10 min in CO, after which CO was evacuated. We show in Figure 6.1 the CO Temperature-Programmed Desorption (TPD) spectra obtained under UHV before and after the HPC CO treatments.

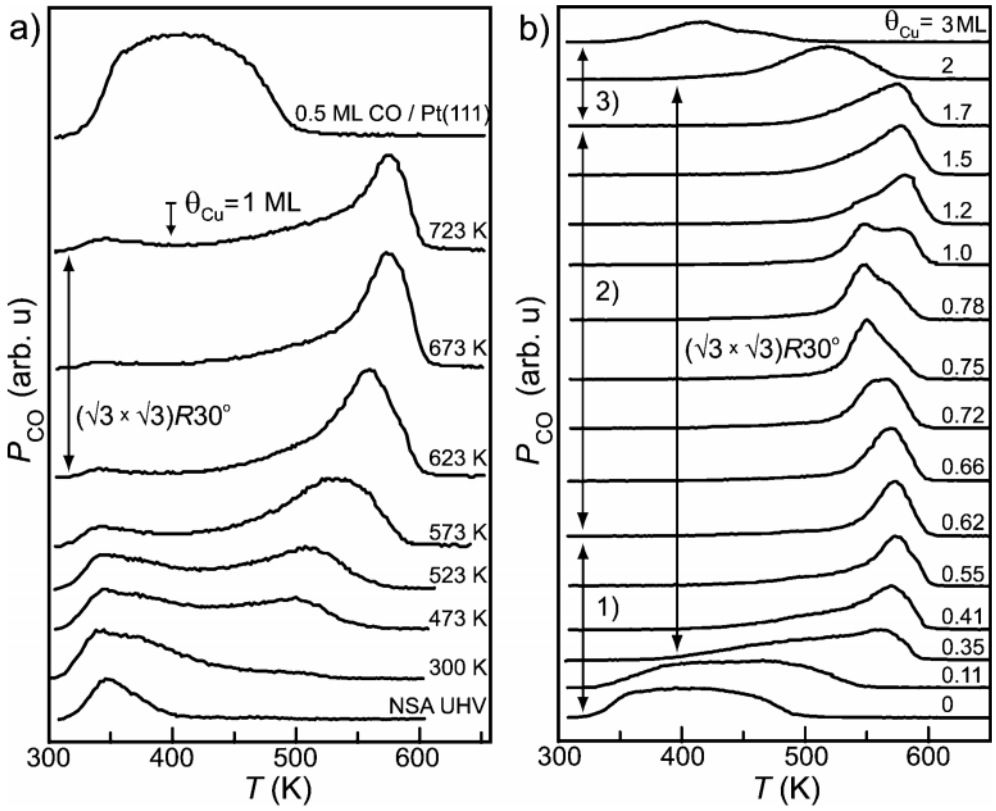

Figure 6.1. CO TPD spectra (2 K/s) recorded under UHV after various sample treatments. a) Reference and post-treatment TPDs for a 1 ML Cu/Pt (111) NSA exposed to CO at 2 mbar for 10 min at the temperatures shown in the figure. Bottom and top traces (reference TPDs): NSA UHV (no high-pressure exposure) and 0.5 ML of CO on clean Pt (111), respectively. b) TPDs after 2 mbar CO treatment at 673 K for varying amounts of Cu as displayed in the figure. Also marked in the figure are three distinctive regions (1, 2, and 3) and observations of a √3x√3 *R*30° LEED pattern. Figure taken from Ref. [119].

First, for adsorption of CO under UHV conditions, we compare the CO desorption from the Pt-Cu NSA (Figure 6.1.a), bottom trace) to that from pure Pt (111) (Figure 6.1.a), top trace). Evidently, less CO is adsorbed at room temperature and binds significantly more weakly (i.e., desorbs at a much lower temperature) on the Pt-Cu NSA. This agrees well with prior findings [120], and with the analyses in Chapter 5. The exposure of the Pt-Cu NSA surface to 2 mbar CO at 300 K results only in very small changes. However, after treatment at temperatures in the range 473-723 K in the 2 mbar CO, the CO desorption peaks are located at temperatures as high as 580 K. For $T_{treatment} \geq 623$ K, the CO coverages are large and saturated at 0.3-0.33 ML. The results demonstrate drastically increased CO binding energy, even compared with that on pure Pt (111), and we conclude that the Pt-Cu NSA is not stable but undergoes changes when in the CO environment at elevated temperatures. The changes are reversible upon desorption of the CO under UHV by annealing to 673-800 K, which regenerates the NSA and its CO adsorption characteristics (Figure 6.1.a), bottom).

On the basis of the TPD spectra measured after HPC CO treatments at 673 K for samples with varying θ_{Cu} in the range 0-3 ML (Figure 6.1.b)), three different regions were established: 1) $\theta_{Cu} <$ 0.62 ML, 2) 0.62 < θ_{Cu} <1.7 ML, and 3) $\theta_{Cu} >$ 1.7ML. The starting surfaces were as-deposited Cu on Pt (111). The treatment temperature, 673 K, was chosen based on the findings in Figure 6.1.a) and is well above the onset for Cu diffusion into Pt [149]. We observe that the high-temperature CO desorption feature at 570-580 K is fully developed at 0.62 ML and remains for a Cu content of up to 1.7ML (region 2) before systematically shifting to lower temperature in region 3. In region 2, the saturation coverage of CO in the 570-580 K peak is very close to 1/3 ML (0.36 (0.02 ML), as for the 1 ML Pt-Cu NSA in Figure 6.1.a).

Distinct surface changes accompanied the high-temperature desorption features in Figure 6.1. At 0.35 ML of Cu, the high temperature desorption feature appeared (Figure 6.1.b)), accompanied by a weak, broad, diffuse (√3x√3) *R*30° LEED pattern that was very sharp and intense at ~0.7 ML of Cu and further observed at up to 2 ML of Cu. The (√3x√3) *R*30° LEED pattern was also clearly observed for the 1 ML NSA sample in Figure 6.1.a) for CO treatments at $T \geq 623$ K. Furthermore, whereas atop-adsorbed CO (~2100-2050 cm^{-1}) was always observed in IR spectra, bridge-bonded CO (~1855 cm^{-1}) was observed neither during nor after HPC CO treatment for any Pt-Cu alloy surface with $\theta_{Cu} \geq 0.35$ ML.

Furthermore, Cu surface segregation was found to be associated with the CO-induced surface structural changes for the samples in Figure 6.1 by using ISS (1.2 keV He+, θ = 125°) and XPS to characterize the elemental composition in the topmost surface layer and near-surface region, respectively. In Figure 6.2.a), the ISS spectrum after treatment of a sample with 2/3 ML of Cu for 10 min at 673 K in 2 mbar CO is compared with the spectrum obtained from the corresponding NSA (~1 s anneal at 673 K under UHV).

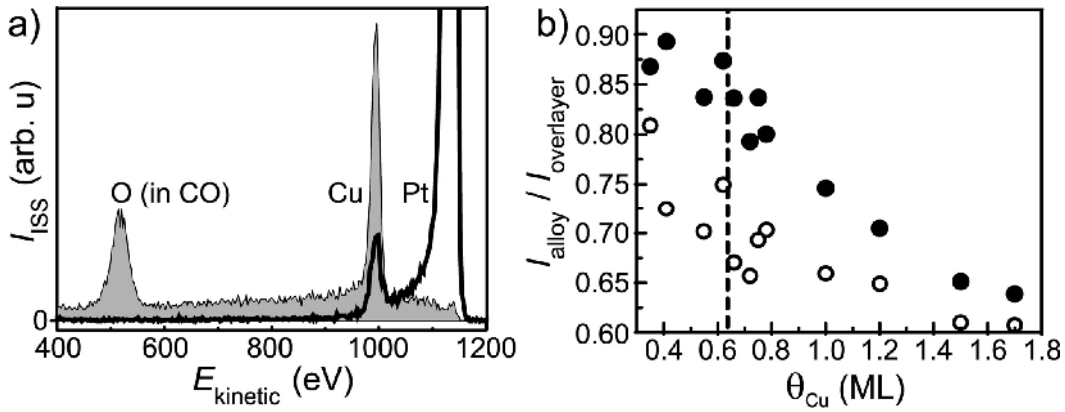

Figure 6.2. ISS and XPS spectra showing Cu surface segregation induced by CO adsorption. a) ISS after 2 mbar CO/673 K treatment of a 0.67 ML Cu/Pt (111) sample (gray) and the corresponding NSA (black). b) XPS Cu 2p/Pt 4d ratio (relative to the case of as-deposited Cu) for the 2 mbar CO/673 K treated samples in Figure 6.1.b) before TPD (●) and the corresponding NSAs after TPD (○).Figure taken from Ref. [119].

For the NSA, the Cu content in the top surface layer is very small (0.03 ML) and the Pt signal is dominant. Contrary to the expected diffusion of Cu into Pt at 673 K, Cu surface segregation due to the HPC CO treatment leads to a large ISS intensity for Cu (0.13 ML), and surface Pt is barely observed, being blocked by adsorbed CO. The Cu surface segregation induced by CO adsorption was also confirmed by XPS, as shown in Figure 6.2.b). Although there is a degree of scatter in the data, in every case the Cu content in the near-surface region after 10 min at 2 mbar CO and 673 K is significantly larger than for the corresponding NSA (~1 s anneal at 673 or 800 K under UHV). Similar results were obtained for $T_{treatment} \geq 523$ K in Figure 6.1.a). For the 0.35 ML < θ_{Cu} < 0.62 ML HPC CO-treated samples, the Cu signal is a nearly constant fraction (0.84-0.9) of the initial amount of Cu deposited, and this signal drops significantly for larger θ_{Cu}. Upon correlation of the XPS data with the ISS results showing large Cu amounts in the first layer, the findings

indicate that essentially all of the Cu remains in the first layer up to ~2/3 ML, after which the superfluous Cu starts to distribute itself in deeper layers (hence the drop in relative intensity).

6.1.2. Density Functional Theory Insight

The stability of the NSA alloy was first calculated by substituting a single Pt atom by a Cu atom in a 2(√3x√3) *R*30° unit cell with 7 layers. Schematics of the process are shown in Figure 6.3.

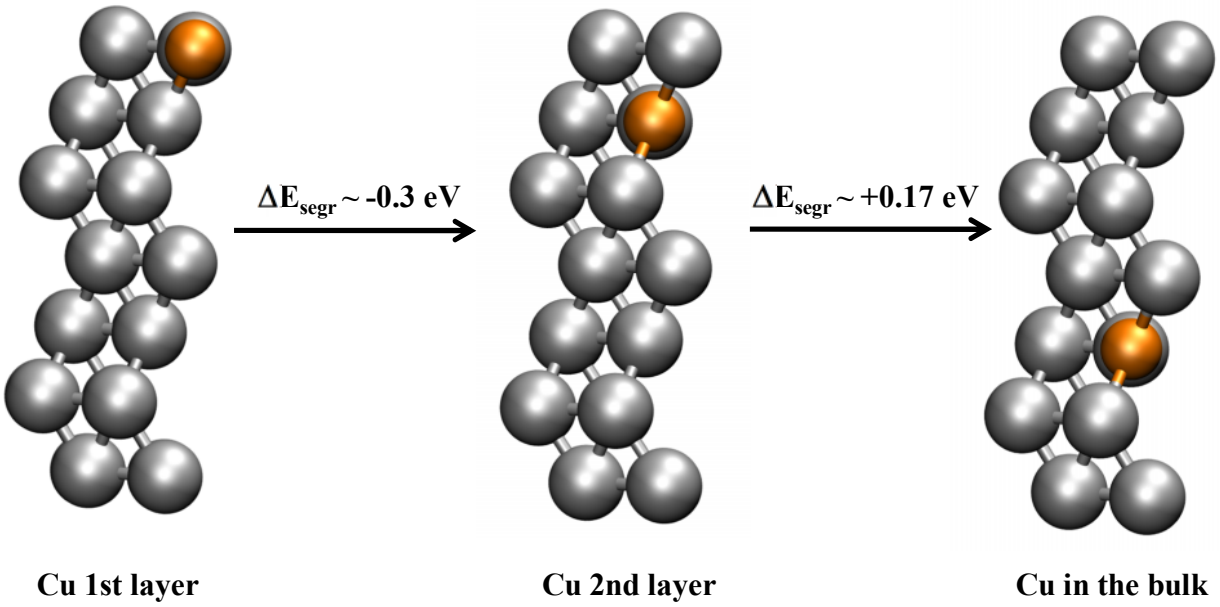

Figure 6.3. Segregation energies of atomic Cu in a Pt (111) surface. From the left to the middle: exothermic segregation of Cu from the first layer to the second one. From the middle to the right: endothermic segregation of Cu from the second layer to the bulk.

According to this figure, when the surface is clean (no adsorbates on it) Cu will tend to move to the second layer due to the favorable energetic difference with respect to the first layer. However, it is not energetically favorable to go to the layers below the second one. The energy for bringing a Cu atom from the bulk to the second layer (ΔE_{SEG-2}) is calculated to be ~ -0.17 eV and the process can be expressed mathematically in the way shown below, where $E^{ALLOY,\min}$ represents the energy of the NSA with the minimum amount of Cu, in this case Pt_3 / Pt_2Cu_1.

$$\Delta E_{SEG-2} = \left(E_{BULK}^{Pt} - E_{SURF}^{Pt}\right) + \left(E_{SURF}^{ALLOY,\min} - E_{BULK}^{ALLOY,\min}\right) \quad (6.1)$$

The complete thermochemical process of forming a NSA, a SA or a combination of both from Cu atoms located in the bulk (energetically described by ΔE_{SEG}) can be divided in the following parts: firstly, a migration of the Cu atoms from the Pt bulk to the second layer (energetically described by $\Delta E_{SEG-2} \approx -0.17\ eV$); and secondly, their distribution in the two topmost layers (energetically described by ΔE_{DIST}). The process is formally expressed in Equation (6.2), where N is the number of Cu atoms in the alloy.

$$\Delta E_{SEG} = N\Delta E_{SEG-2} + \Delta E_{DIST} \quad (6.2)$$

In order to determine how to calculate ΔE_{DIST} we imagine a (√3x√3) $R30°$ surface divided into N+1 parts. If N Cu atoms migrate to the second layer of N parts of the surface (forming N units of Pt_3 / Pt_2Cu_1) and the remaining part has none, i.e. it is Pt_3 / Pt_3, the distribution of the N Cu atoms to form a single unit of alloy (Pt_xCu_{3-x} / Pt_yCu_{3-y}, where $6-x-y=N$) will, at the same time, give origin to N parts made of pure Pt (111). Therefore, the following reaction takes place in the surface:

$$N(Pt_3 / Pt_2Cu_1) + (Pt_3 / Pt_3) \rightarrow (Pt_xCu_{3-x} / Pt_yCu_{3-y}) + (NPt_3 / Pt_3) \quad (6.3)$$

The energetics of Reaction (6.3), equivalent to the distribution energy, is given below.

$$\Delta E_{DIST} = \left(E_{SURF}^{ALLOY} - NE_{SURF}^{ALLOY,\min}\right) + \left(N-1\right)E_{SURF}^{Pt} \quad (6.4)$$

Finally, if we combine the results from Equations (6.1) and (6.4), we obtain a simple expression for the segregation energy.

$$\Delta E_{SEG} = \left(E_{SURF}^{ALLOY} + NE_{BULK}^{Pt}\right) - \left(E_{SURF}^{Pt} + NE_{BULK}^{ALLOY,\min}\right) \quad (6.5)$$

Moreover, the segregation energy when CO is adsorbed on the surface can be calculated according to Equation (6.6), where $\Delta\Delta E_{CO}$ is the differential adsorption energy of the alloy with respect to that of Pt (111).

$$\Delta E_{SEG-CO} = N\Delta E_{SEG-2} + \Delta E_{DIST} + \Delta\Delta E_{CO} \quad (6.6)$$

The stabilities calculated with Equations (6.5) and (6.6) are shown in Table 6.1. Cu was restricted to the first and second layers for total amounts of 1/3, 2/3, 1, 4/3, and 5/3 ML with and without 1/3 ML of CO adsorbed on atop Pt sites.

Table 6.1. Adsorption and segregation energies of Pt-Cu NSAs and SAs. The most stable surfaces appear in bold.

θ_{Cu} (ML)	Description	ΔE_{SEG} (eV)	ΔE_{CO} (eV)	$\Delta\Delta E_{CO}$ (eV)	$\Delta E_{SEG\text{-}CO}$ (eV)
0	Pt_3 / Pt_3	-	-1.37	0.00	-
1/3	Pt_3 / Cu_1Pt_2	-0.17	-1.24	0.13	-0.04
	Cu_1Pt_2 / Pt_3	0.26	-1.71	-0.33	-0.07
2/3	Pt_3 / Cu_2Pt_1	**-0.37**	-1.06	0.31	-0.06
	Cu_1Pt_2 / Cu_1Pt_2	0.20	-1.52	-0.15	0.06
	Cu_2Pt_1 / Pt_3	0.42	-2.02	-0.65	**-0.23**
1	Pt_3 / Cu_3	-0.21	-0.94	0.43	0.22
	Cu_1Pt_2 / Cu_2Pt_1	0.15	-1.31	0.06	0.21
	Cu_2Pt_1 / Cu_1Pt_2	0.53	-1.82	-0.45	0.08
4/3	Cu_1Pt_2 / Cu_3	0.37	-1.14	0.23	0.59
	Cu_2Pt_1 / Cu_2Pt_1	0.63	-1.61	-0.24	0.39
5/3	Cu_2Pt_1 / Cu_3	0.96	-1.39	-0.02	0.94

For the clean surfaces (no CO adsorbed), 2/3 ML of Cu in the second layer is the most stable, and Cu diffusion from the second to the first layer is generally endothermic by 0.3-0.4 eV. With 1/3 ML of CO adsorbed atop surface Pt, the situation is significantly different: Cu surface migration to generate 2/3 ML of Cu in the first layer is now most favorable. Clearly, there is a driving force towards having 2/3 ML of Cu in the first layer when CO is adsorbed atop the

remaining surface Pt sites. As Table 6.1 and Figure 6.4 show, the origin of the exothermicity is the vastly increased Pt-CO bond strength when 2/3 ML of Cu is present in the first layer. Although Cu diffusion to the first layer is endothermic [120], the observed drastic increase in CO binding energy more than compensates for the endothermicity.

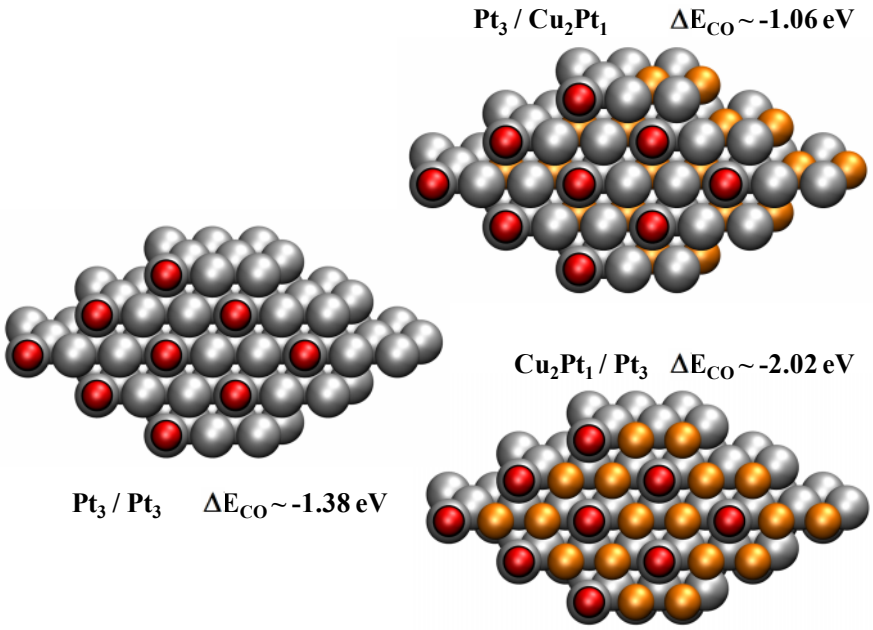

Figure 6.4. Structures and adsorption energies of CO for pure Pt (middle), a NSA with 2/3 ML Cu (top), and a SA with 2/3 ML Cu (bottom).

We note that the results with adsorbed CO in Table 6.1 can explain the θ_{Cu} > 2/3 ML onset of bulk migration of Cu indicated by the XPS data in Figure 6.2. In comparison with the θ_{Cu} = 2/3 ML case, situations with higher Cu content in the top two layers are significantly less stable, leading to a significant Cu bulk migration driving force.

It is clear that CO adsorption at elevated pressures and temperatures on a Pt-Cu NSA induces a large Cu surface segregation, generating a novel Pt-Cu SA to which CO binds very strongly, even compared with pure Pt (111). The Cu content needed for saturation of the SA is ~2/3 ML of Cu, leading to a CO saturation coverage of ~1/3 ML.

The sharp CO TPD spectrum compared with that of pure Pt(111), the observed (√3x√3) *R*30° LEED pattern, and additional IR studies [119] strongly suggest a significantly reduced lateral repulsion between CO adsorbates on atop Pt sites and hence a well-ordered surface with well-

defined, well-dispersed, and isolated Pt sites is formed. Figure 6.5 summarizes the reversible segregation process and shows that Pt islands form in the SA since each Pt atom will have 6 Cu atoms as nearest neighbors in the first layer upon adsorption and segregation.

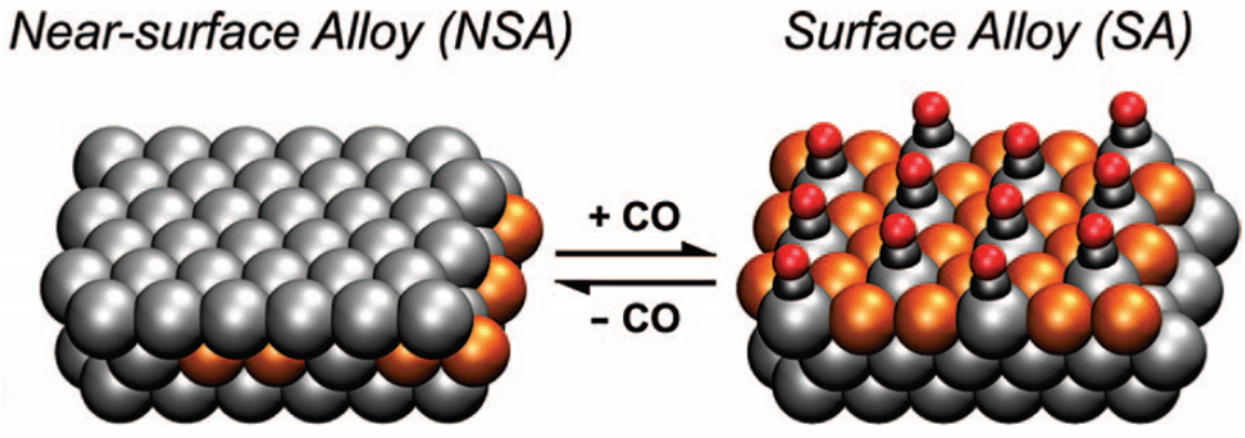

Figure 6.5. CO-induced segregation of Cu to the surface. The great increase in adsorption strength of CO allows the migration of Cu atoms from the second to the first layer.

6.2. Catalytic Activity of the NSAs and SAs of Pt and Cu towards ORR

Density Functional studies have previously suggested that the optimal catalyst for ORR should bind oxygen approximately 0.2 eV weaker than Pt (111) [16], which corresponds, due to the scaling relations [77], to a weakening of the *OH adsorption energy of ~0.1 eV. Given that CO was bound weaker on the NSAs of Pt and Cu than on Pt (111), we anticipated and verified that the same occurs to the ORR intermediates, thus increasing the activity of NSA catalysts.

Cyclic voltammetry experiments can be used for the calculation of the potential at which 1/6 ML *OH is formed on the NSAs. This potential ($\Delta U_{1/6\ \mathrm{ML\ OH}}$) can be used as an estimation of the *OH adsorption energy (ΔE_{OH}), thereby allowing for direct comparisons between DFT and experimental data. Figures 6.6 and 6.7 show a set of cyclic voltammograms of NSAs of Pt with different amounts of Cu deposited.

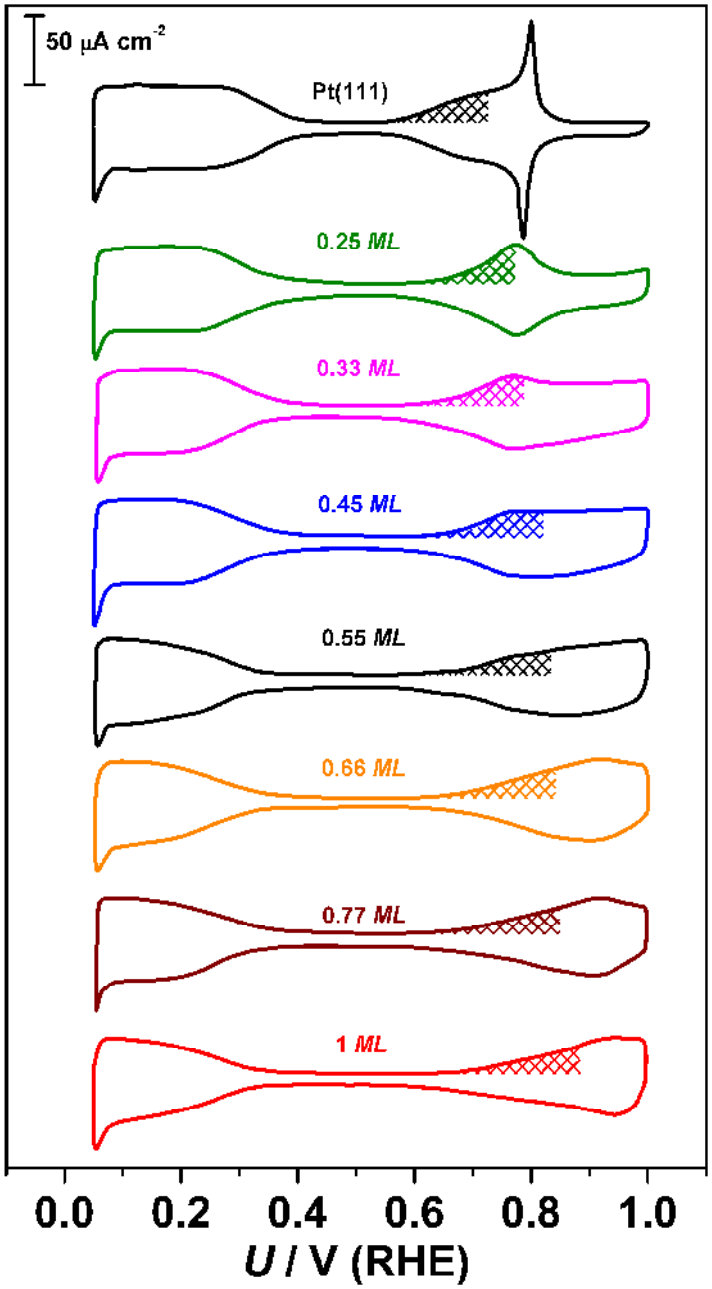

Figure 6.6. A set of cyclic voltammograms for the Pt-Cu NSAs with different amounts of Cu initially deposited. N_2 saturated 0.1M $HClO_4$, dU/dt = 50mV s^{-1}. The hatched area corresponds to 80 μC cm^{-2}, which is the charge required to form 1/6 ML OH*. $\Delta U_{1/6\ ML\ OH}$ was evaluated by comparing the potential at which 1/6 ML OH* is formed, relative to Pt (111).

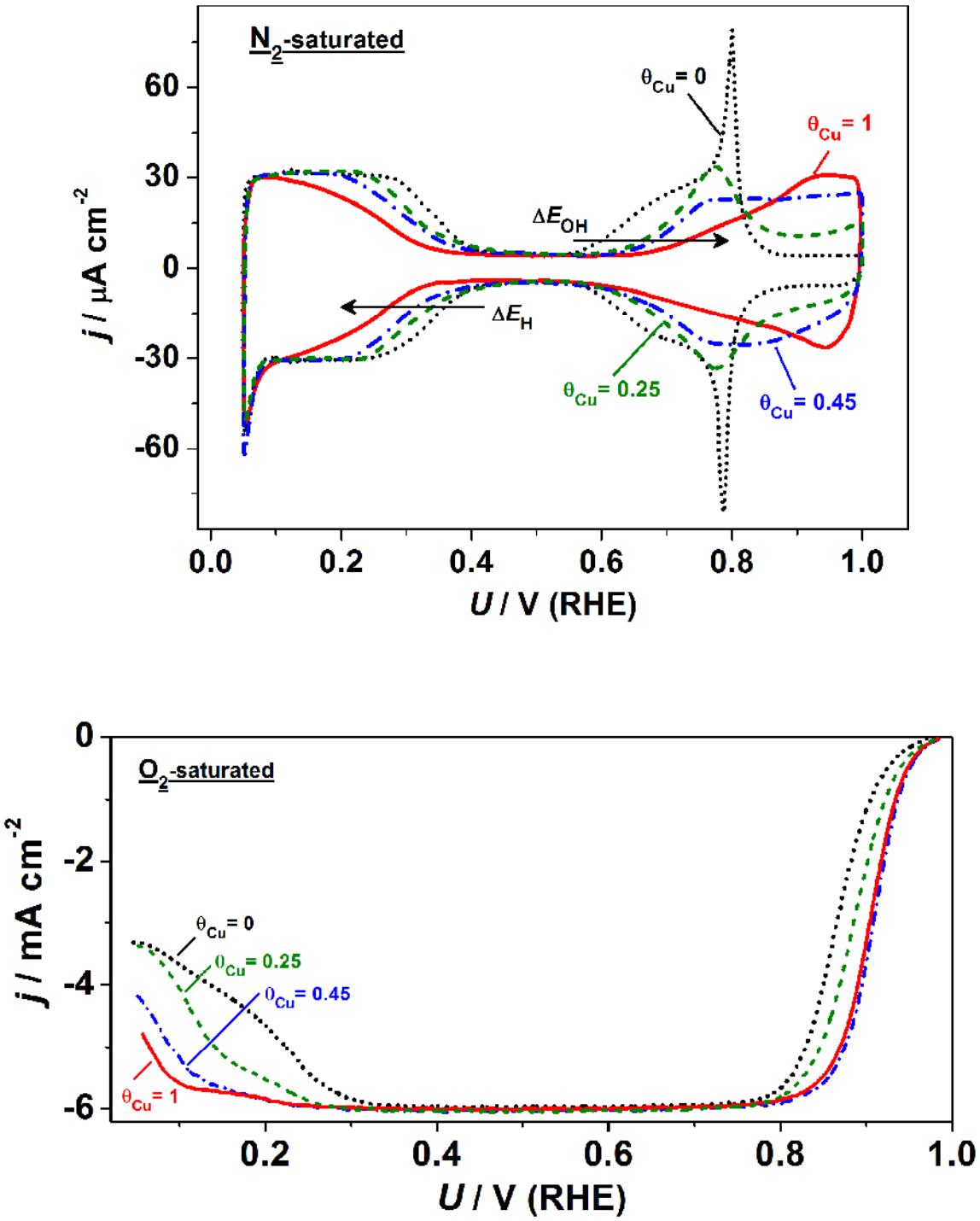

Figure 6.7. Electrochemical characterisation of Pt-Cu NSAs, in comparison with Pt(111), using cyclic voltammetry in 0.1M $HClO_4$, at dU/dt=50mV s^{-1} in N_2-saturated electrolyte (top); RDE-voltammograms (anodic scans only) in O_2-saturated electrolyte, taken at 1600 rpm, 60°C (bottom). θ_{Cu} denotes the amount in ML of Cu initially deposited.

The values extracted from experiments in Figures 6.6 and 6.7 confirmed the expected behavior of the NSAs, as shown in Figure 6.8.The trends agree well until ~0.5 ML of Cu initially deposited. After that, DFT predicts larger weakening of the *OH bond strength to the surface than experimentally observed, which can be due to a saturation of the Cu content at approximately 0.4 ML Cu in the second layer, as observed by Knudsen et al [120]. If the saturation occurs, the final Cu coverage in the second layer will be less than amount initially deposited and the comparison with DFT calculations cannot be done directly.

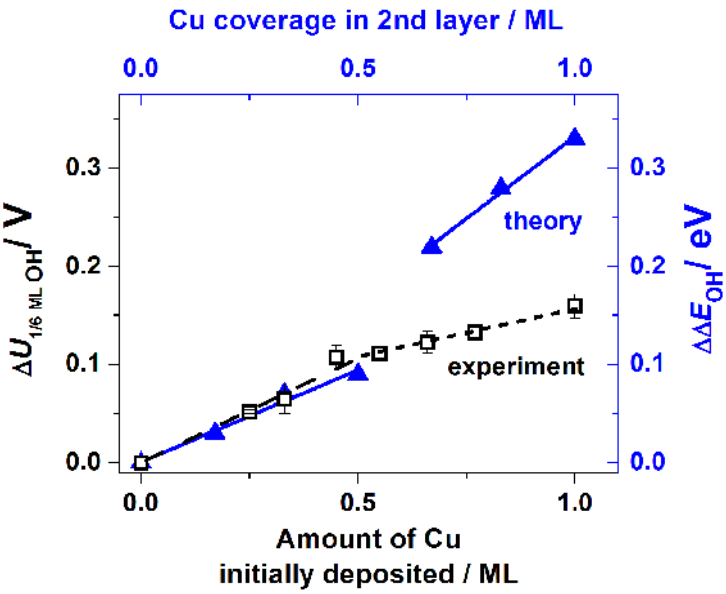

Figure 6.8. Experimental (black) and theoretical (blue) weakening of OH binding, as a function of Cu content; the linear trendlines were produced using a least squares fit.

7. TRENDS IN ADSORPTION ENERGIES OF NEAR-SURFACE ALLOYS OF PLATINUM AND TRANSITION METALS

7.1. Exceptions to the D-Band Model and Alternative Descriptors

We showed in Chapter 5 that the d-band model is unable to capture trends in adsorption energies when NSAs of Pt and late transition metals are studied. In that chapter we looked at the trends when the concentration of the alloying metal in the second layer was varied. A further question would be whether these anomalies appear in the overall trends of transition metals, when a fixed composition is considered for all NSAs. Once again, the answer to that question is affirmative and a solution to the problem is proposed. This part was done in collaboration with Dr Frank Abild-Pedersen.

In this chapter we report calculations on a series of Pt/M/Pt NSAs, where M is a 3d, 4d, or 5d transition metal. All alloys considered contain 1 ML of M in the second layer. A number of different adsorbates are chosen to illustrate to what extent the metal M in the second layer affects the binding. Based on these studies we find that depending on the metal in the second layer a significant effect on the electronic structure at the surface is observed. This will lead to variations in the renormalized coupling i.e. the adsorbate-metal sp-coupling and hence changes in binding that cannot be explained by variations in metal d-states alone.

One of the most remarkable articles on this matter was published by Kitchin et al [123] in 2004. In it, they considered NSAs of Pt with 3d metals from Ti to Ni. The correlation between d-band center of Pt and dissociative adsorption energies (see Equation (7.1)) can be seen in Figure 7.1.

$$\Delta E_{ADS,DISS} = 2E_{SLAB,ADS} - 2E_{SLAB} - E_{MOLECULE} \quad (7.1)$$

Even though the trends seem to be nearly linear, we would like to point at two details in Figure 7.1 that will be of use later: first, the d-band center between Cr, Ti, and V is almost constant, while the dissociative adsorption energies of O_2 change approximately 0.5 eV. Second, the dissociative adsorption energy of O_2 on pure Pt seems to be an outlier in the trends.

In Figure 7.2 we summarize the complete trends in O* adsorption for NSAs of Pt and 3d, 4d, and 5d metals. The oxygen adsorption energies are referred to that of pure Pt.

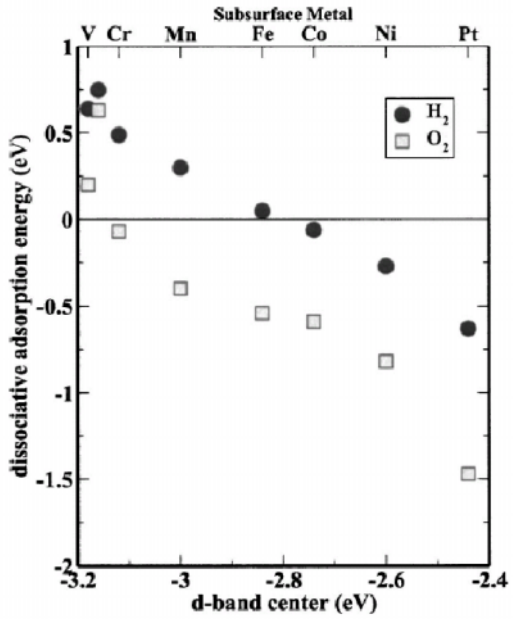

Figure 7.1. Trends in dissociative adsorption energies for H2 and O2 on Pt (111) slabs containing subsurface 3d metals. Taken from Ref. [123].

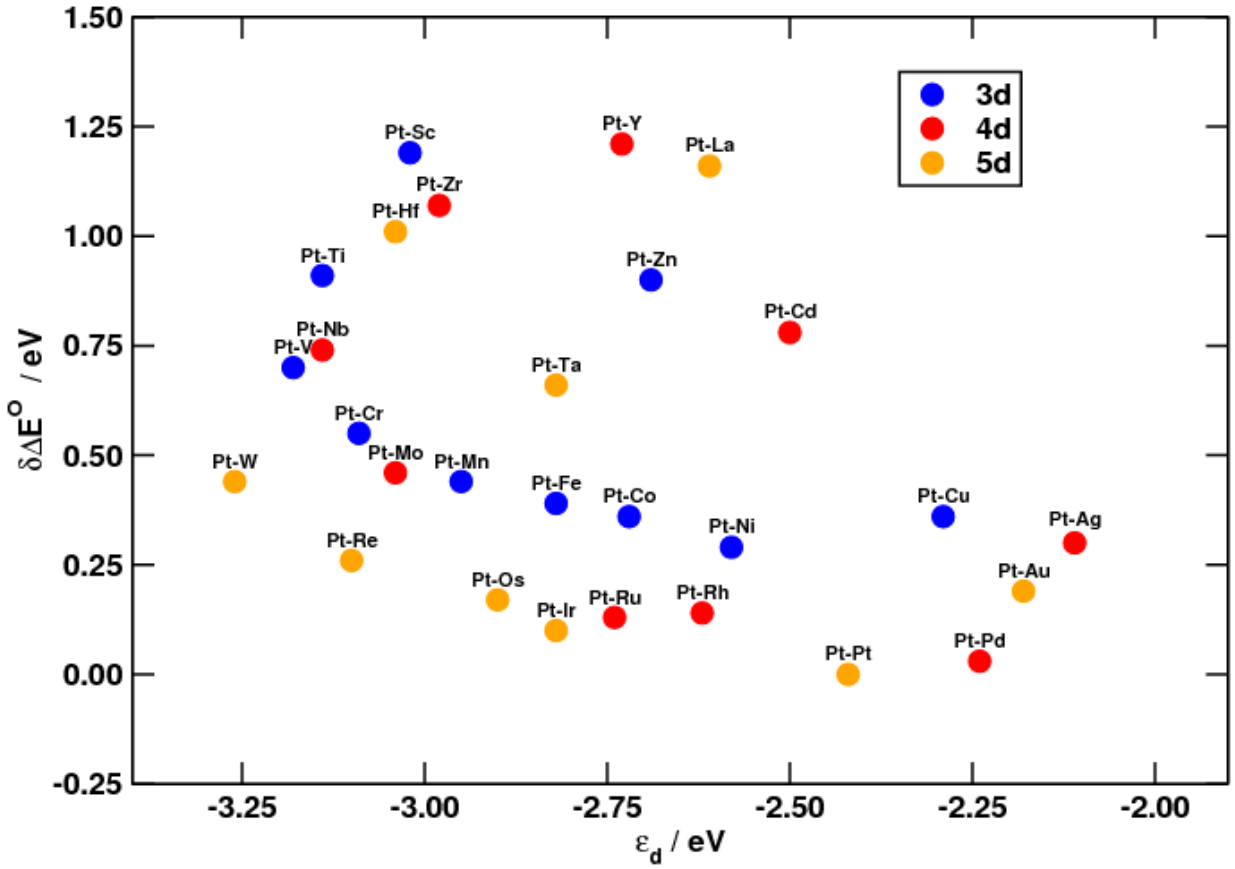

Figure 7.2. Change in oxygen binding energies on NSAs of Pt as a function of the shift in the d-band center.

We note that the values in the x axes in Figures 7.1 and 7.2 coincide for alloys of Ti to Ni, the values in the y axes do not, since the energies are defined differently and referenced to pure Pt (111). Nonetheless, the qualitative trends are identical.

Figure 7.2 supports the two details pointed out in Figure 7.1. The d-band center of the Pt atoms is bounded to the left and right, depending on the element present in the second layer. Therefore, each row, 3d, 4d, and 5d, has a closed loop in this variable, being this the reason why several alloys have similar d-band centers but completely different adsorption energies. For instance, let us take the case of NSAs of Ru, and Y, which have d-band centers of approximately -2.75 eV, but their adsorption energies differ by more than 1 eV.

We remark here that exceptions to the d-band model have been previously reported [150]. In order to clarify the trends in adsorption energies, we change now the descriptor from d-band center to fractional number of d electrons (or alternatively, the group number divided by 10) of the metal in the second layer. We will refer to this descriptor as "d-filling" henceforth. Similar descriptors were useful to capture the trends for perovskite oxides and graphitic materials, and, as shown in Figure 7.3, they also able to describe uniformly the present ones.

We note again that the curves have different minima according to the adsorbate. The bottom of Figure 7.3 shows that the minima are located at Pt for $*CH_3$ and *Li, and at Au for *O, in the 5d series. We see that $O < CH_3 < Li$, is also the electrophilicity rank. Thus, it is evident that the adsorbates follow this behavior because charge is either transferred into or withdrawn from the surface, and the behavior is largely dependent on the adsorbate. The consequences of this are far reaching, because it shows that the reactivity of a transition metal alloy is not only defined by the d-electrons of the atom binding to the adsorbates, but can also be perturbed by electronic interactions with the second layer alone, i.e. by ligand effects.

The variations in adsorption energies are therefore related to changes in the d-band center but also to charge transfer between the first and the second layer, which is an effect not considered in the d-band model. This idea is supported by the fact that binding of oxygen increases while the second layer metals are accepting charge (d-filling > 0.8) and decreases when the second layer switches to being donating (d-filling < 0.8). We also note that the oxygen binding increases as one moves from 3d to 4d and finally to 5d metals, suggesting that the charge transferred correlates with the principal quantum number or the range of d-orbitals.

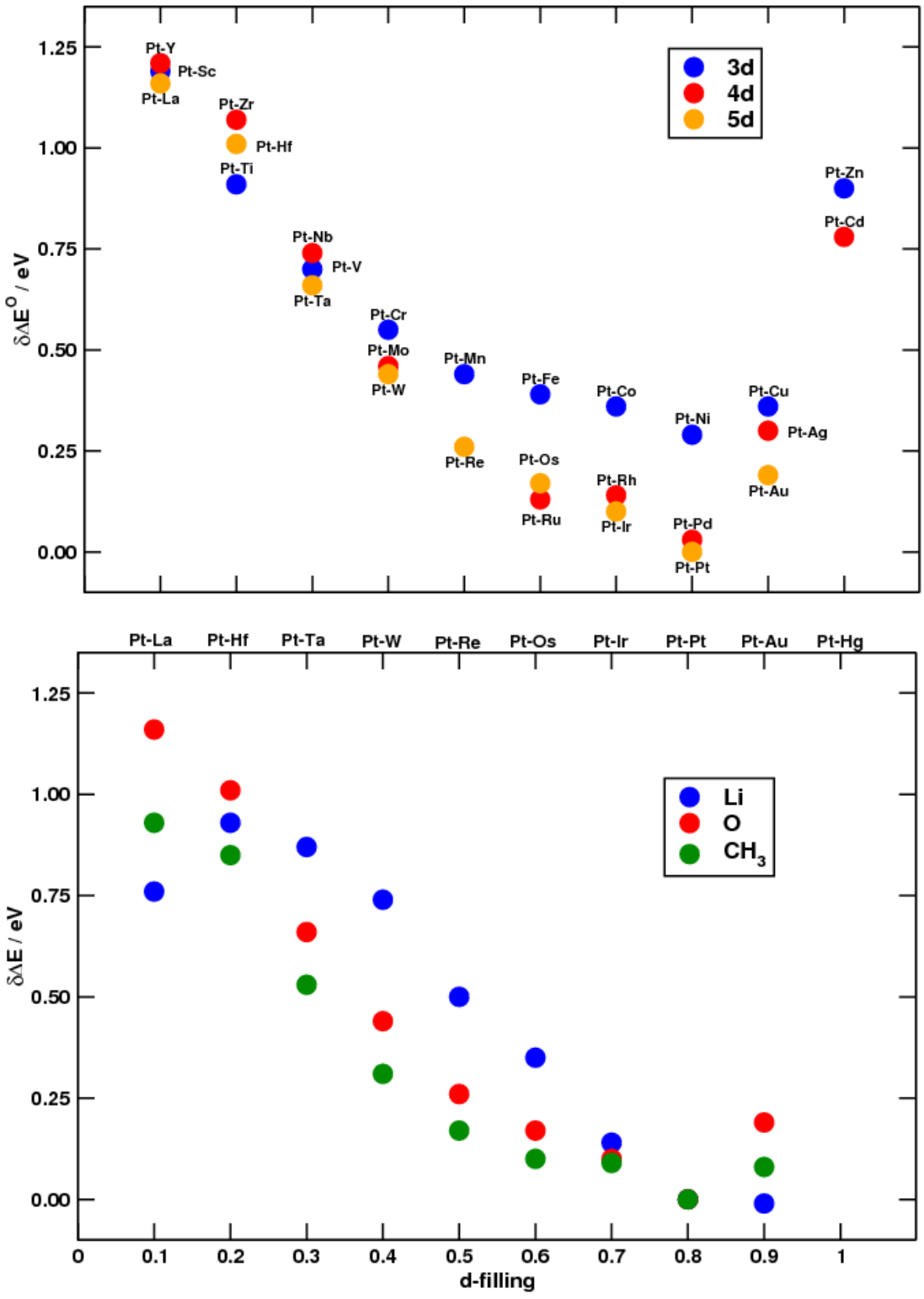

Figure 7.3. Top: Variation of the oxygen binding energies on Pt NSAs relative to pure Pt as a function of the fractional number of d electrons (d-filling) in the second layer metal. Bottom: Variations in the binding energy as a function of d-filling of *Li, *CH_3, and *O on Pt NSAs with 5d metals in the second layer.

If charge is withdrawn from or transferred to the surface layer, then the top layers at the surface have to expand or compress accordingly in the Z direction. In figure 7.4 we map out the slab height (average vertical distance between the 1st and the 2nd layers, and the 2nd and the 3rd layers) as we move through the different transition metals. As can be seen in that figure, there is a clear correspondence between the height of the slab and the binding of oxygen in Figure 7.3. However, the minima of the curves are shifted further to the left compared to what is found for the oxygen binding energy. This immediately suggests that there is some charge transfer between layers due to the insertion of the alloying metal, but also the interaction with adsorbates results in another charge transfer. Furthermore, the change in charge at the surface should affect different adsorbates unlikely. Hence, the stronger the ability of the adsorbate to withdraw or donate electrons the more pronounced the effects one will observe.

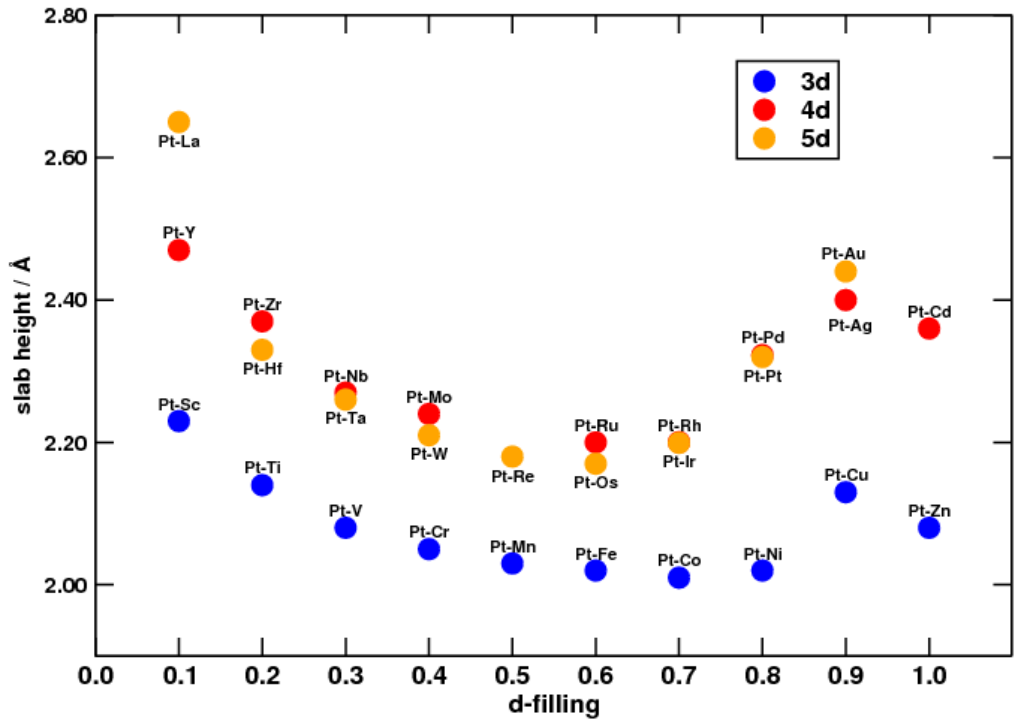

Figure 7.4. Changes in the slab height as a function of d-filling for clean NSAs of Pt.

7.2. Scaling Relations on NSAs of Pt and Transition Metals

We showed in Chapter 3 that the scaling relations [77] are adsorption-site dependent. This was not a problem for perovskite oxides or graphitic materials since their active sites basically

contain a single transition metal surrounded by several ligands, and therefore, *O, *OH, and *OOH bind in the same adsorption site, namely on atop position. For pure metals, this introduces scattering in the data but does not alter the overall trends, as verified by Abild-Pedersen et al in Ref. [77]. Nonetheless, for NSAs of Pt and transition metals the the scalability depends strongly on the considered adsorption sites. This can be observed in Figure 7.5, where we present the scalings between O* adsorbed in the fcc hollow (the most stable site) and atop positions, and *OH adsorbed in atop position (the most stable site).

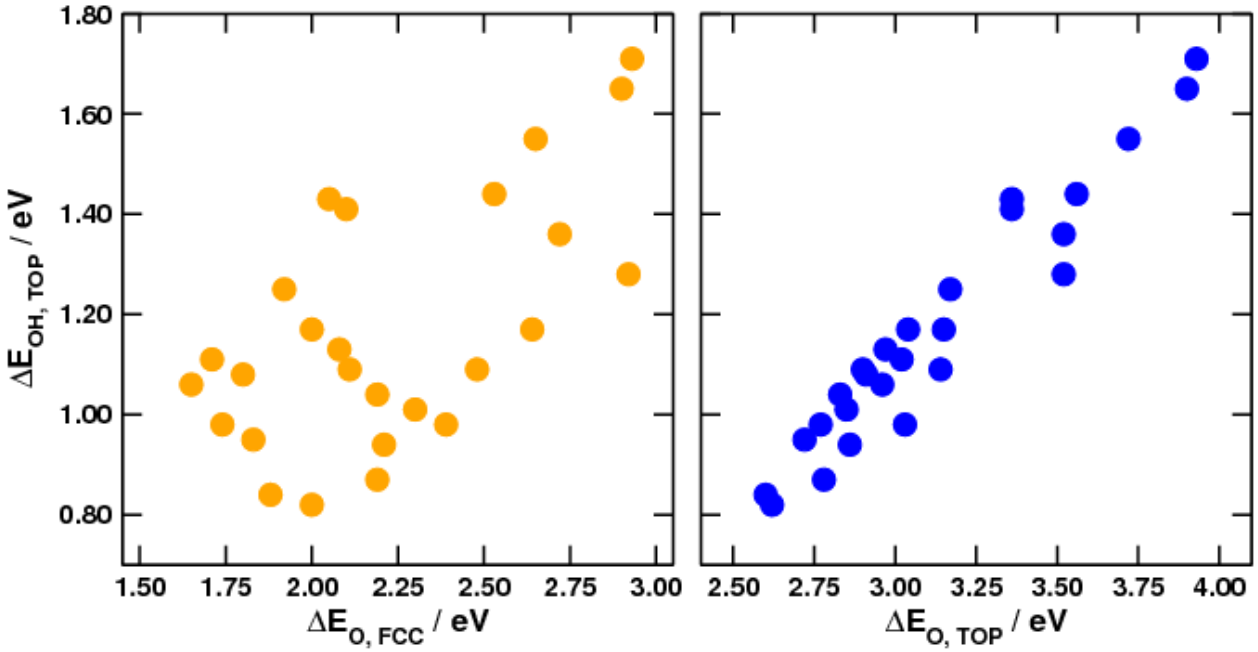

Figure 7.5. Scaling relations between the adsorption energies of O* adsorbed in the fcc hollow (left) and in atop position (right), with that of *OH on top. The scaling relations are only fulfilled when the adsorption site is identical.

As shown in Appendix 3, the minima of the curves for adsorption energy vs. d-filling for *OH adsorption on top and *O on fcc hollow are located in different positions, thus preventing the two variables from scaling adequately. That statement also holds for the d-band center. On the other hand, *O on top and *OH on top display similar curves of adsorption energy vs. d-filling and their scaling is smooth.

7.3. The Surface Formation Energy as Descriptor for Adsorption Energies

It is evident that the adsorbate can be treated as a small perturbation to the substrate system and since the coupling between adsorbate states and surface metal d-states is a fixed number for single metal NSAs, one should be able to estimate the change in adsorption from the alloying energy alone. In the following we will derive a general principle for NSAs based on what we have found on Pt NSAs.

The adsorption of an adsorbate X on a NSA of Pt and the element M can be imagined as a single reaction in which the surface forms from Pt and M, and, simultaneously, X is adsorbed. Such process is represented by Equation (7.2).

$$(Pt/Pt)+M+X \rightarrow (Pt/M/Pt)-X* \tag{7.2}$$

The reaction energy of Equation (7.2), denoted in the following as ΔE_F and shown in Equation (7.3), corresponds to a total cohesive energy of the system. Figure 7.6 shows the variation of ΔE_F according to the d-filling, denoted as N, when Li is adsorbed on NSAs of Pt.

$$\Delta E_F = E_{Pt/M/Pt-X*} - E_{Pt/Pt} - E_M - E_X \tag{7.3}$$

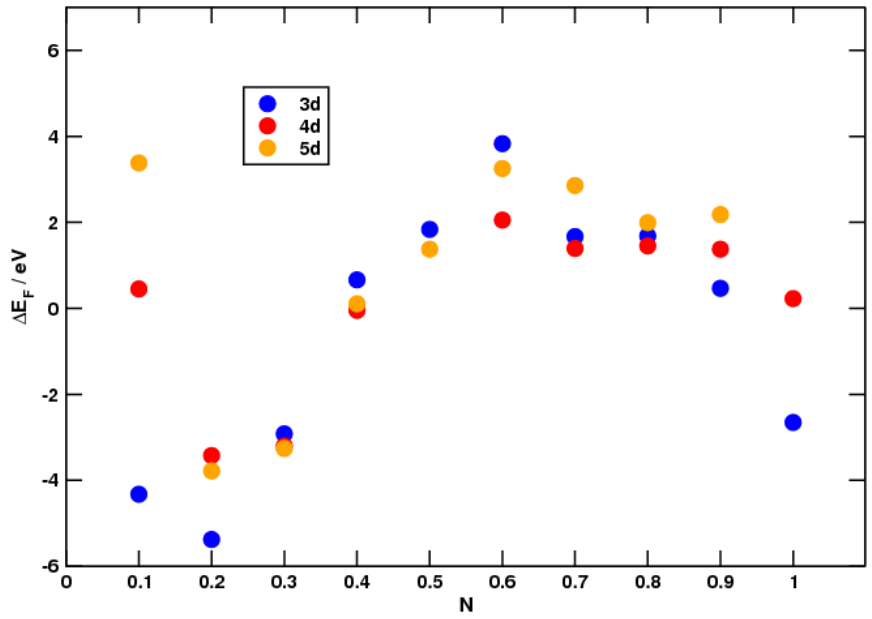

Figure 7.6. Trends in total cohesive energies for NSAs of Pt and d-metals. Alloying elements from the 3d, 4d, and 5d metal series are shown in blue, red and orange, respectively.

Being ΔE_F a sort of cohesive energy, it is reasonable that it varies with the d-filling of the M components in a way that resembles the Friedel model for cohesive energies [125, 151]. Since this energy includes both formation energy and adsorption energy, let us decompose the problem in order to simplify the understanding of the whole phenomenon.

The formation of NSAs of Pt with metal M can be represented in the following way:

$$(Pt/Pt)+M \rightarrow (Pt/M/Pt) \tag{7.4}$$

The reaction energy of Eqn (7.4) corresponds to the alloying energy (ΔE_{alloy}) and is given by the following expression:

$$\Delta E_{alloy} = E_{Pt/M/Pt} - E_{Pt} - E_M \tag{7.5}$$

The variation of the formation energies (ΔE_{alloy}) of the NSAs exhibits a behavior that is similar to ΔE_F. This can be seen in Figure 7.7.

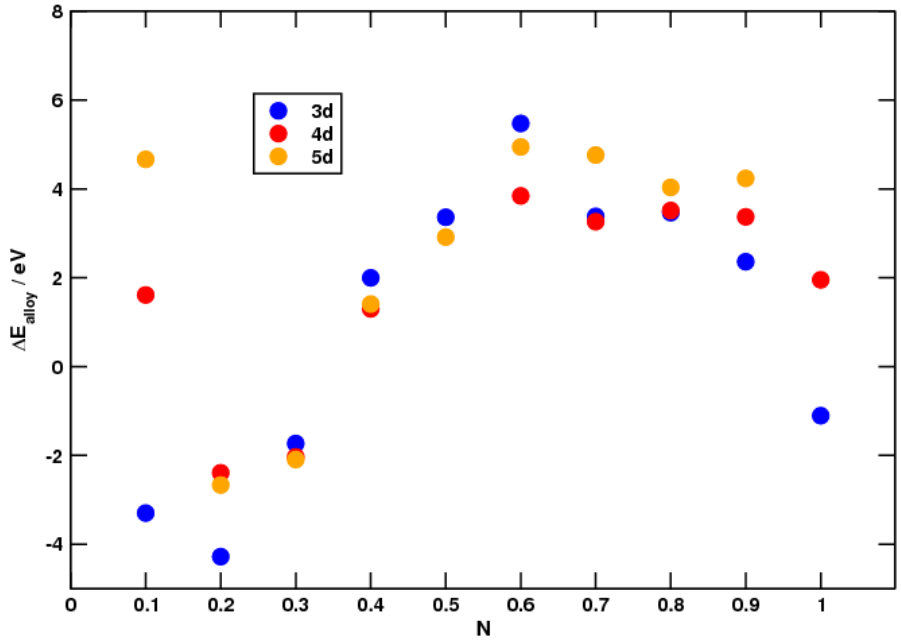

Figure 7.7. Trends in alloying energies for Near Surface Alloys (NSAs) of Platinum and d-metals. Alloying elements from the 3d, 4d, and 5d seriesare shown in blue, red and orange, respectively.

On the other hand, the adsorption energy of the adsorbate X (ΔE_{ADS}), according to the reaction shown in Equation (7.6), is given by Equation (7.7).

$$(Pt/M/Pt)+X \rightarrow (Pt/M/Pt)-X* \quad (7.6)$$

$$\Delta E_{ADS} = E_{Pt/M/Pt-X*} - E_{Pt/M/Pt} - E_X \quad (7.7)$$

The variation of ΔE_{ADS} with N is shown in Figure 7.8, for adsorbed Li species in atop position.

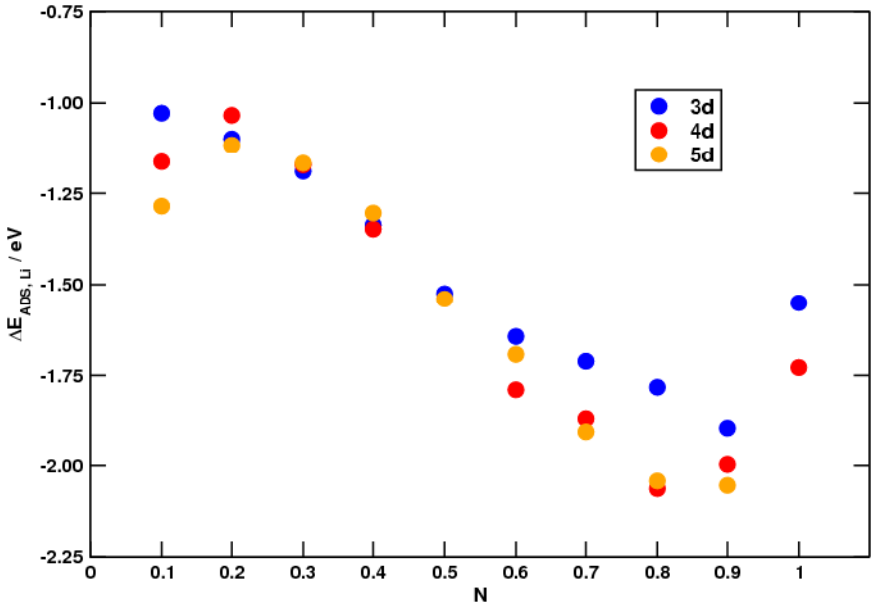

Figure 7.8. Trends in adsorption energies of Lithium for NSAs of Platinum and d-metals. Alloying elements from the third, fourth and fifth rows of the periodic table are shown in blue, red and orange, respectively.

Until now we have divided the hypothetical simultaneous process of forming the surface with the adsorbate into two real separate processes: the NSA formation from Pt and M; and the adsorption of X on the NSA. This means that the 3 reactions are linked and one can easily prove that adding Equation (7.6) to (7.4) leads directly to (7.2). In terms of energetics, we have the following relation:

$$\Delta E_F = \Delta E_{alloy} + \Delta E_{ADS} \quad (7.8)$$

Reorganizing Equation (7.8), we find that the adsorption energies can be found as the difference between the total formation energy (surface + adsorbate) and the formation energy of the surface.

$$\Delta E_{ADS} = \Delta E_F - \Delta E_{alloy} \quad (7.9)$$

Even though Equation (7.9) is a reformulation of the standard way of calculating adsorption energies given by Equation (7.7), it is a simple and clear expression giving a much deeper insight. The behavior of the adsorption energies depends on the superposition of the two effects present in Eqn (7.9), which is general in its applicability to alloys and adsorbates (even though it was derived here only for Pt alloys). Therefore, the trends shown in Figure 7.8 are the result of the linear combination of the relations shown in Figures 7.6 and 7.7.

In the following we will show the benefits of such representation of the adsorption energies. Since ΔE_{alloy} and ΔE_F determine the shape of ΔE_{ADS}, and given that the two former have the same kind of behavior, a natural consequence is that ΔE_{alloy} and ΔE_F are linearly correlated. This is indeed the case, as shown in Figure 7.9.

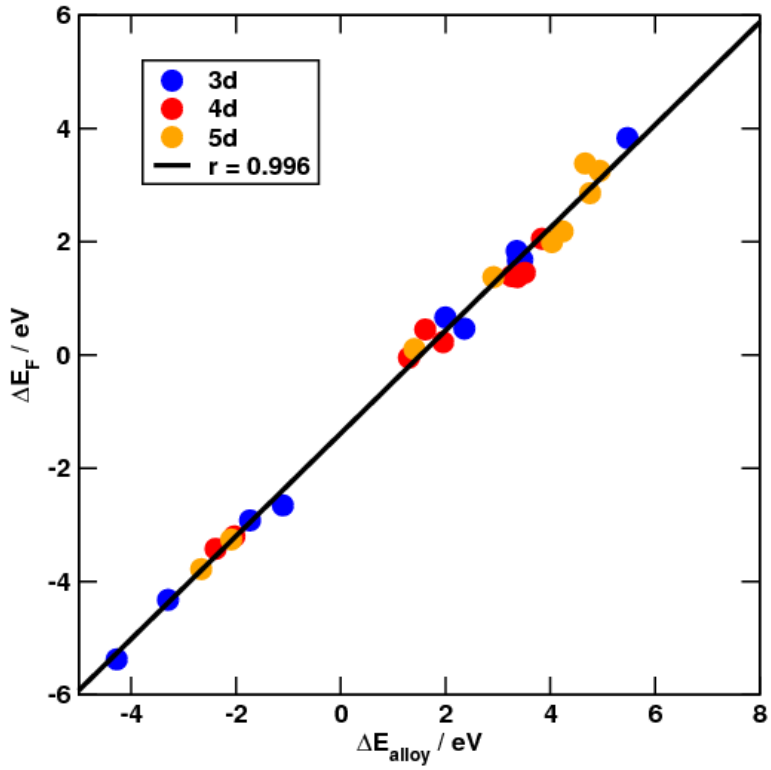

Figure 7.9. Linear correspondence between the two parts of the adsorption energy for NSAs of Pt and d-metals with adsorbed Li. Alloying elements from the 3d, 4d, and 5d series are shown in blue, red and orange, respectively.

Given this linear relation, it is possible to further simplify Equation (7.9) as follows:

$$\Delta E_{ADS} = (\gamma - 1)\Delta E_{alloy} + \sigma \qquad (7.10)$$

The term $(\gamma-1)$ is, in general, close to zero due to the high degree of similarity between ΔE_{alloy} and ΔE_F. Besides, σ is the adsorption energy of the X species on an ideal material whose surface formation energy is null. This constant is the largest term in Equation (7.10), while $(\gamma-1)\Delta E_{alloy}$ is a small but non-negligible perturbation to it. We stress at this point that Pt can be substituted by any other metal without loss of generality in the formulae shown here.

Furthermore, we point out the impossibility of approaching zero in ΔE_{alloy}, since the breaking of bonds in any case implies an energetic change in the structure (Figure 7.9 shows that the change can be either positive or negative, but not zero). Thus, the adsorption energy of a given surface can be seen as a deviation (positive or negative) from that of an ideal, non-realizable surface given that the formation of a surface implies the breaking of bonds, and thus deviations appear due to both the formation of the alloy and the surface. The predictions of adsorption energies based on the formation energies of the NSAs are shown in Figure 7.10 for adsorption of *Li. In Appendix 3 we show the plots for O* and *CH_3.

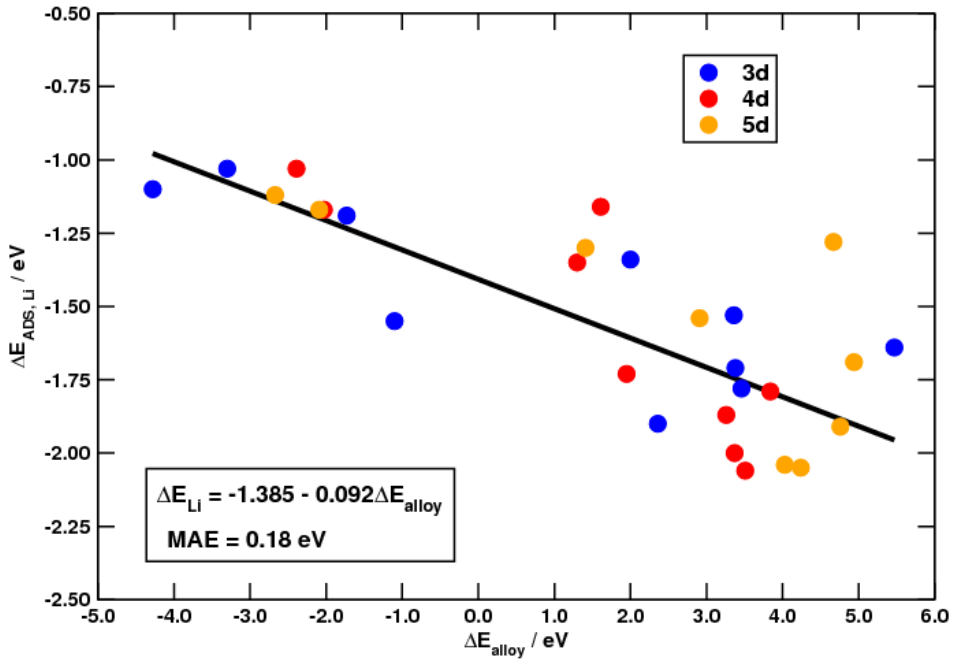

Figure 7.10. Adsorption energies of Li on NSAs of Pt as a function of the alloy formation energy. Alloying elements from the 3d, 4d, and 5d series are shown in blue, red and orange, respectively. The MAE is ~0.18 eV.

We remark that the Mean Absolute Error (MAE) is ~0.18 eV, which is below the accuracy of DFT-GGAs in general [3], in an energy window of ~10eV for ΔE_{alloy}. We also note that the points with the largest deviations appear for alloys containing elements with large atomic sizes, such as Pt/Y/Pt and Pt/La/Pt (with ΔE_{alloy} values of 1.6 and 4.7 eV), and the prediction may be improved by optimizing the lattice constant of the system, and not fixing it to that of Pt, as in the rest of the calculations.

In conclusion, we have shown that there are exceptions to the d-band model when we look at NSAs, but there exist several alternatives to predict adsorption energies based on structural parameters. The exceptions are due to the simplicity of the d-band model in which the contribution from the s-part of the metal electronic structure is treated as a constant, and charge transfer effects are not taken into account. These effects make that model inadequate for the treatment of NSAs. Conversely, the model based on alloy energies has predictive power and again, as in the case of the d-band model, a structural variable belonging to the clean surfaces can be used to accurately describe trends in adsorption energies.

SUMMARY AND OUTLOOK

Stability and Activity of Perovskite Oxides

Perovskite oxides are salient materials due to their multiple properties and applications. However, there had been no ab initio studies of their formation energies and phase stabilities before the one presented here. Our findings evince a direct connection between composition and stability in perovskites, and open up a path to ab initio constructions of complete phase diagrams for them, e.g. Pourbaix diagrams [80], which are of importance if perovskites are to be used in harsh environments such as acids or bases. Moreover, several perovskite oxides appear to be active for several catalytic reactions, due to the wide range of adsorption energies spanned by the different combinations of A and M elements in AMO_3. The trends can, in most cases, be rationalized in terms of simple physical-chemical concepts, such as number of d electrons and electronegativity. The effect of doping needs to be extensively explored in the future and promises to be a good way of tuning adsorption properties. Perovskite oxides were also used to demonstrate the thermochemical origin of the scaling relations and the limitations implied by them. The site-dependence of the scaling relations was proposed and verified with NSAs of Pt and transition metals.

Graphitic Materials Functionalized with Nitrogen and Late Transition Metals

We showed that graphitic materials with active sites composed of 4 nitrogen atoms and transition metals belonging to groups 7 to 9 in the periodic table are active towards ORR, and also towards OER. On the basis of careful spin analyses we observe that the oxidation state of those elements in the active sites should in general be +2. Moreover, our results show that transition metals do not have intrinsic catalytic activities, since their adsorption behavior can be severely altered by changes in the local geometry of the active site, the chemical nature of the nearest neighbors, and the oxidation states. The trends are well captured, to a first approximation, by the number of d-electrons of the transition metal present in the active site. In the future, more kinds of active sites (such as those of phtalocyanines) should be studied and compared with the provided trends.

NSAs and SAs of Pt and Late Transition Metals

DFT has proved useful for the description and explanation of the catalytic activity of pure metals and alloys for various reactions. Now the challenge consists not only in describing the multifunctionalities and ligand or strain effects of alloys, but also in their prediction and exploitation. In order to address this challenge, it is very useful to separate different effects. Since trends in adsorption energies seem not to be directly correlated to changes in the d-band center, we presented a simple systematic way of relating adsorption energies (a key surface property of relevance in catalysis) with a controllable experimental variable in Pt SAs and NSAs: the proportion of the alloy components and their location. The presence of alien metals in the second layer of a Pt (111) surface tends to weaken the binding energies, while in the first they are strengthened due to the change introduced on the coupling between Pt and its nearest neighbors and with the adsorbate. These two effects are independent from each other. Therefore, the ligand effects are layer-dependent and their magnitude increases when the amount of alloying metals is increased. The trends can be explained within a tight binding scheme, containing input from the simulations in terms of Pt-C binding distances and intermetallic distances. We anticipate the methodology to be applicable to other species adsorbed on atop position such as *OH (which was verified in Chapter 7 both theoretically and experimentally), $*NH_2$, $*CH_3$, among others, and the possible extension to other adsorbate sites would also be of significant interest.

Applications of Pt-Cu NSAs and SAs

It is clear that CO adsorption at elevated pressures and temperatures on a Pt-Cu NSA induces a large Cu surface segregation, generating a novel SA to which CO binds very strongly, even compared with pure Pt (111). The Cu content needed for saturation of the SA is ~2/3 ML of Cu, leading to a CO saturation coverage of ~1/3 ML. The sharp CO TPD spectrum compared with that of pure Pt (111), the observed ($\sqrt{3}$x$\sqrt{3}$) *R*30° LEED pattern, and the IR-peak red shift and narrow fwhm strongly suggest a significantly reduced lateral (repulsive) interaction between CO molecules adsorbed atop Pt sites and hence a well-ordered surface with well-defined, well-dispersed, and isolated Pt sites [119]. DFT simulations reproduce the experimental observations

and confirm that the vastly increased CO binding energy with 2/3 ML Cu in the first layer of Pt rationalizes the observed Cu surface segregation. These results add to the promise of using molecular adsorbate-induced surface changes as a tool for selective and dynamical engineering of alloy surfaces [140-141]. Moreover, the Pt-Cu NSA displays improved activity towards ORR compared to Pt. The origin of this improvement is due to the main feature of the Pt-Cu NSAs: they tend to decrease the bond strength between surface and adsorbates which, according to previous theoretical models [16], makes Pt approach the top of the volcano.

Trends in Adsorption Energies of NSAs of Pt and Transition Metals

NSAs of Pt constitute a clear and remarkable exception to the d band model [47]. It seems to be due to a non-constant sp coupling contribution and/or charge transfer between layers. The former is one of the main assumptions of the model, while the latter is definitely an effect not accounted for by it. In any case, this exception suggests two things: firstly, that the d-band model might be incomplete or, secondly, that there only exists correlation between d-band center and adsorption energy. The first idea leads to a corrective solution, i.e. an addition to the current model that accounts for the exceptions and makes it more general, provided that such corrections can be found and rationally explained. The second idea has deeper implications, since it leads to a different approach to the problem, abandoning the idea of correlation seeking for causality. The identification of simple correlations between adsorption energies and structural parameters of the clean surface is extremely valuable, but causality represents a step beyond in comprehension of the phenomena [2]. We explored this option by considering that the adsorbate is a small perturbation to the NSA system. Hence, the NSA and the NSA + adsorbate systems display curves similar to that of the Friedel model for cohesive energies [125, 151], when plotted versus the number of d electrons. Certainly, the stability of the NSA depends strongly on whether the metal in the second layer is able to accept or donate the right amount of electrons and this behavior is mirrored into the binding energies. Hence, the cohesive energy of the NSA and the NSA + adsorbate will correlate linearly with a slope close to zero mimicking the small but non-negligible effect of the adsorbates. Nonetheless, this approach needs to be further tested in other NSA systems.

Appendix 1. Data for Figures in Chapter 2

In this appendix we present the DFT and experimental data reported in Chapter 2.

Table A1.1 contains the DFT calculated and experimental formation energies of all considered perovskites from their elements at 298 K (corresponding to the data in Figure 2.3. a)). References for the experimental data are also provided.

Table A1.1. Gibbs energies of formation of various perovskite oxides. All values are at 298 K.

Perovskite	ΔG_{DFT} (eV)	ΔG_{EXP} (eV)
$LaTiO_3$	-15.70	-
$LaVO_3$	-14.42	-15.37[152]
$LaCrO_3$	-14.00	-14.71[153]
$LaMnO_3$	-13.23	-14.04[154]
$LaFeO_3$	-11.92	-12.96[155]
$LaCoO_3$	-11.40	-12.13[156]
$LaNiO_3$	-10.50	-11.41[42]
$LaCuO_3$	-9.48	-
$SrTiO_3$	-15.38	-16.36[45]
$SrVO_3$	-13.37	-14.13[157]
$SrCrO_3$	-11.74	-12.47[158]
$SrMnO_3$	-11.04	-11.83[159]
$SrFeO_3$	-9.42	-
$SrCoO_3$	-8.47	-
$SrNiO_3$	-7.12	-
$SrCuO_3$	-5.92	-
$CaTiO_3$	-15.40	-16.25[45]
$CaCrO_3$	-11.86	-12.55[158]
$CaMnO_3$	-11.24	-
$CaFeO_3$	-9.46	-
$CaCuO_3$	-6.00	-
$BaTiO_3$	-15.61	-16.30[157]
$BaCrO_3$	-11.89	-
$BaNiO_3$	-7.20	-
$BaCuO_3$	-6.12	-
$YTiO_3$	-15.75	-
YVO_3	-14.46	-15.56[152]
$YCrO_3$	-14.07	-15.24[160]
$YMnO_3$	-13.22	-14.19[152]
$YFeO_3$	-11.93	-
$YCuO_3$	-9.48	-
$La_{0.25}Sr_{0.75}MnO_3$	-11.70	-12.61[161]

$La_{0.5}Sr_{0.5}MnO_3$	-12.33	-13.08[161]
$La_{0.75}Sr_{0.25}MnO_3$	-12.83	-13.55[161]
$La_{0.875}Sr_{0.125}MnO_3$	-13.03	-13.79[161]
$La_{0.25}Sr_{0.75}CrO_3$	-12.38	-
$La_{0.5}Sr_{0.5}CrO_3$	-12.94	-
$La_{0.75}Sr_{0.25}CrO_3$	-13.48	-
$La_{0.25}Sr_{0.75}CoO_3$	-9.26	-
$La_{0.5}Sr_{0.5}CoO_3$	-10.00	-
$La_{0.75}Sr_{0.25}CoO_3$	-10.67	-

Table A1.2 contains the data shown in Figure 2.3.b).

Table A1.2. Experimental and DFT energetics of reactions involving perovskites and monoxides. Values at 1273 K appear in bold.

Perovskite	ΔG_{DFT} (eV)	ΔG_{EXP} (eV)
$LaVO_3$	-2.83	-2.40[152]
$LaMnO_3$	**-1.12**	**-0.94**[91, 162]
$LaFeO_3$	**-1.04**	**1.32[163]**
$LaCoO_3$	**-0.59**	**-0.54**[164]
$LaNiO_3$	**-0.13**	**-0.13**[42]
$SrTiO_3$	-5.68	-5.60[80, 157]
$SrVO_3$	-4.94	-4.24[152, 157]
$SrMnO_3$	**-1.53**	**-1.48**[165]
$BaNiO_3$	-0.98	-1.04[166]
$YMnO_3$	-0.79	-0.62[162]

Table A1.3 contains the data shown in Figure 2.3.c).

Table A1.3. Experimental and DFT energetics of reactions involving perovskites and sesquioxides. Values at 1273 K appear in bold.

Perovskite	ΔG_{DFT} (eV)	ΔG_{EXP} (eV)
$LaCrO_3$	**-0.34**	**-0.31**[167]
$LaMnO_3$	-0.43	-0.48[152]
$LaFeO_3$	**-0.29**	**-0.51**[168]
$SrCrO_3$	-1.24	-1.31[158]
$SrMnO_3$	-1.41	-1.66[161]
$La_{0.25}Sr_{0.75}MnO_3$	-1.28	-1.53[161]
$La_{0.5}Sr_{0.5}MnO_3$	-1.12	-1.24[161]
$La_{0.75}Sr_{0.75}MnO_3$	-0.82	-0.96[161]

$La_{0.875}Sr_{0.125}MnO_3$	-0.63	-0.82[161]

Table A1.4 contains the data shown in Figure 2.3.d).

Table A1.4. Experimental and DFT energetics of reactions involving perovskites and rutile oxides.

Perovskite	ΔG_{DFT} (eV)	ΔG_{EXP} (eV)
$LaMnO_3$	0.13	0.51[169]
$SrTiO_3$	-1.19	-1.24[170]
$SrVO_3$	-1.34	-1.46[152, 157]
$SrCrO_3$	-0.69	-1.09[158]
$SrMnO_3$	-0.85	-0.92[165, 171-
$BaTiO_3$	-1.56	-1.58[173]
$CaTiO_3$	-0.87	-0.84[173]
$CaCrO_3$	-0.48	-0.73[158]
$CaMnO_3$	-0.72	-0.91[174]

The formation energies at 298 K of the monoxides and sesquioxides appearing in the aforementioned reactions are shown in Table A1.5.

Supplementary Table 5. Calculated Gibbs energies of formation of various oxides. The Mean Absolute Error is ~0.77 eV when comparing with available experimental data.

Oxide	ΔG_{DFT} (eV) @	ΔG_{EXP} (eV) @
BaO	-5.44	-5.39[175]
CaO	-5.92	-6.25[175]
SrO	-5.58	-5.82[175]
TiO	-4.38	-5.07[80]
VO	-3.08	-4.17[45]
MnO	-2.84	-3.65[45]
FeO	-1.40	-2.44[45]
CoO	-1.45	-2.15[45]
NiO	-1.04	-2.17[45]
Cr_2O_3	-10.40	-10.91[175]
Mn_2O_3	-8.61	-9.13[91]
Fe_2O_3	-6.27	-7.58[45]
La_2O_3	-16.98	-17.70[44]
Y_2O_3	-17.85	-18.79[45]

Appendix 2. Data for Figures in Chapter 3

In this appendix we present the DFT data reported in Figures from Chapter 3 and some additional information. Table A2.1 contains the DFT calculated adsorption energies of *O, *OH, and *OOH, on atop position of M in MO_2-terminated (001) surfaces of all considered perovskites. Spin polarization effects were taken into account when necessary. The adsorption energies are calculated with the Equations provided in Chapter 3. The mean values of $\Delta E_{O/OH/H2O}$, $\Delta E_{O/OOH/H2/H2O}$, and $\Delta E_{OOH/OH}$ are, in that order, 0.41 eV, 2.69 eV and 3.10 eV. Their standard deviations are 0.22 eV, 0.26 eV, and 0.18 eV, respectively.

Table A2.1. Adsorption energies of ORR intermediates on (001) surfaces of AMO_3. All energies are given in eV.

Perovskite	ΔE_O	ΔE_{OH}	ΔE_{OOH}	$\Delta E_{O/OH/H2O}$	$\Delta E_{O/OOH/H2/H2O}$	$\Delta E_{OOH/OH}$
$SrScO_3$	5.20	2.00	4.82	0.60	2.22	2.82
$SrTiO_3$	3.88	1.22	4.51	0.72	2.58	3.29
$SrVO_3$	-0.10	-0.26	2.96	0.21	3.01	3.22
$SrCrO_3$	0.89	0.37	3.60	0.08	3.16	3.24
$SrMnO_3$	2.27	0.82	4.02	0.31	2.89	3.20
$SrFeO_3$	2.95	1.29	4.30	0.19	2.83	3.02
$SrCoO_3$	2.97	1.15	4.06	0.33	2.57	2.91
$SrNiO_3$	3.82	1.79	4.54	0.12	2.63	2.75
$SrCuO_3$	4.72	1.94	4.92	0.42	2.56	2.98
$LaScO_3$	4.77	1.44	4.49	0.95	2.11	3.06
$LaTiO_3$	-1.85	-1.55	1.84	0.62	2.77	3.39
$LaVO_3$	-0.78	-0.61	2.57	0.22	2.96	3.18
$LaCrO_3$	0.66	0.17	3.30	0.16	2.97	3.13
$LaMnO_3$	1.36	0.27	3.47	0.41	2.79	3.20
$LaFeO_3$	2.27	0.79	3.87	0.50	2.80	3.30
$LaCoO_3$	2.64	1.10	4.12	0.22	2.80	3.01
$LaNiO_3$	3.07	1.15	4.22	0.38	2.69	3.07
$LaCuO_3$	4.89	2.03	5.00	0.41	2.56	2.97

$BaTiO_3$	4.35	1.58	4.70	0.60	2.52	3.12
$BaNiO_3$	3.71	1.47	4.44	0.38	2.58	2.97
$BaCuO_3$	4.77	1.95	4.92	0.44	2.54	2.98
$CaTiO_3$	3.79	1.11	4.47	0.78	2.58	3.36
$CaMnO_3$	2.70	0.77	4.05	0.58	2.70	3.27
$CaFeO_3$	2.96	1.33	4.46	0.15	2.98	3.12
$CaCuO_3$	4.82	2.03	4.74	0.39	2.33	2.72
$YScO_3$	4.89	1.55	4.57	0.89	2.13	3.02
$YTiO_3$	-1.62	-1.39	2.08	0.58	2.89	3.47
YVO_3	-0.70	-0.61	2.63	0.26	2.98	3.24
$YCrO_3$	0.52	0.01	3.30	0.25	3.04	3.28
$YMnO_3$	1.72	0.42	3.60	0.44	2.74	3.18
$YFeO_3$	2.55	0.87	3.91	0.41	2.64	3.04
$YNiO_3$	3.27	1.26	4.33	0.37	2.69	3.06
$YCuO_3$	5.00	2.12	5.00	0.38	2.50	2.88

Table A2.2 contains the entropy and zero point energy corrections of the molecules and adsorbate species involved in the ORR at standard conditions.

Table A2.2. Entropic and zero-point energy corrections to molecules and adsorbates involved in ORR/OER.

Species	TS (eV)	ZPE (eV)
H_2O (l)	0.67	0.56
H_2	0.41	0.27
O_2	0.64	0.10
H_2O_2	0.72	0.72
*O	0.00	0.07
*OH	0.00	0.30
*OOH	0.00	0.40

Figure A2.1 contains the BEP line for CO dissociation on $LaMO_3$ and the variations of dissociation and transition-state energies according to the atoms in the M site, from Sc to Cu.

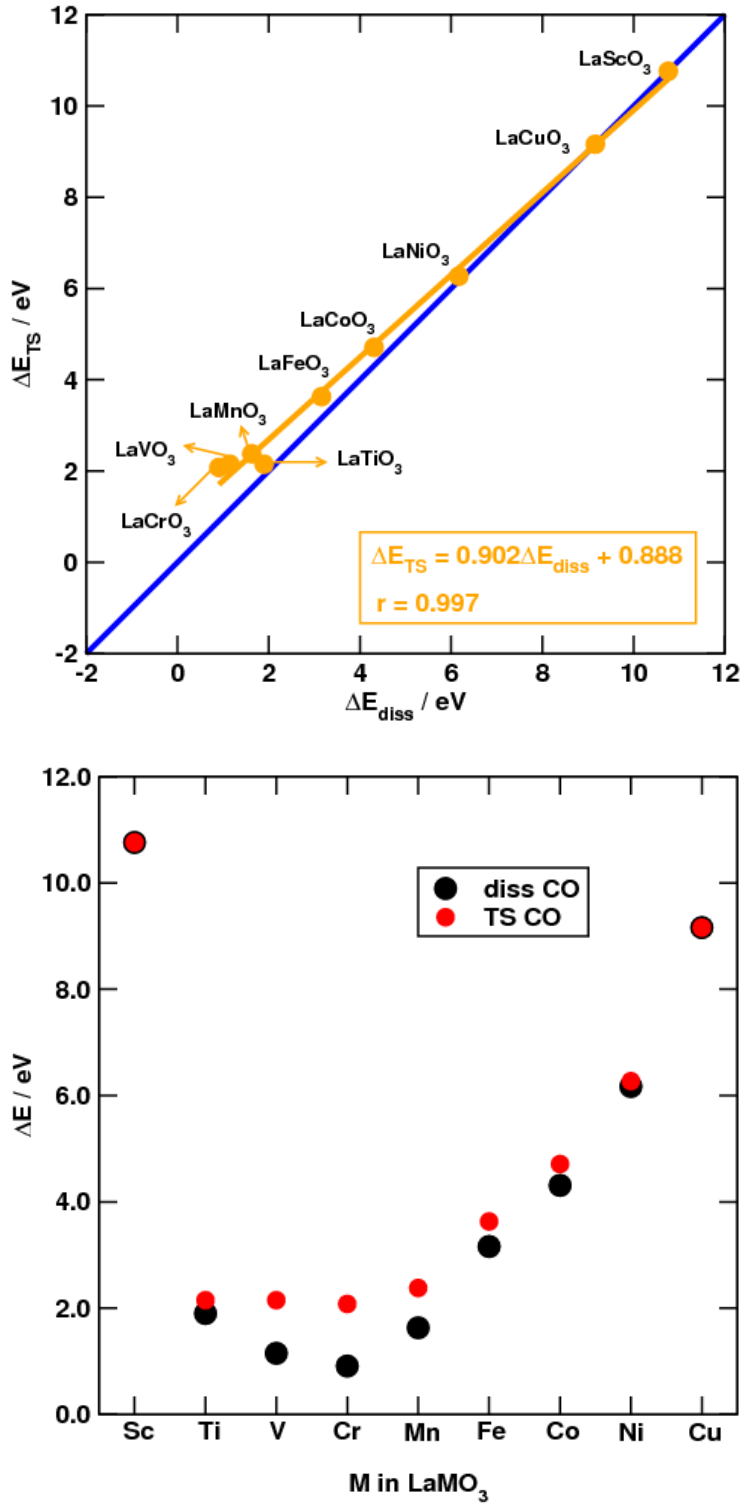

Figure A2.1. Top: BEP line for CO dissociation and comparison with the recombination line. Bottom: Separate variations of the energetics of CO dissociation with the M-site atoms.

Tables A2.3 and A2.4 contain the data used for the transition-state analysis in Chapter 3. These calculations were done without considering possible spin-polarization effects.

Table A2.3. Dissociation energies of various molecules on (001) surfaces of $LaMO_3$. All energies are given in eV.

Perovskite	$\Delta E_{diss\ N2}$	$\Delta E_{diss\ NO}$	$\Delta E_{diss\ O2}$	$\Delta E_{diss\ CO}$
$LaScO_3$	13.57	8.43	5.26	10.76
$LaTiO_3$	2.96	-3.49	-7.89	1.90
$LaVO_3$	0.20	-4.39	-6.96	1.15
$LaCrO_3$	-0.16	-3.75	-5.39	0.91
$LaMnO_3$	0.98	-2.09	-3.38	1.63
$LaFeO_3$	3.34	0.24	-0.94	3.16
$LaCoO_3$	5.74	2.17	0.63	4.31
$LaNiO_3$	8.22	4.26	2.26	6.17
$LaCuO_3$	11.73	7.46	5.14	9.16

Table A2.4. Transition-state energies of various molecules on (001) surfaces of $LaMO_3$. All energies are given in eV.

Perovskite	$\Delta E_{TS\ N2}$	$\Delta E_{TS\ NO}$	$\Delta E_{TS\ O2}$	$\Delta E_{TS\ CO}$
$LaScO_3$	13.57	8.43	5.28	10.76
$LaTiO_3$	2.87	-2.02	-2.87	2.15
$LaVO_3$	2.03	-1.57	-1.68	2.15
$LaCrO_3$	2.02	-1.19	-1.37	2.08
$LaMnO_3$	2.53	-0.78	-1.37	2.38
$LaFeO_3$	4.15	0.89	-0.24	3.63
$LaCoO_3$	5.74	2.14	0.74	4.71
$LaNiO_3$	8.22	4.18	2.29	6.27
$LaCuO_3$	11.73	7.46	5.14	9.16

Appendix 3. Additional Data to the Contents in Chapter 7.

In this appendix we present some additional information to the contents of Chapter 7. Figure A3.1 contains the DFT calculated adsorption energies of *O in top and fcc-hollow sites, and*OH in atop position vs. the d-filling of the alloying metals in NSAs with Pt as host. The adsorption energies are calculated with the equations provided in Chapter 3.

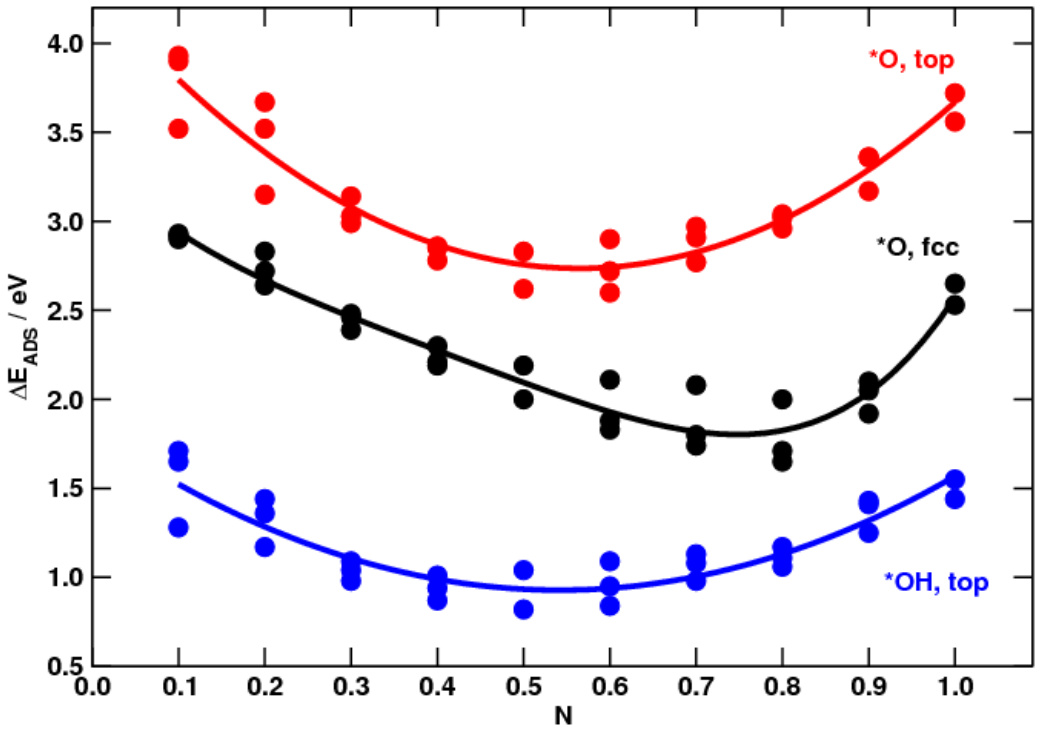

Figure A3.1. Variations of the adsorption energies of *O on top (red) and on fcc hollow sites (black), and *OH on top (blue) with the d-filling. Solid lines as guide to the eye are provided.

We observe that *O adsorbed on fcc hollow and *OH on top do not scale linearly due to the mismatch of their curves in Figure A3.1. Conversely, when *OH and *O are both adsorbed on top sites, they fulfill the scaling relations.

Figure A3.2 presents the total cohesive energies of $*CH_3$ (atop site) and *O (on fcc hollow sites). In both cases the slopes are close to unity, confirming the similarities between both variables and their Friedel-like behavior along the transition metal series.

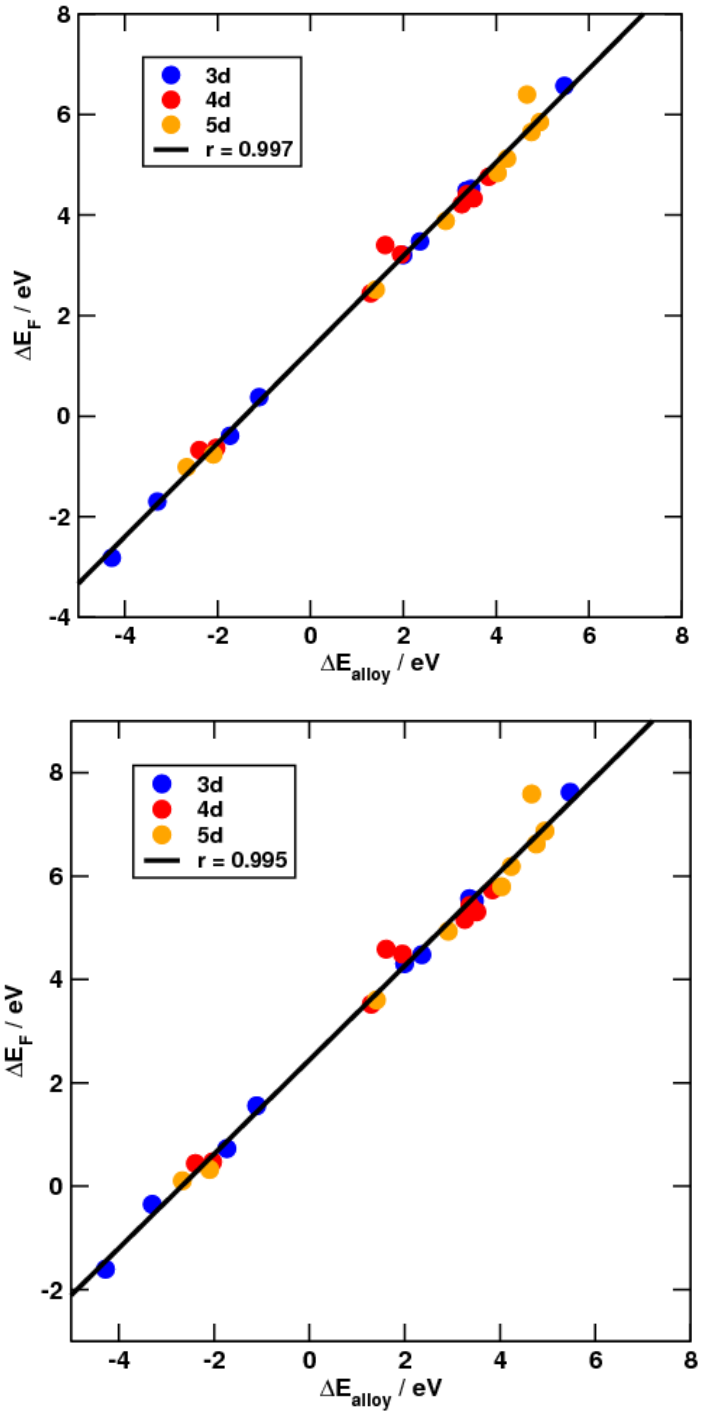

Figure A3.2. Linear dependence of the total cohesive energies on the alloy formation energy for NSAs of Pt and 3d (blue), 4d (red), and 5d (orange). Top: *CH_3; bottom: *O in fcc-hollow sites.

Finally, Figure A3.3 shows the relation between adsorption energies and alloy formation energies. The largest deviations come, in all cases, from alloys of Pt with La and Y. The MAEs between the model and the DFT-calculated adsorption energies are 0.18 eV, 0.14 eV, and 0.18 eV, for *O, *CH_3, and *Li, respectively.

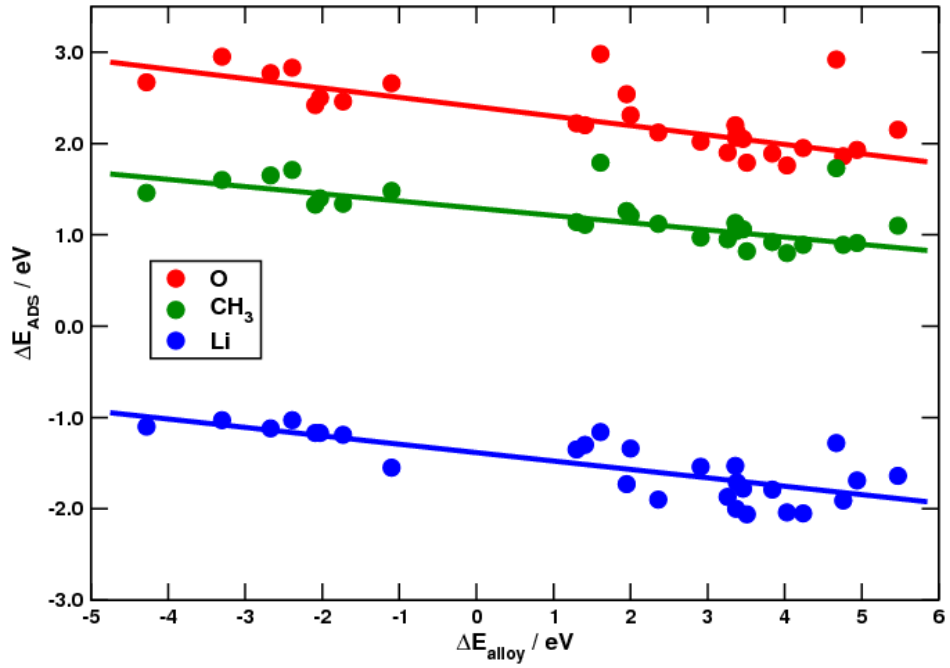

Figure A.3.3. Comparative variations of adsorption and alloy energies on NSAs of Pt with selected adsorbates. Red: *O; green: *CH_3; blue: Li.

REFERENCES

1. Van Ness, H.C., *Understanding Thermodynamics*. 1983, New York: Dover Publications. 103.

2. Bunge, M., *Science, its Method and its Philosophy*. 2005, Buenos Aires: Sudamericana.

3. Fiolhais, C., F. Nogueira, and M. Marques, *A Primer in Density Functional Theory*. 2003, Heidelberg, Germany: Springer-Verlag Berlin Heidelberg. 256.

4. Burke, K. and L. Wagner, *DFT in a nutshell: An essay for the 2nd CAMD summer school.* Preprint from Burke Group archives, 2010: p. 1-6.

5. Capelle, K., *A bird's-eye view of density-functional theory.* Brazilian Journal of Physics, 2006. **36**(4A): p. 1318-1343.

6. Hammer, B., L.B. Hansen, and J.K. Norskov, *Improved adsorption energetics within density-functional theory using revised Perdew-Burke-Ernzerhof functionals.* Physical Review B, 1999. **59**(11): p. 7413-7421.

7. Rogal, J. and K. Reuter, *Ab Initio Thermodynamics for Surfaces: A Primer.* Educational Notes RTO-EN-AVT-142, 2007. **Paper 2**: p. 2-1.

8. Martinez, J.I., et al., *Formation energies of rutile metal dioxides using density functional theory.* Physical Review B, 2009. **79**(4): p. 045120.

9. Atkins, P. and J. De Paula, *Atkins' Physical Chemistry*. 8th ed. 2006, Oxford: Oxford University Press. 1064.

10. Wang, L., T. Maxisch, and G. Ceder, *Oxidation energies of transition metal oxides within the GGA+U framework.* Physical Review B, 2006. **73**(19): p. 195107.

11. Ramani, V., *Fuel Cells.* The Electrochemical Society Interface, 2006. **15**(1): p. 41-44.

12. Ramani, V., H.R. Kunz, and J.M. Fenton, *The Polymer Electrolyte Fuel Cell.* The Electrochemical Society Interface, 2004. **13**(3): p. 17-19, 41.

13. Gasteiger, H.A. and J. Garche, *Fuel Cells*, in *Handbook of Heterogeneous Catalysis*, G. Ertl, et al., Editors. 2008, Wiley-VCH. p. 3081-3121.

14. Gasteiger, H.A., et al., *Activity benchmarks and requirements for Pt, Pt-alloy, and non-Pt oxygen reduction catalysts for PEMFCs.* Applied Catalysis B-Environmental, 2005. **56**(1-2): p. 9-35.

15. Stamenkovic, V., et al., *Changing the activity of electrocatalysts for oxygen reduction by tuning the surface electronic structure.* Angewandte Chemie-International Edition, 2006. **45**(18): p. 2897-2901.

16. Greeley, J., et al., *Alloys of platinum and early transition metals as oxygen reduction electrocatalysts.* Nature Chemistry, 2009. **1**(7): p. 552-556.

17. Strasser, P., et al., *Lattice-strain control of the activity in dealloyed core-shell fuel cell catalysts.* Nature Chemistry, 2010. **2**(6): p. 454-460.

18. Suntivich, J., et al., *Electrocatalytic Measurement Methodology of Oxide Catalysts Using a Thin-Film Rotating Disk Electrode.* Journal of the Electrochemical Society, 2010. **157**(8): p. B1263-B1268.

19. Bockris, J.O. and T. Otagawa, *THE ELECTROCATALYSIS OF OXYGEN EVOLUTION ON PEROVSKITES.* Journal of the Electrochemical Society, 1984. **131**(2): p. 290-302.

20. Lefevre, M. and J.P. Dodelet, *Fe-based catalysts for the reduction of oxygen in polymer electrolyte membrane fuel cell conditions: determination of the amount of peroxide released during electroreduction and its influence on the stability of the catalysts.* Electrochimica Acta, 2003. **48**(19): p. 2749-2760.

21. Lefevre, M., et al., *Iron-Based Catalysts with Improved Oxygen Reduction Activity in Polymer Electrolyte Fuel Cells.* Science, 2009. **324**(5923): p. 71-74.

22. Calle-Vallejo, F., et al., *Trends in Stability of Perovskite Oxides.* Angewandte Chemie-International Edition, 2010. **49**(42): p. 7699–7701.

23. Messing, G.L., et al., *Templated grain growth of textured piezoelectric ceramics.* Critical Reviews in Solid State and Materials Sciences, 2004. **29**(2): p. 45-96.

24. Ahn, C.H., K.M. Rabe, and J.M. Triscone, *Ferroelectricity at the nanoscale: Local polarization in oxide thin films and heterostructures.* Science, 2004. **303**(5657): p. 488-491.

25. Cheong, S.W. and M. Mostovoy, *Multiferroics: a magnetic twist for ferroelectricity.* Nature Materials, 2007. **6**: p. 13-20.

26. DeTeresa, J.M., et al., *Evidence for magnetic polarons in the magnetoresistive perovskites.* Nature, 1997. **386**(6622): p. 256-259.

27. Mawdsley, J.R. and T.R. Krause, *Rare earth-first-row transition metal perovskites as catalysts for the autothermal reforming of hydrocarbon fuels to generate hydrogen.* Applied Catalysis a-General, 2008. **334**(1-2): p. 311-320.

28. Nitadori, T., T. Ichiki, and M. Misono, *CATALYTIC PROPERTIES OF PEROVSKITE-TYPE MIXED OXIDES (ABO3) CONSISTING OF RARE-EARTH AND 3D TRANSITION-METALS - THE ROLES OF THE A-SITE AND B-SITE IONS.* Bulletin of the Chemical Society of Japan, 1988. **61**(3): p. 621-626.

29. Huang, Y.H., et al., *Double perovskites as anode materials for solid-oxide fuel cells.* Science, 2006. **312**(5771): p. 254-257.

30. Thiele, D. and A. Zuttel, *Electrochemical characterisation of air electrodes based on La0.6Sr0.4CoO3 and carbon nanotubes.* Journal of Power Sources, 2008. **183**(2): p. 590-594.

31. West, A.R., *Basic Solid State Chemistry*. Second ed. 1999: John Wiley & Sons. 496.

32. García-Fernández, P., et al., *Key Role of Covalent Bonding in Octahedral Tilting in Perovskites.* Journal of Physical Chemistry Letters, 2010. **1**: p. 647.

33. Bersuker, I.B., *The Jahn-Teller Effect*. 2006, Cambridge University Press. p. 634.

34. Norskov, J.K., et al., *Towards the computational design of solid catalysts.* Nature Chemistry, 2009. **1**(1): p. 37-46.

35. Studt, F., et al., *On the Role of Surface Modifications of Palladium Catalysts in the Selective Hydrogenation of Acetylene.* Angewandte Chemie-International Edition, 2008. **47**(48): p. 9299-9302.

36. Pacchioni, G., *Modeling doped and defective oxides in catalysis with density functional theory methods: Room for improvements.* Journal of Chemical Physics, 2008. **128**(18).

37. van Schilfgaarde, M., T. Kotani, and S. Faleev, *Quasiparticle self-consistent GW theory.* Physical Review Letters, 2006. **96**(22).

38. Wang, L., T. Maxisch, and G. Ceder, *Oxidation energies of transition metal oxides within the GGA+U framework.* Physical Review B, 2006. **73**(19).

39. Kurth, S., J.P. Perdew, and P. Blaha, *Molecular and solid-state tests of density functional approximations: LSD, GGAs, and meta-GGAs.* International Journal of Quantum Chemistry, 1999. **75**(4-5): p. 889-909.

40. Fernandez, E.M., et al., *Scaling relationships for adsorption energies on transition metal oxide, sulfide, and nitride surfaces.* Angewandte Chemie-International Edition, 2008. **47**(25): p. 4683-4686.

41. Pankajavalli, R. and O.M. Sreedharan, *THERMODYNAMIC STABILITIES OF LAVO3 AND LAVO4 BY EMF METHODS.* Materials Letters, 1995. **24**(4): p. 247-251.

42. Cheng, J.H., et al., *Enthalpies of formation of LaMO3 perovskites (M = Cr, Fe, Co, and Ni).* Journal of Materials Research, 2005. **20**(1): p. 191-200.

43. Yokokawa, H., *Understanding materials compatibility.* Annual Review of Materials Research, 2003. **33**: p. 581-610.

44. Grundy, A.N., B. Hallstedt, and L.J. Gauckler, *Thermodynamic assessment of the lanthanum-oxygen system.* Journal of Phase Equilibria, 2001. **22**(2): p. 105-113.

45. Binnewies, M. and E. Milke, *Thermochemical Data of Elements and Compounds*. Second Edition ed. 2002, Weinheim: Wiley-VCH Verlag GmbH. 928.

46. Gelatt, C.D., A.R. Williams, and V.L. Moruzzi, *THEORY OF BONDING OF TRANSITION-METALS TO NON-TRANSITION METALS.* Physical Review B, 1983. **27**(4): p. 2005-2013.

47. Hammer, B. and J.K. Nørskov, *Theoretical surface science and catalysis--calculations and concepts*, in *Advances in Catalysis*, C.G. Bruce and K. Helmut, Editors. 2000, Academic Press. p. 71-129.

48. Pena, M.A. and J.L.G. Fierro, *Chemical structures and performance of perovskite oxides.* Chemical Reviews, 2001. **101**(7): p. 1981-2017.

49. Tejuca, L.G., *PROPERTIES OF PEROVSKITE-TYPE OXIDES .2. STUDIES IN CATALYSIS.* Journal of the Less-Common Metals, 1989. **146**(1-2): p. 261-270.

50. Nakamura, T., M. Misono, and Y. Yoneda, *CATALYTIC PROPERTIES OF PEROVSKITE-TYPE MIXED OXIDES, LA1-XSRXCOO3.* Bulletin of the Chemical Society of Japan, 1982. **55**(2): p. 394-399.

51. Nitadori, T., S. Kurihara, and M. Misono, *CATALYTIC PROPERTIES OF LA1-XSRXMNO3,LA1-XCEXMNO3,LA1-XHFXMNO3.* Journal of Catalysis, 1986. **98**(1): p. 221-228.

52. Nitadori, T. and M. Misono, *CATALYTIC PROPERTIES OF LA1-XAX'FEO3 (A' = SR,CE) AND LA1-XCEXCOO3.* Journal of Catalysis, 1985. **93**(2): p. 459-466.

53. Voorhoeve, R.J.H., J.P. Remeika, and L.E. Trimble, *DEFECT CHEMISTRY AND CATALYSIS IN OXIDATION AND REDUCTION OVER PEROVSKITE-TYPE OXIDES.* Annals of the New York Academy of Sciences, 1976. **272**(APR28): p. 3-21.

54. Shu, J. and S. Kaliaguine, *Well-dispersed perovskite-type oxidation catalysts.* Applied Catalysis B-Environmental, 1998. **16**(4): p. L303-L308.

55. Nagamoto, H., et al., *METHANE OXIDATION OVER PEROVSKITE-TYPE OXIDE CONTAINING ALKALINE-EARTH METAL.* Chemistry Letters, 1988(2): p. 237-240.

56. Lago, R., et al., *Partial oxidation of methane to synthesis gas using LnCoO(3) perovskites as catalyst precursors.* Journal of Catalysis, 1997. **167**(1): p. 198-209.

57. Trikalitis, P.N. and P.J. Pomonis, *CATALYTIC ACTIVITY AND SELECTIVITY OF PEROVSKITES LA1-XSRXV1-X3+VX4+O3 FOR THE TRANSFORMATION OF ISOPROPANOL.* Applied Catalysis a-General, 1995. **131**(2): p. 309-322.

58. Vandamme, H. and W.K. Hall, *PHOTOCATALYTIC PROPERTIES OF PEROVSKITES FOR H-2 AND CO OXIDATION-INFLUENCE OF FERROELECTRIC PROPERTIES.* Journal of Catalysis, 1981. **69**(2): p. 371-383.

59. Vrieland, E.G., *ACTIVITY AND SELECTIVITY OF MN3+ AND MN4+ IN LANTHANUM CALCIUM MANGANITES FOR OXIDATION OF AMMONIA.* Journal of Catalysis, 1974. **32**(3): p. 415-428.

60. Watson, P.R. and G.A. Somorjai, *THE FORMATION OF OXYGEN-CONTAINING ORGANIC-MOLECULES BY THE HYDROGENATION OF CARBON-MONOXIDE USING A LANTHANUM RHODATE CATALYST.* Journal of Catalysis, 1982. **74**(2): p. 282-295.

61. Ulla, M.A., et al., *SURFACE-CHEMISTRY AND CATALYTIC ACTIVITY OF LA1-YSRYCOO3, LA1-YTHCOO3 PEROVSKITE .2. HYDROGENATION OF CO2.* Journal of Catalysis, 1987. **105**(1): p. 107-119.

62. Petunchi, J.O., et al., *CHARACTERIZATION OF HYDROGENATION ACTIVE-SITES ON LACOO3 PEROVSKITE.* Journal of Catalysis, 1981. **70**(2): p. 356-363.

63. Nudel, J.N., B.S. Umansky, and E.A. Lombardo, *BULK, SURFACE AND CATALYTIC CHARACTERIZATION OF THE CO3O4-LA2O3-LACOO3 SYSTEM.* Applied Catalysis, 1986. **26**(1-2): p. 339-351.

64. Ichimura, K., Y. Inoue, and I. Yasumori, *HYDROGENATION AND HYDROGENOLYSIS OF HYDROCARBONS ON PEROVSKITE OXIDES.* Catalysis Reviews-Science and Engineering, 1992. **34**(4): p. 301-320.

65. Seiyama, T., N. Yamazoe, and K. Eguchi, *CHARACTERIZATION AND ACTIVITY OF SOME MIXED METAL-OXIDE CATALYSTS.* Industrial & Engineering Chemistry Product Research and Development, 1985. **24**(1): p. 19-27.

66. Falcon, H., R.E. Carbonio, and J.L.G. Fierro, *Correlation of oxidation states in LaFexNi1-xO3+delta oxides with catalytic activity for H2O2 decomposition.* Journal of Catalysis, 2001. **203**(2): p. 264-272.

67. Tejuca, L.G., J.L.G. Fierro, and J.M.D. Tascon, *STRUCTURE AND REACTIVITY OF PEROVSKITE-TYPE OXIDES.* Advances in Catalysis, 1989. **36**: p. 237-328.

68. Kim, C.H., et al., *Strontium-Doped Perovskites Rival Platinum Catalysts for Treating NOx in Simulated Diesel Exhaust.* Science, 2010. **327**(5973): p. 1624-1627.

69. Bockris, J.O. and T. Otagawa, *MECHANISM OF OXYGEN EVOLUTION ON PEROVSKITES.* Journal of Physical Chemistry, 1983. **87**(15): p. 2960-2971.

70. Otagawa, T. and J.O. Bockris, *LANTHANUM NICKELATE AS ELECTROCATALYST - OXYGEN EVOLUTION.* Journal of the Electrochemical Society, 1982. **129**(10): p. 2391-2392.

71. Kuo, J.H., H.U. Anderson, and D.M. Sparlin, *OXIDATION-REDUCTION BEHAVIOR OF UNDOPED AND SR-DOPED LAMNO3 NONSTOICHIOMETRY AND DEFECT STRUCTURE.* Journal of Solid State Chemistry, 1989. **83**(1): p. 52-60.

72. Meadowcr.Db, *LOW-COST OXYGEN ELECTRODE MATERIAL.* Nature, 1970. **226**(5248): p. 847-&.

73. Wrighton, M.S., et al., *STRONTIUM-TITANATE PHOTOELECTRODES - EFFICIENT PHOTOASSISTED ELECTROLYSIS OF WATER AT ZERO APPLIED POTENTIAL.* Journal of the American Chemical Society, 1976. **98**(10): p. 2774-2779.

74. Sato, S. and T. Kadowaki, *PHOTOCATALYTIC ACTIVITIES OF METAL-OXIDE SEMICONDUCTORS FOR OXYGEN ISOTOPE EXCHANGE AND OXIDATION REACTIONS.* Journal of Catalysis, 1987. **106**(1): p. 295-300.

75. Stambouli, A.B. and E. Traversa, *Solid oxide fuel cells (SOFCs): a review of an environmentally clean and efficient source of energy.* Renewable & Sustainable Energy Reviews, 2002. **6**(5): p. 433-455.

76. Trasatti, S., *ELECTROCATALYSIS IN THE ANODIC EVOLUTION OF OXYGEN AND CHLORINE.* Electrochimica Acta, 1984. **29**(11): p. 1503-1512.

77. Abild-Pedersen, F., et al., *Scaling properties of adsorption energies for hydrogen-containing molecules on transition-metal surfaces.* Physical Review Letters, 2007. **99**(1).

78. Norskov, J.K., et al., *Origin of the overpotential for oxygen reduction at a fuel-cell cathode.* Journal of Physical Chemistry B, 2004. **108**(46): p. 17886-17892.

79. Matsumoto, Y. and E. Sato, *ELECTROCATALYTIC PROPERTIES OF TRANSITION-METAL OXIDES FOR OXYGEN EVOLUTION REACTION.* Materials Chemistry and Physics, 1986. **14**(5): p. 397-426.

80. Pourbaix, M., *Atlas of Electrochemical Equilibria in Aqueous Solutions*. Second English ed. 1974, Houston: National Association of Corrosion Engineers. 644.

81. Bronsted, J.N., *Acid and basic catalysis.* Chemical Reviews, 1928. **5**(3): p. 231-338.

82. Evans, M.G. and M. Polanyi, *Inertia and driving force of chemical reactions.* Transactions of the Faraday Society, 1938. **34**(1): p. 0011-0023.

83. Norskov, J.K., et al., *Universality in heterogeneous catalysis.* Journal of Catalysis, 2002. **209**(2): p. 275-278.

84. Logadottir, A., et al., *The Bronsted-Evans-Polanyi relation and the volcano plot for ammonia synthesis over transition metal catalysts.* Journal of Catalysis, 2001. **197**(2): p. 229-231.

85. Liu, Z.P. and P. Hu, *General trends in CO dissociation on transition metal surfaces.* Journal of Chemical Physics, 2001. **114**(19): p. 8244-8247.

86. Michaelides, A., et al., *Identification of general linear relationships between activation energies and enthalpy changes for dissociation reactions at surfaces.* Journal of the American Chemical Society, 2003. **125**(13): p. 3704-3705.

87. Pallassana, V. and M. Neurock, *Electronic factors governing ethylene hydrogenation and dehydrogenation activity of pseudomorphic Pd-ML/Re(0001), Pd-ML/Ru(0001), Pd(111), and Pd-ML/Au(111) surfaces.* Journal of Catalysis, 2000. **191**(2): p. 301-317.

88. Vojvodic, A., et al., *From Electronic Structure to Catalytic Activity: A Single Descriptor for Adsorption and Reactivity on Transition-Metal Carbides.* Physical Review Letters, 2009. **103**(14).

89. Studt, F., et al., *Volcano Relation for the Deacon Process over Transition-Metal Oxides.* Chemcatchem, 2010. **2**(1): p. 98-102.

90. Bligaard, T., et al., *The Bronsted-Evans-Polanyi relation and the volcano curve in heterogeneous catalysis.* Journal of Catalysis, 2004. **224**(1): p. 206-217.

91. Lide, D.R., *CRC Handbook of Chemistry and Physics*. 85th ed, ed. D.R. Lide. 2005, Boca Raton FL: CRC Press

92. Steele, B.C.H. and A. Heinzel, *Materials for fuel-cell technologies.* Nature, 2001. **414**(6861): p. 345-352.

93. Gasteiger, H.A. and N.M. Markovic, *Just a Dream-or Future Reality?* Science, 2009. **324**(5923): p. 48-49.

94. Bockris, J.O. and T.N. Veziroglu, *Estimates of the price of hydrogen as a medium for wind and solar sources.* International Journal of Hydrogen Energy, 2007. **32**(12): p. 1605-1610.

95. Geim, A.K. and K.S. Novoselov, *The rise of graphene.* Nature Materials, 2007. **6**(3): p. 183-191.

96. Wu, J.S., W. Pisula, and K. Mullen, *Graphenes as potential material for electronics.* Chemical Reviews, 2007. **107**(3): p. 718-747.

97. Castro Neto, A.H., et al., *The electronic properties of graphene.* Reviews of Modern Physics, 2009. **81**(1): p. 109-162.

98. Peres, N.M.R., *The transport properties of graphene.* Journal of Physics-Condensed Matter, 2009. **21**(32).

99. Allen, M.J., V.C. Tung, and R.B. Kaner, *Honeycomb Carbon: A Review of Graphene.* Chemical Reviews, 2010. **110**(1): p. 132-145.

100. Wallace, P.R., *THE BAND THEORY OF GRAPHITE.* Physical Review, 1947. **71**(9): p. 622-634.

101. Novoselov, K.S., et al., *Electric field effect in atomically thin carbon films.* Science, 2004. **306**(5696): p. 666-669.

102. Garcia-Lastra, J.M., *Strong Dependence of the Band Gap Opening at the Dirac Point of Graphene upon Hydrogen Adsorption Periodicity.* Physical Review B, 2010. **82**(23): p. 235418.

103. Denis, P.A., R. Faccio, and A.W. Mombru, *Is It Possible to Dope Single-Walled Carbon Nanotubes and Graphene with Sulfur?* Chemphyschem, 2009. **10**(4): p. 715-722.

104. Maciel, I.O., et al., *Synthesis, Electronic Structure, and Raman Scattering of Phosphorus-Doped Single-Wall Carbon Nanotubes.* Nano Letters, 2009. **9**(6): p. 2267-2272.

105. Stoyanov, S.R., A.V. Titov, and P. Kral, *Transition metal and nitrogen doped carbon nanostructures.* Coordination Chemistry Reviews, 2009. **253**(23-24): p. 2852-2871.

106. Ewels, C.P. and M. Glerup, *Nitrogen doping in carbon nanotubes.* Journal of Nanoscience and Nanotechnology, 2005. **5**(9): p. 1345-1363.

107. Kurak, K.A. and A.B. Anderson, *Nitrogen-Treated Graphite and Oxygen Electroreduction on Pyridinic Edge Sites.* Journal of Physical Chemistry C, 2009. **113**(16): p. 6730-6734.

108. Vayner, E. and A.B. Anderson, *Theoretical predictions concerning oxygen reduction on nitrided graphite edges and a cobalt center bonded to them.* Journal of Physical Chemistry C, 2007. **111**(26): p. 9330-9336.

109. Jaouen, F., F. Charreteur, and J.P. Dodelet, *Fe-based catalysts for oxygen reduction in PEMFCs - Importance of the disordered phase of the carbon support.* Journal of the Electrochemical Society, 2006. **153**(4): p. A689-A698.

110. Medard, C., et al., *Oxygen reduction by Fe-based catalysts in PEM fuel cell conditions: Activity and selectivity of the catalysts obtained with two Fe precursors and various carbon supports.* Electrochimica Acta, 2006. **51**(16): p. 3202-3213.

111. Zagal, J.H., *METALLOPHTHALOCYANINES AS CATALYSTS IN ELECTROCHEMICAL REACTIONS.* Coordination Chemistry Reviews, 1992. **119**: p. 89-136.

112. Chen, R.R., et al., *Unraveling Oxygen Reduction Reaction Mechanisms on Carbon-Supported Fe-Phthalocyanine and Co-Phthalocyanine Catalysts in Alkaline Solutions.* Journal of Physical Chemistry C, 2009. **113**(48): p. 20689-20697.

113. Kiros, Y., *Metal porphyrins for oxygen reduction in PEMFC.* International Journal of Electrochemical Science, 2007. **2**(4): p. 285-300.

114. Kjaergaard, C.H., J. Rossmeisl, and J.K. Norskov, *Enzymatic versus Inorganic Oxygen Reduction Catalysts: Comparison of the Energy Levels in a Free-Energy Scheme.* Inorganic Chemistry, 2010. **49**(8): p. 3567-3572.

115. Ruetschi, P. and P. Delahay, *INFLUENCE OF ELECTRODE MATERIAL ON OXYGEN OVERVOLTAGE - A THEORETICAL ANALYSIS.* Journal of Chemical Physics, 1955. **23**(3): p. 556-560.

116. Rossmeisl, J., et al., *Electrolysis of water on oxide surfaces.* Journal of Electroanalytical Chemistry, 2007. **607**(1-2): p. 83-89.

117. Collman, J.P., L.L. Chng, and D.A. Tyvoll, *ELECTROCATALYTIC REDUCTION OF DIOXYGEN TO WATER BY IRIDIUM PORPHYRINS ADSORBED ON EDGE PLANE GRAPHITE-ELECTRODES.* Inorganic Chemistry, 1995. **34**(6): p. 1311-1324.

118. Bouwkampwijnoltz, A.L., W. Visscher, and J.A.R. Vanveen, *OXYGEN REDUCTION CATALYZED BY CARBON-SUPPORTED IRIDIUM-CHELATES.* Electrochimica Acta, 1994. **39**(11-12): p. 1641-1645.

119. Andersson, K.J., et al., *Adsorption-Driven Surface Segregation of the Less Reactive Alloy Component.* Journal of the American Chemical Society, 2009. **131**(6): p. 2404-2407.

120. Knudsen, J., et al., *A Cu/Pt near-surface alloy for water-gas shift catalysis.* Journal of the American Chemical Society, 2007. **129**(20): p. 6485-6490.

121. Mavrikakis, M., B. Hammer, and J.K. Norskov, *Effect of strain on the reactivity of metal surfaces.* Physical Review Letters, 1998. **81**(13): p. 2819-2822.

122. Kitchin, J.R., et al., *Role of strain and ligand effects in the modification of the electronic and chemical properties of bimetallic surfaces.* Physical Review Letters, 2004. **93**(15).

123. Kitchin, J.R., et al., *Modification of the surface electronic and chemical properties of Pt(111) by subsurface 3d transition metals.* Journal of Chemical Physics, 2004. **120**(21): p. 10240-10246.

124. Mayrhofer, K.J.J., et al., *Adsorbate-Induced Surface Segregation for Core-Shell Nanocatalysts.* Angewandte Chemie-International Edition, 2009. **48**(19): p. 3529-3531.

125. Harrison, W.A., *Elementary Electronic Structure*. 1999, Singapore: World Scientific Publishing Co. Pte. Ltd. 817.

126. Norskov, J.K. and N.D. Lang, *EFFECTIVE-MEDIUM THEORY OF CHEMICAL-BINDING - APPLICATION TO CHEMISORPTION.* Physical Review B, 1980. **21**(6): p. 2131-2136.

127. *Dacapo Simulation Code*. Available from: https://wiki.fysik.dtu.dk/dacapo.

128. Vanderbilt, D., *SOFT SELF-CONSISTENT PSEUDOPOTENTIALS IN A GENERALIZED EIGENVALUE FORMALISM.* Physical Review B, 1990. **41**(11): p. 7892-7895.

129. Chadi, D.J. and M.L. Cohen, *SPECIAL POINTS IN BRILLOUIN ZONE.* Physical Review B, 1973. **8**(12): p. 5747-5753.

130. Besenbacher, F., et al., *Design of a surface alloy catalyst for steam reforming.* Science, 1998. **279**(5358): p. 1913-1915.

131. Chen, M.S., et al., *The promotional effect of gold in catalysis by palladium-gold.* Science, 2005. **310**(5746): p. 291-293.

132. Greeley, J., et al., *Computational high-throughput screening of electrocatalytic materials for hydrogen evolution.* Nature Materials, 2006. **5**(11): p. 909-913.

133. Jacobsen, C.J.H., et al., *Catalyst design by interpolation in the periodic table: Bimetallic ammonia synthesis catalysts.* Journal of the American Chemical Society, 2001. **123**(34): p. 8404-8405.

134. Sinfelt, J., *Bimetallic Cataysts: Discoveries, Concepts and Applications*. 1983, New York: John Wiley & Sons.

135. Studt, F., et al., *Identification of non-precious metal alloy catalysts for selective hydrogenation of acetylene.* Science, 2008. **320**(5881): p. 1320-1322.

136. Bagot, P.A.J., et al., *Automobile exhaust catalysis at the atomic scale: atom-probe investigations on platinum alloys.* Surface and Interface Analysis, 2007. **39**(2-3): p. 172-177.

137. Christoffersen, E., P. Stoltze, and J.K. Norskov, *Monte Carlo simulations of adsorption-induced segregation.* Surface Science, 2002. **505**(1-3): p. 200-214.

138. Hirsimaki, M., et al., *Investigation of the role of oxygen induced segregation of Cu during Cu2O formation on Cu{100}, Ag/Cu{100} and Cu(Ag) alloy.* Surface Science, 2005. **583**(2-3): p. 157-165.

139. Menning, C.A., H.H. Hwu, and J.G.G. Chen, *Experimental and theoretical investigation of the stability of Pt-3d-Pt(111) bimetallic surfaces under oxygen environment.* Journal of Physical Chemistry B, 2006. **110**(31): p. 15471-15477.

140. Nerlov, J. and I. Chorkendorff, *Methanol synthesis from CO2, CO, and H-2 over Cu(100) and Ni/Cu(100).* Journal of Catalysis, 1999. **181**(2): p. 271-279.

141. Nerlov, J., et al., *Methanol synthesis from CO2, CO and H-2 over Cu(100) and Cu(100) modified by Ni and Co.* Applied Catalysis a-General, 2000. **191**(1-2): p. 97-109.

142. Shu, J., et al., *SURFACE SEGREGATION OF PD-AG MEMBRANES UPON HYDROGEN PERMEATION.* Surface Science, 1993. **291**(1-2): p. 129-138.

143. Tao, F., et al., *Reaction-Driven Restructuring of Rh-Pd and Pt-Pd Core-Shell Nanoparticles.* Science, 2008. **322**(5903): p. 932-934.

144. Schumacher, N., et al., *Trends in low-temperature water-gas shift reactivity on transition metals.* Journal of Catalysis, 2005. **229**(2): p. 265-275.

145. Gonzalez, S. and F. Illas, *CO adsorption on monometallic Pd, Rh, Cu and bimetallic PdCu and RhCu monolayers supported on Ru(0001).* Surface Science, 2005. **598**(1-3): p. 144-155.

146. Hager, T., H. Rauscher, and R.J. Behm, *Interaction of CO with PdCu surface alloys supported on Ru(0001).* Surface Science, 2004. **558**(1-3): p. 181-194.

147. Inderwildi, O.R., S.J. Jenkins, and D.A. King, *When adding an unreactive metal enhances catalytic activity: NOx decomposition over silver-rhodium bimetallic surfaces.* Surface Science, 2007. **601**(17): p. L103-L108.

148. Sakong, S., C. Mosch, and A. Gross, *CO adsorption on Cu-Pd alloy surfaces: ligand versus ensemble effects.* Physical Chemistry Chemical Physics, 2007. **9**(18): p. 2216-2225.

149. Schumacher, N., et al., *Interaction of carbon dioxide with Cu overlayers on Pt(111).* Surface Science, 2008. **602**(3): p. 702-711.

150. Xin, H.L. and S. Linic, *Communications: Exceptions to the d-band model of chemisorption on metal surfaces: The dominant role of repulsion between adsorbate states and metal d-states.* Journal of Chemical Physics, 2010. **132**(22).

151. Watson, R.E., L.H. Bennett, and D.A. Goodman, *A D-BAND BONDING THEORY OF THE RELATIVE HEATS OF SOLUTION OF TRANSITION-METAL ALLOYS AND ITS RELATIONSHIP TO SOLUBILITY LIMITS.* Acta Metallurgica, 1983. **31**(8): p. 1285-1291.

152. Yokokawa, H., et al., *CHEMICAL-POTENTIAL DIAGRAMS FOR RARE-EARTH TRANSITION-METAL OXYGEN SYSTEMS - I, LN-V-O AND LN-MN-O SYSTEMS.* Journal of the American Ceramic Society, 1990. **73**(3): p. 649-658.

153. Dzhaoshvili, K.R., et al., *THERMODYNAMIC PROPERTIES OF DYSPROSIUM AND HOLMIUM.* Zhurnal Fizicheskoi Khimii, 1991. **65**(2): p. 560-563.

154. Jacob, K.T. and M. Attaluri, *Refinement of thermodynamic data for LaMnO3.* Journal of Materials Chemistry, 2003. **13**(4): p. 934-942.

155. Parida, S.C., et al., *Thermodynamic studies on LaFeO3(s).* Journal of Alloys and Compounds, 1998. **280**(1-2): p. 94-98.

156. Yokokawa, H., et al., *THERMODYNAMIC ANALYSIS OF REACTION PROFILES BETWEEN LAMO3 (M=NI,CO,MN) AND ZRO2.* Journal of the Electrochemical Society, 1991. **138**(9): p. 2719-2727.

157. Yokokawa, H., et al., *THERMODYNAMIC STABILITY OF PEROVSKITES AND RELATED-COMPOUNDS IN SOME ALKALINE-EARTH TRANSITION-METAL OXYGEN SYSTEMS.* Journal of Solid State Chemistry, 1991. **94**(1): p. 106-120.

158. Yokokawa, H., et al., *CHEMICAL THERMODYNAMIC CONSIDERATIONS IN SINTERING OF LACRO3-BASED PEROVSKITES.* Journal of the Electrochemical Society, 1991. **138**(4): p. 1018-1027.

159. Yokokawa, H., et al., *CHEMICAL THERMODYNAMIC CONSIDERATIONS ON CHEMICAL-STABILITY OF (LA1-XSRX)YMNO3 PEROVSKITE AIR ELECTRODE AGAINST REACTION WITH ZRO2 ELECTROLYTE IN SOFC.* Denki Kagaku, 1990. **58**(2): p. 162-171.

160. Chang-Zhen, W., Y. Shu-Ging, and Z. Xin, Acta Physica Sinica, 1985. **34**: p. 1017.

161. Atsumi, T. and N. Kamegashira, *Decomposition oxygen partial pressures of Ln(1-x)Sr(x)MnO(3) (Ln=La, Nd and Dy).* Journal of Alloys and Compounds, 1997. **257**(1-2): p. 161-167.

162. Atsumi, T., T. Ohgushi, and N. Kamegashira, *Studies on oxygen dissociation pressure of LnMnO(3) (Ln equals rare earth) with the emf technique.* Journal of Alloys and Compounds, 1996. **238**(1-2): p. 35-40.

163. Sreedharan, O.M. and M.S. Chandrasekharaiah, *STANDARD GIBBS ENERGY OF FORMATION OF LAFEO3 AND COMPARISON OF STABILITY OF LAMNO3 LAFEO3*

LACOO3 OR LANIO3 COMPOUNDS. Journal of Materials Science, 1986. **21**(7): p. 2581-2584.

164. Nakamura, T., G. Petzow, and L.J. Gauckler, *Stability of the perovskite phase LaBO3 (B = V, Cr, Mn, Fe, Co, Ni) in reducing atmosphere I. Experimental results.* Materials Research Bulletin, 1979. **14**(5): p. 649-659.

165. Grundy, A.N., B. Hallstedt, and L.J. Gauckler, *Assessment of the Sr-Mn-O system.* Journal of Phase Equilibria and Diffusion, 2004. **25**(4): p. 311-319.

166. Dicarlo, J., et al., *PREPARATION AND THERMOCHEMICAL PROPERTIES OF BANIO2+X.* Journal of Solid State Chemistry, 1994. **109**(2): p. 223-226.

167. Chen, S., et al., *Determination of the Standard Free Energy of Formation of LaCrO3 at 1273K.* Zhongguo Xitu Xuebao, 1987. **5**(3): p. 19.

168. Tanasescu, S., N.D. Totir, and D.I. Marchidan, *Thermodynamic properties of LaFeO3 studied by means of galvanic cells with solid oxide electrolyte.* Materials Research Bulletin, 1997. **32**(7): p. 925-931.

169. Laberty, C., et al., *Energetics of rare earth manganese perovskites A1-xA ' xMnO3 (A = La, Nd, Y and A ' = Sr, La) systems.* Journal of Solid State Chemistry, 1999. **145**(1): p. 77-87.

170. Yokokawa, H., et al., *THERMODYNAMIC STABILITIES OF PEROVSKITE OXIDES FOR ELECTRODES AND OTHER ELECTROCHEMICAL MATERIALS.* Solid State Ionics, 1992. **52**(1-3): p. 43-56.

171. Grundy, A.N., B. Hallstedt, and L.J. Gauckler, *Assessment of the Mn-O system.* Journal of Phase Equilibria, 2003. **24**(1): p. 21-39.

172. Risold, D., B. Hallstedt, and L.J. Gauckler, *The strontium-oxygen system.* Calphad-Computer Coupling of Phase Diagrams and Thermochemistry, 1996. **20**(3): p. 353-361.

173. Kojitani, H., A. Navrotsky, and M. Akaogi, *Calorimetric study of perovskite solid solutions in the CaSiO3-CaGeO3 system.* Physics and Chemistry of Minerals, 2001. **28**(6): p. 413-420.

174. Rormark, L., et al., *Enthalpies of oxidation of CaMnO3-delta, Ca2MnO4-delta and SrMnO3-delta - Deduced redox properties.* Chemistry of Materials, 2001. **13**(11): p. 4005-4013.

175. Chase, M.W., et al., *JANAF THERMOCHEMICAL TABLES - 3RD EDITION .1. AL-CO.* Journal of Physical and Chemical Reference Data, 1985. **14**: p. 1-926.

LIST OF INCLUDED ARTICLES

1) ***Trends in Stability of Perovskite Oxides.*** Calle-Vallejo, F., Martinez, J.I., Garcia-Lastra, J.M., Mogensen, M., Rossmeisl, J. Angewandte Chemie-International Edition 2010, 49, 7699.

2) ***Trends in Metal Oxide Stability for Nanorods, Nanotubes, and Surfaces*****.** Mowbray, D.J., Martínez, J.I., Calle-Vallejo, F., Rossmeisl, J., Thygesen, K.S., Jacobsen, K.W., and Nørskov, J.K. The Journal of Physical Chemistry C. DOI: 10.1021/jp110489u.

3) ***Universality in Oxygen Evolution Electro-Catalysis on Oxide Surfaces.*** Man, I.C., Su, H.Y., Calle-Vallejo, F., Hansen, H.A., Martínez, J.I., Inoglu, N.G., Kitchin, J., Jaramillo, T.F., Nørskov, J.K., and Rossmeisl, J. ChemCatChem. Accepted.

4) ***Probing the Reactivity of Transition-Metal Oxides using Density Functional Theory: Transition State Scaling Relations.*** Vojvodic, A., Calle-Vallejo, F., Abild-Pedersen, F., Guo, W., Wang, S., Toftelund, A., Studt, F., Martínez, J.I., Shen, J., Man, I.C., Rossmeisl, J., Bligaard, T., and Nørskov, J.K. In preparation.

5) ***Adsorption-Driven Surface Segregation of the Less Reactive Alloy Component.*** Andersson, K.J., Calle-Vallejo, F., Rossmeisl, J., and Chorkendorff, Ib, Journal of the American Chemical Society, 2009. 131(6): p. 2404-2407.

6) ***Tuning the activity of Pt(111) for oxygen electroreduction by subsurface alloying.*** Stephens, I.E.L., Bondarenko, A.S., Perez-Alonso, F.J., Calle-Vallejo, F., Bech, L., Johansson, T.P., Jepsen, A.K., Frydendal, R., Knudsen, B.P., Rossmeisl, J., and Chorkendorff, Ib. Submitted.

Perovskite Phases

DOI: 10.1002/anie.201002301

Trends in Stability of Perovskite Oxides**

*Federico Calle-Vallejo, José I. Martínez, Juan M. García-Lastra, Mogens Mogensen, and Jan Rossmeisl**

Perovskite oxides with general formula AMO_3 have a large variety of applications as dielectrics and piezoelectrics,[1] ferroelectrics[2] and/or ferromagnetic materials,[3] among others. Rare earth and alkaline earth metal perovskites are useful as catalysts for hydrogen generation,[4] as oxidation catalysts for hydrocarbons,[5] and as effective and inexpensive electrocatalysts for state-of-the-art fuel cells,[6] mainly due to the possibility of tuning their mixed ionic–electronic conductivity through substitution of A and M and subsequent formation of oxygen vacancies. Despite the general interest in perovskites, so far there have been no ab initio studies devoted to their formation energies, and the trends in stability are unknown.

Among the available theoretical techniques to investigate perovskites, DFT is an appealing candidate, since it has proved useful for understanding metals and alloys at the atomic scale.[7] Nevertheless, the well-known shortcoming of DFT in describing strongly correlated systems has prevented its use for the estimation of properties such as band gaps and electron localization–delocalization of oxides, and there are numerous corrections.[8]

Despite these limitations, Figure 1a shows the experimental formation energies from elements and O_2 of 20 perovskites at 298 K and the corresponding standard DFT energies using the RPBE-GGA[9] exchange-correlation functional. The simulations are able to reproduce trends in the formation energies, and the calculated energies are shifted by about 0.75 eV compared to experiments. The A component is Y, La, Ca, Sr, or Ba, while M is a 3d metal from Ti to Cu. However, it is possible to combine the formation energies of these compounds with those of their sesquioxides (A_2O_3 and M_2O_3), rutile dioxides (MO_2), monoxides (AO and MO), and O_2 to reproduce the energetics of several reactions (Figure 1b–d). The reactions are shown in the Supporting Information. The excellent correspondence between experiments and theory shows that DFT very accurately captures the mixing energies between oxides. The chemical reaction depicted in Figure 1a and the way of representing its Gibbs energy, are given by Equations (1) and (2).

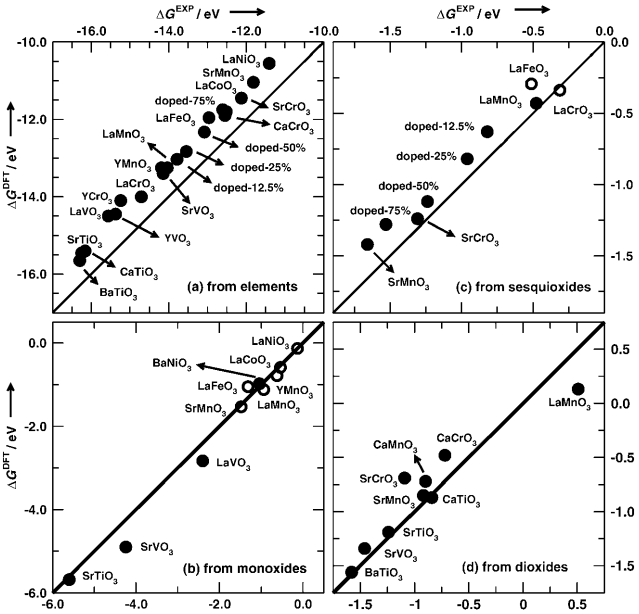

Figure 1. DFT calculated free energies of several reactions versus experimental values available in the literature, from a) A = Y, La, Ca, Sr, Ba and elements, b) A_2O_3/AO and monoxides, c) A_2O_3/AO and sesquioxides, and d) A_2O_3/AO and dioxides. As a guide to the eye, perfect agreement is marked by a line with $y = x$. The percentages of the doped perovskites represent the amount x of Sr in $La_{1-x}Sr_xMnO_3$. Reactions at 298 K are represented by filled circles, whereas empty circles denote reactions at 1273 K. References for the experiments are provided in the Supporting Information.

$$A + M + {}^3/_2O_2 \rightarrow AMO_3 \quad (1)$$

$$\Delta G^{form} = G_{AMO_3} - G_A - G_M - {}^3/_2G_{O_2} \quad (2)$$

In terms of trends the agreement is beyond the expected accuracy of DFT in general, but the shift is about 0.75 eV. We note that imitations in O_2 description by DFT are well known and some alternatives have been proposed, obtaining remarkable agreements with experiments.[8c,10] We obtain the total DFT energy of O_2 indirectly from the tabulated Gibbs energy of formation of water and from the DFT energies of H_2

[*] F. Calle-Vallejo, Dr. J. I. Martínez, Dr. J. M. García-Lastra, Prof. J. Rossmeisl
Center for Atomic-Scale Materials Design
Department of Physics, Technical University of Denmark
2800 Kgs. Lyngby (Denmark)
Fax: (+45) 4593-2399
E-mail: jross@fysik.dtu.dk
Prof. M. Mogensen
Fuel Cells and Solid State Chemistry Department
Risoe National Laboratory for Sustainable Energy, DTU
Frederiksborgvej 399, 4000 Roskilde (Denmark)

[**] CAMD is funded by the Lundbeck foundation. We acknowledge support by the Danish Council for Strategic Research via the SERC project, the DCSC, and the STREP-EU APOLLON-B project through grant nos. 2104-06-0011, HDW-1103-06, and NMP3-CT-2006-033228, respectively. We thank Prof. F. Flores and Prof. H. Yokokawa for their comments.

Supporting information for this article is available on the WWW under http://dx.doi.org/10.1002/anie.201002301.

and H_2O, which are accurately described using the exchange achieved by the RPBE-GGA functional.[8c,11] This reference has previously been used to obtain accurate formation energies of rutile oxides and has also been applied to calculate the adsorption energies of various oxides, including perovskites.[10,12] The reason of the shift is therefore not related to the reference state. We speculate that the localized nature of d electrons of the 3d metals in these perovskites is not well captured at this level of theory due to their self-interaction, giving rise to a large part of the constant shift in Figure 1 a. The rest of the shift comes from the deviations in the formation of the A oxides (A_2O_3 and/or AO). Nevertheless, the differences in formation energies between perovskites are very accurately accounted for by standard DFT, as shown in Figure 2. We remark that the use of another

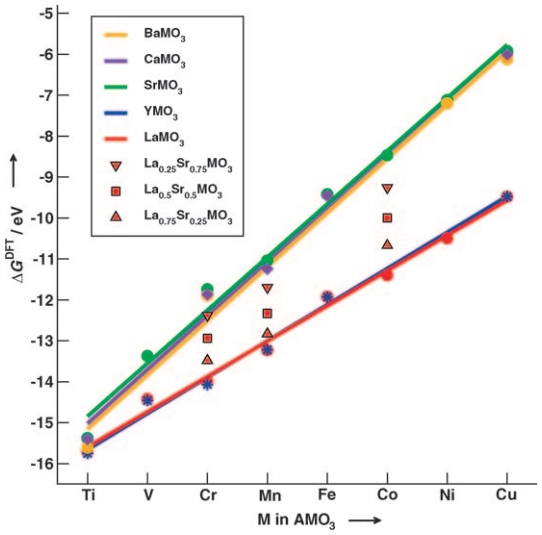

Figure 2. Trends in formation energies from elements for various families of perovskites (AMO_3), in terms of the atomic number of M. Symbols indicate calculated values for individual perovskites, and lines show the best fit for each family. Perovskites having the same oxidation state for A and M (+III, A = Y, La) are more stable than those in which they are different (+II and +IV, A = Ca, Sr, Ba), and their decay in stability is less pronounced. The positions of $La_{1-x}Sr_xMO_3$ perovskites, indicated by ▼, ■, ▲, support the idea that the effect is due to the oxidation states of the constituents. Note that stability with respect to the elements does not guarantee overall stability of the compounds.

exchange-correlation functional or a different value for O_2 would only shift the calculated stabilities by a constant number, while the qualitative trends and the relative differences would remain unchanged.

All families of perovskites exhibit a systematic linear scaling between their energetics and the atomic number of M. The scaling in Figure 2 was previously revealed by experiments only for some La perovskites at 1273 K.[13] We extend this behavior to other families of perovskites, and the insight allows the following generalization: the slope of the lines is determined by the oxidation states of A and M. Therefore, these compounds could be divided into two groups: perovskites with the same oxidation state for A and M (+III for $A'MO_3$; A′ = Y, La), and perovskites in which their oxidation states differ (+II and +IV for $A''MO_3$; A″ = Ca, Sr, and Ba). The former are more stable than the latter and their stabilities along the 3d series decrease more slowly, that is, their lines have less steep slopes. This could be attributed to the higher oxidation state forced onto M in $A''MO_3$ (a further discussion on this aspect is provided in the Supporting Information). The formation energies of perovskites in each group are approximately constant for materials with the same M constituent, independent of A. For example, the energetics of $SrCrO_3$ gives a good estimative of those of $CaCrO_3$ and $BaCrO_3$. Doped perovskites ($A'A''MO_3$) have intermediate formation energies between those of the pure counterparts, in accordance to the degree of doping. This behavior supports the idea that the difference between the groups is a matter of oxidation states. The use of simple parameters like the atomic numbers to estimate the formation energies of perovskites is easier and more intuitive than the common use of structural parameters such as the Goldschmidt factor or the Shannon's radii.[14]

Finally, let us explain the origin of the differences in stability of $A'MO_3$ by means of Figure 3. An expression similar to Equation (2) represents the formation energies of

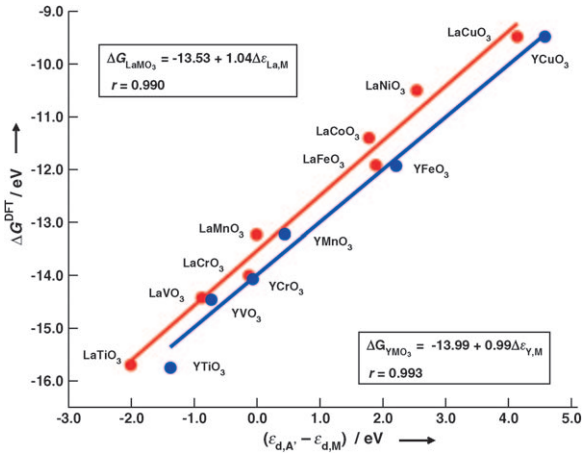

Figure 3. DFT-calculated free energies of formation of $LaMO_3$ (red) and YMO_3 (blue) versus the differences in d-band centers of La/Y and M. The intercept with the *y* axis is equivalent to the formation energy of the sesquioxides A'_2O_3 (A′ = Y, La) plus the deformation energy of these oxides from their most stable symmetries to space group *Pm*3*m*. Therefore, formation of these perovskites can be seen as destabilizations of the A'_2O_3 oxides by M/A′ swapping.

La_2O_3 and Y_2O_3 from the elements. By adding and subtracting $G_{A'}$ to and from Equation (2) and combining with the formation energy of the sesquioxides, one gets Equation (3).

$$\Delta G^{\text{form}} = \Delta G_{A'_2O_3} - \left(G_M + G_{A'_2O_3} - G_{A'MO_3} - G_{A'}\right) \quad (3)$$

The term in parentheses in Equation (3) corresponds to a reaction step in which A′ in an A'_2O_3 lattice is replaced by M to form the perovskite structure. Thus, the reaction could be seen as the formation of A'_2O_3 followed by a lattice deformation and swapping between atoms resulting in

$A'MO_3$. The formation energy can then be expressed as Equation (4).

$$\Delta G^{\text{form}} = \Delta G_{A'_2O_3} + \Delta G_{\text{deformation}} + \Delta G_{\text{swap}} \quad (4)$$

The DFT formation energies of La_2O_3 and Y_2O_3 are -16.98 and -17.85 eV, respectively (-17.70[15] and -18.79 eV,[16] experimentally). The deformation energy is approximately 3.3 eV for La_2O_3, calculated as the energy difference of this oxide in the space groups *P3m*1 and *Pm3m* with a perovskite lattice constant of 3.97 Å. This difference is approximately 4.1 eV for Y_2O_3, calculated as the change from space group *Ia*3 to *Pm3m* with a lattice constant of 3.88 Å. Additionally, the interchange between A' and d-block metal atoms implies breaking and creation of bonds, so the swapping energy can be estimated as the difference in the d-band centers ε_d of these atoms. This turns Equation (4) into Equation (5)

$$\Delta G^{\text{form}} = \gamma_{A'_2O_3} + (\varepsilon_{d,A'} - \varepsilon_{d,M}) \quad (5)$$

where $\gamma_{A'_2O_3}$ is a constant that collects the formation energy of the sesquioxide and its deformation and is around -13.6 eV for La_2O_3 and -13.7 eV for Y_2O_3. This constant can be regarded as an intrinsic stability conferred on $A'MO_3$ by its A′ component. As a result, the differences in energies among these perovskites can be attributed to the relative ease of swapping atoms, whereby Ti is the easiest and Cu the hardest along the 3d metal series.

Furthermore, our model is also in agreement with the works by Gelatt et al.[17] devoted to the theory of bonding between transition metals and nontransition elements, and uses the d-band centers of transition metals as key descriptors for understanding the properties of their compounds as in the model by Hammer and Norskov[18] developed for adsorption energies.

In conclusion, DFT gives sufficient atomic-scale insight into perovskites to study their formation energies, both qualitatively and quantitatively, except for a constant shift, and important trends are found. The analysis shown here could be extended to perovskites with 4d and 5d constituents, to perovskites containing alkaline earth elements, and to $ScMO_3$. The combination of the energetics of several reactions and their variations with pH and applied potential can give rise to Pourbaix diagrams for perovskites, which are not yet available in the literature. This and other stability considerations are of paramount importance in any application, especially if perovskites are to be used in alkaline or proton-exchange membrane fuel cells.

Methods

The DFT calculations were performed with the plane wave code DACAPO,[9] using the RPBE exchange-correlation functional, a converged plane wave cutoff of 400 eV and a density cutoff of 500 eV. DACAPO uses ultrasoft pseudopotentials to represent the ion-electron interaction. Atomic relaxations were done with the quasi-Newton minimization scheme until a maximum force below 0.05 eV Å^{-1} between atoms was reached. Besides, we optimized the lattice vectors by minimizing the strain on $2\times2\times2$ supercells in all periodically repeated directions. The Brillouin zone of all systems was sampled with Monkhorst–Pack grids, guaranteeing in all cases that the product of the supercell dimensions and the k-points was at least 25 Å in all directions. The self-consistent RPBE density was determined by iterative diagonalization of the Kohn–Sham Hamiltonian at $k_B T = 0.1$ eV, using Pulay mixing of densities, and all total energies were extrapolated to $k_B T = 0$ eV. Spin-polarized calculations were carried out when needed. See the Supporting Information for further details.

Received: April 19, 2010
Revised: July 15, 2010
Published online: ■■ ■■, 2010

Keywords: density functional calculations · heats of formation · perovskite phases · thermochemistry

[1] G. L. Messing, S. Trolier-McKinstry, E. M. Sabolsky, C. Duran, S. Kwon, B. Brahmaroutu, P. Park, H. Yilmaz, P. W. Rehrig, K. B. Eitel, E. Suvaci, M. Seabaugh, K. S. Oh, *Crit. Rev. Solid State Mater. Sci.* **2004**, *29*, 45.
[2] C. H. Ahn, K. M. Rabe, J. M. Triscone, *Science* **2004**, *303*, 488.
[3] a) S. W. Cheong, M. Mostovoy, *Nat. Mater.* **2007**, *6*, 13; b) J. M. DeTeresa, M. R. Ibarra, P. A. Algarabel, C. Ritter, C. Marquina, J. Blasco, J. Garcia, A. delMoral, Z. Arnold, *Nature* **1997**, *386*, 256.
[4] J. R. Mawdsley, T. R. Krause, *Appl. Catal. A* **2008**, *334*, 311.
[5] T. Nitadori, T. Ichiki, M. Misono, *Bull. Chem. Soc. Jpn.* **1988**, *61*, 621.
[6] a) Y. H. Huang, R. I. Dass, Z. L. Xing, J. B. Goodenough, *Science* **2006**, *312*, 254; b) D. Thiele, A. Zuttel, *J. Power Sources* **2008**, *183*, 590.
[7] a) J. K. Nørskov, T. Bligaard, J. Rossmeisl, C. H. Christensen, *Nat. Chem.* **2009**, *1*, 37; b) J. Greeley, I. E. L. Stephens, A. S. Bondarenko, T. P. Johansson, H. A. Hansen, T. F. Jaramillo, J. Rossmeisl, I. Chorkendorff, J. K. Norskov, *Nat. Chem.* **2009**, *1*, 552; c) F. Studt, F. Abild-Pedersen, T. Bligaard, R. Z. Sorensen, C. H. Christensen, J. K. Norskov, *Angew. Chem.* **2008**, *120*, 9439; *Angew. Chem. Int. Ed.* **2008**, *47*, 9299.
[8] a) G. Pacchioni, *J. Chem. Phys.* **2008**, *128*, 182505; b) M. van Schilfgaarde, T. Kotani, S. Faleev, *Phys. Rev. Lett.* **2006**, *96*, 226402; c) L. Wang, T. Maxisch, G. Ceder, *Phys. Rev. B* **2006**, *73*, 195107.
[9] B. Hammer, L. B. Hansen, J. K. Norskov, *Phys. Rev. B* **1999**, *59*, 7413.
[10] J. I. Martínez, H. A. Hansen, J. Rossmeisl, J. K. Norskov, *Phys. Rev. B* **2009**, *79*, 045120.
[11] S. Kurth, J. P. Perdew, P. Blaha, *Int. J. Quantum Chem.* **1999**, *75*, 889.
[12] E. M. Fernández, P. G. Moses, A. Toftelund, H. A. Hansen, J. I. Martinez, F. Abild-Pedersen, J. Kleis, B. Hinnemann, J. Rossmeisl, T. Bligaard, J. K. Norskov, *Angew. Chem.* **2008**, *120*, 4761; *Angew. Chem. Int. Ed.* **2008**, *47*, 4683.
[13] R. Pankajavalli, O. M. Sreedharan, *Mater. Lett.* **1995**, *24*, 247.
[14] a) J. H. Cheng, A. Navrotsky, X. D. Zhou, H. U. Anderson, *J. Mater. Res.* **2005**, *20*, 191; b) H. Yokokawa, *Annu. Rev. Mater. Res.* **2003**, *33*, 581.
[15] A. N. Grundy, B. Hallstedt, L. J. Gauckler, *J. Phase Equilib.* **2001**, *22*, 105.
[16] M. Binnewies, E. Milke, *Thermochemical Data of Elements and Compounds*, 2nd ed., Wiley-VCH, Weinheim, **2002**.
[17] C. D. Gelatt, A. R. Williams, V. L. Moruzzi, *Phys. Rev. B* **1983**, *27*, 2005.
[18] B. Hammer, J. K. Nørskov in *Advances in Catalysis*, *Vol. 45* (Eds.: C. G. Bruce, K. Helmut), Academic Press, New York, **2000**, p. 71.

Communications

Perovskite Phases

F. Calle-Vallejo, J. I. Martínez,
J. M. García-Lastra, M. Mogensen,
J. Rossmeisl* _____ ■■■■–■■■■

Trends in Stability of Perovskite Oxides

$$A_{(s)} + M_{(s)} + \frac{3}{2} O_{2(g)} \rightarrow AMO_{3(s)}$$

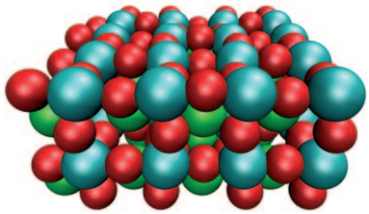

Trends in formation energies ΔG^{form}_{exptl} of 41 perovskites AMO_3 at 298 K are reproduced by ΔG^{form}_{DFT} from DFT calculations with the RPBE-GGA functional (see picture; A green, M blue, O red). Moreover, the calculations rationalize systematic trends in their properties, reveal a direct connection between composition and stability in perovskites, and open up a path to ab initio constructions of complete phase diagrams.

THE JOURNAL OF PHYSICAL CHEMISTRY C

ARTICLE

pubs.acs.org/JPCC

Trends in Metal Oxide Stability for Nanorods, Nanotubes, and Surfaces

D. J. Mowbray,*[,†,‡] J. I. Martínez,[†,§] F. Calle-Vallejo,[†] J. Rossmeisl,[†] K. S. Thygesen,[†] K. W. Jacobsen,[†] and J. K. Nørskov[†]

[†]Center for Atomic-scale Materials Design, Department of Physics, Technical University of Denmark, DK-2800 Kongens Lyngby, Denmark

[‡]Nano-Bio Spectroscopy Group and ETSF Scientific Development Centre, Departamento de Física Materiales, Universidad del País Vasco and DIPC, E-20018 San Sebastián, Spain

[§]Departamento de Física Teórica de la Materia Condensada, Universidad Autónoma de Madrid, E-28049 Madrid, Spain

ABSTRACT: The formation energies of nanostructures play an important role in determining their properties, including their catalytic activity. For the case of 15 different rutile and 8 different perovskite metal oxides, we used density functional theory (DFT) to calculate the formation energies of (2,2) nanorods, (3,3) nanotubes, and the (110) and (100) surfaces. These formation energies can be described semiquantitatively (mean absolute error ≈ 0.12 eV) by the fraction of metal−oxygen bonds broken and the metal d-band and p-band centers in the bulk metal oxide.

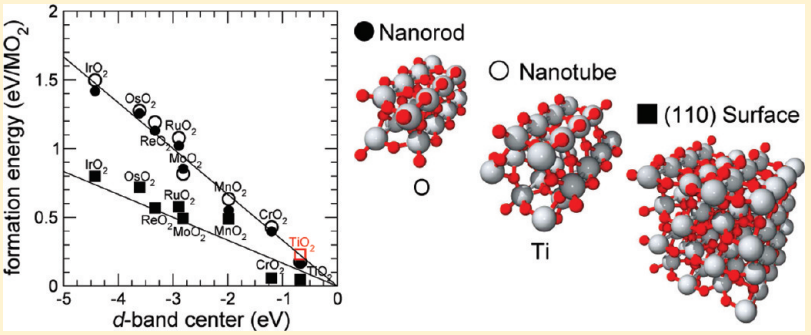

1. INTRODUCTION

The search for cleaner and more sustainable forms of energy provides a strong impetus to the development of more affordable, active, selective, and stable new catalysts to convert solar radiation into fuels.[1,2] Just as the Haber−Bosch process fueled the population explosion of the 20th century,[3,4] it is now hoped that new catalytic processes will provide sustainable energy in the 21st century.[1,2]

Near the top of any list of candidate catalytic materials are metal oxides, which are already used extensively as catalysts, electrocatalysts, and photoelectrocatalysts.[5−17] This is partly owing to their high stability in harsh oxidizing environments compared to that of their pure metal counterparts.

Typically, oxide catalysts are in the form of nanoparticles or highly porous materials. The structure of these oxide nanoparticles can be determined by the surface energy. For instance, for TiO_2, it has recently been shown that it is the surface energies that determine whether it takes the anatase or rutile structure at the nanoscale.[18,19] The catalytic properties of these materials are determined to a high degree by the surface,[20] and control of the surface structure will allow control of the reactivity.[21−24]

This makes the surface and nanostructure formation energy, ΔE_f, which is defined as the total energy difference from the bulk metal oxide per functional unit (MO_2 or $SrMO_3$) of the surface or nanostructure, a quantity of interest. More precisely

$$\Delta E_f \equiv (E - E^{Bulk})/N_f \qquad (1)$$

where E is the total energy of the surface or nanostructure, E^{Bulk} is the total energy of the bulk metal oxide, and N_f is the number of functional units (MO_2 or $SrMO_3$) of the surface or nanostructure. However, formation energies of metal oxide surfaces are difficult to measure experimentally, and only a few values are available in the literature[18,19] For these reasons, finding trends in surface and nanostructure formation energies is an essential first step in understanding the properties of oxide catalysts and the eventual design of novel catalytic materials.

In this study, we provide DFT-calculated (2,2) nanorod, (3,3) nanotube, and (110) surface formation energies for 15 different rutile metal oxides, along with the (100) surface formation energies for 8 different perovskite metal oxides.[21] Both the (2,2) nanorod and (3,3) nanotube structures were obtained by first rolling up a sheet of the material in the PtO_2 structure. However, because of its small diameter, the (2,2) nanorod has a bonding structure resembling that of the bulk metal oxide after relaxation, as shown in Figure 1. For TiO_2 and RuO_2, these structures are quite stable, based on both molecular dynamic simulations[25] and calculated energies relative to other stable forms.[21]

However, serious questions have been raised as to whether standard DFT calculations can describe metal oxides with sufficient accuracy. For the purposes of the present study, it is worth noting that DFT calculations have recently been shown to semiquantitatively reproduce the bulk heats of formation for both rutile[26] and perovskite[27] metal oxides.

Received: November 2, 2010
Revised: December 2, 2010

dx.doi.org/10.1021/jp110489u | J. Phys. Chem. C XXXX, XXX, 000–000

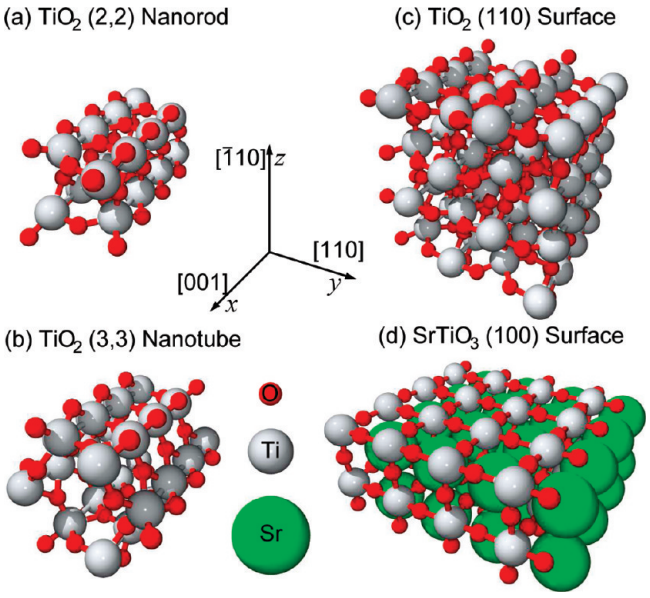

Figure 1. Structural schematics for (a) TiO_2 (2,2) nanorod, (b) TiO_2 (3,3) nanotube, (c) TiO_2 (110) surface, and (d) $SrTiO_3$ (100) TiO_2- and SrO-terminated surfaces. Axes and Miller indices for the rutile structures are shown for a and c.

After describing our methodology for calculating formation energies in section 2, we develop a simple model to describe these energies semiquantitatively in section 3 based on the fraction of metal−oxygen bonds broken and the metal d-band and p-band centers in the bulk metal oxide. Our concluding remarks are followed by a tabulation of all calculated quantities and further comparisons of the bulk heats of formation, d-band centers, numbers of d electrons, cohesive energies, and formation energies for the rutile metal oxides in Appendix A and a detailed analysis of metal−oxide bond strengths based on the bulk metal oxide molecular orbitals in Appendix B.

2. METHODOLOGY

All DFT calculations were performed with the plane-wave code DACAPO using the RPBE exchange-correlation (xc) functional;[28,29] converged plane-wave cutoffs of 350 and 400 eV for rutile and perovskite metal oxides, respectively; and a density cutoff of 500 eV. The occupation of the Kohn−Sham orbitals was calculated at $k_BT \approx 0.1$ eV, with all energies extrapolated to $T = 0$ K. The product of the supercell dimensions and the number of k points[30] is ≳25 Å in all repeated directions. For the antisymmetric perovskite surface slab calculations, a dipole correction was employed.[31] All bulk calculations used a sufficient number of bands (25 per MO_2 and 34−39 per $SrMO_3$) to ensure convergence of the d-band and p-band centers, as shown in Figure 5 of Appendix A for the rutile metal oxides.

We performed structural relaxations until a maximum force below 0.05 eV/Å was obtained. At the same time, we minimized the strain on the unit cell in all periodically repeated directions and employed more than 10 Å of vacuum between repeated nanorods, nanotubes, and surface slabs.

For CrO_2 and MnO_2 rutile metal oxides and for all perovskites considered, we performed spin-polarized calculations. However, the relaxed structures of $SrTiO_3$ and $SrVO_3$ had no magnetic moment. These results are summarized in Tables 1 and 2 of Appendix A.

3. RESULTS AND DISCUSSION

Schematics of the TiO_2 (2,2) nanorod, (3,3) nanotube, and (110) surface, along with the $SrTiO_3$ (100) TiO_2- and SrO-terminated surfaces,[32] are shown in Figure 1. The supercells used were repeated four times along the nanorod and nanotube axes in Figure 1a,b and four times in the surface plane for the surfaces shown in Figure 1c,d.

For the TiO_2 (110) surface, our 4-layer-thick slab yielded surface formation energies of 0.44 J/m^2, as also reported in ref 18, and in reasonable agreement with the GGA[33] 12-layer-thick slab value of 0.50 J/m^2 from ref 18 and the B3LYP[34] 9-layer-thick slab value of 0.67 J/m^2 from ref 35. Differences among these values are attributable to the choices of xc functional and number of layers, especially for uneven slab calculations, which tend to yield higher energies and converge more slowly.[18] As expected, these values are below the experimental nanoparticle surface energy of 2.2 ± 0.2 J/m^2 for TiO_2[19] (see Figure 2), because of the presence of less stable kinked and stepped surfaces in the sample.

The formation energies of the (2,2) nanorod, (3,3) nanotube, and (110) surface depicted in Figure 1 are shown in Figure 2. In the following discussion, we analyze the nature of the formation energies and relate them to other characteristics of the materials. One possible descriptor for the (110) metal oxide surface formation energy, $\Delta E_f^{(110)}$, might be the bulk heat of formation, ΔG_f^{Bulk}, which is defined as the difference in free energy from the clean metal and water relative to H_2. In other words

$$\Delta G_f^{Bulk} \equiv G^{MO_2} - G^M - 2(G^{H_2O} - G^{H_2}) \quad (2)$$

where G^{MO_2}, G^M, G^{H_2O}, and G^{H_2} are the free energies for the metal oxide, clean metal, water, and hydrogen, respectively. With this definition, ΔG_f^{Bulk} is a measure of the metal oxide stability for catalytic reactions in aqueous solution, as discussed in Appendix A.

Although ΔG_f^{Bulk} and $\Delta E_f^{(110)}$ are somewhat correlated, as shown in Figure 2a, this correlation is rather counterintuitive. One might expect that more stable compounds would have stronger bonds and, hence, higher surface formation energies, but Figure 2a shows that the opposite is the case. This makes ΔG_f^{Bulk} a poor choice of descriptor for the (110) surface formation energy.

On the other hand, we observe a stronger correlation between $\Delta E_f^{(110)}$ and the d-band center ε_d for the bulk rutile metal oxides, as shown in Figure 2b. Here, ε_d is the average energy, relative to the Fermi level, ε_F, of the density of states (DOS) projected onto the metal's atomic d-orbitals in the metal oxide $n_d(\varepsilon)$, so that[36]

$$\varepsilon_d \equiv \int (\varepsilon - \varepsilon_F) n_d(\varepsilon)\, d\varepsilon \quad (3)$$

For the nanorod and nanotube formation energies, we also found a qualitative correlation with ΔG_f^{Bulk}, but a near-quantitative correlation with ε_d.

This suggests that metal oxide surface and nanostructure formation energies can be considered perturbations of the bulk metal oxide's electronic structure, which is described by ε_d, due to bond breaking. In this case

$$\Delta E_f \approx \Delta\chi \varepsilon_{M-O} \quad (4)$$

where $\Delta\chi$ is the fraction of metal−oxygen (M−O) bonds broken and ε_{M-O} is the energy stored in M−O bonds, per functional unit of the surface or nanostructure. For the case of (110) surface formation, $\Delta\chi^{(110)} \approx 1/6$ per MO_2, whereas for nanorod and nanotube formation, $\Delta\chi^{NT} \approx 2/6 \approx 1/3$ per MO_2.

dx.doi.org/10.1021/jp110489u |J. Phys. Chem. C XXXX, XXX, 000–000

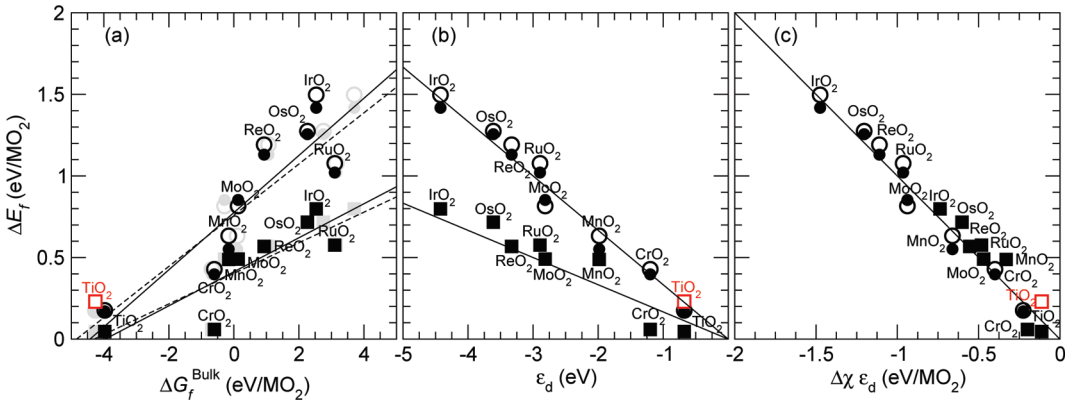

Figure 2. Formation energy, ΔE_f, of rutile metal oxide (●) (2,2) nanorods, (○) (3,3) nanotubes, and (■) (110) surfaces in eV/MO_2 versus (a) theoretical (black) and experimental (gray) bulk heats of formation, ΔG_f^{Bulk}, for rutile metal oxides in eV/MO_2 from ref 26; (b) d-band center, ε_d, for the bulk metal oxide relative to the Fermi energy in eV; and (c) fraction of M−O bonds broken times the d-band center $\Delta\chi\varepsilon_d$ in eV/MO_2. The experimental nanoparticle surface energy[19] is shown for rutile TiO_2 (red box). Linear fits to the theoretical (solid line) and experimental (dashed line) ΔG_f^{Bulk} data are provided for comparison.

Assuming $\varepsilon_{M-O} \approx -\varepsilon_d$, we indeed find that $\Delta E_f \approx -\Delta\chi\varepsilon_d$ with a mean absolute error (MAE) of 0.08 eV, as shown in Figure 2c.

This correlation can be explained qualitatively by recalling that transition metals are most stable when the average energy of the DOS projected onto the d-states of the metal atoms is ε_F, that is, $\varepsilon_d \approx 0$. In most cases, this is equivalent to having a half-full d-band.[36] This is nearly the case for TiO_2, where $\varepsilon_d \approx -0.67$ eV, and the (110) surface becomes very stable ($\Delta E_f^{(110)} \approx 0.046$ eV/TiO_2). As the d-band shifts downward in energy, the energy stored in the M−O bonds increases accordingly, so that $\varepsilon_{M-O} \approx -\varepsilon_d$.

A more detailed analysis based on the molecular orbitals of the bulk metal oxide is provided in Appendix B based on refs 37−39. To summarize, as the number of d electrons, N_d, increases, the M−O coordinately unsaturated (cus) bond becomes stronger. It is only this bond that is broken during (110) surface, nanorod, and nanotube formation for rutile metal oxides. This increase in bond strength occurs as one progresses from noncus bonding (N_d = 2), to M−M bond distortions (N_d = 3), to M−O cus bonding (N_d = 4), to nonbonding M orbitals with reduced distortions (N_d = 5, 6), and to stronger M−O p_σ bonds (N_d = 7). Further, for a fixed number of d electrons, the bond strength increases as the DOS shifts downward in energy. In effect, the energy stored in rutile metal oxide M−O bonds is then equal to the energy cost for "shifting" the bonding metal orbitals so that their d-band is symmetric about the Fermi level. In such a case, both bonding with cus O atoms and distortions of the octahedral structure are minimized.

It is worth noting that we obtain near-quantitative agreement (MAE ≈ 0.08 eV) between the DFT-calculated formation energies and this simple model, when applied to naturally occurring transition metal rutile oxides. We now show how this model

$$\Delta E_f^{Model} \equiv -\Delta\chi\varepsilon_d \tag{5}$$

can be extended to group 14 (group-IV) rutile oxides (GeO_2, SnO_2, and PbO_2) and 3d transition metal perovskites ($SrMO_3$), as shown in Figure 3.

For group 14 metals, the d-band is fully occupied, and does not participate in the M−O bonding. Instead, the M−O bonding should occur via the occupied portion (one-third) of the metal's p-band. This should be described by the metal's p-band center in the metal oxide

$$\varepsilon_p \equiv \int (\varepsilon - \varepsilon_F) n_p(\varepsilon)\, d\varepsilon \tag{6}$$

where $n_p(\varepsilon)$ is the DOS projected onto the metal's atomic p-orbitals in the metal oxide. In any case, we find that the M−O bond energy ε_{M-O} for group 14 rutile oxides is approximately negative one-third times the p-band center, $-\varepsilon_p/3$, so that

$$\Delta E_f \approx -\Delta\chi\varepsilon_p/3 \tag{7}$$

This approximation yields near-quantitative formation energies for group 14 metal oxide nanorods, nanotubes, and (110) surfaces, as seen in parts a−c, respectively, of Figure 3.

Because perovskite metal oxides share the MO_6 octahedral structure of rutile metal oxides with interstitial Sr,[40,41] it is reasonable to expect that the same correlation with the metal d-band centers ε_d should hold. From the DFT calculations for the perovskite (100) surface, we obtain the average of the formation energies for both the MO_2- and SrO-terminated surfaces. As such, our model predicts

$$\Delta E_f^{(100)} \approx -(\Delta\chi^M\varepsilon_d^M + \Delta\chi^{Sr}\varepsilon_d^{Sr})/2 \tag{8}$$

where $\Delta\chi^M \approx 2/6 \approx 1/3$ per $SrMO_3$ and $\Delta\chi^{Sr} \approx 2/12 \approx 1/6$ per $SrMO_3$. From Figure 3d, we find that this is indeed the case, with an MAE of 0.08 eV.

In Figure 3a−c, we also plot the DFT-calculated formation energies versus ΔE_f^{Model} for transition metals whose most stable metal oxide phase is *not* rutile. For these compounds, denoted by red symbols in Figure 3, we find that our model typically overestimates formation energies, yielding an MAE of 0.12 eV.

For the HexABC layer structure of PtO_2,[21] we find that the formation energies are completely independent of ε_d and ε_p, as shown in Figure 4. However, this is also predicted by our model, because no M−O bonds are broken ($\Delta\chi \approx 0$) when forming the HexABC layer. Instead, the energy cost to form the HexABC layer is related to the preference of oxygen to be either sp^2- or sp^3-hybridized in the metal oxide.

dx.doi.org/10.1021/jp110489u |*J. Phys. Chem. C* XXXX, XXX, 000–000

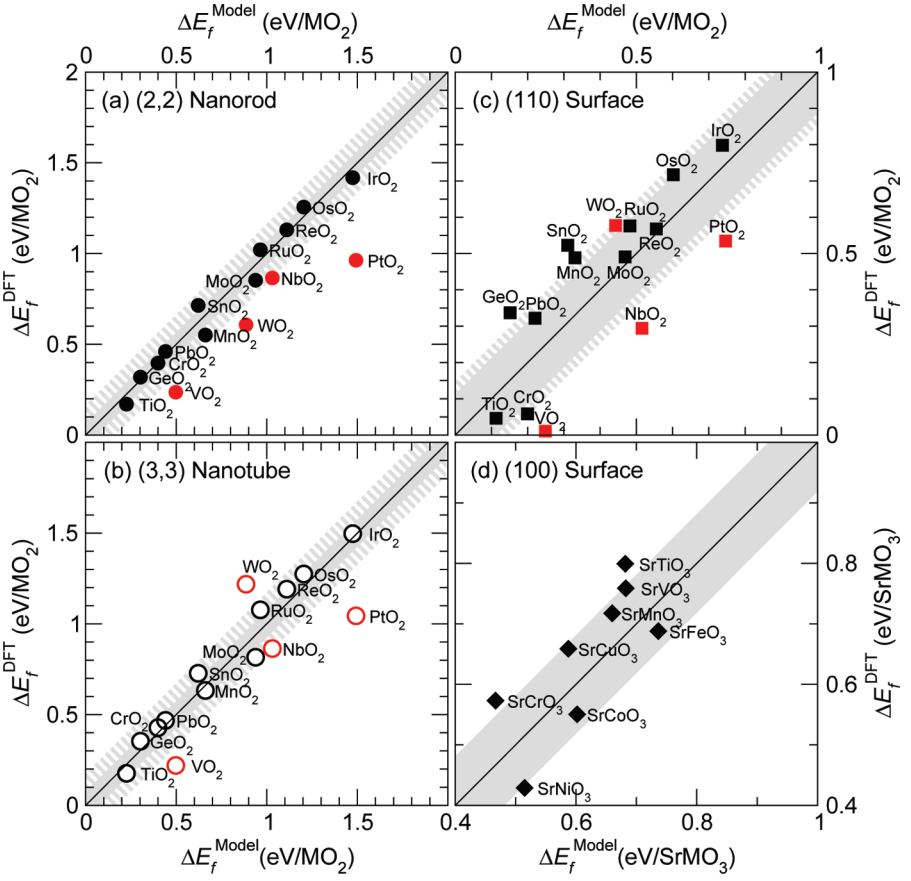

Figure 3. DFT-calculated formation energy, ΔE_f^{DFT}, versus model prediction, ΔE_f^{Model}, for (a) (●) (2,2) nanorods, (b) (○) (3,3) nanotubes, and (c) (■) (110) surfaces in eV/MO_2 for rutiles and (d) (100) MO_2- and SrO-terminated surfaces (♦) in eV/$SrMO_3$ for perovskites. Red symbols denote metal oxides whose most stable phase is not rutile. The standard deviation for each structure from Table 3 of Appendix A is shown by regions of solid and striped gray for naturally occurring and all considered metal oxides, respectively.

4. CONCLUSIONS

In conclusion, we have demonstrated that the formation energies for nanorods, nanotubes, and surfaces of metal oxides can be determined semiquantitatively (MAE ≈ 0.12 eV) from the fraction of M−O bonds that are broken, $\Delta\chi$, and the bonding band centers, ε_d and ε_p, in the bulk metal oxide. We anticipate that such models will prove useful in predicting the formation energy of doped metal oxide surfaces and nanostructures, their reactant adsorption energies, and their activities.

■ APPENDIX A. FORMATION ENERGIES

In this appendix, we provide further details for the interested reader concerning the results of the density functional theory (DFT) calculations and their analysis. We begin by plotting the projected density of states (PDOS) for the bulk rutile metal oxides, from which the d-band and p-band centers for the transition metal and group 14 metal oxides were calculated. A tabulation of calculated d-band and p-band centers and formation energies for the (2,2) nanorod, (3,3) nanotube, HexABC layers, and (110) surface of the rutile metal oxides and the (100) surface of the perovskite metal oxides is also provided. Finally, further comparisons are performed between the bulk heat of formation, ΔG_f; the d-band and p-band centers, ε_d and ε_p; the number of d-electrons, N_d; the cohesive energies, E_{coh}; and the formation energies, ΔE_f, to illustrate their relation to the electronic structure of the metal oxide.

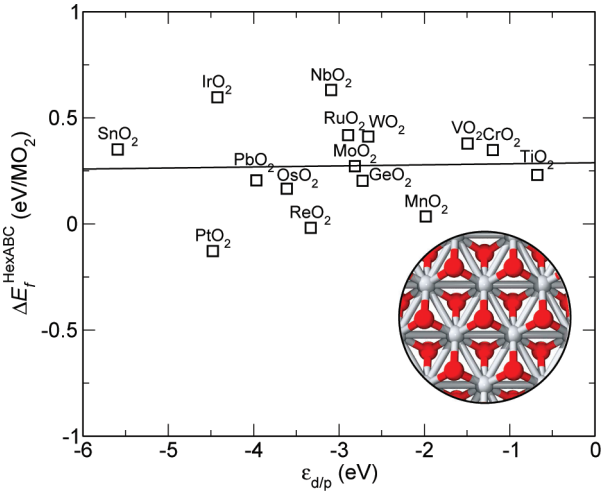

Figure 4. Formation energy for HexABC metal oxide layers, ΔE_f^{HexABC}, in eV/MO_2 obtained from DFT versus the M−O d-band and p-band centers for the metal atom, $\varepsilon_{d/p}$, in the bulk rutile metal oxide.[21] A linear fit of the data (black solid line) demonstrates that ΔE_f^{HexABC} is completely uncorrelated to $\varepsilon_{d/p}$. A schematic of the TiO_2 HexABC structure is shown as an inset.

The DFT-calculated projected density of states (PDOS) for the bulk rutile metal oxides studied is shown in Figure 5. The DOS projections onto the transition metal (TM) d orbitals, n_d;

dx.doi.org/10.1021/jp110489u |J. Phys. Chem. C XXXX, XXX, 000–000

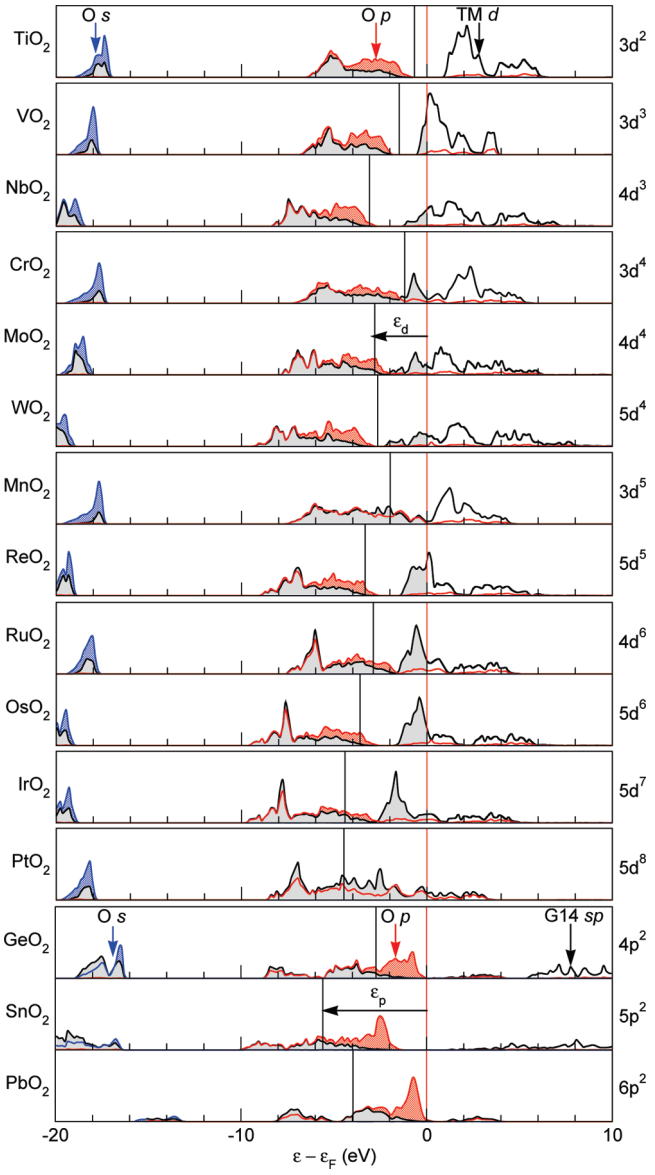

Figure 5. Density of states for bulk rutile metal oxides projected onto the transition-metal (TM) d orbitals n_d, group 14 metal (G14) sp orbitals n_{sp} (black solid line), oxygen p orbitals $n_{O\ 2p}$ (red solid line), and oxygen s orbitals $n_{O\ 2s}$ (blue solid line) versus energy, ε, in eV relative to the Fermi level, ε_F (thin red vertical line). Filling is denoted by the shaded regions. The TM d-band center ε_d and G14 p-band center (black vertical lines) are also shown for each metal oxide.

group 14 metal (G14) sp orbitals, n_{sp}; O s orbitals, $n_{O\ 2s}$; and O p orbitals, $n_{O\ 2p}$, are shown. One can clearly see that a sufficient number of unoccupied bands has been included in the bulk calculations to converge the calculated d-band and p-band centers. Figure 5 also shows how the metal−oxygen (M−O) bonding orbitals shift downward in energy with the d-band center for the TMs. One can also see how the M−O bonding orbitals for the G14 oxides shift with the p-band center.

The d-band and p-band centers for the bulk rutile metal oxides are given in Table 1, along with the formation energies for the (110) surfaces, (2,2) nanorods, (3,3) nanotubes, and HexABC layers, relative to the calculated total energy of the bulk rutile metal oxides provided in ref 26. The perovskite metal oxide d-band centers for M and Sr atoms are provided in Table 2, along with the model- and DFT-calculated formation energies for the (100) surfaces, relative to the calculated total energy of the bulk perovskite metal oxides provided in ref 27.

In Table 3, we provide both the mean absolute error (MAE) and standard deviation σ between the DFT (ΔE_f^{DFT}) and model (ΔE_f^{Model}) values, shown in Figure 3. When consideration is restricted to metal oxides that are most stable in the rutile phase, both MAE and σ are within the anticipated accuracy of DFT calculations (±0.1 eV). Further, even when metal oxides that have other more stable phases are included, the overall MAE of 0.12 eV is commensurate with the predictive power of DFT.

The bulk heat of formation ΔG_f^{Bulk} for rutile metal oxides is taken from ref 26, based on the reaction

$$M(s) + 2H_2O(l) \rightleftarrows MO_2(s) + 2H_2(g) \quad (9)$$

So, if $\Delta G_f^{Bulk} > 0$, then the metal oxide is unstable in aqueous solution. However, by adding the free energy of formation of liquid water (−2.46 eV at 298.15 K and 1 atm) from the reaction

$$O_2(g) + 2H_2(g) \rightleftarrows 2H_2O(l) \quad (10)$$

we can convert ΔG_f^{Bulk} to be with respect to the free metal and atmospheric oxygen

$$M(s) + O_2(g) \rightleftarrows MO_2(s) \quad (11)$$

With respect to O_2, all of the metal oxides studied are thermodynamically stable. In other words, all of the metals studied will oxidize under atmospheric conditions.

To better understand the relationships between ΔE_f, ΔG_f^{Bulk}, and ε_d, we plot the bulk heat of formation versus d-band center in Figure 6. We do not see a strong correlation between the d-band center, ε_d, of the metals in the bulk rutile metal oxide and the bulk heat of formation, ΔG_f, as shown in Figure 6. The squared correlation coefficient, R^2, is 0.62 and 0.65 for the theoretical and

Table 1. Rutile Metal Oxide d-Band and p-Band Centers ($\varepsilon_{d/p}$) for Transition and Group 14 Metals and Formation Energies for the (110) Surface ($\Delta E_f^{(110)}$), (2,2) Nanorod ($\Delta E_f^{(2,2)NT}$), (3,3) Nanotube ($\Delta E_f^{(3,3)NT}$), and HexABC Layer (ΔE_f^{HexABC})

metal oxide	$\varepsilon_{d/p}$ (eV)	$\Delta E_f^{(110)}$ (eV/MO_2)	$\Delta E_f^{(2,2)NT}$ (eV/MO_2)	$\Delta E_f^{(3,3)NT}$ (eV/MO_2)	ΔE_f^{HexABC} (eV/MO_2)
TiO_2	−0.68	0.05	0.17	0.18	0.23
VO_2	−1.49	0.01	0.24	0.23	0.38
CrO_2	−1.20	0.06	0.40	0.43	0.35
MnO_2	−1.98	0.49	0.55	0.63	0.04
NbO_2	−3.09	0.25	0.82	0.82	0.63
MoO_2	−2.81	0.49	0.85	0.82	0.27
RuO_2	−2.89	0.58	1.02	1.08	0.42
WO_2	−2.66	0.58	0.61	1.22	0.41
ReO_2	−3.33	0.57	1.13	1.19	−0.02
OsO_2	−3.61	0.72	1.26	1.27	0.17
IrO_2	−4.42	0.80	1.42	1.50	0.60
PtO_2	−4.48	0.53	0.96	1.04	−0.13
GeO_2	−2.72	0.34	0.32	0.35	0.20
SnO_2	−5.59	0.52	0.71	0.73	0.35
PbO_2	−3.97	0.32	0.46	0.47	0.21

dx.doi.org/10.1021/jp110489u |J. Phys. Chem. C XXXX, XXX, 000–000

Table 2. Perovskite Metal Oxide d-Band Centers for M (ε_d^M) and Sr (ε_d^{Sr}) and Formation Energies for the (100) Surface from the Model (ΔE_f^{Model}) and DFT Calculations (ΔE_f^{DFT})

metal oxide	ε_d^M (eV)	ε_d^{Sr} (eV)	ΔE_f^{Model} (eV/$SrMO_3$)	ΔE_f^{DFT} (eV/$SrMO_3$)
$SrTiO_3$	−1.73	−4.72	0.68	0.80
$SrVO_3$	−2.05	−4.09	0.68	0.76
$SrCrO_3$	−1.60	−2.40	0.47	0.57
$SrMnO_3$	−2.40	−3.12	0.66	0.72
$SrFeO_3$	−2.65	−3.54	0.74	0.69
$SrCoO_3$	−2.36	−2.50	0.60	0.55
$SrNiO_3$	−2.72	−0.75	0.52	0.43
$SrCuO_3$	−3.48	−0.09	0.59	0.66

Table 3. Mean Absolute Error (MAE) and Standard Deviation σ between Calculated (ΔE_f^{DFT}) and Model (ΔE_f^{Model}) Formation Energies Shown in Figure 3 of (2,2) Nanorods, (3,3) Nanotubes, and the (110) Surface for Rutile Metal Oxides, and the MO_2- and SrO-Terminated (100) Surfaces for Perovskites[a]

	mean absolute error (eV/N_f)	standard deviation (eV/N_f)
(2,2) nanorod	0.12 (0.05)	0.17 (0.06)
(3,3) nanotube	0.13 (0.06)	0.18 (0.07)
(110) surface	0.13 (0.11)	0.15 (0.11)
(100) surface	0.08 (0.08)	0.08 (0.08)

[a] Values in parentheses obtained by considering only naturally occurring metal oxides.

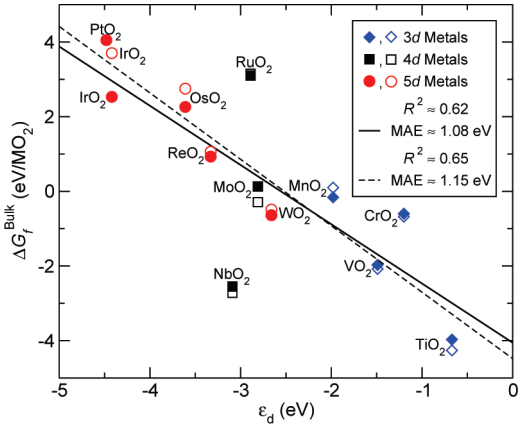

Figure 6. Bulk heat of formation ΔG_f^{Bulk} for 3d (blue diamonds), 4d (black squares), and 5d (red circles) rutile metal oxides in eV/MO_2 versus d-band center ε_d in eV. Theoretical and experimental values for ΔG_f^{Bulk} are shown as solid and open symbols, respectively, as provided in ref 26. A linear fit to the theoretical (solid line) and experimental (dashed line) ΔG_f^{Bulk} data, with squared correlation coefficients of $R^2 \approx$ 0.62 and 0.65 and mean absolute errors (MAEs) of 1.08 and 1.15 eV, respectively, is shown for comparison.

experimental ΔG_f^{Bulk} values, respectively, compared with 0.96 for the surface and nanostructure formation energies.

Based on Figures 6 and 2, one can conclude that the formation energies of the nanostructures depend more on the center of the metal bands that bond to oxygen in the bulk metal oxide than on the bulk heat of formation. This does not at all imply that the bulk heat of formation is not related to its electronic structure, as there does exist a correlation between ΔG_f and the number of d

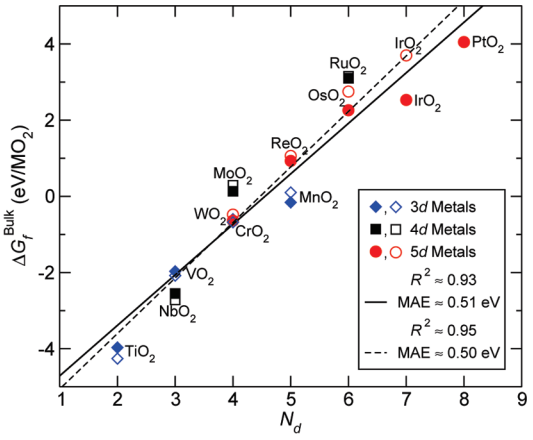

Figure 7. Overall correlation between the bulk heat of formation, ΔG_f^{Bulk}, for 3d (blue diamonds), 4d (black squares), and 5d (red circles) rutile metal oxides in eV/MO_2 and the number of d electrons, N_d. Theoretical and experimental values for ΔG_f^{Bulk} are shown as solid and open symbols, respectively, as provided in ref 25. A linear fit to the theoretical (solid line) and experimental (dashed line) ΔG_f^{Bulk} data, with squared correlation coefficients of $R^2 \approx$ 0.93 and 0.95 and mean absolute errors (MAEs) of 0.51 and 0.50 eV, respectively, is shown for comparison.

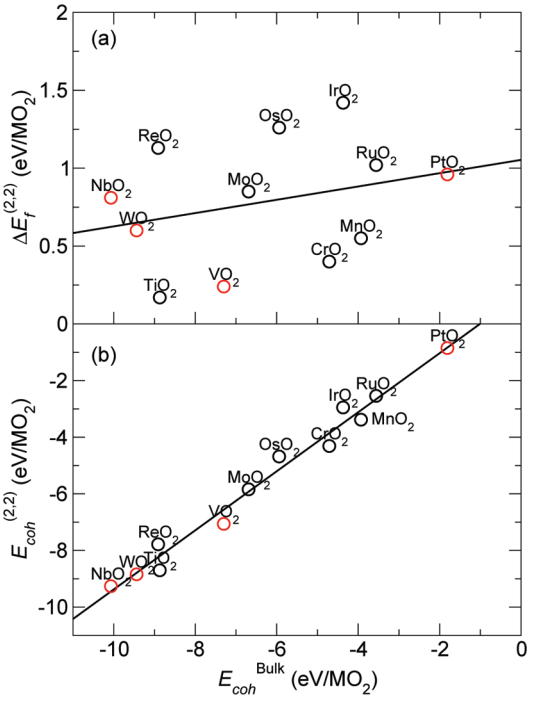

Figure 8. Comparison of the bulk rutile cohesive energy, E_{coh}^{Bulk}, in eV/MO_2 and (a) the formation energy of the (2,2) nanorod, $\Delta E_f^{(2,2)}$, in eV/MO_2, and (b) the cohesive energy of the (2,2) nanorod, $E_{coh}^{(2,2)}$, in eV/MO_2. Red symbols denote metal oxides whose most stable phase is not rutile.

electrons, N_d, in the metal (and the group number) in a given d-line. In fact, ΔG_f shows a stronger overall correlation with N_d than with ε_d for the rutile metal oxides, as shown in Figure 7. Such correlations between N_d and heats of formation have been previously reported for lanthanum perovskites,[42] and a similar correlation is seen when plotting the formation energies of 3d monoxides versus the number of d electrons.

dx.doi.org/10.1021/jp110489u |J. Phys. Chem. C XXXX, XXX, 000–000

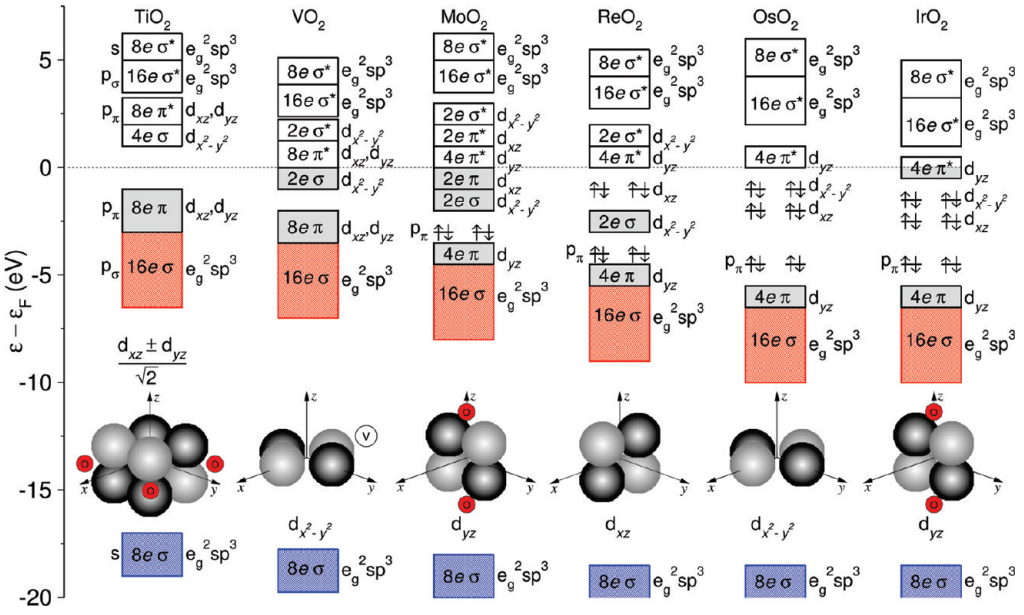

Figure 9. Molecular orbital schemes for rutile TiO_2, VO_2, MoO_2, ReO_2, OsO_2, and IrO_2 versus energy, ε, in eV relative to the Fermi level, ε_F.[37−39] Filling is denoted by the shaded regions for M t_{2g} (gray), O p_σ (red), and O s (blue) orbitals. Cartoons of the Ti−O noncus bonding $(d_{xz} \pm d_{yz})/(2)^{1/2}$, V−V bonding $d_{x^2-y^2}$, Mo−O cus bonding d_{yz}, Re nonbonding d_{xz}, Os nonbonding $d_{x^2-y^2}$, and Ir−O antibonding d_{yz} orbitals are shown below.

In Figure 8, we compare the formation energy and cohesive energy for the (2,2) nanorods with the cohesive energy for the bulk rutile metal oxide. The cohesive energy, E_{coh}, is defined as the total energy relative to the isolated metal atoms and O_2 in the gas phase

$$E_{coh} \equiv E - E^{M} - E^{O_2} \qquad (12)$$

As is shown in Figure 8b, there is a general correlation between the cohesive energies for the bulk rutile metal oxides and the (2,2) nanorods. However, this correlation is only qualitative and over a large range of energy values between −10 and 0 eV. When we consider the formation energies of the (2,2) nanorods, we find little correlation, $\Delta E_f^{(2,2)} \approx E_{coh}^{(2,2)} - E_{coh}^{Bulk} \neq E_{coh}^{Bulk}$. Although energy differences for metal oxide surfaces, nanostructures, and the bulk relative to the clean metal (ΔG_f) or metal atoms (E_{coh}) are somewhat correlated, this correlation is insufficient to allow predictions of the surface and nanostructure formation energies.

The cohesive energy, E_{coh}, and the M−O bond energy, ε_{M-O}, do not have a straightforward relationship, as the former also contains the M−M interaction. The largest contribution to the cohesive energy of transition metals and, therefore, of their compounds, is due to the formation of a d-band from the atomic d-orbitals. The M−O bonds formed by the hybridization of the metal's d-band with the p-states of oxygen is described in ref 43. However, some M−M bonds will be present as well. As discussed in Appendix B, this is indeed the case for N_d = 3, 4, and 5.

On the other hand, because ε_d is the average energy of the d-band relative to the Fermi level, it is expected that this value will describe all states, namely, bonding, nonbonding (if there are any), and antibonding. In other words, ε_d and ε_p specifically describe the electronic structure of the metal states in the bulk metal oxide. As such, we can use these descriptors to obtain a near-quantitative description of surface and nanostructure formation energies. This model should be valid as long as the structural changes of the metal oxides under surface and nanostructure formation are primarily related to bond breaking.

APPENDIX B. MOLECULAR ORBITAL ANALYSIS

We now provide a detailed review of the molecular orbital analysis of bulk rutile metal oxide bonding presented in refs 37−39.

N_d = 2: TiO_2. As seen in Figure 9, for the octahedral structure of TiO_2, the e_g orbitals (d_{z^2}, d_{xy}) are less stable and are at higher energies than their t_{2g} (d_{yz}, $d_{x^2-y^2}$, d_{xz}) counterparts. For this reason, the first two sets of Ti−O bonding orbitals are predominantly O 2s and O $2p_{x,y}$ in character, whereas the opposite is true for their higher energy antibonding counterparts. This means that the σ bonding between the apex O atoms and Ti is weak. It is this bond that is broken upon forming the (110) metal oxide surface, leaving a Ti coordinately unsaturated (cus) site, which is occupied by the apex O atom in the bulk.

On the other hand, the Ti d_{xz} and d_{yz} orbitals are rather close in energy to the O p_π orbitals, yielding a stronger bond. However, Ti's empty d_{xz} and d_{yz} states can both be "filled" only if they form bonds with the planar O atoms, as depicted schematically in Figure 9. Because only bonds between metal and cus oxygen atoms are broken when nanotubes, nanorods, and the (110) surface are formed, this explains why their formation energies are so low for rutile TiO_2.

N_d = 3: VO_2 and NbO_2. In VO_2, the $d_{x^2-y^2}$ orbital forms new V−V σ bonds preferentially with one of the two V neighbors, as depicted in Figure 9. This induces strain in the octahedral structure, so that VO_2 and NbO_2 are "monoclinic". This induced stress explains why the metal oxides with three d electrons (N_d = 3) are somewhat less stable than those of TiO_2.

N_d = 4: CrO_2, MoO_2, and WO_2. For CrO_2, MoO_2, and WO_2 the fourth d electron occupies a bonding d_{xz} M−M π orbital, as it can no longer overlap with the filled O p_π lone pairs in the plane. The empty d_{yz} orbital now forms a M−O π bond with the apex oxygen, as shown in Figure 9.

Whereas the M−M π bonds induce further distortions in the octahedral structure, the O−M π orbital acts as a strong bond with the cus O atom. This bond must first be broken to form the (110) surface and increases ΔE_f for the nanostructures and (110) surfaces.

dx.doi.org/10.1021/jp110489u |J. Phys. Chem. C XXXX, XXX, 000–000

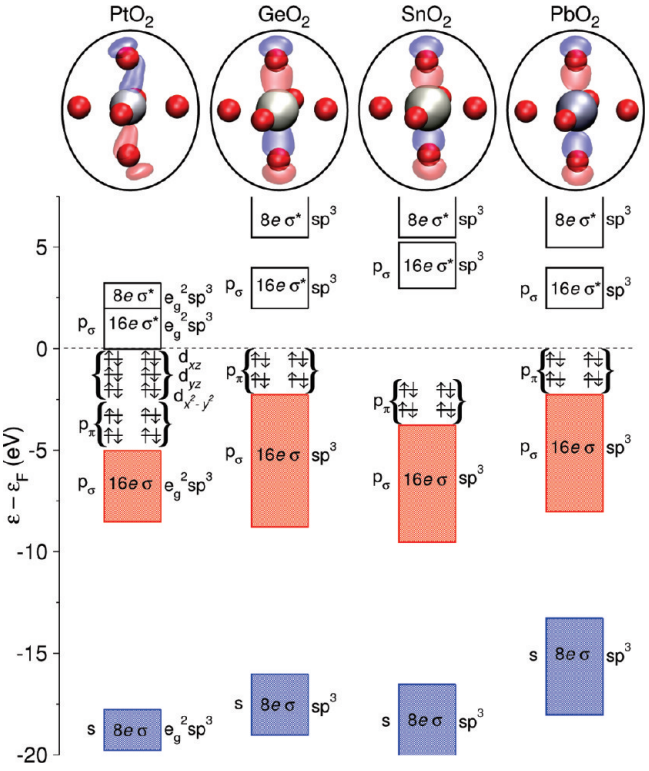

Figure 10. Molecular orbital schemes for rutile PtO_2, GeO_2, SnO_2, and PbO_2 versus energy, ε, in eV relative to the Fermi level, ε_F. Filling is denoted by the shaded regions. Schematics of the M−O cus bonding wave functions are shown above with isosurfaces of ± 0.2 Å$^{-3/2}$.

N_d = 5: MnO_2 and ReO_2. The fifth d electron for MnO_2 and ReO_2 breaks the M−M π bond, so that d_{xz} now becomes a nonbonding orbital. This will remove distortions of the octahedral structure induced by this bond and should increase the strength of the M−O π bond with the cus O. We find this increases the formation energies.

N_d = 6: RuO_2 and OsO_2. Similarly to the N_d = 5 metal oxides, for RuO_2 and OsO_2, the sixth d electron breaks the M−M σ bond, making the $d_{x^2-y^2}$ orbitals nonbonding. This removes most distortions from the octahedral structure and makes the M cus O bond even stronger, resulting in an even higher surface energy.

N_d = 7: IrO_2. IrO_2's seventh d electron occupies the M−O π^* antibonding states. In and of itself, this should weaken the M cus O bond. However, two competing factors, namely, the smaller energy gap between Ir e_g^2 sp^3 and Op_σ orbitals and the greater instability of a single half-occupied Ir d_{yz} orbital in the surface cus, tend to strengthen the Ir−O σ bonds and destabilize the (110) surface, respectively. As a result, we find that IrO_2 has the highest formation energy cost for both the surfaces and the nanostructures.

N_d = 8: PtO_2. For PtO_2, the M−O π^* antibonding orbital would be completely filled, so that only M−O σ orbitals play a role in Pt−O bonding. For this reason, PtO_2 is rather unstable in its rutile form. The formation energies for the PtO_2 (110) surface and nanostructures are thus significantly lower than those for IrO_2, but at the same time much higher than those for TiO_2.

N_p = 2: GeO_2, SnO_2, and PbO_2. For group 14 metals, there is only p-bonding of the σ type. However, these bonds are closer in energy to the O p_σ states, whereas the O p_π states are nonbonding. Here, there is a stronger M p_z−O p_z bond than for the transition metals, as shown in Figure 10. It is the shifting of the p band due to the core states that determines the stability of the group 14 metal oxide nanostructures and surfaces.

AUTHOR INFORMATION

Corresponding Author

*E-mail: Duncan.Mowbray@gmail.com.

ACKNOWLEDGMENT

The authors acknowledge financial support from the Danish Center for Scientific Computing and NABIIT. Financial support is acknowledged by D.J.M. from the HPC-EUROPA2 Project, by J.I.M. from the STREP EU APOLLON-B Project, and by F.C.-V. from the Strategic Electrochemistry Research Center (SERC). The Center for Atomic-scale Materials Design (CAMD) is sponsored by the Lundbeck Foundation.

REFERENCES

(1) *The Energy Challenges Report: New Science for a Secure and Sustainable Energy Future*; Hemminger, J., Crabtree, G., Kastner, M., Eds.; Argonne National Laboratory: Argonne, IL, 2008.
(2) Whitesides, G. M.; Crabtree, G. W. *Science* **2007,** *315*, 796–798.
(3) Smil, V. *Nature* **1999,** *400*, 415.
(4) Erisman, J. W.; Sutton, M. A.; Galloway, J.; Klimont, Z.; Winiwarter, W. *Nat. Geosci.* **2008,** *1*, 636–639.
(5) *Electrochemistry in Transition: From the 20th to the 21st Century*; Murphy, J., Srinivasan, S., Conway, B. E., Eds.; Plenum: New York, 1992.
(6) Trasatti, S. *Electrochim. Acta* **1984,** *29*, 1503–1512.
(7) Marshall, A.; Børresen, B.; Hagen, G.; Sunde, S.; Tsypkin, M.; Tunold, R. *Russ. J. Electrochem.* **2006,** *42*, 1134–1140.
(8) Guerrini, E.; Chen, H.; Trasatti, S. *J. Solid State Electrochem.* **2007,** *11*, 939–945.
(9) Chrétien, S.; Metiu, H. *J. Chem. Phys.* **2008,** *129*, 074705.
(10) Rossmeisl, J.; Qu, Z.-W.; Zhu, H.; Kroes, G.-J.; Nørskov, J. *J. Electroanal. Chem.* **2007,** *607*, 83–89.
(11) Valdés, Á.; Qu, Z.-W.; Kroes, G.-J.; Rossmeisl, J.; Nørskov, J. K. *J. Phys. Chem. C* **2008,** *112*, 9872–9879.
(12) Fujishima, A.; Honda, K. *Nature* **1972,** *238*, 37–38.
(13) Khan, S. U. M.; Al-Shahry, M.; Ingler, W. B. *Science* **2002,** *297*, 2243–2245.
(14) Hoffmann, M. R.; Martin, S. T.; Choi, W. Y.; Bahnmann, D. W. *Chem. Rev.* **1995,** *95*, 69–96.
(15) Khaselev, O.; Turner, J. A. *Science* **1998,** *280*, 425–427.
(16) Heller, A. *Science* **1984,** *223*, 1141–1148.
(17) Grätzel, M. *Nature* **2001,** *414*, 338–344.
(18) Perron, H.; Vandenborre, J.; Domain, C.; Drot, R.; Roques, J.; Simoni, E.; Ehrhardt, J.-J.; Catalette, H. *Surf. Sci.* **2007,** *601*, 518–527.
(19) Ranade, M. R.; Navrotsky, A.; Zhang, H. Z.; Banfield, J. F.; Elder, S. H.; Zaban, A.; Borse, P. H.; Kulkaml, S. K.; Doran, G. S.; Whitfield, H. J. *Proc. Natl. Acad. Sci. U.S.A.* **2001,** *99*, 6476–6481.
(20) Rogal, J.; Reuter, K. *Experiment, Modeling and Simulation of Gas-Surface Interactions for Reactive Flows in Hypersonic Flights*; Educational Notes RTO-EN-AVT-142; NATO Research and Technology Organisation: Neuilly-sur-Seine, France, 2007; pp 2-1−2-18.
(21) Mowbray, D. J.; Martínez, J. I.; García Lastra, J. M.; Thygesen, K. S.; Jacobsen, K. W. *J. Phys. Chem. C* **2009,** *113*, 12301–12308.
(22) Tafen, D. N.; Lewis, J. P. *Phys. Rev. B* **2009,** *80*, 014104.
(23) Bandura, A.; Evarestov, R. *Surf. Sci.* **2009,** *603*, L117–L120.
(24) Bavykin, D. V.; Friedrich, J. M.; Walsh, F. C. *Adv. Mater.* **2006,** *18*, 2807–2824.
(25) Molecular dynamic simulations of TiO_2 and RuO_2 (2,2) nanorods and (3,3) nanotubes showed them to be stable between 300 and 500 K over a time range of 20 ps. These results are to be published elsewhere.

(26) Martínez, J. I.; Hansen, H. A.; Rossmeisl, J.; Nørskov, J. K. *Phys. Rev. B* **2009,** *79*, 045120.
(27) Calle-Vallejo, F.; Martínez, J. I.; García-Lastra, J. M.; Mogensen, M.; Rossmeisl, J. *Angew. Chem.* **2010,** *122*, 7864–7867.
(28) Hammer, B.; Hansen, L. B.; Norskov, J. K. *Phys. Rev. B* **1999,** *59*, 7413–7421.
(29) Bahn, S. R.; Jacobsen, K. W. *Comput. Sci. Eng.* **2002,** *4*, 56–66.
(30) Monkhorst, H. J.; Pack, J. D. *Phys. Rev. B* **1976,** *13*, 5188–5192.
(31) Bengtsson, L. *Phys. Rev. B* **1999,** *59*, 12301–12304.
(32) Schrott, A. G.; Misewich, J. A.; Copel, M.; Abraham, D. W.; Zhang, Y. *Appl. Phys. Lett.* **2001,** *79*, 1786–1788.
(33) Perdew, J. P.; Wang, Y. *Phys. Rev. B* **1992,** *45*, 13244–13249.
(34) Becke, A. D. *J. Chem. Phys.* **1993,** *98*, 5648–5652.
(35) Beltrán, A.; Andrés, J.; Sambrano, J. R.; Longo, E. *J. Phys. Chem. A* **2008,** *112*, 8943–8952.
(36) Bligaard, T.; Nørskov, J. K. *Electrochim. Acta* **2007,** *52*, 5512–5516.
(37) Jiang, B.; Zuo, J. M.; Jiang, N.; O'Keeffe, M.; Spence, J. C. H. *Acta Cryst. A* **2003,** *59*, 341–350.
(38) Rogers, D. B.; Shannon, R. D.; Sleight, A. W.; Gillson, J. L. *Inorg. Chem.* **1969,** *8*, 841–849.
(39) Goodenough, J. B. *Prog. Solid State Chem.* **1971,** *5*, 145–399.
(40) Yokokawa, H. *Annu. Rev. Mater. Res.* **2003,** *33*, 581–610.
(41) Cheng, Z.; Zha, S.; Aguilar, L.; Liu, M. *Solid State Ionics* **2005,** *176*, 1921–1928.
(42) Pankajavalli, R.; Sreedharan, O. M. *Mater. Lett.* **1995,** *24*, 247–251.
(43) Gelatt, C. D.; Williams, A. R.; Moruzzi, V. L. *Phys. Rev. B* **1983,** *27*, 2005–2013.

DOI: 10.1002/cctc.200((will be filled in by the editorial staff))

Universality in Oxygen Evolution Electro-Catalysis on Oxide Surfaces

Isabela C. Man [a], Hai-Yan Su[a] , Federico Calle-Vallejo [a], Heine A. Hansen[b], José I. Martínez [c], Nilay G. Inoglu [d], John Kitchin [d], Thomas F. Jaramillo[e], Jens K. Nørskov[f], Jan Rossmeisl*[a]

Abstract

Trends in electrocatalytic activity of the oxygen evolution reaction (OER) are investigated on the basis of a large database of HO* and HOO* adsorption energies on oxide surfaces. The theoretical overpotential was calculated applying standard density functional theory in combination with the computational standard hydrogen electrode model (SHE). We show that by the discovery of a universal scaling relation between the adsorption energies of HOO* vs. HO* it is possible to analyze the reaction free energy diagrams of all the oxides in a general way. This gives rise to an activity volcano that is the same for a wide variety of oxide catalyst materials and a universal descriptor for the oxygen evolution activity. This suggests a fundamental limitation on the maximum oxygen evolution activity for a class of planar oxide catalysts.

Introduction

Electrochemical water splitting has attracted substantial interest in the recent years as a key process in hydrogen production from sunlight and other sources of electricity [1] . The clean, renewable conversion of solar radiation into fuels can be done directly by photons exciting electrons in a semi-conductor where the energy level of the valence band is sufficiently low. The conversion could also be done, in an indirect way, by electrolysis using a potential difference obtained from a photovoltaic cell or from a wind turbine. In both cases, effective catalysis for water oxidation to molecular oxygen, i.e. the oxygen evolution reaction (OER), is needed. There are, however, several challenges that have to be solved for the process to become economically attractive. One of them is associated with the substantial overpotential and thereby energy losses at the anode, where oxygen is evolved, according to the following overall reaction, involving four electron transfers [2].

$$2H_2O(l) + 4 \times 1.23\ eV \rightarrow O_2 + 4H^+ + 4e^-$$

Substantial effort has been devoted to find more effective catalysts for the oxygen evolution reaction and to elucidate the reaction mechanism [3]. An excellent review describing the development in this field can be found in [4].

To improve upon current electrocatalysts it is important to develop a fundamental understanding of the reactions on different materials [3f-h]. The electrocatalytic activity is to a large extent determined by the binding strength of the reaction intermediates to the electrode surface. Plotting the activity as a function of a binding energy can give rise to a volcano plot. This concept has been previously successfully applied to the oxygen evolution reaction[3a, 3c, 3h]. Since the binding energies are difficult to measure, other descriptors believed to correlate with the reactivity, have been used. An example is the use of the standard enthalpy of lower to higher oxide transformation ($MO_x \rightarrow MO_{x+1}$)[3b, 3d-g] .

Advances in Density Functional Theory (DFT) calculations make it possible to accurately determine surface binding energies that can hence be used as activity descriptors [3h]. The reverse reaction, the oxygen reduction reaction (ORR) in which molecular oxygen is reduced to water, involves the same general reaction intermediates as the OER. Recently, new alloy electrocatalysts for the ORR have been suggested on the basis of computational studies, where the values of the activity descriptor is calculated, followed by identification of promising candidates[5].

Previously, the OER has been studied using computational methods on two classes of materials: metals[6] and rutile oxides[7]. A similar computational approach has been used for the OER reaction which is in competition with chlorine evolution on rutile

[a] Chem. Eng. I.C.Man, Chem. Eng. F. Calle-Vallejo, Dr. H.Y.Su, Prof. J. Rossmeisl
Center for Atomic-Scale Materials Design
Department of Physics, Technical University of Denmark
DK-2800 Kgs. Lyngby (Denmark)
Fax: (+45) 4593-2399
E-mail: jross@fysik.dtu.dk

[b] Dr. H.A. Hansen
Department of Materials Science and Engineering, Northwestern University, Evanston, IL 60208

[c] Dr. J. I. Martínez
Dpto. de Física Teórica de la Materia Condensada, Universidad Autónoma de Madrid, E-28049 Madrid, Spain

[d] N.G. Inoglu, Prof. J. Kitchin
Department of Chemical Engineering, Carnegie Mellon University, Pittsburgh, Pennsylvania 15213, USA

[e] Prof. T.F. Jaramillo
Department of Chemical Engineering, Stanford, California, 94305 – 5025, USA

[f] Prof. J.K. Nørskov
SLAC National Accelerator Laboratory, Stanford, California, 94025-7015,USA

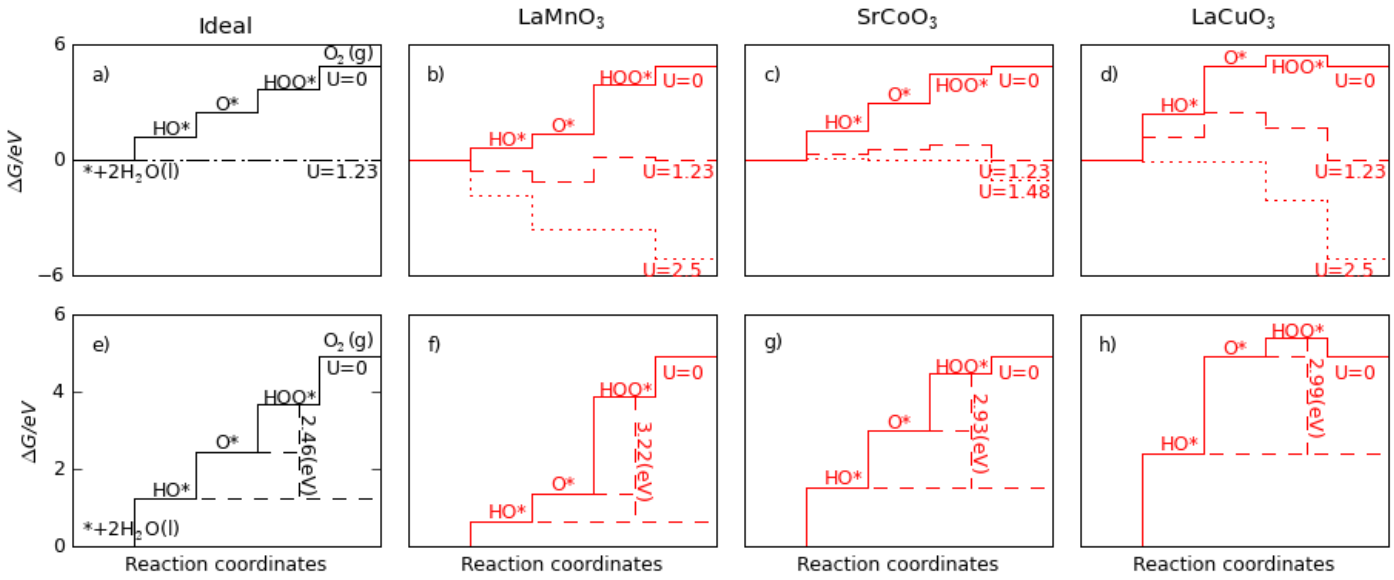

Figure 1. Standard Free energy diagram for the oxygen evolution reaction (OER) at zero potential (U = 0), equilibrium potential for oxygen evolution (U = 1.23) and at the potential where all steps becomes downwards at pH 0 and T = 298K over: a) the ideal catalyst b) $LaMnO_3$ c) $SrCoO_3$ d) $LaCuO_3$. Standard free energies at U =0 for e) ideal catalyst f) $LaMnO_3$ g) $SrCoO_3$ d) $LaCuO_3$. For all three cases $\Delta G_{HOO^*} - \Delta G_{HO^*}$ (vertical dashed lines) is approximately constant with an average value of 3.2 eV, while the optimum value should be 2.46 eV. The variation of ΔG_{O^*} between ΔG_{HO^*} and ΔG_{HOO^*} differs for each one. For the ideall case ΔG_{HO^*} is 1.23 eV, ΔG_{HOO^*} is 3.69 eV, and ΔG_{O^*} in the middle at 2.46 eV.

oxides[8]. In these studies, the proposed reaction mechanism consists of four consecutive proton and electron transfer steps. Considering the OER intermediates to be HO*, O* and HOO*, free energy diagrams have been constructed and the oxygen evolving activity has been estimated using O^* binding energies as a descriptor. Our previous studies [6-7] have shown that scaling relationships can be established between the binding energies of HO*, HOO* and O* species on oxide surfaces. The scaling relations suggest that there is only one free parameter that determines the free energy diagram and thereby the activity. In other words, the activity can be plotted as a function of only one parameter, e.g. the oxygen binding energy. The result is a volcano-shaped relationship between catalytic activity and the calculated oxygen adsorption energy. We found that on the surfaces that bind oxygen too strongly the rate is limited by the formation of HOO* species, whereas for surfaces that bind oxygen too weakly is the oxidation of HO*.

In the present paper, we revisit the origin of the overpotential for oxygen evolution on the basis of an extensive database of calculated binding energies on oxide surfaces. We include rutile, perovskite, spinel, rock salt and bixbyite oxides in our calculations. The scaling relationship between HO* and HOO* is found to be universal for all the studied materials. We introduce a new descriptor, the energy of a reaction step, which gives rise to a universal description of oxygen evolving activities on the studied materials. Excellent agreement is found in terms of trends, between the calculated overpotentials and the experimental results reported in literature.

Results and Discussion

Free energy diagram

We consider the following four electron reaction path:

$$H_2O(l) + * \leftrightarrow HO^* + H^+ + e^- \quad (1)$$

$$\Delta G_1 = \Delta G_{HO^*} - \Delta G_{H2O(l)} - eU + k_bT\ln a_{H+}$$

$$HO^* \leftrightarrow O^* + H^+ + e^- \quad (2)$$

$$\Delta G_2 = \Delta G_{O^*} - \Delta G_{HO^*} - eU + k_bT\ln a_{H+}$$

$$O^* + H_2O(l) \leftrightarrow HOO^* + H^+ + e^- \quad (3)$$

$$\Delta G_3 = \Delta G_{HOO^*} - \Delta G_{O^*} - eU + k_bT\ln a_{H+}$$

$$HOO^* \leftrightarrow * + O_2(g) + H^+ + e^- \quad (4)$$

$$\Delta G_4 = \Delta G_{O2} - \Delta G_{HOO^*} - eU + k_bT\ln a_{H+}$$

We apply a method previously developed for modeling the thermochemistry of electrochemical reactions based on density functional calculations[7]. We calculate $\Delta G_{1\text{-}4}$ using the computational standard hydrogen electrode (*SHE*) allowing us to replace a proton and an electron with half a hydrogen molecule at U = 0V vs. *SHE* [9]. The free energy of the intermediates along the reaction path, ΔG_{HO^*}, ΔG_{O^*} and ΔG_{HOO^*} are thereby calculated at U = 0V and standard conditions. Since the barriers between the intermediates are not included, the free energy diagrams we obtain are a first step towards a complete picture of the reaction path.

A very important parameter which can be deduced from the free energy diagram is the size of the potential determining step. This concept was developed in many other previous papers [6-7]. More precisely, the catalytic performance is estimated by the

magnitude of the potential-determining step for the OER, G^{OER}. This is the last step to become downhill in free energy as the potential increases, i.e. the specific reaction step in the four step mechanism with the largest ΔG:

$$G^{OER} = \text{Max}\,[\Delta G_1, \Delta G_2, \Delta G_3, \Delta G_4] \quad (5)$$

The theoretical overpotential at standard conditions is then:

$$\eta^{OER} = (G^{OER}/e) - 1.23V \quad (6)$$

The energy diagram for the ideal (but hereto non-existent) oxygen evolution catalyst is shown in Figure 1a. This ideal catalyst should be able to facilitate water oxidation just above the equilibrium potential. This requires all the four charge transfer steps to have reaction free energies of the same magnitude at zero potential (4.92 eV/4=1.23eV). This is equivalent to all the reaction free energies being zero at the equilibrium potential, 1.23V (Figure 1a). The catalyst that fulfills this requirement is thermochemically ideal. Real catalysts do not show this behavior. We show the calculated free energy diagrams at standard conditions of the OER on the surfaces of $LaMnO_3$ (strong binding), $SrCoO_3$ (intermediate binding) and $LaCuO_3$ (weak binding) in Figure 1a, 1c and 1d. The most representative potentials are at *U* = 0 eV where all steps are uphill, at equilibrium potential for oxygen evolution *U* = 1.23 eV, when some of the steps become downhill but some still remain uphill and at the G^{OER} potentials when the potential determining step become downhill. Accordingly, $LaMnO_3$ has a rather large overpotential due to ΔG_3. For $SrCoO_3$ ΔG_2 and ΔG_3 have almost the same value and the overpotential is small, whereas for $LaCuO_3$ ΔG_2 is the potential-determining step.

Scaling relations

Figures 1g, f, h show that the bond strength of all the intermediates decreases from left to right ($LaMnO_3$, $SrCoO_3$, $LaCuO_3$). Note that the levels of the intermediates move together, i.e. if one reaction energy decreases, the others do too. This correlated energy phenomenon has been observed on metal and metal oxide surfaces as a result of the scaling relations between the intermediates [6-7, 10]. An example is the linear relation between the binding energy of HO* and O*, where the slope of one half reflects that oxygen has two bonds to the surface, whereas HO* has only one bond. The intercept is determined by the type of binding site, meaning that there are different intercepts for HO*(ontop) vs. O*(ontop) scaling compared to the HO*(hollow) vs. O*(hollow) scaling. This gives rise to different intercepts for metals and oxides since the binding sites are different. Figures 1e, f, g and h show that the free energy difference between HO* and HOO* is almost constant, independent on the binding strength to the surface. It was pointed out in a recent review by M. Koper[11] that the bindings of HO* and HOO* are related to each other by a constant of ~ 3.2eV both for metals and oxide surfaces regardless of the binding site. This implies that there is a universal scaling relation between HO* and HOO*.

Here we establish the formal scaling relationship between HO* and HOO* binding energies over a wide range of oxides. Figure 2 shows that the binding energies of HOO* and HO* species on the various oxide surfaces considered here are linearly correlated, with a slope of approximately 1, and an intercept of 3.2eV. The Mean Absolute Error (MAE) of the linear fit is 0.17 eV, indicating an extremely strong correlation between the two species.

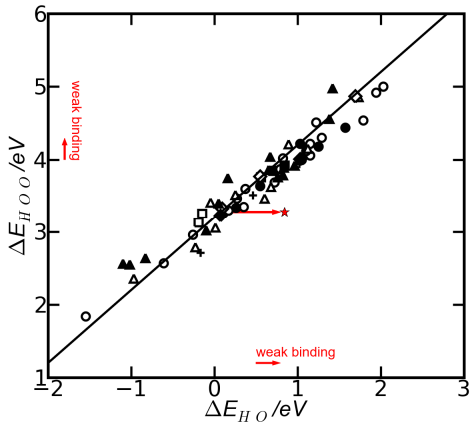

Figure 2. Adsorption energy of HOO* plotted against the adsorption energy of HO* on perovskites, rutiles, anatase, Mn_xO_y, Co_3O_4 and NiO oxides. Hollow symbols represent the adsorption energy on the clean surfaces: ○ – perovskites, Δ - rutiles, □ – Mn_xO_y, ◊ - anatase, + - Co_3O_4, NiO. Solid symbols represent the adsorption energies on high coverage surfaces, with oxygen atoms representing nearest neighbors. The best fit of all points is $\Delta E_{HOO^*} = \Delta E_{HO^*} + 3.20$ eV and with 68% of the points within ±0.2 eV and 95% within ±0.4 eV. The red star indicates where the binding energies need to be for an ideal electrocatalyst.

The slope of unity in the correlated binding energies of HO* and HOO* reflects the fact that both species have a single bond between an O atom and the surface. The constant intercept implies that HO* and HOO* normally prefer the same type of binding site. Seen from the point of view of the surface, HO* and HOO* look very similar. This results in the approximately constant difference of $\Delta E_{HOO^*} - \Delta E_{HO^*}$ of 3.2 eV for all the oxides considered. We note that this difference is also observed on metal surfaces [6].

Interestingly, the constant difference between the adsorption energies of HO* and HOO* of 3.2 eV regardless of the binding energy of O* defines a lower limit for the OER overpotential[11]. Since two proton and electron transfer steps separate the two intermediates, the perfect separation in terms of energy should be 2.46 eV as illustrated in Figure 1e. The difference in the energetic of these two steps between actual catalysts and an ideal one (3.2 eV-2.46 eV)/2e gives a minimum overpotential of 0.4 - 0.2 eV, even if we could find a material where the O* level is placed optimally between those of HO* and HOO* , as shown in the example from the Figure 1g (with the value -0.2eV that comes from standard deviation of the population from 3.2 eV value: $2\sigma = \pm$ 0.4eV with 95% of the values expected to lie within this confidence interval). The thermochemically ideal catalyst is characterized by having $\Delta G_1 = \Delta G_2 = \Delta G_3 = \Delta G_4 = 1.23$ eV. This can only be achieved at a specific binding of all intermediates indicated by the red star in Figure 2. It is seen that this point clearly falls outside the general trends and there is no oxide-based material in the classes considered here that provides an optimum binding of both HO*

and HOO*. In this picture, the challenge is to find a way to modify oxide surfaces or the electrochemical interface, such that the relative stability of HOO* and HO* changes.

Descriptor and activity volcano

Given the constant difference between the HOO* and HO* levels, the variation in the overpotential, η^{OER} from one oxide surface to the next is determined by the O* adsorption energy. This means that, either step 2 or step 3 is potential-determining:

$$G^{OER} = \mathrm{Max}[\Delta G_2, \Delta G_3] = \mathrm{Max}[(\Delta G_{O^*} - \Delta G_{HO^*}), (\Delta G_{HOO^*} - \Delta G_{O^*})]$$

$$\approx \mathrm{Max}[(\Delta G_{O^*} - \Delta G_{HO^*}), 3.2\mathrm{eV} - (\Delta G_{O^*} - \Delta G_{HO^*})] \quad (7)$$

The difference, $(\Delta G_{O^*} - \Delta G_{HO^*})$, is therefore a unique descriptor for the OER activity, and the theoretical overpotential at standard conditions is:

$$\eta^{OER} = \{\mathrm{Max}[(\Delta G_{O^*} - \Delta G_{HO^*}), 3.2\mathrm{eV} - (\Delta G_{O^*} - \Delta G_{HO^*})]/e\} - 1.23\mathrm{V} \quad (8)$$

We note that theoretical overpotential is independent of pH.
Plotting η^{OER} as function of $\Delta G_{O^*} - \Delta G_{HO^*}$ for the classes of materials considered here will therefore lead to a universal volcano relationship independent on the catalyst material. For clarity, the trends are shown separately for perovskites (
Figure 3a) and rutiles (Figure 4a), and the points represent the calculated value for each oxide.

Figure 3 a) Activity trends towards oxygen evolution plotted for perovskites. The negative theoretical overpotential is plotted against the standard free energy of the $\Delta G_{HO^*} - \Delta G_{O^*}$ step. The low coverage regime was considered and

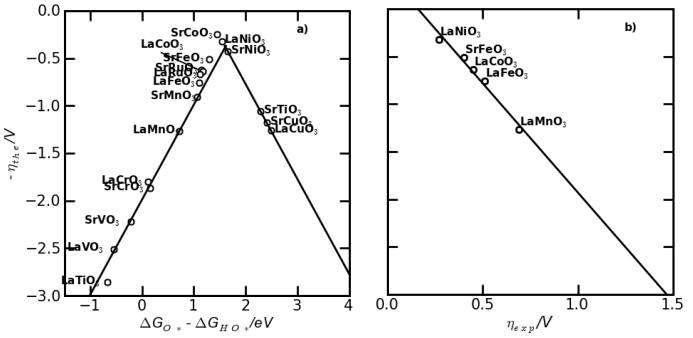

the calculated values were used to show the activity of each oxide. The volcano curve was established by using the scaling relation between $G_{HOO^*} - G_{O^*}$ and $G_{O^*} - G_{HO^*}$. b) Theoretical overpotential vs. the experimental overpotential in alkaline media. Experimental data were adapted from the study of O.M. Bockris and T. Otagawa [3a, 12]. All experimental values were recorded at 10 mA cm^{-2}, room temperature and pH = 14.

This theoretical analysis leads to the following ordering of catalyst activities for the following perovskites: $SrCoO_3 > LaNiO_3 > SrNiO_3 > SrFeO_3 > LaCoO_3 > LaFeO_3 > LaMnO_3$. The trend agrees well with experimental findings by Bockris et al. and Y. Matsumoto et al. [3a] [12] under alkaline conditions, see
Figure 3b.

A quantitative comparison between the theoretical and experimental overpotentials is extremely difficult. The theoretical overpotential is not directly comparable to experimentally determined values, since activation barriers are neglected. Furthermore, the experiments are performed using electrodes with oxide nanoparticles, where the effective surface area is often unknown or not reported. Hence, the current per geometric area is not directly available. In addition the experimentally measured overpotential depends on the current density at which it is measured. On the other hand also the theoretical overpotentials are expected to vary a little bit with increasing the size of the unit cells and with the coverage regimes. In spite of these uncertainties, it should be possible to compare trends in overpotentials for a set of different oxides. This is what we do in
Figure 3b for the perovskites. According to our calculations, $SrCoO_3$ has a $\Delta G_{HO^*} - \Delta G_{O^*}$ of 1.48 eV, close to the very top of the volcano. The high activity of $SrCoO_3$ was predicted also theoretically by Y. Matsumoto et. all [13] , but the main problem is experimentally and is related to how to obtain $SrCoO_3$ with perovskite type structure, since experimentally $SrCoO_3$ was obtained under a non perovskite type structure and exists as $SrCoO_{2.5}$ in composition .

For the other oxides such as rutiles (anatases), Mn oxides, and Co oxides, the activity order given by the theoretical calculations is extracted from Figure 4a: $Co_3O_4 \approx RuO_2 > PtO_2$ - rutile phase $\approx RhO_2 > IrO_2 \approx PtO_2$ β-phase($CaCl_2$) $\approx Mn_xO_y \approx NiOb_2 \approx RuO_2$ and IrO_2 anatase phase $> PbOb_2 >>$ Ti, Sn, Mo, V, Nb, Re oxides. The anatase phases with crystallographic orientation 001, such as RuO_2 and IrO_2, show approximately the same activity as the rutile phases. A similarly good agreement between the theoretical and experimental values of overpotentials on oxides other than perovskites is illustrated in Figure 4b.

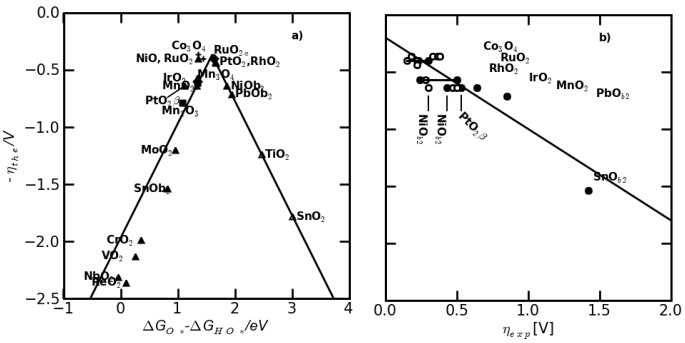

Figure 4. a) Activity trends towards oxygen evolution, for rutile, anatase, Co_3O_4, Mn_yO_x oxides. The negative value of theoretical overpotential is plotted against the standard free energy of $\Delta G_{HO^*} - \Delta G_{O^*}$ step. Solid triangles - the effect of interaction with the oxygen from the neighboring site is considered: ▲ rutile oxides, ■ –Mn_xO_y. For NiO_{b2}, PbO_{b2} and SnO_{b2} cus sites are empty, and the reaction takes place on the bridge sites. Hollow triangles are for low coverage regime b) Theoretical overpotential vs. the experimental overpotential in acidic media (solid circles) and in alkaline media (open circles). Experimental data were taken from Y. Matsumoto and E. Sato[12] . All experimental values are considered at 10 mA cm^{-2} and room temperature.

Even the comparisons between different experimental values are difficult to establish, due to many factors that affect the potential including *pH*, effective surface area, particle size, etc. A slight discrepancy exists between the calculated and measured Co_3O_4 activity. DFT calculations show that Co_3O_4 is slightly more reactive than RuO_2, whereas most of the experimental studies suggest that Co_3O_4 has a higher overpotential than RuO_2, by 0.2-0.25 V [12]. It was shown that Co_3O_4 is non-stoichiometric with an excess of oxygen and that the size of crystallites vary with the calcination temperature [3g]. Recently, Singh et. al. synthesized a spinel type of Co_3O_4 thin film which showed a low overpotential

[14] in agreement with our calculations. It has also been reported that the overpotential on Co-oxide nanoparticle electrocatalysts is size-dependent with lower overpotentials on smaller particles [15]. Other Co oxide structures with a low overpotential have been reported as well[16]. In Figure 4b we compare for Co_3O_4, three experimental overpotentials from the literature to the computed overpotential. Starting from left to right, the most active is the value reported by Singh et. all [14], followed by three values reported by Esswein et. all [15a]. A slight discrepancy is also observed in the case of NiO, but the theoretical value is only for NiO, while in reality, NiO is expected to have a more complicated composition, including species in higher oxidation states [3g, 17].

We emphasize that the reaction mechanism is more flexible for the oxides close to the top of the volcano where the intermediates have a better compromise in interaction strength. This could be the case of Mn_xO_y oxides and detailed results will be discussed in a future manuscript. However, at the top of the volcano the overpotential is small and other reaction paths could be also relevant if their overpotential is smaller than the values reported in this study. This flexibility of reaction mechanism might result in a slight variation in the theoretical overpotentials, and the details of this matter are out of the scope of this paper.

The actual surface of an oxide catalyst can experience oxidation and/or dissolution in the highly corrosive OER environment. For instance, some oxides such as NbO_2, ReO_2, VO_2, MoO_2, CrO_2 [17a] are not stable. Still, the theoretical values may be interesting as a guide in designing mixed oxides that could show improved activity [18]

Given the robustness of this theoretical model as applied to oxide materials of well-defined stoichiometry and crystal structure, one can potentially apply these methods to non-stoichiometric oxide catalysts as well.

Conclusion

First principles periodic DFT calculations have been used to revisit the origin of the overpotential for oxygen evolution for a wide range of oxides including rutile, perovskite, spinel, rock salt and bixbyite. A universal scaling relationship between the binding energy of HOO* and HO* is identified. The scaling relation leads to an approximately constant difference between the binding energies of HOO* and HO*, which in turn defines the lowest possible theoretical overpotential for the OER on a wide variety of oxides. Few catalyst materials operate at this minimum theoretical overpotential, the remaining hundreds of catalyst materials are further burdened by an additional overpotential arising from a sub-optimal O* binding energy. Thus the origin of the overpotential for oxygen evolution catalysis has been elucidated, whereby a single descriptor ($\Delta G_{O^*} - \Delta G_{HO^*}$) is introduced which results in a universal description of oxygen-evolving activities. Experimental trend studies from the literature can be described and understood within the model.

This study provides an understanding of the fundamental limitations for the OER activity on oxide-based electrocatalysts. Our results show that for the classes of structures considered here the OER activity cannot be significantly improved beyond RuO_2 by tuning the binding between the intermediates and the catalyst surface.

To avoid the limitations defined by the universal scaling relation, one must find ways to stabilize HOO* compared to HO*. It is possible that three dimensional structures, such as rough surface structures, zeolites or co-adsorbates on the surface could accomplish this by allowing for a selective hydrogen bond to HOO*. Effects such as these are likely present in enzymes that catalyze water oxidation very effectively in nature [19] .

Experimental Section

We calculated the binding energies of the intermediates O*, HO*, and HOO* on the rutile, perovskite, Mn, Co and Ni oxide surfaces:

$$\Delta E_{HO^*} = E(HO^*) - E(^*) - (E_{H2O} - 1/2E_{H2}) \quad (9)$$

$$\Delta E_{HOO^*} = E(HOO^*) - E(^*) - (2E_{H2O} - 3/2E_{H2}) \quad (10)$$

$$\Delta E_{O^*} = E(O^*) - E(^*) - (E_{H2O} - E_{H2}) \quad (11)$$

Where E(*), E(HO*), E(O*), E(HOO*) represent the calculated DFT energies of the clean surface and respectively with adsorbates. E_{H2O}, E_{H2} calculated DFT energies of H_2O and H_2 molecules in the gas phase.

The surface structures together with the unit cells we used are shown in

Figure 5**.** The stoichiometric surfaces were considered for rutile oxides, with the exception of PbO_2, SnO_2 and NiO_2, on which the binding of intermediates are thermodynamically favored on non stoichiometric surfaces (denoted by the subscript b). The results presented here, were obtained using density functional theory (DFT) [20]**,** with the RPBE [21] exchange-correlation functional using DACAPO[22]. The Kohn – Sham equations were solved using a plane wave basis with a cutoff of 350 - 400 eV for the eigenstates and a cutoff of 500 eV for the.kinetic energy. The ionic cores and their interaction with valence electrons are described by ultrasoft pseudopotentials [21]. The occupancy of the one-electron states was calculated using an electronic temperature of k_BT = 0.1 eV for surfaces and 0.01 eV for molecules in vacuum. All energies were extrapolated to T = 0K. The ionic degrees of freedom were relaxed using the quasi-Newton minimization scheme until the maximum force component was smaller than 0.05 $eVÅ^{-1}$. Spin-polarization calculations were carried out for CrO_2 , Mn, Ni and Co oxides and for perovskites when appropriate. More about the surfaces and other computational details can be found in the supplementary material.

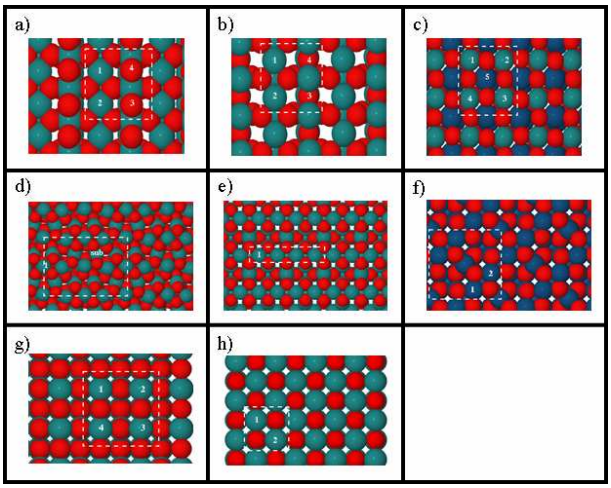

Figure 5 Visualization of the considered surface structures of metal oxides. The reaction takes place only on one site at a time a) Rutile-like stoichiometric surface (110) for MO_2 with M = Ti, V, Cr, Mn, Nb, Mo, Ru, Rh, Re, Ir, Pt, Sn. Red and light blue spheres represent O and metal atoms, respectively. Positions 1 and 2 represent the active sites (CUS). 3,4 represent the inactive sites (BRIDGE) and are covered with oxygen. b) Rutile-like reduced surface (110) for MO_2. Positions 3,4 represent the active position (BRIDGE) and 1,2 the inactive position (CUS) with M = Ni, Pb, Sn. Red and light blue represent O and metal atoms, respectively c) Perovskite structure for $LaMO_3$ and $SrMO_3$ (100) surface with M = Ti, V, Mn, Fe, Co, Ni, Cu. Red, dark blue and light blue spheres represent O, La(Sr) and metal respectively. Sr and La are in the subsurface. (1,2,3,4) – represent the active sites/unit cell. 5 – represents the subsurface atom. d) Mn_2O_3 (110) surface structure. 1- represents the binding site e) Mn_3O_4 (001) surface structure. f) Co_3O_4 g) (001) Anatase-like surface h) MO(100) surface with M = Mn, Ni.

Acknowledgements:

The authors thank Dr. Marc Koper and Dr. Peter Strasser for sharing preprints. This research was supported in part by the European Commission (Marie Curie Research Training Network MRTN-CT-2006-032474), by the Danish Council for Strategic Research via SERC project through grant no. 2104 -06-011 and by the Catalysis for Sustainable Energy (CASE) initiative. NI and JRK gratefully acknowledge support from the DOE Office of Science Early Career Research program (DE-SC0004031). This work was partially supported by the IMI Program of the National Science Foundation under Award No. DMR 0843934. TFJ and JKN acknowledge support from the Global Climate and Energy Program (GCEP) Stanford University. JIM acknowledges funding from Spanish MICINN through Juan de la Cierva Program

Keywords: Density Functional Calculations • Oxide surfaces • Oxygen • Scaling relation • Theoretical and experimental overpotentials

[1] J. O. Bockris, T. N. Veziroglu, *International Journal of Hydrogen Energy* **2007**, *32*, 1605.

[2] J. O. Bockris, *International Journal of Hydrogen Energy* **2008**, *33*, 2129.

[3] a)J. O. Bockris, T. Otagawa, *Journal of the Electrochemical Society* **1984**, *131*, 290; b)S. Trasatti, *Journal of Electroanalytical Chemistry* **1980**, *111*, 125; c)S. Trasatti, *Electrochimica Acta* **1991**, *36*, 225; d)Klissurs.Dg, R. P. Dikova, *Zeitschrift Fur Physikalische Chemie-Leipzig* **1969**, *241*, 101; e)E. R. S. Winter, *Journal of the Chemical Society a -Inorganic Physical Theoretical* **1968**, 2889; f)G. K. Boreskov, *Advances in Catalysis* **1964**, *15*, 285; g)S. Trasatti, *Electrochimica Acta* **1984**, *29*, 1503; h)P. Ruetschi, P. Delahay, *Journal of Chemical Physics* **1955**, *23*, 556.

[4] H. Dau, C. Limberg, T. Reier, M. Risch, S. Roggan, P. Strasser, *Chemcatchem* **2010**, *2*, 724.

[5] a)J. K. Norskov, T. Bligaard, J. Rossmeisl, C. H. Christensen, *Nature Chemistry* **2009**, *1*, 37; b)J. Greeley, I. E. L. Stephens, A. S. Bondarenko, T. P. Johansson, H. A. Hansen, T. F. Jaramillo, J. Rossmeisl, I. Chorkendorff, J. K. Norskov, *Nature Chemistry* **2009**, *1*, 552.

[6] J. Rossmeisl, A. Logadottir, J. K. Norskov, *Chemical Physics* **2005**, *319*, 178.

[7] J. Rossmeisl, Z. W. Qu, H. Zhu, G. J. Kroes, J. K. Norskov, *Journal of Electroanalytical Chemistry* **2007**, *607*, 83.

[8] H. A. Hansen, I. C. Man, F. Studt, F. Abild-Pedersen, T. Bligaard, J. Rossmeisl, *Physical Chemistry Chemical Physics* **2010**, *12*, 283.

[9] J. K. Norskov, J. Rossmeisl, A. Logadottir, L. Lindqvist, J. R. Kitchin, T. Bligaard, H. Jonsson, *Journal of Physical Chemistry B* **2004**, *108*, 17886.

[10] a)F. Abild-Pedersen, J. Greeley, F. Studt, J. Rossmeisl, T. R. Munter, P. G. Moses, E. Skulason, T. Bligaard, J. K. Norskov, *Physical Review Letters* **2007**, *99*; b)E. M. Fernandez, P. G. Moses, A. Toftelund, H. A. Hansen, J. I. Martinez, F. Abild-Pedersen, J. Kleis, B. Hinnemann, J. Rossmeisl, T. Bligaard, J. K. Norskov, *Angewandte Chemie-International Edition* **2008**, *47*, 4683.

[11] T.M.Koper, Leiden Institute of Chemistry, Leiden University, Leiden (Netherlands), **2010**.

[12] Y. Matsumoto, E. Sato, *Materials Chemistry and Physics* **1986**, *14*, 397.

[13] Y. Matsumoto, S. Yamada, T. Nishida, E. Sato, *Journal of the Electrochemical Society* **1980**, *127*, 2360.

[14] R. N. Singh, D. Mishra, Anindita, A. S. K. Sinha, A. Singh, *Electrochemistry Communications* **2007**, *9*, 1369.

[15] a)A. J. Esswein, M. J. McMurdo, P. N. Ross, A. T. Bell, T. D. Tilley, *Journal of Physical Chemistry C* **2009**, *113*, 15068; b)F. Jiao, H. Frei, *Angewandte Chemie-International Edition* **2009**, *48*, 1841.

[16] M. W. Kanan, J. Yano, Y. Surendranath, M. Dinca, V. K. Yachandra, D. G. Nocera, *Journal of the American Chemical Society* **2010**, *132*, 13692.

[17] a)M. Pourbaix, Pergamon Press, **1966**; b)S. M. Jasem, A. C. C. Tseung, *Journal of the Electrochemical Society* **1979**, *126*, 1353.

[18] a)M. V. Makarova, J. Jirkovsky, M. Klementova, I. Jirka, K. Macounova, P. Krtil, *Electrochimica Acta* **2008**, *53*, 2656; b)R. Forgie, G. Bugosh, K. C. Neyerlin, Z. C. Liu, P. Strasser, *Electrochemical and*

Solid State Letters **2010**, *13*, D36; c)K. C. Neyerlin, G. Bugosh, R. Forgie, Z. C. Liu, P. Strasser, *Journal of the Electrochemical Society* **2009**, *156*, B363; d)K. Macounova, M. Makarova, J. Franc, J. Jirkovsky, P. Krtil, *Electrochemical and Solid State Letters* **2008**, *11*, F27; e)K. Macounova, J. Jirkovsky, M. V. Makarova, J. Franc, P. Krtil, *Journal of Solid State Electrochemistry* **2009**, *13*, 959; f)K. Macounova, M. Makarova, P. Krtil, *Electrochemistry Communications* **2009**, *11*, 1865; g)H. Y. Kim, H. M. Lee, R. G. S. Pala, H. Metiu, *Journal of Physical Chemistry C* **2009**, *113*, 16083; h)H. Y. Kim, H. M. Lee, R. G. S. Pala, V. Shapovalov, H. Metiu, *Journal of Physical Chemistry C* **2008**, *112*, 12398.

[19] J. Rossmeisl, K. Dimitrievski, P. Siegbahn, J. K. Norskov, *Journal of Physical Chemistry C* **2007**, *111*, 18821.

[20] a)W. Kohn, L. J. Sham, *Physical Review* **1965**, *140*, 1133; b)P. Hohenberg, W. Kohn, *Physical Review B* **1964**, *136*, B864.

[21] B. Hammer, L. B. Hansen, J. K. Norskov, *Physical Review B* **1999**, *59*, 7413.

[22] http://wiki.fysik.dtu.dk/dacapo.

Received: ((will be filled in by the editorial staff))
Published online: ((will be filled in by the editorial staff))

Entry for the Table of Contents (Please choose one layout only)

FULL PAPER

Based on the scaling relations between HO* and HOO* species and on the constant difference of 3.2 eV between the two levels, theoretical overpotential trends towards OER are reported for a wide range of oxides including rutile, perovskites, spinel rock salt and bixbyte. A good match exists between the theoretical and experimental trends. Comparing 3.2 eV with the ideal value of 2.46 eV, show the limitations for OER on oxide based electrocatalysts.

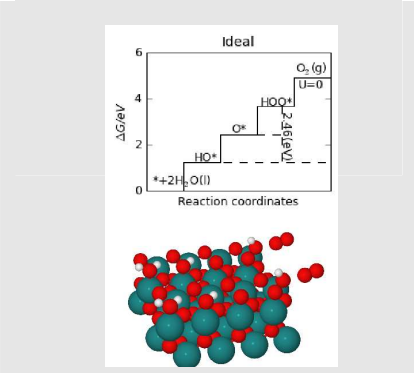

I.C.Man, H-Y.Su, F. Calle-Vallejo, H.A. Hansen, J.I. Martinez, N.G. Inoglu, J. Kitchin, T.F. Jaramillo, J.K. Nørskov, J. Rossmeisl *

Page No. – Page No.

Universality in Oxygen Evolution Electro-Catalysis on Oxide Surfaces

Supplementary material

1.1 Detailed calculation details:

A more detailed description of surface calculations are presented in the following paragraphs. In the **Figure 6** (which is shown also in the original paper) are shown all surfaces used in the calculations:

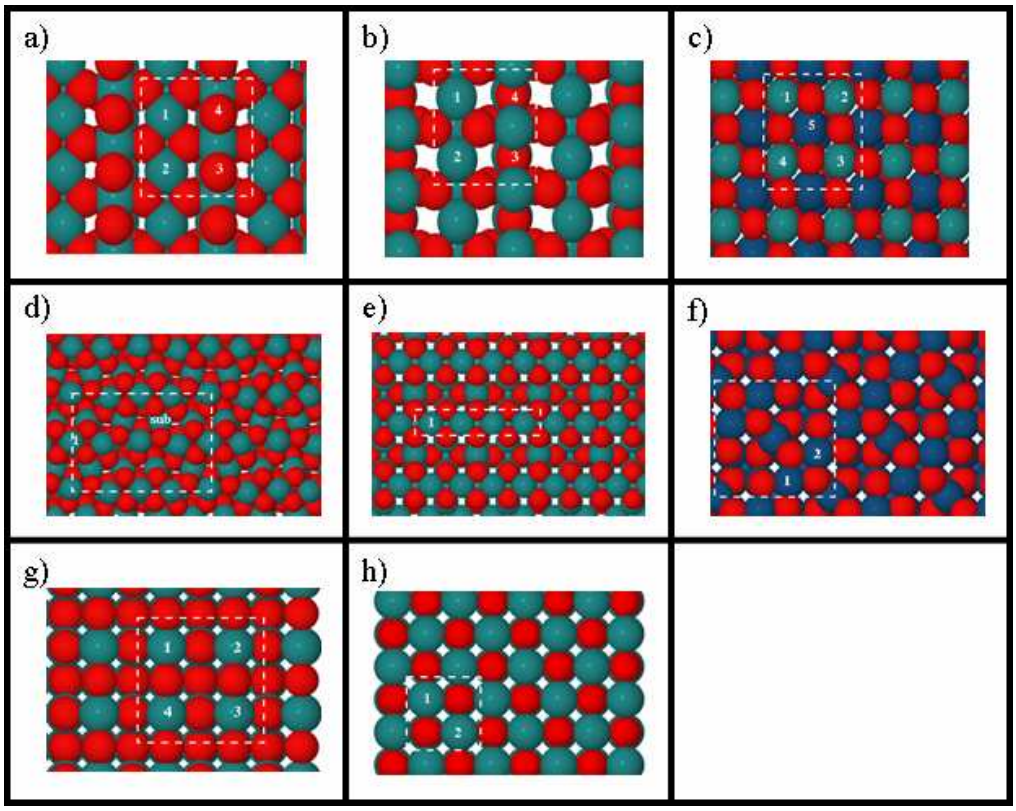

Figure 6. Visualization of the considered surface structures of metal oxides. The reaction takes place only on one site at a time a) Rutile -like stoichiometric surface (110) for MO_2 with M = Ti,V,Cr,Mn,Nb,Mo,Ru,Rh,Re,Ir,Pt,Sn. Red and light blue spheres represent O and metal atoms, respectively. Positions 1 and 2 represent the active sites (CUS). 3,4 represent the inactive sites (BRIDGE) and are covered with oxygen. b) Rutile like reduced surface (110) for MO_2. Positions 3,4 represent the active position (BRIDGE) and 1,2 the inactive position (CUS) with M = Ni, Pb, Sn. Red and light blue represent O and metal atoms, respectively c) Perovskites structure for $LaMO_3$ and $SrMO_3$ (100) surface with M = Ti, V, Mn, Fe, Co, Ni, Cu. Red, dark blue and light blue spheres represent O, La(Sr) and metal respectively. Sr and La are in the subsurface. (1,2,3,4) – represent the active sites/unit cell. 5 – represent the subsurface atom. d) Mn_2O_3 (110) surface structure. 1- represent the binding site e) Mn_3O_4 (001) surface structure. f) Co_3O_4 g) (001) Anatase like surface h) MO(100) surface with M = Mn, Ni.

We used a (2x2) unit cells for perovskite type oxides, (1x2) unit cells for rutile, anatase type oxides, PtO_2β($CaCl_2$) type and Mn_3O_4, and (1x1) unit cell for Co_3O_4 and Mn_2O_3. A four layer slab for rutile, anatase, perovskites and PtO_2β($CaCl_2$) and a 8 layer slab for Mn_2O_3, Mn_3O_4 and Co_3O_4 were employed, separated by a more than 16 Å of vacuum. A dipole correction was applied as well. The adsorbates together with the two topmost layers for the rutiles, anatase, persovskites oxides and PtO_2β($CaCl_2$), the four topmost layers for Mn_2O_3, Mn_3O_4 and Co_3O_4 were allowed to fully relax, while the other layers were fixed to their optimized bulk positions. The Brillouin zone of the systems was sampled with 4x4x1 Monkhorst – Pack grid for the rutile, anatase, persovskites oxides and PtO_2 -β($CaCl_2$) surfaces, and 2x3x1, 2x4x1, and 3x3x1 Monkhorst – Pack grid for Mn_2O_3, Mn_3O_4, and Co_3O_4 respectively.

When the reaction takes place on the clean surface, we call it low coverage regime. When coadsorbed species at next neighbors are present, the surface is said to be in a high coverage regime.

It has been shown that on rutile oxides oxygen on the bridge sites binds much stronger than on the cus sites , accordingly it is less likely for these positions to be active [1]. A stoichiometric surface with bridge sites occupied by oxygen was used for low coverage regimes, whereas the surface with one cus occupied by oxygen (see Figure 6a one of the two sites 1 or 2 is occupied with oxygen or another species, and the reaction is considered to take place on the other site) was considered for high coverage regime. The distance

between two neighboring cus sites on the rutile oxides is much smaller in comparison with perovskites and therefore the interaction of adsorbates at the sites can be expected to be stronger. For TiO_2 and SnO_2 only the low coverage regime is studied since the surface structures at high coverage regimes are unstable. PtO_2 was studied within the β ($CaCl_2$) symmetry which results from a small orthorhombic distortion of the rutile structure.

When the intermediates on rutile (110) surfaces are not stable on cus sites at all, nor even at low coverage regime, bridge positions are expected to act as the active sites (reduced surface to be seen in the Figure 6b, sites 1 and 2 are the inactive sites(cus) while 3 and 4 are the active site(bridge). PbO_{b2}, SnO_{b2} and NiO_{b2} present the reduce form. NiO_{b2} was studied under the $CaCl_2$ symmetry. For these systems high coverage regime means that the neighboring bridge site is occupied by oxygen (Figure 6b, site 3 or 4 is occupied by an oxygen atom while and on the other one the reaction is considered to take place; sites 1 and 2 are empty).

Anatase phase was considered for RuO_2, IrO_2 and $TiO_{2\,at}$ low and high coverage regime. High coverage regime means that all metallic sites are occupied with oxygens with the exception of one site where the reaction is considered to take place. (Figure 6f sites 1, 2, 3, and 4)

Also for the other three oxides: Mn_2O_3, Mn_3O_4 and Co_3O_4, low and high coverage regimes were considered (Figure 6d, Figure 6e and Figure 6f all the sites in line with 1 sites should be occupied with oxygen for high coverage regimes).

1.2 Derivation of the free energy relations:

In the following paragraph, we describe the relation between the reference electrode, which in our case is the Standard Hydrogen Electrode (SHE) and the chemical potential of protons and electrons, as seen from previous papers[1-2]. All these relations are used to calculate the free energy of the intermediates along the proposed reaction path. We assume the hydrogen electrode to be in equilibrium, i.e. the solvated protons and electrons are in equilibrium with the hydrogen in the gas phase:

$$H^+(aq) + e^- \leftrightarrow 1/2\, H_2(g)$$

In terms of chemical potentials the equilibrium is expressed as follows:

$$\mu_{H^+} + \mu_{e^-} = 1/2\, \mu_{H_2(g)} \tag{12}$$

The chemical potential of protons, electrons and hydrogen could be derived further as follow:

$$\mu_{H^+} = \mu^0_{H^+} + k_B T \ln a_{H^+} \tag{13}$$

$$\mu_{e^-} = \mu^0_{e^-} - eU \tag{14}$$

$$\mu_{H_2(g)} = \mu^0_{H_2} + k_B T \ln p_{H_2} \tag{15}$$

where a_{H^+} represents the activity of the protons, *eU* represents the shift in electron energy when a bias is applied and p_{H_2} is the partial pressure of hydrogen. $\mu^0_{H^+}$, $\mu^0_{e^-}$, $\mu^0_{H_2(g)}$ represent the chemical potential of protons, electrons and hydrogen at standard conditions ($p_{H_2} = 1bar$, $a_{H^+} = 1$, $T = 298.15K$). Thereby at these conditions, the relation can be written as:

$$\mu^0_{H^+} + \mu^0_{e^-} = \mu^0_{H_2(g)} \tag{16}$$

From computational point of view the chemical potential of hydrogen in the gas phase is much easier to calculate than the chemical potential of protons.

Formally μ is a Gibbs' free energy (G) while E_{DFT} becomes an enthalpy, H, if we add to it the zero-point energy correction (ZPE), calculated using DFT calculations of vibrational frequencies. These variables are related via the equation below:

$$G(T, p) = H(T, p) - TS(T, p) \tag{17}$$

where S is the entropy of the system. At T = 0, G and H become identical. The entropy values are taken from standard tables. Therefore we can define the standard chemical potential of hydrogen on the DFT scale as:

$$\mu^0_{H_2(g)} = E^{H_2(g)}_{DFT} + ZPE_{H_2(g)} - TS^0_{H_2(g)} \quad (18)$$

where S^0 is the standard entropy of hydrogen and is taken from thermodynamic tables for gas-phase molecules [3].
Another approximation is that for water in the liquid phase, by taking water in the gas phase as reference system. Since the pressure at which the chemical potential of liquid water is equal to the chemical potential of water in the gas phase, at *T* = 298.15 K is 0.035 bars, the approximation is done at this pressure:

$$\mu_{H_2O(l)} = \mu_{H_2O(g)} \quad (19)$$

On DFT scale, the potential of water in the gas phase is described as follows:

$$\mu_{H_2O(g)} = E^{H_2O(g)}_{DFT} + ZPE - TS^0(0.035bars) \quad (20)$$

The reason for this approximation is due to the difficulty in the calculation of the hydrogen bonds contribution to the total energy of water within standard DFT.
The last approximation we have done is the DFT energy of the oxygen in the gas phase. This is done indirectly since is hard to calculate accurately with DFT the oxygen molecule. We use the experimental value of 2.46 eV of the standard free energy change of the reaction: $H_2O(l) \leftrightarrow 1/2\,O_2(g) + H_2(g)$. Thereby we leave from the following relation:

$$G^0_{H_2O(l)} - 1/2 G^0_{O_2(g)} - G^0_{H_2(g)} = 2.46eV \quad (21)$$

Thus if we write everything in terms of DFT energy, we replace Eq. 7 and 9 in Eq. 10 and thereby we can approximate the free energy of an oxygen molecule in terms of the $H_2O(g)$, $H_2(g)$ energetic as follows:

$$(E^{O_2(g)}_{DFT} + ZPE_{O_2(g)} - TS^0_{O_2(g)}) = 4.92 + 2(E^{H_2O(g)}_{DFT} + ZPE_{H_2O(g)} - TS^0_{H_2O(g)}) - 2(E^{H_2(g)}_{DFT} + ZPE_{H_2(g)} - TS^0_{H_2(g)}) \quad (22)$$

Since the proposed mechanism for OER consists of four intermediate steps, the free energies for all steps will be derived further on, for the temperature *T* = 298.15 K. The first step is water splitting on the active site with a release of a proton and an electron:

$$H_2O(l) + * \leftrightarrow HO* + H^+ + e^-$$

$$\Delta G_1 = G_{HO*} + \mu_{H^+} + \mu_{e^-} - G_* - \mu_{H_2O(l)} \quad (23)$$

where G_{HO*} and G_* are the free energies of the surface with and without HO* respectively and could be written in terms of DFT energies:

$$G_{HO*} = E^{HO*}_{DFT} + ZPE_{HO*} - TS^0_{HO*} \quad (24)$$

$$G_* = E^*_{DFT} \quad (25)$$

The free energy of the slab is calculated at athermal limit and its temperature dependence is ignored as it is negligible compared to that of the gas.

Replacing relations 2, 3 and 8 in 12 we get:

$$\Delta G_1 = G_{HO*} + \mu^0_{H^+} + k_B T \ln a_{H^+} + \mu^0_{e^-} - eU - G_* - \mu_{H_2O(g)} \quad (26)$$

Further on, substituting equations 5, 7, 9, 13 and 14 in 15, allows to express the free energy of the reaction on the DFT energy scale:

$$\Delta G_1 = E_{DFT}^{HO*} - E_{DFT}^{*} - (E_{DFT}^{H_2O(g)} - 1/2\, E_{DFT}^{H_2(g)}) + (\Delta ZPE - T\Delta S^0) + k_B T \ln a_{H^+} - eU \quad (27)$$

The second step of the reaction is oxidation of the HO* species to O* with release of a proton and of an electron:

$$HO* \leftrightarrow O* + H^+ + e^- \quad (28)$$

The change in free energy for the forward reaction is:

$$\Delta G_2 = G_{O*} - G_{HO*} + \mu_{H^+} + \mu_{e^-} \quad (29)$$

where G_{O*} , G_{HO*} represent the free energies of the surfaces with O* and HO* species.

Replacing again the same equations as in the case for the first step in Eq. 17, the free energy could be expressed as follows:

$$\Delta G_2 = E_{DFT}^{O*} - E_{DFT}^{HO*} + 1/2\, E_{DFT}^{H_2(g)} + (\Delta ZPE - TS^0) + k_B T \ln a_{H^+} - eU \quad (30)$$

The third step is represented by the water splitting on top of oxygen with the corresponding change in free energy:

$$O* + H_2O(l) \leftrightarrow HOO* + H^+ + e^- \quad (31)$$

$$\Delta G_3 = G_{HOO*} + \mu_{H^+} + \mu_{e^-} - G_{O*} - \mu_{H_2O(l)} \quad (32)$$

The same equations as for step one and two are replaced gradually in the Eq. 21. The relation for G_{O*} in terms of DFT energies is similar to the relation for G_{HO*}. In the end we get:

$$\Delta G_3 = E_{DFT}^{HOO*} - E_{DFT}^{O*} - (E_{DFT}^{H_2O(g)} - 1/2 E_{DFT}^{H_2(g)}) + (\Delta ZPE - T\Delta S^0) + k_B T \ln a_{H^+} - eU \quad (33)$$

The last step is the evolution of oxygen:

$$HOO* \leftrightarrow * + O_2(g) + H^+ + e^- \quad (34)$$

$$\Delta G_4 = G_* + G_{O_2(g)} + \mu_{H^+} + \mu_{e^-} - G_{HOO*} \quad (35)$$

With Eq.24, we proceed again as in the previous steps, and we use also Eq.11, to obtain the expression in terms of DFT energies:

$$\Delta G_4 = E_{DFT}^{*} - E_{DFT}^{HOO*} + (2E_{DFT}^{H_2O(g)} - 1/2 E_{DFT}^{H_2(g)}) + 4.92 + (\Delta ZPE - T\Delta S^0) + k_B T \ln a_{H^+} - eU \quad (36)$$

In Table 2 **:** Binding energies of HOO*, HO*, O* species on oxide surfaces at low and high coverage regime, ZPE and TS for all the relevant species are listed at *T* = 298.15 K. For the adsorbed species the ZPE have been calculated for an adsorbate at the cus-site of RuO_2 and is considered to be the same for each oxide. The entropy corrections for the adsorbates on the surface are considered zero, since the main contribution to the entropy is due to the translational entropy.

Table 1: Zero point energies and entropic corrections at 298 K.

	TS	TΔS	ZPE	ΔZPE	ΔZPE̦-TΔS
$H_2O(l)$	.67	0	.56	0	0
$*OH+1/2H_2$	.20	-.47	.50	-.06	.41
$*O+H_2$	.41	-.27	.34	-.22	.05
$1/2O_2+H_2$	.73	.05	.32	-.24	-.29
H_2	.41	-	.27	-	
$1/2O_2$	.32	-	.05	-	
O*	0	-	.07	-	
OH*	0	-	.36	-	

Table 2 : Binding energies of HOO*, HO*, O* species on oxide surfaces at low and high coverage regime

Low coverage regime			
	ΔE_{O*}(eV)	ΔE_{HO*} (eV)	ΔE_{HOO*} (eV)
MoO_2	0,66	-0,02	3,02
IrO_2	1,32	-0,23	2,79
RuO_2	2,34	0,60	3,47
PtO_2	3,23	1,14	
TiO_2	4,57	1,73	4,86
SnO_2	5,00	1,61	
RhO_2	2,64	0,68	3,63
NbO_2	-0,86	-0,97	2,36
ReO_2	-1,03	-0,96	
VO_2	0,48	0,25	3,52
MnO_2	2,70	1,095	4,15
CrO_2	1,64	1,12	4,15
$PtO_{2\beta}$	2,3	0,83	3,89
NiO_{2b}	2,66	0,65	
PbO_{2b}	2,34	0,89	4,21
SnO_{2b}	0,52	-0,05	3,41
$SrTiO_3$	3,88	1,22	4,51
$SrVO_3$	-0,10	-0,26	2,96
$SrCrO_3$	0,89	0,37	3,60
$SrMnO_3$	2,27	0,82	4,02
$SrFeO_3$	2,95	1,29	4,30
$SrCoO_3$	2,97	1,15	4,06
$SrNiO_3$	3,82	1,79	4,54
$SrCuO_3$	4,72	1,94	4,92
$SrRuO_3$	2,23	0,72	3,69
$LaTiO_3$	-1,85	-1,55	1,84
$LaVO_3$	-0,78	-0,61	2,57
$LaCrO_3$	0,66	0,17	3,30
$LaMnO_3$	1,36	0,27	3,47
$LaFeO_3$	2,2675	0,79	3,87

$LaCoO_3$	2,64	1,10	4,12
$LaNiO_3$	3,07	1,15	4,22
$LaCuO_3$	4,89	2,03	5,00
$LaRuO_3$	1,84	0,35	3,35
Mn_3O_4	2,04	0,56	3,76
Mn_2O_3(I)	1,25	-0,19	3,13
Mn_2O_3(II)	0,93	-0,15	3,26
MnO_2	2,75	1,14	4,24
Co_3O_4	2,74	1,02	3,94
NiO	2,27	0,46	3,51
High coverage regime			
MoO_2	1,02	0,05	3,40
IrO_2	1,61	-0,10	3,02
RuO_2	2,68	0,96	3,92
PtO_2	2,77	0,74	
TiO_2	5,53	2,39	
SnO_2	5,28	1,90	
RhO_2	2,8	0,76	3,76
NbO_2	-0,51	-0,83	2,64
ReO_2	-0,64	-1,10	2,56
VO_2	0,78	0,16	3,75
MnO_2	3,08	1,38	4,556304
CrO_2	2,14	1,42	4,976006
$PtO_{2\beta}$	2,31	0,82	3,7942
NiO_{2b}	2,89	0,65	3,8557
PbO_{2b}	2,98	0,67	4,0409
SnO_{2b}	0,17	-1,02	2,5509
Mn_3O4	2,4	0,69	3,85
Mn_2O_3 (II)	2,29	0,84	3,92
Co_3O_4	2,74	1,02	3,94

.

References:

[1] J. Rossmeisl, Z. W. Qu, H. Zhu, G. J. Kroes, J. K. Norskov, *Journal of Electroanalytical Chemistry* **2007**, *607*, 83.

[2] a)J. K. Norskov, J. Rossmeisl, A. Logadottir, L. Lindqvist, J. R. Kitchin, T. Bligaard, H. Jonsson, *Journal of Physical Chemistry B* **2004**, *108*, 17886; b)J. Rossmeisl, A. Logadottir, J. K. Norskov, *Chemical Physics* **2005**, *319*, 178.

[3] P. W. Atkins, *Physical Chemistry*, sixth ed., Oxford University Press., **1998**.

Probing the Reactivity of Transition-Metal Oxides using Density Functional Theory: Transition State Scaling Relations

A. Vojvodic,[1,2,*] F. Calle-Vallejo,[2] F. Abild-Pedersen,[1,2] W. Guo,[2] S. Wang,[2] A. Toftelund,[2] F. Studt,[1,2] J. I. Martinez,[2,3] J. Shen,[2] I. C. Man,[2] J. Rossmeisl,[2] T. Bligaard,[2] and J. K. Nørskov[1,4,2]

[1]*SLAC National Accelerator Center, SUNCAT Center for Interface Science and Catalysis Stanford University, Stanford, CA 94025 USA*
[2]*Center for Atomic-scale Materials Design, Department of Physics, Technical University of Denmark, DK-2800 Kgs. Lyngby, Denmark*
[3]*Dpto. de Física Teórica de la Materia Condensada, Universidad Autónoma de Madrid, E-28049 Madrid, Spain*
[4]*Department of Chemical Engineering, Stanford University, Stanford, CA 94305 USA*

(Dated: December 17, 2010)

Versatile transition state scaling relations, sometimes referred to as Brønsted-Evans-Polanyi (BEP) relations, are found for a wide range of transition-metal oxides including rutiles and perovskites. For oxides, the relation depends on the type of oxide, the active site and the dissociating molecule. Hence, the universality rule previously found for metals in not valid for oxides. The slope of the BEP relation is tightly coupled to the adsorbate geometry in the transition state. If it is final state-like the dissociative chemisorption energy can be considered as a descriptor for the dissociation. If it is initial state-like, on the other hand, the dissociative chemisorption energy is not suitable as descriptor for the dissociation. Dissociation of strongly bond molecules belongs to the former and weakly bond molecules to the latter group. We show, for the prototype system La-perovskites, that there is a continuous "cyclic" behavior in the transition state characteristics upon change of the active transition metal of the oxide. Taken together the findings imply that the BEP relation concept should be generalized, which we also discuss.

INTRODUCTION

Brønsted-Evans-Polanyi (BEP) relations [1, 2] have in the last couple of years been established quantitatively from density functional theory (DFT) calculations for a number of molecular surface reactions on different transition-metal surfaces [3–8] and for a few transition-metal compound systems [9, 10]. Several reactions on transition metals are found to follow a universality rule, that is, they obey a reactant independent but surface structure dependent linear BEP relation [3, 4, 11, 12]. In this paper, the more stringent term transition state scaling relations, derived from the concept scaling relations [13] that describe the linear relationship between molecular adsorption energies and atomic adsorption energies, is used interchangeably with the term BEP relation. In other words, the term transition state scaling relation is based on the fact that there is a linear scaling relation at every point along the dissociation path.

In spite of considerable progress [14], theoretical understanding of the reactivity of transition-metal oxides is less established than that of pure transition metals. This paper aims to shed new light on the reactivity of oxides. The focus is to probe the reactivity by (i) investigating whether BEP relations exist for dissociation of small molecules on transition-metal oxides and (ii) whether these obey the universality rule found for metals [3, 11]. The findings have implications for understanding reactions that can be characterized by dissociation or association of diatomic molecules, which is the case for many catalytic reactions. Together with scaling relations [15, 16] the results of this paper lay the basis for microkinetic modeling of different reactions where the considered molecules are a part of. This because it was shown in Ref. [11] that the existence of linear BEP relations directly leads to volcano curves where the key parameter is the dissociative energy of the reactants. Hence, our results may enable the derivation of a volcano curve for the activity of oxides. Also, this study shows that the transitions state scaling relations are strongly dependent on the bond properties of the dissociating molecules.

This study includes a large group of oxides from two subgroups, namely binary MO_2 oxides in the rutile structure and ternary oxide ABO_3 in the perovskite structure. In this study, the rutile surface under consideration is the most stable (110) surface [17]. For perovskites, the (001) surface can be either AO- or MO_2- terminated. Here, the MO_2-terminated perovskite surface is considered due to its higher stability [18]. Also, results on and a comparison with pure metal surfaces are presented. The different metal constituents in the oxides are M = Ti, Mo, Ru, Ir, Pt, and A = Sr, La, and B = Sc, Ti, V, Cr, Mn, Fe, Ru, Co, Ni, Cu. The chosen probing molecules are the homonuclear diatomic molecules H_2, N_2, O_2, Cl_2, Br_2, and I_2, the heteronuclear diatomic molecules NO, CO, OH, HCl, HBr, and HI, and the triatomic molecule H_2O. Dissociation is studied not only on different oxide surfaces but also on different active sites on a given surface.

It should be noted that while ordinary DFT calculations within the generalized gradient approximation (GGA) have proven to give reliable and accurate results

for adsorption energies [19, 20] on transition metals, similar calculations for oxides are fewer and not as well tested, although, there are studies of oxides where a good agreement between DFT calculations and experiments exists, for example, Refs. [17, 21]. The possible limitations and shortcomings of GGA on oxides is a current research topic [22–25]. This study is based on the variations in dissociation and transition state energies between different systems and should hence not be as sensitive as the absolute energies.

CALCULATION DETAILS

All calculations are performed using the plane wave DFT method as implemented in the DACAPO code [19, 26]. The surfaces are modeled using slabs consisting of four stoichiometric layers in a 2×2 unit cell geometry. Repeated slabs are separated by a vacuum region of at least 15 Å (18 Å) for rutiles (perovskites). During structure relaxation, the topmost two layers are relaxed while the others are kept in the optimized bulk positions. The Kohn-Sham equations are solved using a basis set of plane waves with an energy (density) cutoff of 350-400 eV (500 eV) and the Brillouin zone is sampled with a $4\times4\times1$ Monkhorst-Pack grid. To describe the core electrons, the Vanderbilt ultrasoft pseudopotentials [27] are used. The exchange correlations interactions are modeled with the RPBE functional [19] and the dipole correction is included according to the scheme in Ref. [28].

Both the dissociative chemisorption energies (ΔE_{diss}) and the transition state (TS) energies (ΔE_{TS}) are calculated relative to the gas phase diatomic molecule, if not stated otherwise. The O_2 energy is calculated from H_2O and H_2 to avoid the well-known DFT error in the O_2 energy . The transition state is determined by utilizing a fix-bond length method, where the energy for various fixed bond lengths of the molecule are calculated while the remaining degrees of freedom of the system are completely relaxed. For the considered systems where there is no TS barrier, ΔE_{TS} is defined as the highest energy along the reaction pathway.

The adsorbate coverage in all systems is 1/4 ML relative to the number of metal atoms in the surface layer. In addition, the influence of the adsorbate–adsorbate interaction on the BEP relations is investigated by performing calculations of N_2 and NO on RuO_2 and PtO_2 in a 2×3 unit cell geometry corresponding to a 1/6 ML coverage. The results show that the BEP relations are not affected by the coverage even though the absolute ΔE_{diss} and ΔE_{TS} energies change slightly, but in the same amount to preserve the BEP relation.

TABLE I: Linear relations between ΔE_{TS} and ΔE_{diss} values for the considered systems. For each individual fit the α and β values (see Eq. 1) are given together with the mean absolute error. Note that for some systems there exist several BEP lines, see the text for more details.

	molecule	α	β	MAE
rutile				
cus–cus	N_2	0.95	0.46	0.08
	O_2	0.84	0.42	0.35
	NO	1.10	0.18	0.32
	CO	0.93	0.42	0.03
	all	0.93	0.48	0.25
	Cl_2	0	0	0
	Br_2	0	0	0
		1.0	0	0
	I_2	0	0	0
		1.0	0	0
br–br	O_2	0.75	1.94	0.53
br–cus	O_2	0.83	0.40	0.13
	NO	0.86	0.40	0.06
	all	0.84	0.42	0.10
O_{cus}–cus	H_2O	1.30	0.07	0.02
O_{br}–cus	OH	0.92	0.06	0.10
	H_2O	0.87	0.16	0.05
	all	0.97	0.21	0.09
	HCl	0	0	0
	HBr	0	0	0
	HI	0	0	0
O_{cus}–O_{cus}	H_2	0.14	2.73	0.27
O_{br}–O_{br}	H_2	0	0	0
		1.0	0	0
perovskite				
$LaBO_3$	N_2	0.73	1.75	?
	O_2	0.42	0.24	?
	NO	0.68	0.92	?
	CO	1.39	1.33	0.28
$SrBO_3$	N_2	0.75	1.40	?
	NO	0.65	0.82	?
	all	0.71	1.42	0.68
metal				
(211)	N_2	0.83	1.85	0.20
	O_2	0.58	0.89	0.26
	NO	0.71	1.09	0.29
	all	0.81	1.56	0.36
(111)	N_2	0.74	2.36	0.23
	O_2	0.64	1.69	0.09
	NO	0.68	1.66	0.15
	all	0.74	2.06	0.31

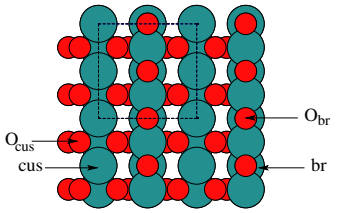

FIG. 1: Top view of the (110) rutile surface together with different considered adsorption sites and the unit cell. Here, cus denotes the coordinately unsaturated cite on top of a fivefold coordinated metal atom, the br denotes the bridge site between two fourfold coordinated metal atoms [note this corresponds to a (110) surface without O atoms], O_{br} denotes the site on top of a O in the bridge site, O_{cus} denotes the cite on top of a O in the bridge site between two fivefold metal atoms. [OBS: Remake fig in vmd]

RESULTS AND DISCUSSION

The general result is that there exists a characteristic correlation between ΔE_{TS} and ΔE_{diss} for every molecule on a given dissociation site of an oxide or metal, see Figs. 2, 3, and 4. It is, however, a priori not given that one should be able to describe a BEP relation by a single linear relation. Due to the versatile nature of this correlation on oxides, as will be discussed in more detail below, we introduce the concept of generalized BEP relations to distinguish between the different situations that may occur. Such a generalized BEP relation consists of piecewise linear BEP lines, each given by

$$\Delta E_{TS} = \alpha \Delta E_{diss} + \beta, \quad (1)$$

see Table I for the individual fits. For a given dissociation site on an oxide surface, we have found two major classes either I) a single BEP line or II) a collection of piecewise linear BEP lines (see Fig. 2). The latter can in turn be classified in two subclasses, given by whether the BEP relation is a single- or multi-valued function of ΔE_{diss}, denoted as IIa) and IIb), respectively. Our findings also show that the universality rule previously found for transition metals [3] is on a detailed scale not valid for oxides. In the following, the different material classes are discussed individually and compared with each other.

Rutiles

For rutiles, the calculations reveal (see Fig. 2) discrete BEP lines for each and one of the considered dissociation sites: cus–cus, br–br, br–cus, O_{cus}–cus, O_{br}–cus, O_{cus}–O_{cus}, and O_{br}–O_{br}. The notation of the dissociation site follows the geometry of the final state, see Fig. 1 where the different sites are indicated. For example, O_{cus}–cus denotes that one of the two molecule fragments is adsorbed on a O_{cus} site and the other one on a cus site.

Class I: We find that the br–br site, br–cus site, and the O_{cus}–O_{cus} site (see the respective subfigure in Fig. 2) belong to class I with a simple BEP relation consisting of only one line. The slopes of the BEP lines depend on the active site ($\alpha_{br-br} = 0.75$, $\alpha_{br-cus} = 0.84$, and $\alpha_{O_{cus}-O_{cus}} = 0.14$).

The adsorbate geometry in the TS differs between the active sites. For the br–cus site, the bond length between the two molecular fragments in the TS is considerably elongated, which means the adsorbed molecule has lost its molecular identity, and the TS geometry resembles the one of the final state (FS), that is the TS is FS-like. The TS geometry has more FS character the closer the point is to the recombination line, which is the line defined by $\Delta E_{TS} = \Delta E_{diss}$. For the O_{cus}–O_{cus} site, the bond length in TS is close to the bond length of a free molecule, that is the TS geometry is IS-like. The TS geometry in the br–br site is less FS-like than the one of the br–cus site, and therefore $\alpha_{br-br} < \alpha_{br-cus}$. Hence, one can conclude that a FS-like TS geometry results in a BEP line with a slope close to unity. The more IS-like the TS geometry is, the larger the deviation from the recombination line and the closer to zero the α is. This in turn indicates that ΔE_{TS} is very weakly if at all dependent on ΔE_{diss}.

Class IIa: We find one site, the O_{br}–O_{br} site, that can be classified as IIa (see the O_{br}–O_{br} subfigure in Fig. 2). The BEP line consists of two linear parts, one that follows the recombination line, with a TS geometry which is FS-like, and one where ΔE_{TS} is independent on ΔE_{diss}, where the TS geometry is IS-like. This illustrates that ΔE_{diss} is not suitable as descriptor for dissociation for this active site for the H_2 molecule. The origin of the discontinuity in the BEP relation can thus be correlated to the TS geometry, which in turn may be traced to the properties of the H_2 molecule with its short bond length and the H atom's tendency to donate its only electron.

Class IIb: The cus–cus and the O_{br}–cus sites (see the respective subfigure in Fig. 2) belong to class IIb, which is the class with a BEP relation with largest amount of features. It again consists of two parts as the BEP of case IIa but now the BEP relation is a multivalued function of ΔE_{diss}. This means that different molecules follow significantly different BEP lines. Hence, the universality found for metals is not applicable to all molecules on oxides, but rather to groups of molecules with similar properties. For the molecule group with a BEP line with $\alpha \sim 0$, ΔE_{TS} is independent of the ΔE_{diss}. This supports the finding of case IIa, that ΔE_{diss} is not a descriptor for dissociation of some molecules. From the geometrical investigation, we again find that the slope of the BEP line depends on whether the adsorbates TS geometry is FS-like, which results in an α value close to unity, or if it is IS-like, which results in an α value that approaches

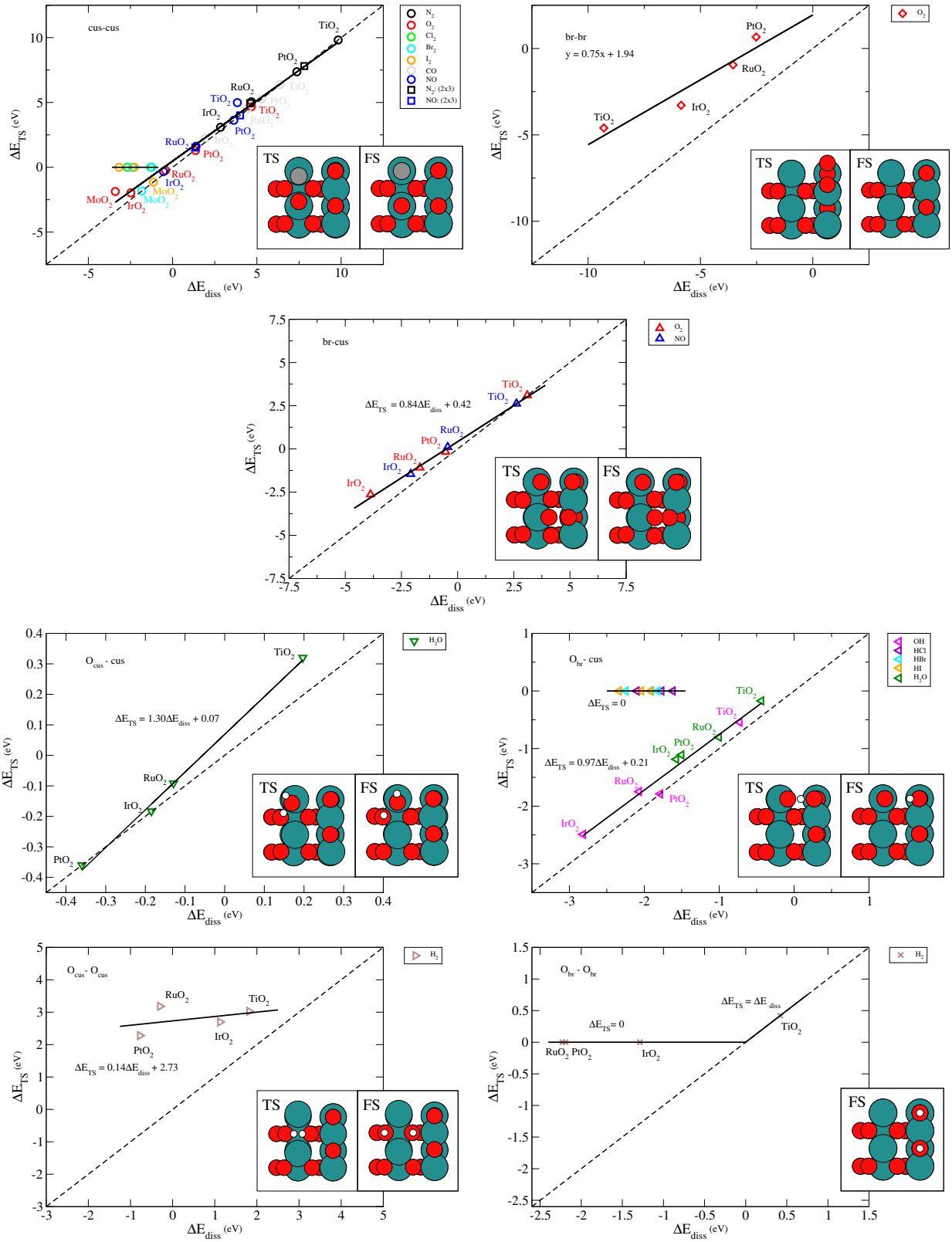

FIG. 2: Calculated transition state energy ΔE_{TS} for dissociation as a function of dissociative chemisorption energy ΔE_{diss} of diatomic molecules on rutile (110) surfaces. The dissociation site is indicated in each panel. The solid black line represents the linear fit to the calculated data. The dashed line illustrates the recombination line *i.e.* $\Delta E_{TS} = \Delta E_{diss}$. Also, a top view of the structures for the transition state (TS) and the dissociated state, that is final state (FS), are shown. The blue, red, gray, and white balls represent Ru, O, C, and H atoms, respectively. [OBS:Redraw fig with only one legend to make more space for each subfigure. Make new structure figures in vmd.]

zero.

From the above analysis, the molecules can be grouped in two groups: molecules with quite strong or very strong intramolecular bonds, fore example, N_2, O_2, CO, and NO, and very reactive molecules, for example, the diatomic homogeneous halide based molecules or diatomic heteronuclear weakly bond molecules containing halide atoms. Exceptions to this are I_2 and Br_2 on MoO_2 which are found to have TSs that are FS-like. In conclusion, the BEP relation is strongly dependent on the dissociating molecule.

It is also found that many molecules prefer to dissociate over the symmetric cus–cus site. This is presumably because of the completion of the octahedral geometry of the otherwise under-coordinated surfaces atoms, which also can be seen as a natural continuation of the bulk. Nevertheless the heteronuclear diatomic molecules that contain H prefer the asymmetric O_{br}–cus site, where the H recombines with O.

Dissociation of the triatomic molecule H_2O into OH and H over the O_{br}–cus site shows similar features as the diatomic molecules, see the O_{br}–cus subfigure in Fig. 2. The BEP line for H_2O on the O_{cus}–cus site has a slope larger than one, which can be attributed to the TiO_2 and the RuO_2 result. Since $\alpha > 1$ is unphysical it means that there are probably several BEP lines. This might be due to the different substrates belonging to different periods in the periodic table. A difference has been found for the formation energies of perovskites in Ref. [29] due to this effect. Another explanation for this deviation is existence of several BEP lines for different energy regions just as for H_2 dissociation on O_{br}–O_{br}. It is the OH group that determines the trend for both activation sites.

Comparing sites where only surface metal atoms are involved in the dissociation, *i.e.* the cus–cus, br–br, br–cus site, one finds that for a given adsorbate the magnitude of the slopes of the BEP relations can be ordered as $\alpha_{\text{br–br}} < \alpha_{\text{br–cus}} < \alpha_{\text{cus–cus}}$. This clearly illustrates the BEP slope dependence on the active site and that the α values can be extrapolated. On a br site (note that this site is obtained by removing the O atoms and forming a non-stoichiometric termination of the MO_2(110) surface, see Fig. 1) each adsorbate atom interacts with two fourfold coordinated surface metal atoms, while on the cus site each adsorbate atom interacts only with one fivefold surface metal atom. Hence, the br site, which resembles a vacancy site to some extent, is highly under-coordinated and therefore substantially more reactive than the cus site. The BEP slope is smallest for br–br since the surface atoms are more reactive and the intramolecular bonds will break more easily, resulting in a TS geometry that is less FS-like.

For some molecules *e.g.* N_2 on metal surfaces it has been shown that there is a geometric effect influencing the form of the BEP relation [3, 30]. One could possibly talk about such an effect for the br–br site, which as described above has a clearly different geometry than the rest of the considered active sites. Another site where the BEP line experiences a rigid shift away from the recombination line is the O_{br}–cus site. This should be compared with the cus–cus site. Dissociation over these two active sites involves the same amount of surface atoms, however, these surface atoms have different coordination and are of different atomic species. Despite of that there is no straightforward one-to-one correspondence between the geometry of the topology of the active site and the α value for the oxides.

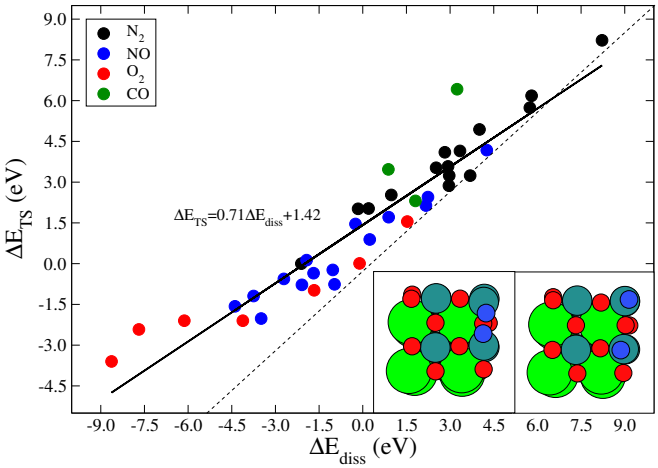

FIG. 3: Same as in Fig. 2 but for the (100) perovskite surfaces.

In conclusion, the BEP relations for rutiles show a delicate interplay between the type of molecule and the electronic structure of the active site in the conformation of the TS.

Perovskites

Figure 3 shows the results for the (100) surfaces of La- and Sr-perovskites. Also for this group of oxides transition state scaling relations exist with an averaged BEP relation given by $\Delta E_{TS} = 0.71\Delta E_{diss} + 1.42$. On a zoomed out level the averaged BEP relation can can be classified as I. However, the partial relations for each adsorbate and perovskite group, presented in Table I, show that different adsorbates obey their own BEP relations and therefor the perovskites fall in the class IIa or IIb depending on the interpretation of the generalized concept. In other words, the universality is not valid for perovskites either.

The considered adsorption site on perovskites is atop of the surface B atoms, which leads to a locally fully coordinated structure around the surface B atom (see inset in Fig. 3). For the perovskites adopting or being very close to the ideal cubic symmetry, the relaxed adsorbate geometry is where the two adsorbed molecule atoms are positioned symmetrically atop of the B surface atoms.

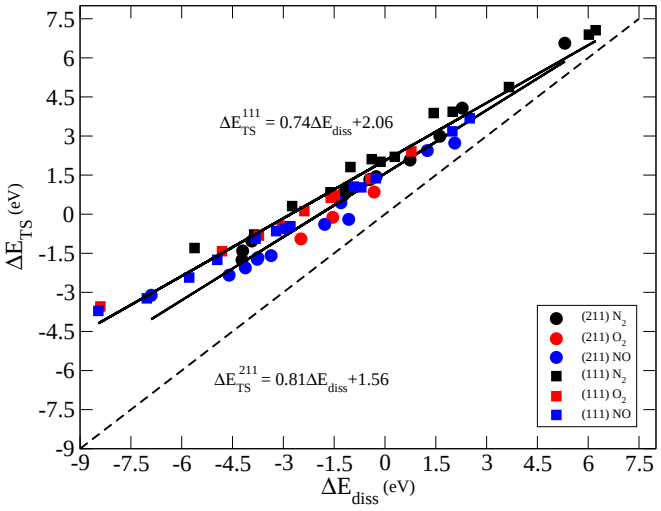

FIG. 4: Same as in Fig. 2 but for the (211) and the (111) transition-metal surfaces.

Otherwise the adsorbates geometry gets skewed due to tilting of the octahedral framework.

When it comes to the transition state geometries, the perovskites to the left in ΔE_{diss} have shorter N–N, N–O, and O–O distances (d_{N-N}, d_{N-O}, and d_{O-O}, respectively) in the TS compared with the ones to the right, which approach the recombination line. Therefore, the latter have a TS that resembles much more the FS. This is a result in agreement with the results for the rutiles and will be further discussed below.

Metals

For comparison we present some data for dissociation on the (211) and (111) metal surfaces, in Fig. 4. The BEP relations for the lowest TS barriers can be characterized as class I, with the averaged relations given by $\Delta E_{TS} = 0.81\Delta E_{diss} + 1.56$ and $\Delta E_{TS} = 0.75\Delta E_{diss} + 2.06$ for the (211) and (111) surfaces, respectively. They are in agreement with the relations $\Delta E_{TS} = 0.87\Delta E_{diss} + 1.34$ and $\Delta E_{TS} = 0.90\Delta E_{diss} + 2.07$, for the (211) and (111) surfaces, respectively, from Ref. [3]. The difference in the relations found in the current study and the one in Ref. [3] is assigned to the somewhat different composition of the calculated data points on which the linear regressions are made. In the current study, metal surfaces in a broader reactivity range are included showing that inclusion of the more reactive metals, that is more negative ΔE_{diss}, results in a bigger deviation from the recombination line. The individual fits for each adsorbate on these surfaces are given in Table I. It is found that O_2 has an α-value that is substantially different from the averaged BEP α-value. Again implying that there is a fine structure in the BEP relation that so far has been not taken into account.

Comparison between surfaces of different materials

A comparison between the transition state scaling relations associated with the lowest TS barriers for metals and oxides is needed at this point. We find (considering the N_2, O_2 and NO molecules) that both oxides groups obey relations that are closer to the recombination line, which is the desirable BEP relation with no TS barriers, than the (111) and (211) metal surfaces. The rutiles have very low if any TS barriers at all, while the perovskites have clear TS barriers. The averaged α-value for perovskites is closer to the one of (111) of the two groups of metal surfaces, while the averaged β-value is closer to the one of the (211) surfaces. Hence, there is a major difference between the two oxides groups. The fact that the strongly bond molecules on rutiles dissociate without any substantial barriers has a great impact on their applications. In the for catalysis relevant energy region, ΔE_{diss} in the vicinity of zero, we find rutiles as RuO_2 and IrO_2.

Dissociation energetics: example La-perovskites

If the reactivity of an oxide solely would be based on the position of the metal atom constituent in the periodic table, the reactivity trend should be monotonous along a period. The situation is, however, more complicated see for example results for O_2 dissociation on the cus-cus site in Fig. 2. To pinpoint one example from the perovskite results, the reactivity of the $LaBO_3$ perovskites for N_2 dissociation is $LaScO_3$ <$LaCuO_3$ <$LaNiO_3$ < $LaCoO_3$ < $LaFeO_3$ < $LaTiO_3$ < $LaMnO_3$ < $LaVO_3$ < $LaCrO_3$.

To elucidate this non-monotonous effect, we consider the example of N_2, NO, and O_2 dissociation on $LaBO_3$ perovskites with different B metal atoms belonging to the same period, here taken as 3*d*. For each dissociating molecule the transition state scaling relation, see the upper panel of Fig. 5, (i) approaches the recombination line for high ΔE_{diss} values and (ii) deviates away from the recombination line as the ΔE_{diss} becomes more negative. The α-values change as $0.73 \rightarrow 0.68 \rightarrow 0.42$ for $N_2 \rightarrow$NO$\rightarrow O_2$. This is the same order as the combined electronegativity of the individual adsorbate atoms, *i.e.* their tendency to take away electrons from the surface.

For each adsorbate, we will based on the calculated ΔE_{diss} and ΔE_{TS} values as a function of the group number of the B metal (see lower panel of Figure 5) together with the calculated potential energy along the dissociation path (see Figure 6) argue on the form of the BEP relation.

We find that the ΔE_{diss} and ΔE_{TS} vary in a characteristic way as a function of the group number of the B metal. As the group number of B changes from $3 \rightarrow 11$, the $|\Delta E_{diss} - \Delta E_{TS}|$ difference takes the value from zero through a maximum and becomes zero again, that is a

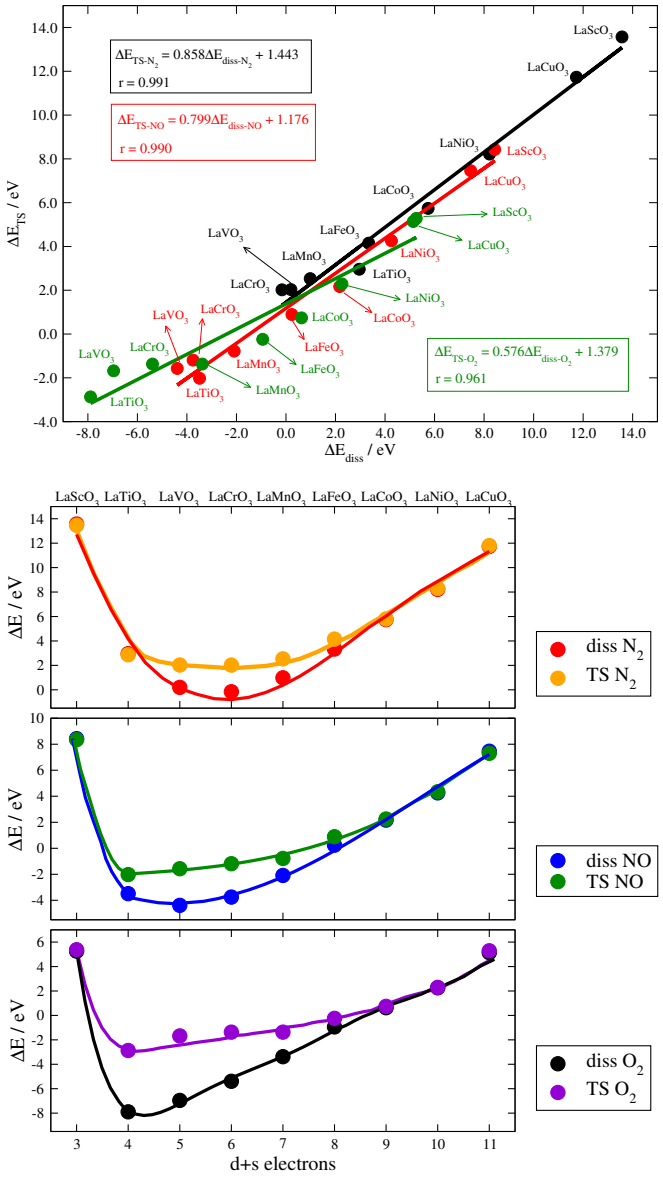

FIG. 5: (upper panel) The BEP relation for $LaBO_3$ for consecutive B metals belonging to the 3*d* metals. (lower panel) The dissociation energy ΔE_{diss} and the transition states energy ΔE_{TS} as a function of group number of the B constituent in the perovskite. The solid lines represents a third order polynomial fit to the calculated data given by the circles.

"cyclic" behavior. The biggest $|\Delta E_{diss} - \Delta E_{TS}|$ value coincides with the minimum in ΔE_{diss} and ΔE_{TS}. These minima occur for group number 6 ($LaCrO_3$), 5 ($LaVO_3$), and 4 ($LaTIO_3$) for N_2, NO, and O_2, respectively. It is these surfaces at the minimum that coincide with the leftmost points on the three individual BEP lines (see Figure 5).

Since the ΔE_{diss} and ΔE_{TS} curves coincide for group numbers 3 and 11 this means that the α-value is correlated to the $|\Delta E_{diss} - \Delta E_{TS}|$ value for $LaCrO_3$ (for N_2), $LaVO_3$ (for NO), and $LaTIO_3$ (for O_2) in a way that a big difference gives a bigger deviation from the recombination line and hence a smaller α-value.

???It is interesting to note that, if looking at the total amount of valence electrons of the system, that is, N plus the valence electrons of the dissociating molecule, places the minima at the same place with a total of 16 electrons. This opens up for predictability possibilities.???

The fact that the reactivity order of the La-perovskites does not follow the monotonous behavior that one would expect, as discussed in the beginning of this section is due to the existence of a minimum in ΔE_{diss} and ΔE_{TS}. This will lead to a mixing of surfaces to the left and right of the minimum and hence change the order of the surfaces on the BEP line. The reason behind the minimum can be explain by studying the adsorption energy along the dissociation path, which for these diatomic molecules simply is the bond length (see Figure 6). We find that the PESs for the three different adsorbates on the considered La-perovskites have common and different features. First of all, for group 11 surfaces, the PESs shows that the dissociation is uphill all the way from the gas phase, that is the TS is FS-like. Secondly, as the group number decreases so does the position of the TS and its character. To begin with it becomes more IS-like.Thirdly, for each adsorbate there is a surface with the most IS-like TS. Fourthly, decreasing the group number even more results in a TS that gets more FS-like character.

For N_2, the TS is FS-like for $LaCuO_3$, it becomes less FS-like as the group number decrease, it turns to be maximally IS-like for $LaCrO_3$, and becomes less IS-like and eventually approaches FS character for substrates as the group number decreases. A similar analysis for NO yields that the most IS-like TS state is found for dissociation on $LaVO_3$, which is the last point to the left on the BEP line. For O_2, the TSs have an overall more IS-like character than the ones for N_2 and NO. Due to this property the α value is smallest for this adsorbate. The TS with most IS-like character found for $LaTiO_3$.

The conclusion is that when moving along a period from right to left the TS goes through a "cycle" from being FS-like, where the points fall on the recombination line, to IS-like, with the most IS-like TS corresponding to the most deviating points on the left-hand side on the BEP line, and becoming FS-like, falling back on the recombination line. Theres is no reason not to believe that this "cyclic" behavior should be valid for substrates with B metals with other group numbers outside the studied range.

Another support for determining the nature of the TS is the adsorbate geometry in the TS. The adsorbate–adsorbate distances (see Fig. 7) in the dissociated state (d_{diss}) are almost unchanged along a period while the adsorbate-adsorbate distances in the TS (d_{TS}) change in the same way as the ΔE_{TS} curves. This means for example that the La-perovskite at the minimum (the furthest to the left in the BEP line) has the smallest d_{TS} value

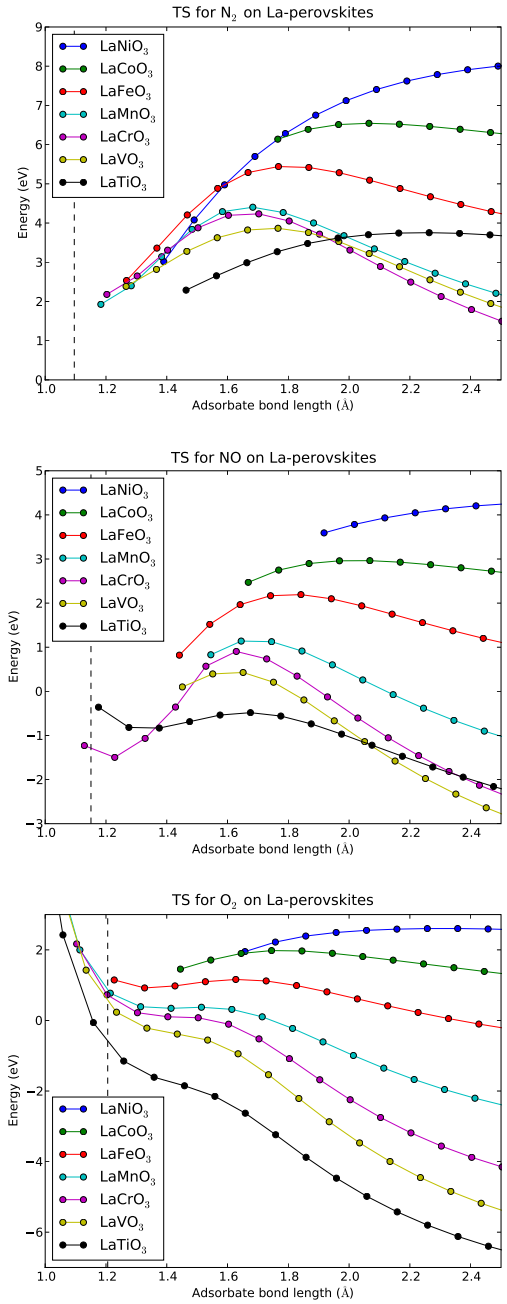

FIG. 6: Calculated adsorption energies along as a function of the molecular bond length for N_2, NO and O_2 on the considered La-perovskite (100) surfaces. The vertical dashed line indicates the bond length of the molecule in gas phase. [OBS: Add Sc and Cu results]

that is it closest to the gas phase bond length of the adsorbate. Hence, this point has the most IS character among the studied systems and deviates the most from the recombination line.

Hence, the coincidence of the BEP line with the recombination line, property (i), is attributed to the FS-like nature of the TS, while the deviation from the recombination line, property (ii), is attributed to the TS being more IS-like.

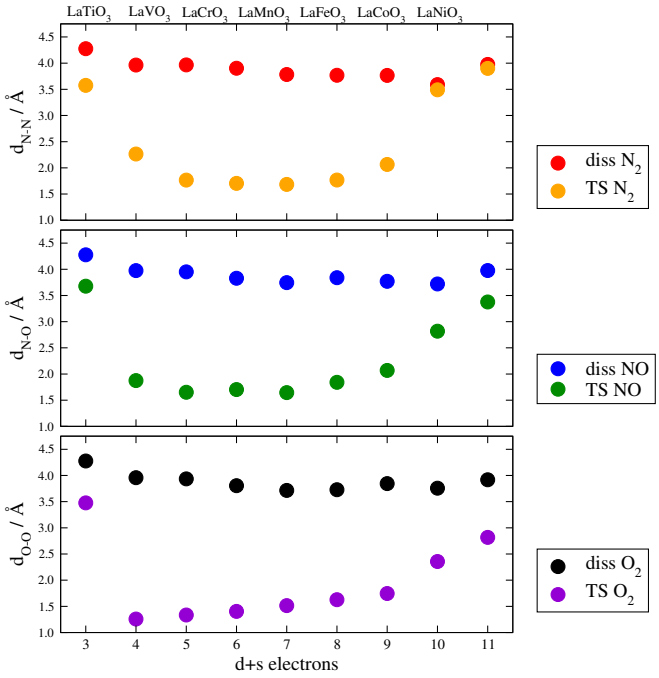

FIG. 7: Calculated adsorbate atom distances in the transition states and the dissociated states for N_2, NO and O_2.

SUMMARY AND OUTLOOK

In summary, density functional theory calculations show that transition state scaling relations also exist for oxides and have a rich detailed structure. Among the molecules and oxides investigated in this study, one finds the whole spectrum of relations with slopes from zero to one. We find that the universality found for metals is not valid for oxides.

Our results show that if the underlying nature of bonding in the TS and the dissociated state are the same, that is the TS is FS-like, these are correlated via a BEP relation with a slope close to unity. This is the case for molecules with strong intramolecular bonds. On the other hand, if the TS is more IS-like the BEP relations become FS-independent and the dissociative chemisorption energy is not a good descriptor for the dissociation. This is the case for very reactive surfaces or molecules with weak intramolecular bonds. We also find a "cyclic" nature in the TS character, that is it can change from being FS to IS and back to FS as the metal constituent of the surface changes along a period.

It is also found that, for a given molecule and active site, the transition state scaling relation can consist of several linear BEP relations. This is a form of generalized BEP relation, however, at the moment we do not have a

completely predictive approach of what the form of the BEP relation should look like for a given molecule and group of surfaces. This will be apart of future studies.

The combined knowledge of transition states scaling relations and scaling relations opens up the possibility to evaluate the activity of oxides. Hence, extending the fundamental knowledge of the reaction chemistry and physics at the atomic level may widen our perspectives of oxides as future heterogeneous catalysts.

Acknowledgments

The Catalysis for Sustainable Energy initiative is funded by the Danish Ministry of Science, Technology and Innovation. CAMD is funded by the Lundbeck foundation. The authors acknowledge support from the Danish Center for Scientific Computing. FCV acknowledges support from the Danish Council for Strategic Research, via the SERC project, through grant no. 2104-06-0011.

* Electronic address: alevo@fysik.dtu.dk

[1] J. N. Brønsted, Chem. Rev. **5**, 231 (1928), pdf.
[2] M. G. Evans and M. Polanyi, Trans. Faraday Soc. **34**, 11 (1938), pdf.
[3] J. K. Nørskov, T. Bligaard, A. Logadottir, S. Bahn, L. B. Hansen, M. Bollinger, H. Bengaard, B. Hammer, Z. Sljivancanin, M. Mavrikakis, et al., J. Catal. **209**, 275 (2002), pdf.
[4] A. Logadottir, T. H. Rod, J. K. Nørskov, B. Hammer, S. Dahl, and C. J. H. Jacobsen, J. Catal. **197**, 229 (2001), pdf.
[5] Z.-P. Liu and P. Hu, J. Chem. Phys. **114**, 8244 (2001), pdf.
[6] A. Michaelides, Z.-P. Liu, C. J. Zhang, A. Alavi, D. A. King, and P. Hu, JACS **125**, 3704 (2003), pdf.
[7] V. Pallassana and M. Neurock, J. Catal. **191**, 301 (2000), pdf.
[8] H. Falsig, B. Hvolbæk, I. S. Kristensen, T. Jiang, T. Bligaard, C. H. Christensen, and J. K. Nørskov, Angew. Chem. Int. Ed. **47**, 4835 (2008), pdf.
[9] A. Vojvodic, A. Hellman, C. Ruberto, and B. I. Lundqvist, Phys. Rev. Lett. **103**, 146103 (2009), pdf.
[10] F. Studt, F. Abild-Pedersen, H. Hansen, I. Man, J. Rossmeisl, and T. Bligaard, ChemCatChem **2**, 98 (2010), pdf.
[11] T. Bligaard, J. K. Nørskov, S. Dahl, J. Matthiesen, C. H. Christensen, and J. Sehested, J. Catal. **224**, 206 (2004), pdf.
[12] S. Wang, G. Jones, L. Grabow, F. Studt, T. Bligaard, F. Abild-Pedersen, J. K. Nørskov, B. Temel, and C. H. Christensen (2010), pdf.
[13] F. Abild-Pedersen, J. Greeley, F. Studt, J. Rossmeisl, T. R. Munter, P. G. Moses, E. Skulason, T. Bligaard, and J. K. Nørskov, Phys. Rev. Lett. **99**, 016105 (2007), pdf.
[14] pp. – (2008), pdf.
[15] J. Rossmeisl, Z. W. Qu, H. Zhu, G. J. Kroes, and J. K. Nørskov, J. Electroanal. Chem. **607**, 83 (2007), pdf.
[16] E. M. Fernández, P. G. Moses, A. Toftelund, H. A. Hansen, J. I. Martínez, F. Abild-Pedersen, J. Kleis, B. Hinnemann, J. Rossmeisl, T. Bligaard, et al., Angew. Chem. Int. Ed. **47**, 4683 (2008), pdf.
[17] K. Reuter and M. Scheffler, Phys. Rev. B **65**, 035406 (2001), pdf.
[18] A. G. Schrott, J. A. Misewich, M. Copel, D. W. Abraham, and Y. Zhang, Appl. Phys. Let. **79**, 1786 (2001), pdf.
[19] B. Hammer, L. B. Hansen, and J. K. Nørskov, Phys. Rev. B **59**, 7413 (1999), pdf.
[20] J. Greeley and M. Mavrikakis, J. Phys. Chem. **109**, 3460 (2005), pdf.
[21] J. I. Martínez, H. A. Hansen, J. Rossmeisl, and J. K. Nørskov, Phys. Rev. B **79**, 045120 (2009), pdf.
[22] G. Pacchioni, J. Chem. Phys. **128**, 182505 (2008), pdf.
[23] L. Wang, T. Maxisch, and G. Ceder, Phys. Rev. B **73**, 195107 (2006), pdf.
[24] S. Kümmel and L. Kronik, Reviews of Modern Physics **80**, 3 (2008), pdf.
[25] R. M. Nieminen, Modell. Simul. Mater. Sci. Eng. **17**, 084001 (2009), pdf.
[26] S. Bahn and K. W. Jacobsen, Comput. Sci. Eng. **4**, 56 (2002), pdf.
[27] D. Vanderbilt, Phys. Rev. B **41**, 7892 (1990), pdf.
[28] L. Bengtsson, Phys. Rev. B **59**, 12301 (1999), pdf.
[29] F. Calle-Vallejo, J. I. Martnez, J. M. García-Lastra, M. Mogensen, and J. Rossmeisl, Angew. Chem. Int. Ed. Engl. **49**, 7699 (2010), pdf.
[30] J. K. Nørskov, T. Bligaard, B. Hvolbaek, F. Abild-Pedersen, I. Chorkendorff, and C. H. Christensen, Chem. Soc. Rev. **37**, 2163 (2008), pdf.

J|A|C|S ARTICLES

Published on Web 01/23/2009

Adsorption-Driven Surface Segregation of the Less Reactive Alloy Component

Klas J. Andersson,[†] Federico Calle-Vallejo,[‡] Jan Rossmeisl,[‡] and Ib Chorkendorff*,[†]

Center for Individual Nanoparticle Functionality (CINF) and Center for Atomic-Scale Materials Design (CAMD), Department of Physics, NanoDTU, Technical University of Denmark, DK-2800 Kgs. Lyngby, Denmark

Received November 13, 2008; E-mail: ibchork@fysik.dtu.dk

Abstract: Counterintuitive to expectations and all prior observations of adsorbate-induced surface segregation of the more reactive alloy component (the one forming the stronger bond with the adsorbate), we show that CO adsorption at elevated pressures and temperatures pulls the less reactive Cu to the surface of a CuPt near-surface alloy. The Cu surface segregation is driven by the formation of a stable self-organized CO/CuPt surface alloy structure and is rationalized in terms of the radically stronger Pt−CO bond when Cu is present in the first surface layer of Pt. The results, which are expected to apply to a range of coinage (Cu, Ag)/Pt-group bimetallic surface alloys, open up new possibilities in selective and dynamical engineering of alloy surfaces for catalysis.

1. Introduction

Bimetallic alloys offer a way of tuning electronic structure and catalytic properties of metal surfaces.[1−6] Crucial to the catalytic performance of an alloy surface is its composition and structure. The bonding of adsorbates may induce changes in local atomic composition and surface structure, changing the activity and selectivity of the catalyst. Capitalizing on such effects for catalyst preparation means greater flexibility in alloy surface design for low-temperature applications. The expected response to adsorbates is that the more reactive alloy component (i.e., the one forming the strongest chemical bond with the adsorbates) segregates to the surface.[7−14] Counterintuitive to this picture, we show that CO adsorption induces surface segregation of the *less* reactive alloy component, Cu, switching a CuPt *near-surface* alloy[15] to a novel well-ordered CuPt *surface* alloy. This provides a new tool for selective and dynamical CuPt alloy surface engineering as, illustrated in Figure 1. The near-surface and surface alloys are hereafter denoted NSA and SA, respectively.

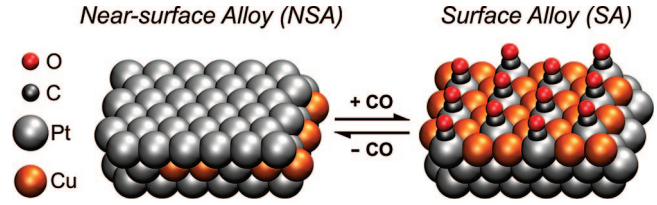

Figure 1. Illustration of (left) the CuPt NSA and (right) CO-induced Cu surface segregation and the novel SA resulting from it.

The CuPt NSA was recently suggested as a promising water-gas shift ($CO + H_2O \rightarrow H_2 + CO_2$) catalyst because of reduced Pt−CO bonding on a Pt catalyst surface with Cu present in the second layer,[15] alleviating possible CO-poisoning problems.[16] Expanding our work on the Cu/Pt(111) system,[17,18] we show that the NSA is unstable at elevated CO pressures and sample temperatures, forming instead a self-organized CO/CuPt SA

[†] Center for Individual Nanoparticle Functionality (CINF).
[‡] Center for Atomic-Scale Materials Design (CAMD).

(1) Sinfelt, J. *Bimetallic Catalysts: Discoveries, Concepts and Applications*; Wiley: New York, 1983.
(2) Besenbacher, F.; Chorkendorff, I.; Clausen, B. S.; Hammer, B.; Molenbroek, A. M.; Nørskov, J. K.; Steensgaard, I. *Science* **1998**, *279*, 1913–1915.
(3) Greeley, J.; Jaramillo, T. F.; Bonde, J.; Chorkendorff, I.; Nørskov, J. K. *Nat. Mater.* **2006**, *5*, 909–913.
(4) Chen, M.; Kumar, D.; Yi, C.-W.; Goodman, D. W. *Science* **2005**, *310*, 291–293.
(5) Studt, F.; Abild-Pedersen, F.; Bligaard, T.; Sørensen, R. Z.; Christensen, C. H.; Nørskov, J. K. *Science* **2008**, *320*, 1320–1322.
(6) Jacobsen, C. J. H.; Dahl, S.; Clausen, B. S.; Bahn, S.; Logadottir, A.; Nørskov, J. K. *J. Am. Chem. Soc.* **2001**, *123*, 8404–8405.
(7) Shu, J.; Bongondo, B. E. W.; Grandjean, B. P. A.; Adnot, A.; Kaliaguine, S. *Surf. Sci.* **1993**, *291*, 129–138. Gonzalez, S.; Neyman, K. M.; Shaikhutdinov, S.; Freund, H. J.; Illas, F. *J. Phys. Chem. C* **2007**, *111*, 6852–6856.
(8) Christoffersen, E.; Stoltze, P.; Nørskov, J. K. *Surf. Sci.* **2002**, *505*, 200–214.
(9) Menning, C. A.; Hwu, H. H.; Chen, J. G. G. *J. Phys. Chem. B* **2006**, *110*, 15471–15477.
(10) Hirsimäki, M.; Lampimäki, M.; Lahtonen, K.; Chorkendorff, I.; Valden, M. *Surf. Sci.* **2005**, *583*, 157–165.
(11) Bagot, P. A. J.; Cerezo, A.; Smith, G. D. W.; de Bocarme, T. V.; Godfrey, T. J. *Surf. Interface Anal.* **2007**, *39*, 172–177.
(12) Tao, F.; Grass, M. E.; Zhang, Y.; Butcher, D. R.; Renzas, J. R.; Liu, Z.; Chung, J. Y.; Mun, B. S.; Salmeron, M.; Somorjai, G. A. *Science* **2008**, *322*, 932–934.
(13) Nerlov, J.; Chorkendorff, I. *J. Catal.* **1999**, *181*, 271–279.
(14) Nerlov, J.; Sckerl, S.; Wambach, J.; Chorkendorff, I. *Appl. Catal., A* **2000**, *191*, 97–109.
(15) Knudsen, J.; Nilekar, A. U.; Vang, R. T.; Schnadt, J.; Kunkes, E. L.; Dumesic, J. A.; Mavrikakis, M.; Besenbacher, F. *J. Am. Chem. Soc.* **2007**, *129*, 6485–6490.
(16) Schumacher, N.; Boisen, A.; Dahl, S.; Gokhale, A. A.; Kandoi, S.; Grabow, L. C.; Dumesic, J. A.; Mavrikakis, M.; Chorkendorff, I. *J. Catal.* **2005**, *229*, 265–275.
(17) Schumacher, N.; Andersson, K.; Grabow, L. C.; Mavrikakis, M.; Nerlov, J.; Chorkendorff, I. *Surf. Sci.* **2008**, *602*, 702–711.
(18) Schumacher, N.; Andersson, K. J.; Nerlov, J.; Chorkendorff, I. *Surf. Sci.* **2008**, *602*, 2783–2788.

10.1021/ja8089087 CCC: $40.75

structure. The earlier density functional theory (DFT) study[15] indicated increased Pt−CO bonding when Cu is present in the first layer, similar to what is observed for other coinage/Pt-group metal systems.[19−22] Here we prove Cu surface segregation induced by a drastically stronger Pt−CO bond in the self-organized CO/CuPt SA structure. The results are confirmed by extended DFT calculations.

2. Methods

The ultrahigh vacuum (UHV)/high-pressure cell (HPC) system combined with a polarization modulation infrared reflection absorption spectroscopy (PM-IRAS) setup has been described elsewhere.[17] PM-IRAS is an FT-IR method utilizing s- and p-polarized radiation to distinguish between adsorbed and gas-phase molecules. Cu was deposited at a rate of ∼0.2 atomic layers/min on Pt(111) held at 425 K. No surface contaminants were observed by X-ray photoelectron spectroscopy (XPS), He^+ ion scattering spectroscopy (ISS), low-energy electron diffraction (LEED), or IR before, during, or after CO treatments. In particular, possible Ni impurities from $Ni(CO)_4$[14] were consistently measured to be ≤0.005 monolayer (ML) as judged by XPS.

The DFT calculations were performed using the DACAPO code.[23] Electron−ion interactions were described by ultrasoft pseudopotentials[24] within a plane-wave basis with a cutoff energy of 350 eV. Electron exchange and correlation effects were described by the RPBE[23] generalized gradient approximation functional. The electron density of the valence states was obtained by a self-consistent iterative diagonalization of the Kohn−Sham Hamiltonian with Pulay mixing of the densities.[25] The occupation of the one-electron states was calculated using an electronic temperature of $k_BT = 0.1$ eV (0.01 eV for CO in vacuum); all of the energies were extrapolated to $T = 0$ K. The surface [$(\sqrt{3} \times \sqrt{3})R30°$ unit cell] was modeled by a periodic array of four layers separated by more than 10 Å of vacuum. Adsorption energies were converged to within ∼0.05 eV with respect to slab thickness; energy differences are expected to be even more accurate. The energetics of Cu in the second layer relative to the bulk was evaluated using $(2\sqrt{3} \times \sqrt{3})R30°$ periodically repeated four-layer slabs with and without vacuum separation. For the surface calculations, the top two layers including CO were allowed to fully relax during geometry optimizations, and for the bulk calculations, all of the atoms were relaxed. Monkhorst−Pack grids with dimensions 3 × 3 × 1, 2 × 3 × 1, and 3 × 8 × 4 were used for sampling the Brillouin zones of the surface $(\sqrt{3} \times \sqrt{3})R30°$, surface $(2\sqrt{3} \times \sqrt{3})R30°$, and bulk $(2\sqrt{3} \times \sqrt{3})R30°$ structures, respectively. The experimentally determined Pt lattice parameter of 3.92 Å was used throughout.

3. Results and Discussion

Initially, a CuPt NSA was prepared by depositing one atomic layer of Cu ($\theta_{Cu} = 1$ ML) on Pt(111) and annealing to 800 K. XPS, ISS, and LEED analyses supported prior findings[15] that Cu is preferentially located in the second layer. The NSA's stability against CO adsorption was tested by a CO treatment in an HPC. The sample was exposed to CO at a pressure of 2 mbar for 10 min at various sample temperatures and then cooled to room temperature (RT) over 10 min in the CO, after which the CO was evacuated.

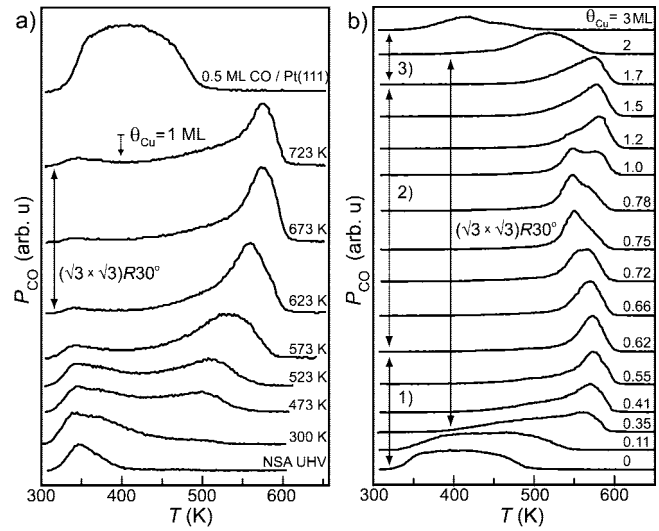

Figure 2. CO TPD spectra (2 K/s) recorded under UHV after various sample treatments. (a) Reference and post-treatment TPDs for a 1 ML Cu/Pt(111) NSA exposed to CO at 2 mbar for 10 min at the temperatures shown in the figure. Bottom and top traces (reference TPDs): NSA UHV (no high-pressure exposure) and 0.5 ML of CO on clean Pt(111), respectively. (b) TPDs after 2 mbar CO treatment at 673 K for varying amounts of Cu as displayed in the figure. Also marked in the figure are three distinctive regions (1, 2, and 3) and observations of a $(\sqrt{3} \times \sqrt{3})R30°$ LEED pattern, as discussed in the text.

We show in Figure 2 the CO temperature-programmed desorption (TPD) spectra obtained under UHV before and after the HPC CO treatments. First, for adsorption of CO under UHV conditions, we compare the CO desorption from the CuPt NSA (Figure 2a, bottom trace) to that from pure Pt(111) (Figure 2a, top trace). Evidently, less CO is adsorbed at RT and binds significantly more weakly (i.e., desorbs at a much lower temperature) on the CuPt NSA. This agrees well with prior findings.[15]

Exposing the CuPt NSA surface to 2 mbar CO at 300 K results only in very small changes, (see Figure 2a). However, after treatment at temperatures in the range 473−723 K in the 2 mbar CO, the CO desorption peaks are located at temperatures as high as 580 K. For $T_{treatment} \geq 623$ K, the CO coverages are large and saturated at 0.3−0.33 ML. The results demonstrate drastically increased CO binding energy, even compared with that on pure Pt(111), and we conclude that the CuPt NSA surface is not stable but undergoes changes when in the CO environment at elevated temperatures. The changes are reversible upon desorption of the CO under UHV by annealing to 673−800 K, which regenerates the NSA and its CO adsorption characteristics (Figure 2a, bottom).

On the basis of the TPD spectra measured after HPC CO treatments at 673 K for samples with varying θ_{Cu} in the range 0−3 ML (Figure 2b), three different regions were established: (1) $\theta_{Cu} < 0.62$ ML, (2) $\theta_{Cu} = 0.62-1.7$ ML, and (3) $\theta_{Cu} > 1.7$ ML. The starting surfaces were as-deposited Cu on Pt(111). The treatment temperature, 673 K, was chosen on the basis of the findings in Figure 2a and is well above the onset for Cu diffusion into Pt.[17] The high-temperature CO desorption feature at 570−580 K is fully developed at 0.62 ML (no traces of lower temperature states) and remains for a Cu content of up to 1.7 ML (region 2) before systematically shifting to lower temperature in region 3. An observed deviation at 0.72−1.2 ML of

(19) Hager, T.; Rauscher, H.; Behm, R. J. *Surf. Sci.* **2004**, *558*, 181–194.
(20) Gonzalez, S.; Illas, F. *Surf. Sci.* **2005**, *598*, 144–155.
(21) Sakong, S.; Mosch, C.; Gross, A. *Phys. Chem. Chem. Phys.* **2007**, *9*, 2216–2225.
(22) Inderwildi, O. R.; Jenkins, S. J.; King, D. A. *Surf. Sci.* **2007**, *601*, L103–L108.
(23) Hammer, B.; Hansen, L. B.; Nørskov, J. K. *Phys. Rev. B* **1999**, *59*, 7413.
(24) Vanderbilt, D. *Phys. Rev. B* **1990**, *41*, 1510.
(25) Kresse, G.; Furthmuller, J. *Comput. Mater. Sci.* **1996**, *6*, 15.

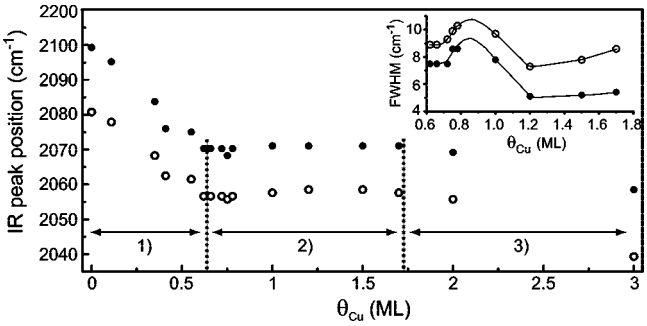

Figure 3. Correlation between atop-CO IR peak positions and (inset) fwhm's for the samples in Figure 2b during the 2 mbar CO/673 K treatment (○) and under UHV at 300 K after the treatment (●). Lines serving as guides to the eye are shown in the inset.

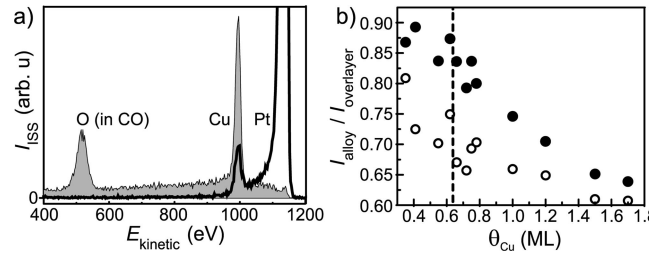

Figure 4. ISS and XPS spectra showing Cu surface segregation induced by CO adsorption. (a) ISS after 2 mbar CO/673 K treatment of a 0.67 ML Cu/Pt(111) sample (gray) and the corresponding NSA (black). (b) XPS Cu 2p/Pt 4d ratio (relative to the case of as-deposited Cu) for the 2 mbar CO/673 K treated samples in Figure 2b before TPD (●) and the corresponding NSAs after TPD (○). In (b), the line at ~0.62 ML of Cu marks an apparent Cu saturation in the first layer of the surface alloy (●).

Cu using the described sample-preparation procedure, with a ~550 K CO TPD peak, is discussed later in connection with our XPS results. In region 2, the saturation coverage of CO in the 570−580 K peak is very close to $^1/_3$ ML (0.36 ± 0.02 ML), as for the 1 ML CuPt NSA in Figure 2a.

Distinct surface changes accompanied the high-temperature desorption features in Figure 2. At 0.35 ML of Cu, the high-temperature desorption feature appeared (Figure 2b), accompanied by a weak, broad, diffuse $(\sqrt{3} \times \sqrt{3})R30°$ LEED pattern that was very sharp and intense at ~0.7 ML of Cu and further observed at up to 2 ML of Cu. The $(\sqrt{3} \times \sqrt{3})R30°$ LEED pattern was also clearly observed for the 1 ML NSA sample in Figure 2a for CO treatments at $T \geq 623$ K. Furthermore, whereas atop-adsorbed CO (~2100−2050 cm^{-1}) always was observed in IR spectra, bridge-bonded CO (~1855 cm^{-1}) was observed neither during nor after HPC CO treatment for any CuPt alloy surface with $\theta_{Cu} \geq 0.35$ ML.

When PM-IRAS was used to compare IR peak characteristics for atop-site-adsorbed CO (see Figure 3) the correlation between our in situ (2 mbar CO, 673 K) and ex situ (UHV, RT) data was found to be very high. The nearly constant shifts in IR peak position and fwhm broadening for the in situ data with respect to the ex situ data are most likely due to the temperature difference. The three regions 1, 2, and 3 already identified in the TPD data are strongly reflected in the IR data. From observations of a peak in fwhm in the range 0.72−1.2 ML of Cu, it is also apparent that the ~550 K CO TPD peak is reflected in the IR data. The in situ and ex situ IR peak positions and fwhm's for CO treatments of the sample with 1 ML of Cu at $T \geq 623$ K (Figure 2a) were identical (within 4 cm^{-1}) to those in region 2 of Figure 3. All of the results obtained under UHV at 300 K after HPC CO treatment strongly reflect the in situ surface characteristics during treatment.

Cu surface segregation was found to be associated with the CO-induced surface structural changes for the samples in Figure 2 by using ISS (1.2 keV He^+, $\theta = 125°$) and XPS to characterize the elemental composition in the topmost surface layer and near-surface region, respectively. In Figure 4a, the ISS spectrum after treatment of a sample with $^2/_3$ ML of Cu for 10 min at 673 K in 2 mbar CO is compared with the spectrum obtained from the corresponding NSA (~1 s anneal at 673 K under UHV). For the NSA, the Cu content in the top surface layer is very small (0.03 ML) and the Pt signal is dominant. Contrary to the expected diffusion of Cu into Pt at 673 K, Cu surface segregation due to the HPC CO treatment leads to a large ISS intensity for Cu (0.13 ML), and surface Pt is barely observed, being blocked by adsorbed CO. The maximum amount of Cu in the top surface layer observed for the samples in Figure 2 according to ISS was 0.14 ML. However, the actual coverage should be much higher, since experiments for 0.5 ML of CO on Pt(111) showed that adsorbed CO also blocks remaining surface sites from He^+ ion impingement.

The Cu surface segregation induced by the CO adsorption was also confirmed by XPS (see Figure 4b). Although there is a degree of scatter in the data, in every case the Cu content in the near-surface region after 10 min at 2 mbar CO and 673 K is significantly larger than for the corresponding NSA (~1 s anneal at 673 or 800 K under UHV). Very similar results were obtained for $T_{treatment} \geq 523$ K in Figure 2a. For the 0.35 ML ≤ $\theta_{Cu} \leq 0.62$ ML HPC CO-treated samples, the Cu signal is a nearly constant fraction (0.84−0.9) of the initial amount of Cu deposited, and this signal drops significantly for larger θ_{Cu}. Upon correlation of the XPS data with the ISS results showing large Cu amounts in the first layer, the findings indicate that essentially all of the Cu remains in the first layer up to ~$^2/_3$ ML, after which the superfluous Cu starts to distribute itself in deeper layers (hence the drop in relative intensity). The IR and TPD results suggest heterogeneity in the CO adsorption site, with some Cu in the second layer in the range 0.72−1.2 ML of Cu. The heterogeneity may be due to a small transition period after the onset of the Cu bulk migration at $\theta_{Cu} > {}^2/_3$ ML suggested by XPS, where some superfluous Cu still remains in the second layer, leading to the somewhat lowered (~25 K) CO desorption temperature in this region. At $\theta_{Cu} > 1.7$ ML, the origin of the lowered CO adsorption energy is likely a large second-layer Cu population even after the HPC CO treatment.

Although Cu diffusion to the first layer is endothermic,[15] the observed drastic increase in CO binding energy more than compensates for the endothermicity. This was established using DFT calculations. A $(\sqrt{3} \times \sqrt{3})R30°$ unit cell was used, and Cu was restricted to the first and second layers for total Cu amounts of $^1/_3$, $^2/_3$, 1, $^4/_3$, and $^5/_3$ ML with and without $^1/_3$ ML of CO adsorbed on atop Pt sites. Stabilities were calculated relative to Cu in the bulk and CO adsorption on clean Pt(111), as shown in Table 1.

For the clean surfaces (no CO adsorbed), $^2/_3$ ML of Cu in the second layer is the most stable, and Cu diffusion from the second to the first layer is generally endothermic by 0.3−0.4 eV. With $^1/_3$ ML of CO adsorbed atop surface Pt, the situation is very different: Cu surface migration to generate $^2/_3$ ML of Cu in the first layer is now most favorable. Clearly, there is a driving force toward having $^2/_3$ ML of Cu in the first layer when CO is adsorbed atop the remaining surface Pt sites. As Table 1 shows, the origin of the exothermicity is the vastly increased

Table 1. DFT Results for Cu Segregation Energies ($\Delta E_{segr,Cu}$) with and without $^1/_3$ ML of CO Adsorbed atop Pt and Differential ($\Delta E_{ads,CO}$) and Absolute ($E_{ads,CO}$) CO Adsorption Energies[a]

Cu content (ML)	distribution in 1st and 2nd layers (1st:2nd)	clean surface $\Delta E_{segr,Cu}$ (eV)	$\Delta E_{ads,CO}$ ($E_{ads,CO}$) (eV)	with CO adsorbed $\Delta E_{segr,Cu}$ (eV)
0	Pt_3Cu_0:Pt_3Cu_0	−	0 (−1.38)	−
$^1/_3$	Pt_3Cu_0:Pt_2Cu_1	−0.17	+0.08 (−1.30)	−0.09
	Pt_2Cu_1:Pt_3Cu_0	+0.13	−0.22 (−1.60)	−0.09
$^2/_3$	Pt_3Cu_0:Pt_1Cu_2	**−0.36**	+0.21 (−1.17)	−0.15
	Pt_2Cu_1:Pt_2Cu_1	0.00	−0.04 (−1.42)	−0.04
	Pt_1Cu_2:Pt_3Cu_0	+0.32	−0.64 (−2.03)	**−0.32**
1	Pt_3Cu_0:Pt_0Cu_3	−0.11	+0.23 (−1.16)	+0.12
	Pt_2Cu_1:Pt_1Cu_2	−0.09	+0.19 (−1.20)	+0.09
	Pt_1Cu_2:Pt_2Cu_1	+0.36	−0.37 (−1.75)	−0.01
$^4/_3$	Pt_2Cu_1:Pt_0Cu_3	+0.14	+0.37 (−1.02)	+0.51
	Pt_1Cu_2:Pt_1Cu_2	+0.50	−0.19 (−1.58)	+0.31
$^5/_3$	Pt_1Cu_2:Pt_0Cu_3	+0.85	+0.07 (−1.31)	+0.92

[a] Cu in the bulk and CO adsorption on clean Pt(111) were used as reference states. The most stable configurations are highlighted in bold print.

Pt−CO bond strength when $^2/_3$ ML of Cu is present in the first layer. The calculations also show weakening of the Pt−CO bond with increasing Cu content in the second layer. Both results strongly support our experimental findings, and the 0.6−0.85 eV increase in CO binding energy in going from the NSA to the SA with $^2/_3$ ML of Cu agrees very well with the value of 0.7 eV derived from our TPD data (peak positions, 350 vs 580 K; heating rate, 2 K/s; assumed first-order desorption and pre-exponential factor, $\upsilon \approx 10^{14}$ s^{-1}).[27]

For the very important case of $^2/_3$ ML of Cu and $^1/_3$ ML of adsorbed CO, the calculated higher stability of the CuPt SA compared with Cu in the bulk with CO adsorption on clean Pt(111) is nearly equal to the free-energy difference (ΔG). This is true because ΔG in this case can be taken as the enthalpy difference ΔH, since the estimated CO equilibrium coverages at 2 mbar CO and 673 K are very similar (close to $^1/_3$ ML) on Pt(111) (∼0.4 ML, from ref 26) and the CuPt SA (0.36 ± 0.02 ML).

We note that the results with adsorbed CO in Table 1 can explain the $\theta_{Cu} > \sim^2/_3$ ML onset of bulk migration of Cu indicated by our XPS data. In comparison with the $\theta_{Cu} = ^2/_3$ ML case, situations with higher Cu content in the top two layers are significantly less stable, leading to a significant Cu bulk migration driving force.

(26) Davies, J. C.; Nielsen, R. M.; Thomsen, L. B.; Chorkendorff, I.; Logadóttir, Á.; Lodziana, Z.; Nørskov, J. K.; Li, W. X.; Hammer, B.; Longwitz, S. R.; Schnadt, J.; Vestergaard, E. K.; Vang, R. T.; Besenbacher, F. *Fuel Cells* **2004**, *4*, 309–319.

(27) Chorkendorff, I.; Niemantsverdriet, J. W. *Concepts of Modern Catalysis And Kinetics*; Wiley-VCH: Weinheim, Germany, 2003.

Finally, although we have no atomistic picture of the actual mechanism for Cu migration in and out, the kinetic barriers are apparent in our data. The interdiffusion of Cu and Pt becomes significant at ∼460 K,[17] and this is also approximately where both the formation and breakup of the stable CO-induced surface alloy start to occur (see Figure 2). In forming the SA from the NSA, the interdiffusion mobility allows for Cu migration events to the first layer, and this Cu can then be trapped in the new low-energy SA configuration with CO adsorbed.

4. Summary and Conclusions

It is clear that CO adsorption at elevated pressures and temperatures on a CuPt near-surface alloy induces a large Cu surface segregation, generating a novel CuPt surface alloy to which CO binds very strongly, even compared with pure Pt(111). The Cu content needed for saturation of the SA is $\sim^2/_3$ ML of Cu, leading to a CO saturation coverage of $\sim^1/_3$ ML. The sharp CO TPD spectrum compared with that of pure Pt(111), the observed $(\sqrt{3} \times \sqrt{3})R30°$ LEED pattern, and the IR-peak red shift and narrow fwhm strongly suggest a significantly reduced lateral (repulsive) interaction between CO molecules adsorbed atop Pt sites and hence a well-ordered surface with well-defined, well-dispersed, and isolated Pt sites. DFT calculations reproduce the experimental observations and confirm that the vastly increased Pt−CO binding energy with $^2/_3$ ML of Cu in the first layer of Pt rationalizes the observed Cu surface segregation.

An important consequence of our results is that they add to the promise of using molecular adsorbate-induced surface changes as a tool for selective and dynamical engineering of alloy surfaces.[13,14] In view of the earlier indications of increased Pt-group metal bonding to CO when Cu or Ag is present in the first layer with a Pt-group metal,[19−22] our results for the CuPt system at elevated temperatures and CO pressures, where a novel stable CO-induced surface alloy forms, likely extend to a wide variety of coinage (Cu, Ag)/Pt-group bimetallic surface alloys.

Acknowledgment. CINF is sponsored by The Danish National Research Foundation, and CAMD is funded by the Lundbeck Foundation. K.J.A. acknowledges a postdoctoral grant from the Wenner-Gren Foundations, and F.C.-V. acknowledges support from the Strategic Electrochemistry Research Center. Dr. Martin Johansson, CINF, is gratefully acknowledged for helpful discussions.

JA8089087

Tuning the activity of Pt(111) for oxygen electroreduction by subsurface alloying

Ifan E.L. Stephens,[1] Alexander S. Bondarenko,[1,3] Francisco J. Perez-Alonso,[1] Federico Calle-Vallejo[2], Lone Bech,[1] Tobias P. Johansson[1], Anders K. Jepsen,[1] Rasmus Frydendal,[1] Brian P. Knudsen,[1] Jan Rossmeisl[2], Ib Chorkendorff.[1,]*

1. Center for Individual Nanoparticle Functionality, Department of Physics, Building 312, Technical University of Denmark, DK-2800 Lyngby, Denmark.

2. Center for Atomic-scale Materials Design, Department of Physics, Building 311, Technical University of Denmark, DK-2800 Lyngby, Denmark.

3. Center for Electrochemical Sciences, Ruhr-Universität Bochum, Universitätsstr. 150 NC 4/73, D-44780 Bochum, Germany.

EMAIL: ibchork@fysik.dtu.dk

RECEIVED DATE (to be automatically inserted after your manuscript is accepted if required according to the journal that you are submitting your paper to)

ABSTRACT

To enable the development of low temperature fuel cells, significant improvements are required to the efficiency of the Pt electrocatalysts at the cathode, where oxygen reduction takes place. Herein, we study the effect of subsurface solute metals on the reactivity of Pt, using a Cu/Pt(111) near-surface alloy. Our investigations incorporate electrochemical measurements, ultra high vacuum experiments, and density functional theory. Changes to the OH binding energy, ΔE_{OH}, were monitored in-situ, and adjusted continuously through the subsurface Cu coverage. The incorporation of submonolayer quantities of Cu into Pt(111) resulted in an 8-fold improvement in oxygen reduction activity. The most optimal catalyst for oxygen reduction has an $\Delta E_{OH} \sim 0.1$ eV weaker than pure Pt, validating earlier theoretical predictions.

INTRODUCTION

The widespread deployment of electric vehicles would reduce our dependence on fossil fuels and decrease our emissions of greenhouse gases. Polymer electrolyte membrane fuel cells (PEMFC's) are an attractive source of power for such vehicles.[1-2] However, at present, PEMFC's are prohibitively expensive. Further technological advances are needed to decrease the cost and improve the efficiency of the Pt catalysts at the cathode, where the oxygen reduction reaction (ORR) takes place:

$$O_2 + 4\,H^+ + 4\,e^- \rightarrow 2\,H_2O \quad (1)$$

Such breakthroughs would require (a) the replacement of Pt with active and abundant alternatives, or (b) improving the activity of Pt, for instance by alloying it with other metals.[2-4]

In order to meet this key challenge, a framework was developed to describe and *predict* the overall trends in ORR activity, using density functional theory (DFT) calculations.[5-8] There are at least two to three adsorbed intermediates in the ORR, OH*, OOH* and O* (where * denotes an adsorbed species). In order to catalyze the reaction, the binding to all these intermediates need to be optimized.

On the Pt nanoparticles which catalyze oxygen reduction in PEMFC's, it is widely believed that the active sites are located upon the terraces, in particular the (111) facets.[9-10] More under-coordinated sites bind the intermediates too strongly, and would tend to get poisoned. On (111) facets, the overpotential is either due to the hydrogenation of oxygen:[7-8,11]

$O_2 + H+ + e^- + * \rightarrow OOH*$ (2)

or the electroreduction of OH* to form water:

$OH* + H+ + e^- \rightarrow H_2O + *$ (3)

On Pt(111), the overpotential needed for OH* electrodesorption is marginally higher than that of OOH* formation, which means that step (3) is potential determining.[6,8] It follows that a catalyst which binds to OH* more weakly than Pt(111) would result in a decrease in the overpotential required for OH* reduction. However, it turns out that a surface that binds to OH* more weakly would also bind to OOH* more weakly, in which case OOH* formation, (2), would become potential determining. This is because the stability of O*, OH* and OOH* all scale linearly.[12-13] Therefore, knowledge of the OH adsorption energy, ΔE_{OH} allows us to describe ΔE_{OOH} and ΔE_{O}. This is essentially a modern day version of the 'Sabatier principle', which states that the most active catalyst for a given reaction should not bind too strongly or too weakly to the reaction intermediates.[14] There are numerous other examples in the recent literature where this principle, corroborated by electronic structure theory, has led to the development of quantitative models that describe important trends in gas phase heterogeneous catalysis and electrocatalysis. [5,7,15-22] According to a simple 'Sabatier analysis', the most optimal metal catalyst for the ORR has an OH adsorption energy, ΔE_{OH}, ~ 0.1 eV weaker than Pt(111).[5]

Several strategies have been employed to improve the ORR activity of Pt. These include: (a) the utilization of bulk alloys such as Pt_xY, Pt_xSc, Pt_xCo, Pt_xNi and Pt_xFe;[3,7,23-28] (b) dealloyed $PtCu_x$[29-31] and (c) the 'Pt monolayer' approach, whereby monolayer quantities of Pt are deposited onto a core composed of another, less expensive metal.[32-34] All of these catalysts have a surface overlayer composed entirely of Pt. DFT calculations support the notion that the Pt surface atoms on these catalysts exhibit mildly weaker binding to O* or OH* than pure Pt.[7,29] Indeed, the discovery of Pt_3Y

and Pt_3Sc as stable and active catalysts for the ORR was a direct output of the theoretical model, demonstrating its practical application.[7]

Thus far, it has not been possible to probe the descriptor, ΔE_{OH}, experimentally on a number of different surfaces with the same crystal orientation. However, Markovic and co-workers demonstrated that it was possible to estimate the d-band centre, ex-situ on a series of polycrystalline Pt_3M alloys, where M=Ni,Co,Fe,Ti,V, using ultraviolet photoemission spectroscopy.[23] The d-band centre is a general measure of surface reactivity.[35] A volcano relationship was demonstrated between the d-band centre and ORR activity, thus supporting the theoretical model.

On a given crystal facet, the binding of Pt to OH*, OOH* or O* can be adjusted by two different effects: ligand effects and strain effects.[35-37] Ligand effects occur when the electronic structure of the atoms sitting at the active sites are modified by neighboring atoms of a dissimilar atomic number.[38] For catalysts with a Pt overlayer, ligand effects will be more pronounced when the solute atoms are in the second layer; they are already negligible when the solute atoms are embedded in the fourth atomic layer.[39-40]

Strain effects occur when the catalyst is strained parallel to its surface.[29,39,41] The surface will tend to appropriate the lattice parameter of the bulk. Therefore, a change in the bulk composition will result in a corresponding change in the interatomic Pt-Pt distance at the surface. Compressive lattice strain weakens the binding of the Pt surface atoms to adsorbed intermediates, whereas tensile strain will have the opposite effect.

On Pt monolayer catalysts, ligand and strain effects are inseparable.[32-34] This is also the case for bulk Pt-alloy catalysts such as Pt_3Y, Pt_3Ni and Pt_3Co. Their surfaces should always be strained, as their bulk lattice parameters are dissimilar to Pt.[7,42-43] However, the most active forms of Pt_3Co and Pt_3Ni are those with an enrichment of the solute in the subsurface region, suggesting that ligand effects are also important for these catalysts.[25,27]

Strasser and co-workers demonstrated that the high ORR activity of dealloyed $PtCu_x$ could be attributed entirely to strain effects.[29,31] Ex-situ analysis suggested that the catalysts have a thick Pt skin

and a Cu-rich core. The smaller lattice parameter of Cu, with respect to Pt, effects a lateral strain to the Pt surface atoms. This, in turn, weakens the binding of the Pt surface atoms to OH*, OOH* and O*, resulting in a 4-6 fold enhancement in activity over pure Pt.[29] Their study confirmed that bulk lattice strain can be used as a tool to control the ORR activity of Pt. On the contrary, equivalent evidence to demonstrate the role of subsurface alloying has remained elusive.

In the current investigation, we study near-surface alloys (NSA's) of Cu/Pt(111). NSA's have unique catalytic properties, distinct from bulk alloys.[21,38,44-47] In a NSA, the solute atoms are only located in the subsurface region, as shown in Figure 3a. Therefore, in a Pt-based NSA, both the surface and the bulk are essentially composed of pure Pt. NSA's have been the focus of several fundamental surface science investigations, conducted under ultra high vacuum (UHV) conditions.[21,45-48] However, to the best of our knowledge, they have not previously been studied for continuous catalytic reactions (i.e. involving turnover) under ambient conditions. Using the Cu/Pt(111) NSA, we aim to elucidate how the catalytic activity of Pt can be tuned by the presence of subsurface metals, in the absence of bulk lattice strain.

Our attention was particularly drawn to the Cu/Pt(111) NSA by an investigation by Besenbacher and co-workers.[46] Their DFT calculations suggested that OH* was significantly destabilized on its surface, relative to Pt(111). In the light of the above discussion, this led us to believe that it could have favorable activity for the ORR.

EXPERIMENTAL SECTION

Full details of the experimental and theoretical methods used can be found in the Supporting Information.

RESULTS

Our experiments capitalize upon the detailed knowledge of the Cu/Pt(111) NSA gained from earlier surface science investigations.[46-48] In order to prepare and characterize the Cu/Pt(111) NSA in-situ, we designed and built a custom setup (further details can be found in the Supporting Information). Briefly, to prepare the desired NSA, up to 1 ML of Cu was electrodeposited onto a Pt(111) single crystal.[49] It

was annealed in Ar and H_2 at 400 °C, using an induction heater attached to the cell. The electrode was then characterized in the same cell, using cyclic voltammetry (CV) in 0.1 M $HClO_4$. To measure the ORR activity, the crystal was transferred to a separate cell with a rotating ring disk electrode (RRDE) assembly. The surface structures were independently verified ex-situ, under UHV conditions, using angle resolved X-ray photoelectron spectroscopy (AR-XPS). DFT calculations were used to provide a microscopic interpretation of our experimental observations (further details can be found in the Supporting Information).

Non-destructive depth profiles of the Cu/Pt(111) NSA were obtained using AR-XPS, as shown in Figure 1. A profile of a Cu/Pt(111) NSA is compared with a pseudomorphic Cu-overlayer on Pt(111)[50-51] and a Cu/Pt(111) surface alloy (SA), where the first layer consists of both Cu and Pt.[47,52] These data should be interpreted qualitatively rather than quantitatively, due to inherent uncertainties in the XPS measurements and the fitting procedures. Nonetheless, the profiles match closely with our expectations, formed on the basis of previous surface science studies.[46-47,50-52] Moreover, they provide a clear indication that the desired structures are formed.

To quantify the amount of Cu in the near-surface region, in Figure 2 we compare the Cu:Pt intensity ratio, as determined by XPS, for different Cu/Pt(111) NSA samples. The dashed line models the intensity ratio for the case where the amount of Cu initially deposited is equal to the amount of Cu in the second layer. When less than 0.5 ML Cu was initially deposited (where ML denotes monolayer), there appears to be a 1:1 correspondence between the amount of Cu initially deposited and the final subsurface Cu coverage in the NSA. However, when more than 0.5 ML Cu is initially deposited, the data suggest that some of the Cu is lost from the near-surface region, most likely into the bulk of the crystal. Our observations are consistent with those of Knudsen et al.[46] Their DFT calculations suggested that Cu was stabilized in the second layer of the Cu/Pt(111) NSA, in comparison to deeper layers. On the basis of their XPS results, they estimated that the coverage of Cu in the second layer was 40%, when 1 ML Cu had been deposited initially.

The CV's taken in N_2-saturated 0.1 M $HClO_4$, shown on Figure 3 provide further evidence for the formation of a Pt-skin on the NSA. In the case of the Cu overlayer, there is a sharp anodic peak at ~ 0.75 V, where Cu dissolves irreversibly into the solution as Cu^{2+}.[51] In the case of the Cu/Pt(111) SA, the Cu dissolution peak is shifted to more anodic potentials, and centered around ~0.85 V. The higher potential required to strip the Cu from the SA suggests that the Cu is stabilized, relative to the overlayer.[53-54] The Cu electrooxidation features are absent from subsequent cycles; presumably this is because the Cu^{2+} has diffused into the solution. On the contrary, the NSA does not show any features which would suggest that Cu is stripped from the surface. Instead, there is a reversible oxidation feature, unchanged with cycling. This is likely to be due to OH* electrosorption, i.e. the reverse of reaction (3).

Cyclic voltammetry in N_2-saturated solution was also used to probe the strength of the interaction of the Cu/Pt(111) NSA with H* and OH*, in-situ. Typical CV's of the NSA's with 0-1 ML Cu initially deposited, are shown on Figure 4a (a complete set of CV's is shown in the Supporting Information). The shifts in the H* and OH* adsorption peaks show that the presence of Cu in the subsurface destabilizes these adsorbates. Similar features were observed on $Pt_3Ni(111)$ and Pt overlayers on Ru(0001).[24,37] However, unique to the Cu/Pt(111) NSA is the ability to *continuously* adjust the interaction with H* and OH* through the subsurface solute concentration.

The ORR activity was measured for the different NSA surfaces, using CV, as shown in Figure 4b. The activity of Pt(111) reported here compares well with the literature.[24] For each of the catalysts, the current initially shows an exponential increase as the potential is lowered, due to decreasing activation barriers. At higher current densities, the flux of O_2 consumed by the ORR is greater than that which can be sustained by diffusion to the surface. This causes a depletion of O_2 at the electrode, until the current saturates at its diffusion limited value, ~ 6 mA cm^{-2}. The decrease in current below ~0.4 V reflects a change in the reaction pathway, from the complete 4 electron reduction of O_2 to H_2O, to the 2 electron pathway to H_2O_2 (evidence for this is provided in the Supporting Information). In the region of mixed kinetic-diffusion control, between $0.8 < U < 1.0$V (RHE), there is a pronounced positive shift of up to

~45 mV for the NSA's in comparison with Pt(111), revealing the significantly higher ORR activity of the NSA's.

The ORR activity of the Cu/Pt(111) NSA is stable during the course of the experiment. This observation is consistent with the XPS data shown in Figure 2. The NSA with 0.45 ML Cu initially deposited was analysed using XPS before and after 90 minutes of the ORR activity measurement. Within the limits of experimental accuracy, the Cu:Pt ratio remained unchanged.

DISCUSSION

The overall relationship between the amount of Cu deposited and ORR activity can be deduced from Figure 5a. It is clear that the ORR activity is highly sensitive to the presence of subsurface Cu. Our results confirm that it is possible to optimize the activity of a Pt(111) surface by varying the concentration of Cu in the subsurface region. The curve forms a 'volcano', with a broad maximum at ~0.5 ML Cu, representing an 8-fold increase in activity over Pt(111) at 0.9 V. This enhancement is close to the highest recorded to date, that of $Pt_3Ni(111)$.[24]

In order to understand our data in a broader context, it is perhaps more meaningful to relate the activity enhancement to a more universal descriptor, such as the OH binding energy, ΔE_{OH}. Changes to ΔE_{OH}, relative to Pt, i.e. $\Delta\Delta E_{OH} = \Delta E_{OH} - \Delta E_{OH}^{Pt}$, can be monitored in-situ, through the base voltammograms in N_2, shown in Figure 3a. The shift in potential required to reach 1/6 ML coverage of OH*, $\Delta U_{1/6\ ML\ OH}$, corresponds to the median value of $\Delta\Delta E_{OH}$. On a completely homogeneous Cu/Pt(111) NSA, $\Delta U_{1/6\ ML\ OH} = \Delta\Delta E_{OH}$.[6,24]

On Figure 5b, $\Delta U_{1/6\ ML\ OH}$ is plotted (in black) as a function of the initial amount of Cu electrodeposited onto the crystal. Evidently, $\Delta U_{1/6\ ML\ OH}$ increases with the Cu content. This trend is reflected in the theoretical plot of $\Delta\Delta E_{OH}$ versus the Cu coverage in the second layer, also shown (in blue) on Figure 5b. Up to ~0.5 ML Cu, the agreement between experiment and theory is good. However, at higher coverages, the large shift in $\Delta\Delta E_{OH}$ that is predicted by DFT is not replicated through $\Delta U_{1/6\ ML\ OH}$. This is analogous to the trend conveyed by the XPS data shown on Figure 2 and

described earlier. Together, these data suggest that it is not possible to obtain a high Cu coverage in the subsurface layer.

It is difficult to ascertain conclusively whether the destabilization of OH* in the NSA arises solely from ligand effects or strain effects. The DFT calculations implicitly assume that the structure is unstrained. The data shown in Figure 5b suggest that the calculations model the experiments well. On that basis, the observed modifications to the binding of the Pt surface could be entirely due to the ligand effect. Even so, there is experimental evidence to suggest that subsurface Cu could introduce some compressive strain to a Pt(111) surface.[48]

Combining the data from Figure 5a and Figure 5b allows us to plot the activity enhancement of the NSA as a function of $\Delta U_{1/6\ \mathrm{ML\ OH}}$, as shown in Figure 5c. The dashed blue line represents our earlier theoretical prediction, based on a simple Sabatier analysis.[5-6] There is a clear maximum in activity for the surface that binds OH* ~0.1 eV weaker than Pt(111), in agreement with earlier theoretical predictions.[5]

We note, from Figure 5c, that the peak activity enhancement from our experiments is around a factor of ~5 lower than that at the peak of the theoretical volcano. This discrepancy could be attributed to kinetic parameters which were not taken into account by the Sabatier analysis.[6] Moreover, it seems likely that the subsurface Cu concentration across the crystal is not uniform. Consequently, $\Delta U_{1/6\ \mathrm{ML\ OH}}$ may not correspond exactly to the $\Delta\Delta E_{\mathrm{OH}}$ of the active sites. The most active sites, with the value of $\Delta\Delta E_{\mathrm{OH}}$ being closest to the optimum, will dominate the ORR. Nevertheless, a clear trend persists between theory and experiment, as evidenced by the volcano shown in Figure 5c.

The current study complements Strasser and co-workers' investigations of the effect of bulk lattice strain on ORR activity, using dealloyed $PtCu_x$.[29,31] In comparison to dealloyed $PtCu_x$, the Cu/Pt(111) NSA's exhibited slightly higher activity enhancements over pure Pt, and also a clear maximum in activity as a function of Cu concentration. It seems that the peak of the volcano can be reached more easily when the solute metal is present in the subsurface. This supports the notion that an important goal in ORR catalysis is the preparation of stable Pt-alloy nanoparticles with a high subsurface concentration

of the solute component.[25] Moreover, from the data shown on Figure 3, it appears that subsurface Cu is more stable in the NSA than in dealloyed $PtCu_x$.[29,31] One could speculate that our annealing procedure stabilized the solute in the subsurface region, analogous to the observations made for bulk Pt-alloys.[55]

CONCLUSION

We have demonstrated that the presence of subsurface 3d metals can weaken the binding of a Pt surface to OH*. This corroborates previous theoretical studies of NSA's.[38,46] We make use of this phenomenon to engineer an ~8-fold enhancement in ORR activity over Pt(111).

We have also shown that it is possible to (a) monitor *in-situ* the binding energy of a simple adsorbate, in this case OH*, on a single crystal surface (b) tune this binding energy *continuously* (c) use this binding energy as an experimental descriptor for the activity of the surface for a catalytic reaction. We confirm the theoretical prediction that only a *slight* weakening of the descriptor, ΔE_{OH}, by ~0.1 eV, relative to Pt(111), will lead to optimal activity for the oxygen reduction reaction. To the best of our knowledge, this is the first time that the Sabatier principle has been demonstrated *in situ* for a continuous catalytic reaction on a well-defined single crystal surface. There is good reason to believe that this principle will continue to be used for the design of yet more active (and ideally abundant) catalysts to meet our future energy requirements.

ACKNOWLEDGMENTS: Funding by the Danish Strategic Research Council's (DSRC)'s HyCycle program and SERC project (grant no. 2104-06-0011) as well as the Spanish Government's, "Programa Nacional de Movilidad de Recursos Humanos del PN de I-D+I 2008-2011" is gratefully acknowledged. ASB acknowledges additional financial support from the European Union and the MWIFT-NRW (Hightech.NRW competition). The Center for Atomic-scale Materials Design is supported by the Lundbeck Foundation. The Center for Individual Nanoparticle Functionality is supported by the Danish National Research Foundation.

SUPPORTING INFORMATION

Full details of the experiments and calculations can be found in the Supporting Information section, including the results of additional electrochemical experiments and the raw AR-XPS data.

a. **Cu/Pt (111) near-surface alloy (NSA)**

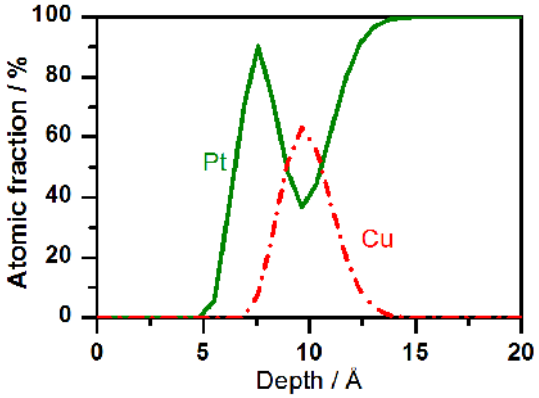

b. **Cu overlayer on Pt(111)**

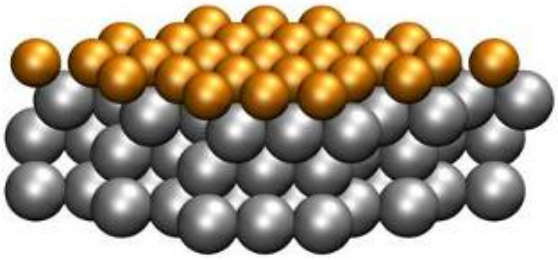

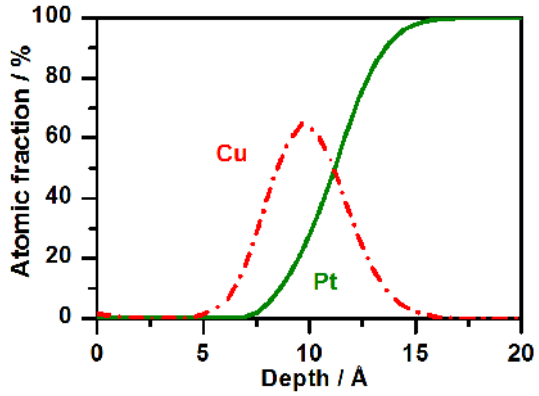

c. **Cu/Pt(111) surface alloy (SA)**

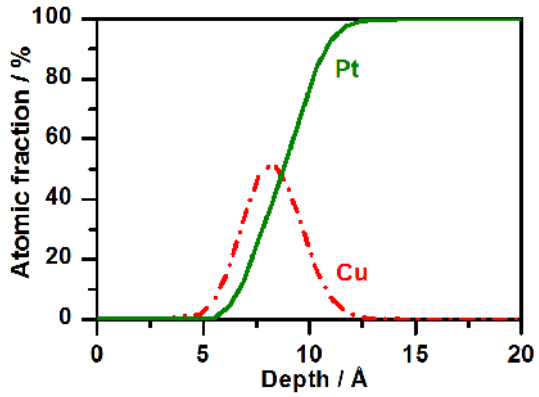

Figure 1. Non destructive depth profiles, of (a) the Cu/Pt(111) NSA, with 0.45 ML Cu initially deposited, in comparison to (b) the Cu overlayer on Pt(111), with 1 ML Cu initially deposited and (c) the Cu/Pt(111) surface alloy, with 1 ML Cu initially deposited. In a the Cu/Pt NSA had been exposed to ~ 90 minutes cycling between 0 and 1 V at 60 ºC in O_2-saturated 0.1 M $HClO_4$. The outermost ~5 Å were comprised of C and O, presumably accumulated from airborne contamination during

the transfer from the electrochemical cell, through the laboratory atmosphere to the UHV chamber. The C and O traces have been omitted, for clarity.

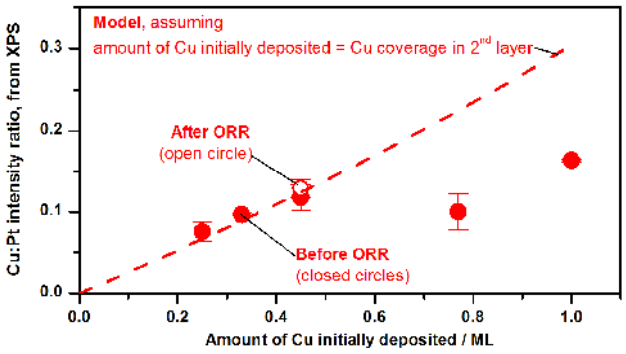

Figure 2. Cu:Pt intensity ratio, from XPS, for the different NSA structures. The analysis was based on the photoelectrons emitted at four different angles between 21 ° and 35 ° to the sample normal. The Cu:Pt intensity ratio is corrected for the excitation cross section, mean free path and the analyzer transmission (full details can be found in the Supporting Information). The error bars show the standard deviations from the data taken at different angles. The dashed line shows the modeled ratio, assuming that the amount of Cu initially deposited (as determined coulometrically), is equal to the subsurface Cu coverage, and that all the Cu is confined to the second layer. The open circle represents the Cu/Pt NSA sample with 0.45 ML Cu initially deposited, after exposure to ~90 minutes cycling between 0 and 1 V at 60 ºC in O_2-saturated 0.1 M $HClO_4$, (the corresponding depth profile is shown in Figure 1a.

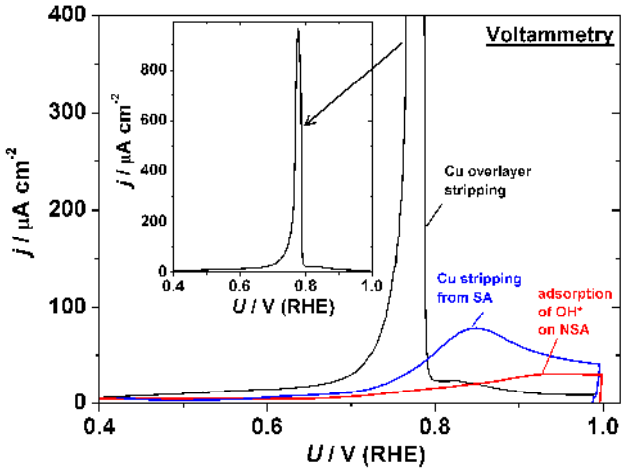

Figure 3. Cyclic voltammograms of the structures shown in Figure 1, , in N_2-saturated 0.1 M $HClO_4$, at room temperature, in the absence of Cu^{2+} in solution, dU/dt = 50 mVs^{-1}, anodic portion only; in each case 1 ML was deposited initially.

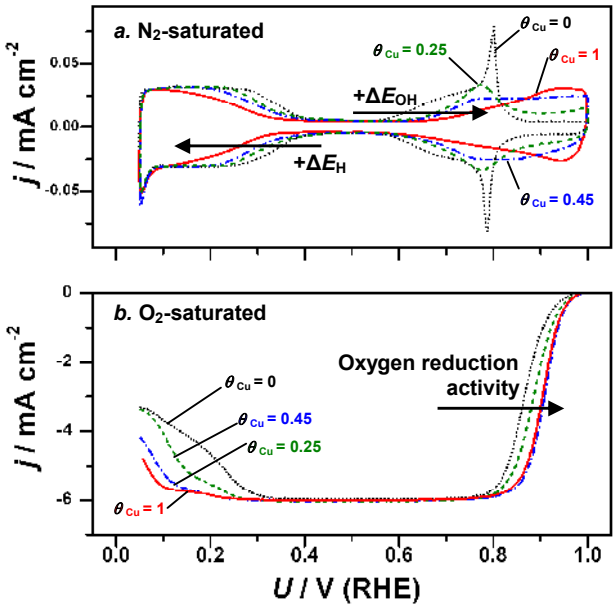

Figure 4 Electrochemical characterisation of Cu/Pt(111) NSA's, in comparison with Pt(111), using cyclic voltammetry in 0.1M $HClO_4$, at dU/dt=50mV s^{-1} (a) in N_2-saturated electrolyte (b) RRDE-voltammograms (anodic scans only) in O_2-saturated electrolyte, taken at 1600 r.p.m, 60°C. θ_{Cu} denotes the amount of Cu initially deposited, in monolayers (determined coulometrically, as described in the Supporting Information).

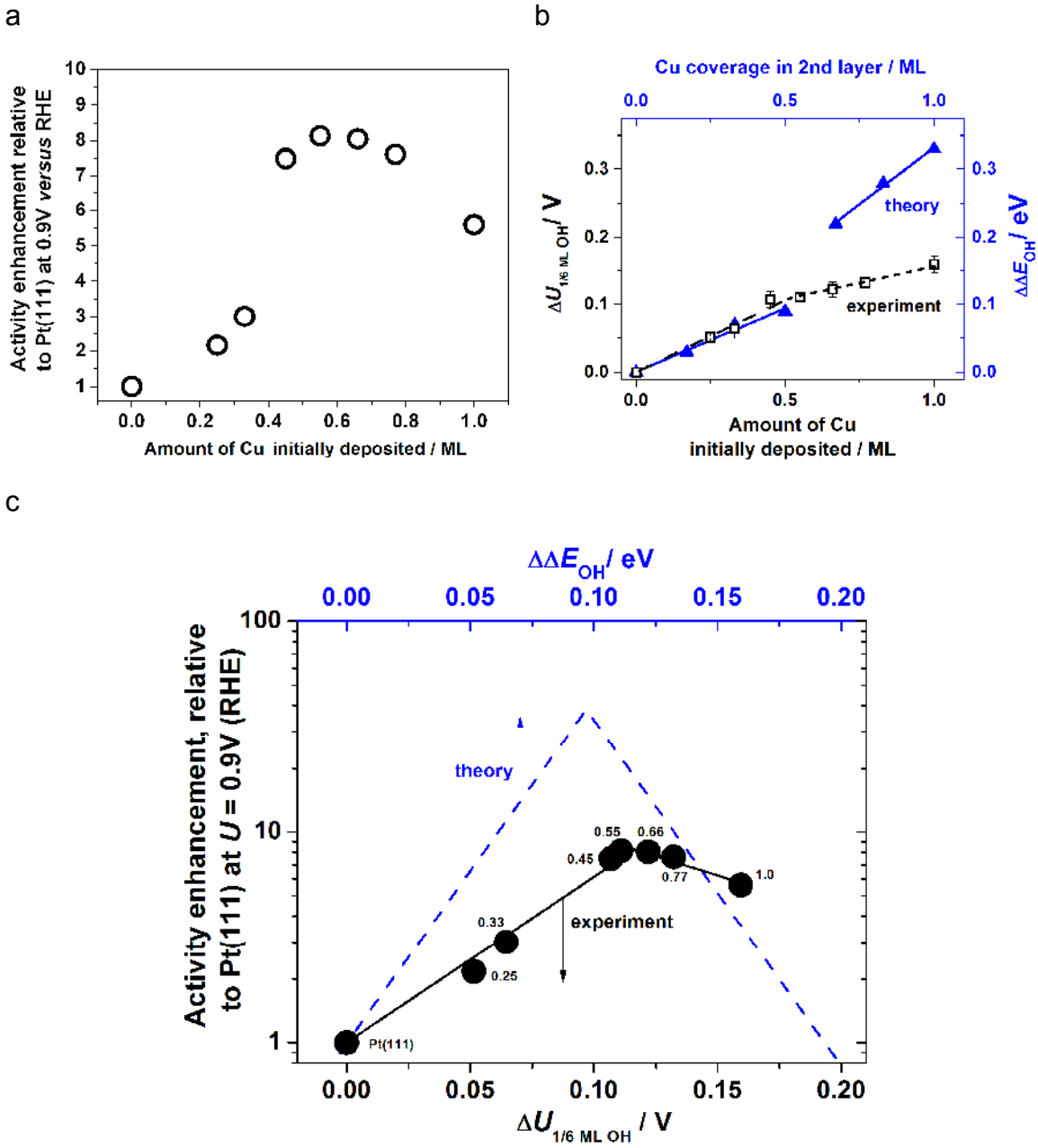

Figure 5. (a) Activity enhancement, relative to Pt(111) at U = 0.9 V as a function of the amount of Cu initially deposited. (b) Experimental and theoretical weakening of OH binding, as a function of Cu content; the linear trendlines were produced using a least squares fit. (c) Activity enhancement, relative to Pt(111) at U = 0.9 V versus RHE as a function of $\Delta U_{1/6\ ML\ OH}$ and $\Delta\Delta E_{OH}$. The experimental data points are the mean values, taken from 30 independent measurements, distributed across the entire composition range. The circular data points represent experimental data, produced by combining data from *a* and *b*. The dashed line represents earlier theoretical predictions, based upon a simple model using a Sabatier analysis.[5-6] The volcano here is plotted as a function of $\Delta\Delta E_{OH}$ instead of the oxygen adsorption energy, $\Delta\Delta E_O$; the two binding energies, relative to Pt (111), are related by the function $\Delta\Delta E_{OH} \sim 0.5\ \Delta\Delta E_O$.[13]

REFERENCES

(1) Eberle, U.; von Helmolt, R. *Energy & Environmental Science* **2010**, *3*, 689.

(2) Wagner, F. T.; Lakshmanan, B.; Mathias, M. F. *Journal of Physical Chemistry Letters* **2010**, *1*, 2204.

(3) Gasteiger, H. A.; Kocha, S. S.; Sompalli, B.; Wagner, F. T. *Applied Catalysis B-Environmental* **2005**, *56*, 9.

(4) Gasteiger, H. A.; Markovic, N. M. *Science* **2009**, *324*, 48.

(5) Nørskov, J. K.; Rossmeisl, J.; Logadottir, A.; Lindqvist, L.; Kitchin, J. R.; Bligaard, T.; Jonsson, H. *Journal of Physical Chemistry B* **2004**, *108*, 17886.

(6) Rossmeisl, J.; Karlberg, G. S.; Jaramillo, T.; Nørskov, J. K. *Faraday Discussions* **2008**, *140*, 337.

(7) Greeley, J.; Stephens, I. E. L.; Bondarenko, A. S.; Johansson, T. P.; Hansen, H. A.; Jaramillo, T. F.; Rossmeisl, J.; Chorkendorff, I.; Nørskov, J. K. *Nature Chemistry* **2009**, *1*, 552.

(8) Tripkovic, V.; Skúlason, E.; Siahrostami, S.; Nørskov, J. K.; Rossmeisl, J. *Electrochimica Acta* **2010**, *55*, 7975.

(9) Greeley, J.; Rossmeisl, J.; Hellman, A.; Nørskov, J. K. *Zeitschrift Fur Physikalische Chemie-International Journal of Research in Physical Chemistry & Chemical Physics* **2007**, *221*, 1209.

(10) Lee, S. W.; Chen, S.; Suntivich, J.; Sasaki, K.; Adzic, R. R.; Shao-Horn, Y. *Journal of Physical Chemistry Letters* **2010**, *1*, 1316.

(11) Janik, M. J.; Taylor, C. D.; Neurock, M. *J. Electrochem. Soc.* **2009**, *156*, B126.

(12) Abild-Pedersen, F.; Greeley, J.; Studt, F.; Rossmeisl, J.; Munter, T. R.; Moses, P. G.; Skulason, E.; Bligaard, T.; Nørskov, J. K. *Physical Review Letters* **2007**, *99*, 016105

(13) Rossmeisl, J.; Logadottir, A.; Nørskov, J. K. *Chemical Physics* **2005**, *319*, 178.

(14) Sabatier, P. *Berichte Der Deutschen Chemischen Gesellschaft* **1911**, *44*, 1984.

(15) Logadottir, A.; Rod, T. H.; Nørskov, J. K.; Hammer, B.; Dahl, S.; Jacobsen, C. J. H. *J. Catal.* **2001**, *197*, 229.

(16) Bligaard, T.; Nørskov, J. K.; Dahl, S.; Matthiesen, J.; Christensen, C. H.; Sehested, J. *J. Catal.* **2004**, *224*, 206.

(17) Nørskov, J. K.; Bligaard, T.; Logadottir, A.; Kitchin, J. R.; Chen, J. G.; Pandelov, S.; Stimming, U. *J. Electrochem. Soc.* **2005**, *152*, J23.

(18) Ferrin, P.; Nilekar, A. U.; Greeley, J.; Mavrikakis, M.; Rossmeisl, J. *Surf. Sci.* **2008**, *602*, 3424.

(19) Grabow, L. C.; Mavrikakis, M. *Angew. Chem.-Int. Edit.* **2008**, *47*, 7390.

(20) Nørskov, J. K.; Bligaard, T.; Rossmeisl, J.; Christensen, C. H. *Nature Chemistry* **2009**, *1*, 37.

(21) Hansgen, D. A.; Vlachos, D. G.; Chen, J. G. G. *Nature Chemistry* **2010**, *2*, 484.

(22) Neurock, M. *Ind. Eng. Chem. Res.* **2010**, *49*, 10183.

(23) Stamenkovic, V.; Mun, B. S.; Mayrhofer, K. J. J.; Ross, P. N.; Markovic, N. M.; Rossmeisl, J.; Greeley, J.; Nørskov, J. K. *Angew. Chem.-Int. Edit.* **2006**, *45*, 2897.

(24) Stamenkovic, V. R.; Fowler, B.; Mun, B. S.; Wang, G. F.; Ross, P. N.; Lucas, C. A.; Markovic, N. M. *Science* **2007**, *315*, 493.

(25) Stamenkovic, V. R.; Mun, B. S.; Arenz, M.; Mayrhofer, K. J. J.; Lucas, C. A.; Wang, G. F.; Ross, P. N.; Markovic, N. M. *Nature Materials* **2007**, *6*, 241.

(26) Toda, T.; Igarashi, H.; Uchida, H.; Watanabe, M. *J. Electrochem. Soc.* **1999**, *146*, 3750.

(27) Mayrhofer, K. J. J.; Juhart, V.; Hartl, K.; Hanzlik, M.; Arenz, M. *Angew. Chem.-Int. Edit.* **2009**, *48*, 3529.

(28) Chen, S.; Ferreira, P. J.; Sheng, W. C.; Yabuuchi, N.; Allard, L. F.; Shao-Horn, Y. *J. Am. Chem. Soc.* **2008**, *130*, 13818.

(29) Strasser, P.; Koh, S.; Anniyev, T.; Greeley, J.; More, K.; Yu, C. F.; Liu, Z. C.; Kaya, S.; Nordlund, D.; Ogasawara, H.; Toney, M. F.; Nilsson, A. *Nature Chemistry* **2010**, *2*, 454.

(30) Koh, S.; Strasser, P. *J. Am. Chem. Soc.* **2007**, *129*, 12624.

(31) Yang, R.; Leisch, J.; Strasser, P.; Toney, M. F. *Chemistry of Materials* **2010**, *22*, 4712.

(32) Zhang, J. L.; Vukmirovic, M. B.; Xu, Y.; Mavrikakis, M.; Adzic, R. R. *Angew. Chem.-Int. Edit.* **2005**, *44*, 2132.

(33) Zhou, W. P.; Yang, X. F.; Vukmirovic, M. B.; Koel, B. E.; Jiao, J.; Peng, G. W.; Mavrikakis, M.; Adzic, R. R. *J. Am. Chem. Soc.* **2009**, *131*, 12755.

(34) Adzic, R. R.; Zhang, J.; Sasaki, K.; Vukmirovic, M. B.; Shao, M.; Wang, J. X.; Nilekar, A. U.; Mavrikakis, M.; Valerio, J. A.; Uribe, F. *Topics in Catalysis* **2007**, *46*, 249.

(35) Bligaard, T.; Nørskov, J. K. *Electrochimica Acta* **2007**, *52*, 5512.

(36) Kitchin, J. R.; Nørskov, J. K.; Barteau, M. A.; Chen, J. G. *Physical Review Letters* **2004**, *93*, 156801.

(37) Hoster, H. E.; Alves, O. B.; Koper, M. T. M. *ChemPhysChem* **2010**, *11*, 1518.

(38) Kitchin, J. R.; Nørskov, J. K.; Barteau, M. A.; Chen, J. G. *J. Chem. Phys.* **2004**, *120*, 10240.

(39) Schlapka, A.; Lischka, M.; Gross, A.; Kasberger, U.; Jakob, P. *Physical Review Letters* **2003**, *91*, 016101.

(40) Lischka, M.; Mosch, C.; Gross, A. *Electrochimica Acta* **2007**, *52*, 2219.

(41) Mavrikakis, M.; Hammer, B.; Nørskov, J. K. *Physical Review Letters* **1998**, *81*, 2819.

(42) Bardi, U.; Beard, B. C.; Ross, P. N. *J. Catal.* **1990**, *124*, 22.

(43) Fowler, B.; Lucas, C. A.; Omer, A.; Wang, G.; Stamenkovic, V. R.; Markovic, N. M. *Electrochimica Acta* **2008**, *53*, 6076.

(44) Greeley, J.; Mavrikakis, M. *Nature Materials* **2004**, *3*, 810.

(45) Menning, C. A.; Chen, J. G. *Topics in Catalysis* **2010**, *53*, 338.

(46) Knudsen, J.; Nilekar, A. U.; Vang, R. T.; Schnadt, J.; Kunkes, E. L.; Dumesic, J. A.; Mavrikakis, M.; Besenbacher, F. *J. Am. Chem. Soc.* **2007**, *129*, 6485.

(47) Andersson, K. J.; Calle-Vallejo, F.; Rossmeisl, J.; Chorkendorff, L. *J. Am. Chem. Soc.* **2009**, *131*, 2404.

(48) Tsay, J. S.; Mangen, T.; Linden, R. J.; Wandelt, K. *Surf. Sci.* **2001**, *482*, 866.

(49) Herrero, E.; Buller, L. J.; Abruna, H. D. *Chemical Reviews* **2001**, *101*, 1897.

(50) Leung, L. W. H.; Gregg, T. W.; Goodman, D. W. *Langmuir* **1991**, *7*, 3205.

(51) Markovic, N.; Ross, P. N. *Langmuir* **1993**, *9*, 580.

(52) Andersson, K. J.; Chorkendorff, I. *Surf. Sci.*, *604*, 1733.

(53) Strasser, P.; Koh, S.; Greeley, J. *Physical Chemistry Chemical Physics* **2008**, *10*, 3670.

(54) Greeley, J.; Nørskov, J. K. *Electrochimica Acta* **2007**, *52*, 5829.

(55) Stamenkovic, V. R.; Mun, B. S.; Mayrhofer, K. J. J.; Ross, P. N.; Markovic, N. M. *J. Am. Chem. Soc.* **2006**, *128*, 8813.